PERFORMANCE ASSESSMENT & DUCTILITY ENHANCEMENT OF BEAMS SUBJECTED TO CYCLIC LOADING

By

MOHAMED LARBI DAALI

A Thesis
Submitted to the school of Graduate Studies
in Partial Fulfilment of the Requirements
for the Degree
Doctor of Philosophy

McMaster University
May 1995

DOCTOR OF PHILOSOPHY (1995)
(Civil Engineering)

McMASTER UNIVERSITY
Hamilton, Ontario

TITLE: PERFORMANCE ASSESSMENT & DUCTILITY ENHANCEMENT OF BEAMS SUBJECTED TO CYCLIC LOADING

AUTHOR: Mohamed Larbi Daali, B.A.Sc. (Constantine University)

M.A.Sc. (Waterloo University)

SUPERVISOR: Professor R.M. Korol

NUMBER OF PAGES: xxv, 247

PERFORMANCE ASSESSMENT & DUCTILITY ENHANCEMENT OF BEAMS SUBJECTED TO CYCLIC LOADING

ABSTRACT

Structural frames designed or proportioned to resist seismic forces, must possess adequate ductility to redistribute internal forces or have needed energy absorbing capability. This research investigation touches on a number of aspects that deal with or relate to the above characteristics, while the principal aim is to assess and compare the rotation capacity and energy absorption of locally web stiffened beams with unstiffened beams. .

An approach which allows for the prediction of the initiation of local buckling in the design of wide-flanged beams under moment gradient, is first presented. The method described represents a refined moment-rotation model that includes the effects of strain hardening. This same approach helps define more accurately the appropriate slenderness limits of a beam's plate-elements in relation to the required rotation capacity at maximum moment.

The study then addresses the interaction effects of a steel member's plate slenderness values and its lateral slenderness on rotation capacity at ultimate deformation. It is shown that members with slenderness values close to the limits specified by codes of practice may not be able to redistribute moments adequately under seismic loading.

To further ascertain and assess the ductility and energy dissipation capabilities of W-shaped beams, a series of test specimens subjected to monotonic and quasi-static cyclic loading was conducted. The specimens were meant to represent beams in ductile moment resisting frames undergoing cyclic lateral loads. Of direct relevance to seismically designed moment resisting steel frames, the experimental results of this research effort clearly highlight the superiority of herring-bone style stiffened specimens over unstiffened specimens. To provide further supporting evidence, as well as insights into the behaviour of herring-bone stiffeners, an inelastic large deformation analytical study was undertaken using cubic-quadratic shell finite elements. This work allowed a parametric study to be undertaken on the effects of stiffener thickness on strength and ductility properties. Based on these, and the experimental results, preliminary design guidelines have been proposed. Another important objective was to assess and document the strength and energy deterioration occurring under conditions of low cycle fatigue and which involve local buckling.

The results of a series of W-shaped test specimens subjected to fatigue type of loading under constant amplitude are presented. This work has permitted strength and energy deterioration and damage models to be developed for the W-shape steel beams. A generalized model which uses plate slenderness values together with lateral slenderness is proposed for predicting the rate in strength deterioration per reversal and cumulative damage after a given number of reversals.

The research investigation concludes with a review of some of the concepts used in damage assessment; simple damage parameters such as ductility ratio and realistic mathematical models reflecting the deterioration of steel beams due to maximum response, and, dissipated energy are then discussed. Damage models are then presented that combine maximum response with repeated effects in low-cycle fatigue loading. The proposed models calibrated through the use of cyclic tests on steel beams, are then used to yield deterministic parameters that predict adequate ductility values for steel beams under cyclic loading. This phase of the work was completed by having the damage models incorporated into a non-linear dynamic analysis of a sample building and ends with the recommendation of employing a new "adequate ductility" design parameter.

ACKNOWLEDGEMENTS

I would like first of all to thank my supervisor, Dr. R.M. Korol, for his encouragements, kindness and continuous moral support.

Grateful acknowledgement is also extended to other members of the supervisory committee, Dr. Ghobarah, Dr. Tso, Dr. A. Osman and Dr. Sowerby, for their valuable suggestions and comments.

The author also wishes to acknowledge with thanks the discussions and review of some of the work by Dr. Peter Fajfar of the University of Ljubljana and the Slovenian Academy of Sciences and Arts, and by Mr. E. Chien of the Canadian Institute of Steel Construction.

Last but not least, I thank all the staff and faculty members of the Civil Engineering Department for their kindness and the graduate students with whom I had many stimulating discussions.

To my parents, to my wife Karima.

TABLE OF CONTENTS

List of Figures

List of Figures (cont'd)

List of Figures (cont'd)

List of Figures

List of Figures (cont'd)

List of Figures (cont'd)

List of Figures (cont'd)

List of Tables

LIST OF SYMBOLS

b = Flange width

C_f = Parameter that reflects the level of restraint between the flange and web

D = Cumulated damage in N reversals

d = Deterioration per reversal

d_s = Cumulated deterioration in strength

dE = Increment of dissipated energy

dx = Element of length

E = Young's modulus

E_s =Modulus at failure

E_h = Energy dissipated in a given one full reversal

E_u = Energy dissipated in the first full reversal before a significant degradation takes place

e = Ratio of E to E_s

e_e = Dissipated energy normalized by the elastic energy

e_p = Dissipated energy normalized by the elasto-plastic energy

F_y = Resisting force at yield

F_p = Plastic load

F_u = Resisting force at ultimate

FR = Force reduction factor in NEHRP

List of Symbols (cont'd)

FR_w = Force reduction factor in UBC

h = Clear depth of web between flanges

h_e = Equivalent depth

K = Plate buckling coefficient

K_r = Reduced secant stiffness

K_y = Elastic stiffness

K_u = Stiffness at ultimate

L = Span length, or, unsupported length

L_{hw} = Length of half the buckling wave-length

M = Beam moment

M_p = Plastic moment

M_{cr} = Critical moment

R_u = Rotation capacity at ultimate deflection

R_m = Rotation capacity at maximum responce

R_μ = Ductility reduction factor

r_y = Radius of gyration about a section's weak axis

s = Ratio of strain at commencement of strain hardening to yield strain

t = Flange thickness

w = Web thickness

Z = Plastic section modulus

List of Symbols (cont'd)

α_f = Modified flange slenderness

α_l = Modified lateral slenderness

α_w = Modified web slenderness

α_e = Effective slenderness ratio

β_1 = Calibration factor

β_2 = Calibration factor

θ = End rotation

θ_m = Rotation corresponding to maximum moment

θ_u = Rotation corresponding to maximum ductility

θ_{pl} = Rotation corresponding to plastic moment

ϵ_b = Critical strain

η = Ratio of L_{hw} to L

ζ = $\sqrt{(300/\sigma_y)}$

μ = Ductility

μ_A = Adequate ductility

μ_m = Material ductility

μ_u = Member ductility

μ_s = System ductility

μ_{mono} = Monotonic ductility

List of Symbols (cont'd)

μ_{max} = Maximum experienced ductility

μ_i = Ductility measured from zero load intercept and experienced during the ith reversal

Δd = Rate of deterioration (in strength, stiffness, or dissipated energy)

Δd_s = Rate of deterioration in strength

Δd_e = Rate of deterioration in dissipated energy)

Δ_p = Displacement associated with F_p

Δ_u = Displacement at ultimate

Δ_i = Displacement at some characteristic point

Δ_{rp} = Residual plastic deformation

π_d = Plasticity ratio

σ_y = Actual yield stress

σ_u = Ultimate stress

σ_{cr} = Critical stress

σ_{av} = Average stress

σ_{yf} = Actual yield stress in flange

σ_{yw} = Actual yield stress in flange

ν = Poisson's ratio

Ψ = Experimentally determined parameter

List of Symbols (cont'd)

χ = Parameter that depends on the relative rigidity of connecting members

Ω = Overstrength factor

$\sum e_e$ = Cumulated elastic normalized energy

$\sum e_p$ = Cumulated elasto-plastic normalized energy

ϕ = Curvature

ϕ_p = Curvature at the plastic load

Θ_p = Plastic rotation range

CHAPTER 1

INTRODUCTION

1.1 General:

When subjected to strong earthquake motion, fully ductile moment resisting frames (M.R.F's) will undergo large plastic deformations in critical moment locations, such as at beam ends, in columns at floor levels, and at panel joints. Each one of the structural elements corresponding to these above-mentioned locations can be a possible candidate as a preselected critical section.

To resist design seismic forces, moment resisting frames must have their structural elements able to absorb energy inelastically during a strong motion earthquake. To do so, adequate plastic deformation capacity of the steel members must be achieved throughout selected points in the structure. Beams are one of the structural elements that have the ability to dissipate large amounts of energy. Hence, it is reasonable to expect that efficiently designed earthquake-resistant structures will generally depend at least in part on the ability of the beams, columns and panel zones to absorb energy (Galambos 1967).

In recent design codes, members classified as plastic design sections are assumed to sustain a resisting moment without loss of strength until a required rotation capacity is achieved, thus permitting full redistribution of bending moments to other parts of the structure. The response of such members to transverse loading is generally well understood up to the initiation of local buckling. However, concern arises about their ability to achieve adequate plastic rotation in the inelastic range.

Indeed, the present Canadian code applicable to the design of steel moment resisting frames (CAN/CSA-S16.1-M89) prescribes the use of class 1 sections for ductile moment resisting frames. This is meant to ensure that severe plastic straining can take place without loss of strength during load reversals. What perhaps needs to be raised is the question of whether a member possessing a desirable monotonic moment rotation curve for plastic design will satisfy the requirements of maintenance of resistance at hinge locations for several seismic cycles. Stated another way: does the member possess sufficient ductility and strength at the end of the seismic event to meet the specified requirements?

Several researchers have pointed out, under cyclic loading, weaknesses of some structural elements that satisfy the requirements of plastic design. Beamish (1987) noted that under load reversals, local flange buckling can occur at relatively low ductility in members having plate slenderness ratios close to the plastic design limits. Mitani et al. (1977) and Takanashi et al. (1973) highlighted the poor ductility achievement of some members complying with the requirements of plastic design. More recently, Ghobarah et al. (1990) pointed out that the slenderness limits of the flanges, (b/2t), and the web, (h/w), for steel beams in moment resisting frames located in highly seismic areas may be unconservative in certain situations, thus leading to a reduction in their load carrying capacity.

A prime reason for such above-described response appears to be linked to the nature and duration of the load histories and the associated modes of failure that can take place. Cyclic tests done by Krawinkler et al. (1971) showed that the development of local instabilities in a beam's plate elements is accelerated and accentuated by load reversals. Hence, it is not logical to expect these sections to sustain the same level of damage under loadings that are non-monotonic. Consequently, there is a possibility of progressive damage during the inelastic response of a member being subjected to the loading history of a given earthquake. It seems clear, therefore, that the use of slenderness limits derived on the basis of monotonic loading should not be directly applied to beams subjected to a load history consisting of a number of inelastic excursions.

The flanges and web of a beam tend to behave as plate elements (Walpole 1985). Provided that these plates have edge restraint, they are able to sustain significant levels of load even when distorted after local buckling. In this context, Climenhaga and Johnson (1972) compared monotonic tests of unstiffened continuous composite beams with ones that were longitudinally web stiffened. Their tests showed improved moment-rotation characteristics for the specimens with longitudinal web stiffeners. Kemp (1986) studied the influence of having pitched-roofs locally stiffened; he concluded that the use of local diagonal stiffeners approximately doubled the rotation capacity in monotonic test specimens in which the critical modes were local flange or web buckling.

1.2 Objective and Scope:

It seems that no in-depth study has been undertaken on the assessment of a steel beam's ductility or rotation capacity, as it relates to combined slenderness limit ratios. The duration of the load history may also have a significant detrimental effect on the response characteristics of the beams. On the other hand, it appears that the contribution of local stiffeners, in a potential plastic hinge region, may enlarge the plastic plateau, enhance the energy dissipation capability but indeed also justify a relaxation of stringent requirements for the member's flange plate slenderness (b/2t) and web plate slenderness (h/w) ratios.

The prime focus of this research is, therefore, to:

1) Assess the design rules as they relate to plate slenderness, lateral slenderness and ductility demands under monotonic loading.

2) Report on an experimental investigation into the assessment of sections selected according to design rules and tested under monotonic and cyclic loading. The effects of adding local stiffeners to W-shaped beams on the enhancement of rotation capacity and energy absorption when subjected to cyclic loading are also investigated.

3) Propose preliminary design guidelines that may be used to permit retrofit or reinforcement of steel beams that are identified as critical elements.

4) Shed some light on the effects of low-cycle fatigue on the resistance and energy deterioration in stiffened and unstiffened steel beams. It is also the aim here to develop a comprehensive model for prediction of the rate of deterioration in strength and dissipated energy for W-shaped beam sections in general.

5) Address damage assessment in steel beams when repeated loads with low-cycle fatigue characteristics are allowed for simultaneously. We also endeavor to develop damage models that would permit quantification of damage in steel beams; criteria that may be used when selecting beams for earthquake type loading will also

be proposed.

6) Finally, apply the damage models in nonlinear dynamic analysis for identification of beam elements that may have been inadequately selected.

A flowchart that illustrates all these steps for the specimens investigated is presented in Fig. 1.1

1.3 Organisation of the research program

In Chapter 2 of this thesis is presented a methodology that discusses the assessment of the local buckling design rules at maximum monotonic response and ultimate deformation. An experimental program that investigates unstiffened and stiffened Class 1 section beams is described in Chapter 3. The same Chapter discusses a parametric numerical study and presents preliminary design guidelines for beams locally stiffened. This is followed in Chapter 4 by an investigation into the effects of low-cycle fatigue on the resistance and energy deterioration in steel beams. Chapter 5 discusses damage models that were developed for the quantification of damage in beams. An application of the damage models is demonstrated, in Chapter 6, in a nonlinear dynamic analysis of a seven-storey steel moment resisting frame. Finally, a summary of the research work and conclusions along with recommendations for future work are drawn and presented in Chapter 7.

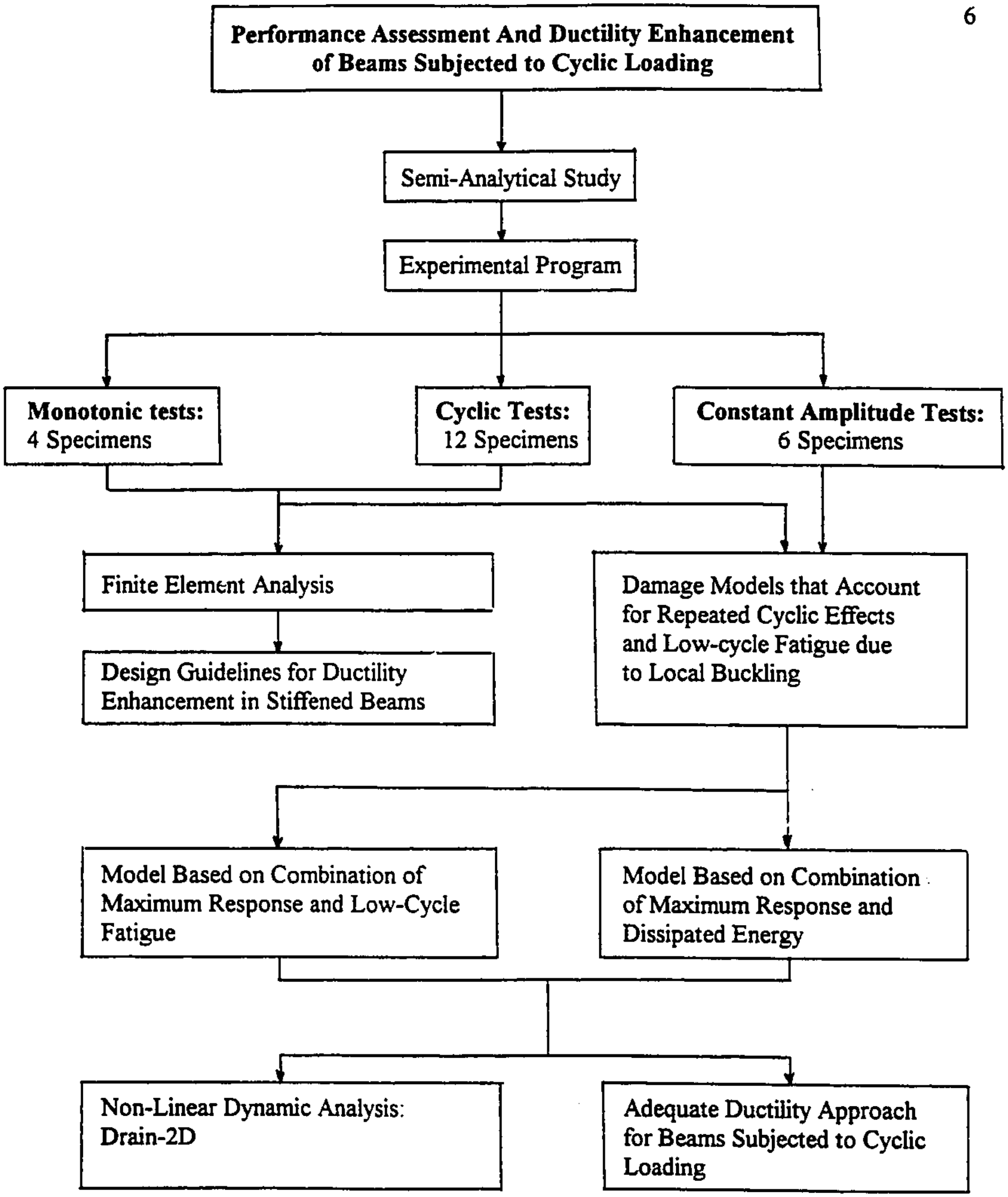

Fig. 1.1 Flowchart of Plan of Study

CHAPTER 2

ASSESSMENT OF CLASS 1 SECTION BEAMS

2.1. Introduction

A desirable attribute of a Class 1 (or plastic design) steel beam subjected to static loading is the maintenance of its full moment capacity under extensive plastic deformation. Such a response is perhaps best exhibited in the member's moment-curvature relationship as shown in Fig. 2.1. In a rigid frame structure, this type of behaviour permits sufficient inelastic rotations at potential plastic hinge locations to form, thus achieving full redistribution of moments prior to collapse. Such a response is desirable since it results in economic savings and provides adequate warning of possible failure. To achieve this objective, one of the easiest procedures is to limit plate slenderness and the lateral slenderness to their critical limits. The local buckling limits which are in use (Bild & Kulak 1991) were derived, mainly in the sixties and seventies, from simple plate-models. On the basis of Haaijer and Thurlimann's (1958) suggestion, namely that a plastic section reach strain hardening before local buckling occurs, researchers such as Lay (1965), Lay and Galambos (1965, 1967), Kato (1965), Climenhaga (1972) and Dawe and Kulak (1984) worked out design guidelines in the form of well known plate slenderness limits on the flange, (b/2t) and on the web, (h/w). Another important parameter is the lateral slenderness limit (L/r_y).

In the response of plastic design sections, two points on the monotonic moment-rotation curve (Fig. 2.1) are of major importance. These are the point at which strength degradation is initiated $(\theta=\theta_m)$ and the location corresponding to maximum ductility $(\theta=\theta_u)$ which denotes moment M dropping below the plastic moment, M_p. The rotation limits as expressed by θ_m and θ_u are associated with what are known as rotation capacities. R_m represents the rotation capacity at maximum moment and R_u is the rotation capacity at what will be termed ultimate displacement or rotation, i.e $\theta=\theta_u$ (Fig. 2.2). In the sections which follow, we shall discuss the flange slenderness (b/2t) and the web slenderness (h/w) ratios for loading cases where the rotation capacity requirements, R_m and R_u, at maximum moment and at ultimate displacement, respectively, are just met. An assessment of the plate slenderness limits will be done depending on whether the rotation capacity value is specified at maximum moment or at ultimate displacement.

2.2. Initiation of strength degradation and rotation capacity at maximum moment

Buildings may suffer significant over-stress and local failures when subjected to strong intensity earthquakes. In the numerical nonlinear analysis of moment resisting building frames, it is usually assumed that beams develop plastic hinges at their ends when the end moment reaches its plastic limit. At a limiting critical strain, local buckling of plastic sections is initiated; this local buckling inhibits the further increase in the member's resistance. Numerical methods of nonlinear analysis usually employ the elasto-perfectly plastic form of the moment-curvature relation or the bilinear form with strain hardening moment-curvature relationship to model the ductility response of the members; however, these approximations do not enable predictions of response associated with the apex point of the force-deflection or moment-rotation curves. The use of a bilinear moment curvature relationship with strain hardening (Fig. 2.1) may be acceptable if the section used in the analysis can be shown to develop a rotation, at maximum moment, greater than or equal to the rotational demand.

In the following an approach which permits the prediction of the initiation of strength degradation, under a moment gradient, is developed. The method permits the prediction of the rotation capacity corresponding to the maximum moment, and allows for definition of plate slenderness values linked to the initiation of plastic buckling. Flange and web slenderness interaction diagrams are developed prescribing the limits necessary to attain the required rotation capacity at maximum moment.

2.2.1 Analysis

A cantilever beam with a concentrated load at its tip will have a bending moment of the sort shown in Fig. 2.3-b. If use is made of a simplified stress strain relationship shown in Fig. 2.3-d, the curvature in the member becomes the variation assumed in Fig. 2.3-c from elementary beam theory.

2.2.2 Local Buckling

It has been found from tests (Daali and Korol 1994, Lukey and Adams 1969 and

Kuhlmann 1989) on structural steel beams transversely loaded, that plate buckling and associated strength deterioration of W-shape plastic sections is usually initiated at stresses varying between 1.10 to 1.4 (with an average of 1.25) times the yield stress. With such post yield stresses, the extremities of the cross-section locally undergo very high plastic strains. At some limiting critical value of strain, it has been observed that one or more of the plates will likely buckle locally. This local buckling phenomenon, then, tends to inhibit a further increase in a member's bending resistance.

The rotations, θ_m and $\theta_{pl.}$, corresponding respectively to the maximum moment and the plastic moment (Fig. 2.1), are obtained by integrating the areas under the corresponding curvatures between the support and the tip of the beam (Fig. 2.3-c). The rotation capacity, R_m, can be obtained as a function of the material characteristics, e, i.e., the ratio of E to E_s, s, the ratio of the strain at commencement of strain hardening to the yield strain, and the ratio, η, representing the yielded length of the flange to the overall length, $\eta = L_{hw}/L$, where the expression for evaluating L_{hw} is given in section 3.6.2 of Chapter 3. The expression for R_m can be written (Kemp, 1986) as:

$$R_m = \frac{\theta_m}{\theta_{pl.}} - 1 = \eta\left((2s-1) + e\frac{\eta}{1-\eta}\right) \tag{2.1}$$

Eqn. (2.1) permits prediction of the rotation capacity, at maximum moment, for specific values of the yielded proportion of the flange in compression for which the stress strain relationship for the material is as shown in Fig. 2.3-d.

2.2.3 Stress ratio

A plastic section reaches its plastic moment when yielding extends over virtually all cross-sectional fibres. This yielding situation occurs when strains in the flange reach strain hardening. However, the plastic moment is exceeded shortly after strain hardening begins, since stresses in the flanges would now exceed the yield stress. From Fig. 2.3-d, it can easily be shown that for a tip loaded cantilever beam, the yield stress to critical stress σ_y/σ_{cr} ratio can be expressed in terms of the yielded proportion of the flange, η, as:

$$\frac{\sigma_y}{\sigma_{cr}} = 1 - \eta \tag{2.2}$$

where σ_{cr} is the stress associated with the commencement of strength degradation. It follows that the critical moment is thus given by:

$$M_{cr} = \frac{Z\sigma_y}{(1-\eta)}$$

2.2.4 Flange-Web interaction

In general, local buckling strength varies inversely with the slenderness of the plate elements constituting the member. For W-shaped sections, this was experimentally confirmed by tests done by Lukey and Adams (1969).

Because of observations specific to the strength of W-shape beams at incipient buckling, experimental results from stub columns were used as the basis for the determination of a relationship for the ratio of yield to critical stress, σ_y/σ_{cr}. From the data of 68 tests, Kato (1985) used a multivariable linear regression analysis to express the stress ratio, σ_y/σ_{cr}, in terms of plate slenderness, for stub columns, as:

$$\frac{\sigma_y}{\sigma_{cr}}=0.6003+\frac{1.6}{\left(\frac{E}{\sigma_{yf}\left(\frac{2t}{b}\right)^2}\right)}+\frac{0.1535}{\left(\frac{E}{\sigma_{yw}\left(\frac{w}{h}\right)^2}\right)} \tag{2.3}$$

where b/2t and h/w represent slenderness ratios of the half flange and the web respectively.

Because Eqn. (2.3) was derived for stub columns, it is not directly applicable to beams. The reason is that stub columns, under a compressive load, are subjected to a uniform stress distribution (Fig. 2.4-a). Beams, of course, have stresses which can be approximated by a distribution as shown in Fig. 2.4-b. To remediate this difference, an equivalent depth, h_e, of a beam in flexure is used.

Consider the case of a stub column (Fig. 2.4-a); the critical buckling stress of a simply supported rectangular plate is given by Bleich (1952) as:

$$\sigma_{cr.}=\frac{4\pi^2E\sqrt{\frac{1}{e}}}{12(1-\nu^2)}\left(\frac{w}{h}\right)^2 \tag{2.4-a}$$

where (1/e) is the strain hardening to Young's modulus ratio at the given state of stress. Employing a Poisson's ratio ν of 0.3 and a (1/e) value of 0.028, and based on the flange buckling limit given in section 11 of CAN/CSA-S16.1-M89, results in eqn (2.4a) becoming:

$$\sigma_{cr.}=0.745\frac{\pi^2E}{12}\left(\frac{w}{h}\right)^2 \tag{2.4}$$

In the case of a beam in flexure, Haaijer and Thurlimann (1958) give the critical buckling stress for the web for two rectangular stress blocks abcd which approximate the actual stress distribution a'b'cd as noted in Fig. 2.4-b. Assuming simply supported edges, the critical average buckling stress is therefore given by :

$$\sigma_{av.}=\frac{\pi^2 E}{12(1-\nu^2)}(\frac{w}{h_e})^2\psi^2 K \qquad \textbf{(2.5)}$$

where Ψ is an experimentally determined parameter which is a function of the critical web buckling strain, and K is the plate buckling coefficient equal to 10.3.

For simplicity, let us associate the value of critical stress (point a' in Fig. 2.4-b) with that of an average stress denoted by point a in the same figure. Since the critical stress is $\sigma_{cr}=1.25\sigma_y$, then the average stress, σ_{cr} is $=1.125\sigma_{av}$. Along with that, taking $\upsilon=0.3$ and $\Psi=0.69$, Eqn. (2.5) reduces to:

$$\sigma_{cr}=6.025\frac{\pi^2 E}{12}(\frac{w}{h_e})^2 \qquad \textbf{(2.6)}$$

If the critical buckling stress of the stub column (Eqn. 2.4) is equated to the one of the beam in flexure (Eqn. 2.6), it then follows that:

$h= 0.351\ h_e$

To take into account the stress variation in beams, h_e should be used instead of h in Eqn. (2.3). This will subsequently give a new relationship for the stress ratio as:

$$\frac{\sigma_y}{\sigma_{cr}}=0.6003+\frac{1.6}{(\dfrac{E}{\sigma_{yf}(\dfrac{2t}{b})^2})}+\frac{0.1535}{(\dfrac{E}{\sigma_{yw}(\dfrac{w}{.351h_e})^2})} \qquad \textbf{(2.7)}$$

To check the validity of Eqn. (2.7) for beams in flexure, the predicted values of the stress ratios were compared with those obtained from the 24 tests performed by Kuhlmann (1989); the predicted values compare well with the observed ones (Table 2.1).

Equating Eqn. (2.2) with Eqn. (2.7), we obtain the optimal proportion of the yielded length at which the maximum moment occurs as :

$$\eta = 0.3997 - \frac{\alpha_f^2}{(\frac{E}{480})} - \frac{\alpha_w^2}{(\frac{E}{5.695})} \tag{2.8}$$

where:

$$\alpha_f = \frac{b}{2t\zeta}, \qquad \alpha_w = \frac{h}{w\zeta}, \qquad \text{and} \quad \zeta = \sqrt{\frac{300}{\sigma_y}}$$

and all values of the material characteristics are in SI units.

Eqn. (2.8) with Eqn. (2.1) was used to compare the predicted rotation capacity, R_m, at maximum moment, with those observed in the tests done by Lukey and Adams (1969). In using Eqn. (2.1), test values of the ratio E/E_s were used. Also from these experiments, an average value of 9 was used for s, the ratio of the strain at the commencement of strain hardening to the yield strain. The predicted rotation capacity, R_m, is in good agreement with the experimental values for members belonging to Class 1 sections as noted in Table 2.2.

For a given value of the rotation capacity, R_m, and hence a corresponding value for the proportion of yielded length, η, (at which the load apex occurs), Eqn. (2.8) then gives a uniquely defined set of plate slenderness values.

2.2.5 Example

For the purpose of illustration, a section from the Lukey & Adams (1969) tests was considered. The section has: b=203.45 mm, t=10.795 mm, h=208.53 mm, w=7.64 mm and the yield stress is 285 MPa. This results in a value of $\zeta=\sqrt{(300/285)}=1.026$. Hence, the section will have:

- $(b/2t\zeta)^2=84.34$
- $(h/w\zeta)^2=923$

Now, using Eqns. (2.1) and (2.8) with the test values of s=9 and e=36, the section having the above mentioned slenderness ratios would develop a rotation capacity, R_m, at maximum moment of 4.17. This compares very well with the value of 4.15 observed by Lukey and Adams (1969). Other comparisons have been tabulated in Tables 2.2 and 2.3.

2.2.6 Discussion

Use has been made of Eqns. 2.1 & 2.8 to develop interaction diagrams (Figs. 2.5 & 2.6) relating the flange slenderness to the web slenderness and lateral slenderness. In each of the interaction diagrams, a range of buckling limits specified by most codes is shown; In particular, the CSA S16.1 (1989) buckling limits, $b\sqrt{\sigma_y}/2t$ and $h\sqrt{\sigma_y}/w$, are shown as reference lines after being divided by a normalizing value of $\sqrt{300}$ so that they will be comparable to the slenderness parameters α_f and α_w.

From Fig. 2.5, it is shown that the current CSA S16.1 (1989) buckling limits are well within a safe domain if a required rotation capacity of 2 were deemed to be adequate; on the other hand, for a value of 3, it is seen in Fig. 2.6 that the buckling limits are marginally in a safe zone. This means that a section selected according to the CAN/CSA- S16.1-M89 buckling limits will deliver a rotation capacity value of 3, at maximum moment. Neither the current CAN/CSA-S16.1-M89 standard nor its commentary explicitly prescribes a rotation capacity value for plastic and seismic design. As such, comparisons are being made with other codes of practice. According to Kemp (1986), the value of $R_m=3$ satisfies the plastic design requirements for the South African Code. For slenderness limits less than those from the Canadian code CAN/CSA-S16.1-M89 buckling limits, greater rotation capacity values can easily be achieved.

Fig. 2.6 shows that to achieve a rotation capacity of 3, use can be made of the (b/2t)-(h/w) interaction curve for values of plate slenderness. Using this inter-relationship, much wider flexibility is offered to the designer for selection of members. Rather than having fixed values of the buckling limits, one can select from a broad set of coupled values. Therefore, selecting for instance a flange slenderness of 7.0 with a web slenderness of 76 gives an R_m value of 3. and results in a corresponding value of web slenderness of no more than 76.0.

In applications where high rotation capacities are desirable, e.g. moment resisting frames in highly active seismic zones, slenderness limits defining initiation of strength degradation require the use of Class 1 sections. As such, rotation capacity curves were developed, in Fig. 2.7, based on Eqn. (2.1) and (2.8). The curves were developed for values of flange slenderness ranging from 6.5 to 9.5 and web slenderness ranging from 25 to 65. The range of plastic design buckling limits used by most codes is also shown together with the CAN/CSA-S16.1-M89 values which is used as a reference line. It is shown in Fig. 2.7 that with increasing R_m values, both flange slenderness and web slenderness must decrease. Thus, if a value of R_m=4 were to be specified, beams having α_f=8.37 and α_w=58 or 7.9 and 63.5 respectively would be equally satisfactory. A detailed discussion of this subject may be found in Daali and Korol (1994).

2.3. Buckling rules for rotation capacity at ultimate deformation

Frequently, local flange buckling is observed simultaneously with lateral buckling.

Alternatively, it has been noted that an interaction of local flange buckling with local web buckling may occur also. However, lateral slenderness has not so far been included in analyses. About the same time, Kuhlmann (1989) showed that the rotation capacity is governed by three parameters - flange slenderness, web slenderness and the steepness of the moment gradient, defined in terms of unsupported length over the width of the section, L/B. The interaction of the parameters mentioned above is of a highly complex nature. The Japanese standard (AIJ LSD 1990) has attempted to address this issue, while other codes do not cover combined responses even for monotonic loading. For instance, slenderness limits for flanges and webs do not reflect combined buckling phenomena. Thus, making design rules overly simple may result in potentially inaccurate member selection.

With the aforementioned in mind, a procedure accounting simultaneously for flange and web plate width or depth to thickness ratios and lateral slenderness is proposed. Critical values of normalized flange and web slenderness ratios are obtained in accordance with the normalized lateral slenderness and the required rotation capacity for the requirements of plastic design. A tool is offered to researchers and design engineers for defining maximum plate slenderness ratios (flanges and webs), and lateral slenderness requirements to achieve a given amount of rotation capacity at ultimate displacement.

2.3.1 Required rotation capacity

For a plastically designed member subjected to bending moment and laterally braced in accordance with the specification in use, the available rotation capacity, R_u, is a ductility parameter that determines how effectively internal moments can be redistributed once M_p is reached at a given cross section (Fig. 2.2). It is here defined by the amount of total rotation beyond the plastic limit that can be sustained before unloading below M_p takes place and is herein given by:

$$R_u = \frac{\theta_u}{\theta_{pl}} - 1 \qquad (2.9)$$

In general, steel members of an open style cross section may fail by either local buckling or lateral buckling or both. Because of requirements in design to prevent lateral buckling, the most important aspect which governs the rotation capacity of a member is its potential for local buckling. Since the latter mode is crucial, the width-thickness ratios of compression elements will dramatically affect the delivered rotation capacity.

Recently, Bild & Kulak (1991) compared rules governing local buckling of plastic sections for 13 different specifications. They noted that the modified flange slenderness, $(b/2t)\sqrt{\sigma_y}$, expressed in SI units, ranges from 131 to 174. Meanwhile, the modified web slenderness, $(h/w)\sqrt{\sigma_y}$, was observed to range from 981 to 1365.

In seismic design, there is no agreed upon value for the required rotation capacity. The situation is complicated further by the fact that there are not only different types of ductility to be considered, but also the notion of force modification needs to be embraced. Popov (1980) distinguishes among the material ductility, μ_m, the member ductility, μ_u, and the system ductility, μ_s and suggests the relationship that $\mu_m > \mu_u > \mu_s$; note that the same suggestion holds true in terms of rotation capacity. Hall (1978) recommends employing a member capacity, R_u, having a value of $1.5R_s+0.5$, where R_s is the system capacity. Meanwhile Chopra & Newmark (1980) suggest that it is prudent to provide a required rotation capacity R_u of 6 to 8 while Fukomoto & Itoh (1992), quoting from AIJ LSD (1990) propose a value of 4. To complicate matters further, Cosenza et al. (1988) link a member's rotation capacity, R_u, to the system ductility, μ_s. They suggest a value for R_u of $(\mu_s-1)/\chi$ with χ fluctuating between 0.36 and 1.

The current Canadian Code (NBCC 1990) for the design of fully ductile moment resisting frames employs a system ductility μ_s of 4. If Cosenza's suggestion is to be used, and with $\chi=0.5$ representing an average of the maximum and minimum system ductility suggested values, a required member capacity R_u of about 5.5 to 6 would then apply for seismic design in Canada. A graphical representation of the system ductility-rotation capacity relationship is given in Fig. 2.8.

In the United States, NEHRP (1992) and UBC (1991) recommend, for special moment resisting steel frames, force reduction factors FR and FR_w with values of 8 and 12 respectively. The difference is because the former one uses limit state design philosophy, while the latter still uses working stress design. Uang (1991) expressed the NEHRP and UBC force reduction factors in terms of a ductility reduction factor, R_μ, and an overstrength factor, Ω, as $FR=R_\mu\Omega$ for NEHRP and $FR_w=R_\mu\Omega Y$ for UBC; here, Y is a factor evaluated as 1.4 (Uang 1991). Newmark and Hall (1982) relate the ductility reduction factor to the system ductility as follows:

$R_\mu= \mu_s$ for velocity and displacement amplification regions (or medium and long period structures).

$R_\mu= \sqrt{(2\mu_s-1)}$ for an acceleration amplification region (or short period structures).

Other relationships that relate the ductility reduction factor to the system ductility may be found, for instance, in Fischinger and Fajfar (1993).

The standards NEHRP (1992) and UBC (1991) do not explicitly specify the value of the overstrength factor. This leaves the possibility of combining the system ductility, μ_s, with the overstrength factor in various ways. If, however, the overstrength factor is chosen to have a value of 2.3 as suggested by Uang (1991), then the force reduction factor of NEHRP and UBC, via the ductility reduction factor for fully ductile moment resisting frames, give average system ductility values, μ_s, of 3.6 in the velocity region and 6.9 in the acceleration region. If Cosenza's suggestion is to be used, an average required member rotation capacity, R_u, of about 4.9 and 11.1 would result for the respective velocity and acceleration regions. These limiting values represent an excessive range for purposes of designing members for redistribution of forces. The range 6 to 8 suggested by AISC is more realistic. For member assessment purposes, an average AISC value of 7 will be used in further work herein described.

2.3.2 Available rotation capacity

From results of tests done by Kuhlmann (1989) and conducted on rolled I section steel beams in which lateral deflection was prevented at the critical moment section, an empirical expression was developed, to fit the predictions of a model for the relationship between the available rotation capacity, R_u, and the effective slenderness ratio, α_c. Linear programming was used to minimize the objective function which represents the sum of the squared differences of the observed and predicted rotation capacity values. The empirical expression obtained using this technique is given by:

$$R_u = -9.2\alpha_e + 10.71\alpha_e^{-.293} \quad \textbf{(2.10)}$$

where the effective slenderness is expressed in terms of the product of the flange slenderness, the web slenderness and the lateral slenderness as follows:

$$\alpha_e = \frac{\alpha_f \alpha_w \alpha_l}{30072} \quad \text{in which,} \quad \alpha_l = \frac{L}{r_y \zeta}$$

The normalized slenderness α_f and α_l were defined earlier in section 2.2.

Values of rotation capacity obtained with Eqn. 2.10 were compared with experimental values from the Kuhlmann's (1989) tests. They were found to be in good agreement; a summary of the compared values are given in Table 2.3. Moreover, a second independent comparison against experimental values from Lukey's tests (1969) was also made (Table 2.4). Again, predicted values compare well to the observed values of the rotation capacity.

2.3.3 Discussion

From Eqn. 2.10, available rotation capacity curves (Fig. 2.9-2.11) for various normalized lateral slenderness (α_l) and normalized web slenderness (α_w) values have been developed. Values of normalized flange slenderness (α_f) were selected to have a range from 5 to 9 while the α_w ranged from 25 to 75; these values cover the usual spectrum of Class 1 (plastic design) sections. Three basic values for the normalized lateral slenderness, specifically 30, 40 and 50 were examined. It is clearly seen in Figs. 2.9 to 2.11 that the normalized lateral slenderness considerably influences the local buckling rules. Thus, for example, within the limits α_f=8.37 and α_w=63.5 (ζ=1.0) specified by CAN/CSA-S16.1-M89

(1989), and for α_f=7.91 and α_w=78.8 as specified by AISC (1992), it is evident that the values of the available rotation capacity decrease by the same order of magnitude both by increasing flange slenderness and lateral slenderness. The latter parameter, not explicitly recognized by the codes cited above, is clearly evident as being important (Figs. 2.9 to 2.11). Meanwhile, R_u decreases by a lesser order of magnitude with increasing web slenderness.

If Canadian buckling limits are used as reference lines (CSA S16.1 M-89), then a careful study of Fig. 2.10 shows that members, with a normalized lateral slenderness of 40 and having plate elements satisfying the Class 1 section limits, will reach a required rotation capacity of about 6. A normalized lateral slenderness of 40 can therefore be taken as the critical limit which should be used in parallel with the current buckling rules in order for a section to be able to redistribute moments in accordance with plastic design. For a normalized lateral slenderness greater than 40, it is clearly shown in Fig. 2.11, that the required value of the rotation capacity of 6 is reached only if more stringent buckling limits are imposed on the plate elements. Thus, for example, with an $\alpha_l=L/r_y\sqrt{(300/\sigma_y)}$ of 50, a normalized flange slenderness of 6.25 would be required for $\alpha_w=h/w\sqrt{(300/\sigma_y)}$ of 63.5. For the American buckling limits, it is found that a critical lateral slenderness of about 30 should be used along with the current rules in order to achieve a rotation capacity of about 7.

Interaction curves, relating flange slenderness and web slenderness for three basic values of the lateral slenderness and four required rotation capacities are shown in Figs. 2.12 to 2.14. These were developed from Eqn. 2.10. As reference lines in the interaction diagrams, vertical lines positioned at $8.37\sqrt{(300/\sigma_y)}$ and $7.91\sqrt{(300/\sigma_y)}$ represent respectively the CSA S16.1 M-89 and the AISC-LRFD flange buckling limits while horizontal lines positioned at

$63.5\sqrt{(300/\sigma_y)}$ and $78.8\sqrt{(300/\sigma_y)}$ denote the respective web buckling limits. A study of the interaction curves in Fig. 2.12 shows that members with lateral slenderness values less than or equal to 40, together with the Canadian code limits will develop an available rotation capacity of 6 or greater. For higher values of lateral slenderness, more stringent limits have to be satisfied for a member to reach an available rotation capacity of 6. Interaction diagrams for R_u=5 to 7 are shown in Fig. 2.12 to 2.14 respectively.

2.3.4 Example

For the purpose of illustration, two cantilever beam sections subjected to tip loading are selected to be compared to the plastic design (Class 1) limits. The length L is taken as 1920mm and σ_y=300 MPa.

1) According to CSA S16.1 M-89 local buckling design rules, a W310*39 section has;

- $(b/2t)=(165/2*10)=8.25< (145/\sqrt{\sigma_y})=8.37$
- $(h/w)=(290/6)=48.33< (1100/\sqrt{\sigma_y})=63.5$
- $(L/r_y)=(1920/38.4)=50< (980/\sqrt{\sigma_y})=56.6$

Hence, the member would satisfy plastic section and lateral support requirements in Canada.

Now, according to the procedure developed in this section, a member having these same characteristics would develop, according to Fig. 2.11, an available rotation capacity of about 5.9. This is slightly less than the minimum required rotation capacity of 6 required for fully ductile structures. Note that for this example, the actual section slenderness ratios are conservatively lower than the code specified ones; on the other hand, when limits very close to the code buckling limits are used, it is highly likely that the developed rotation capacity will be lower than 6.

2) Now, according to the AISC local buckling design rules, a W360*33 section has;

- $(b/2t)=(127/2*8.5)=7.47<(137/\sqrt{\sigma_y})=7.91$
- $(h/w)=(332/6)=55.3<(1365/\sqrt{\sigma_y})=78.8$
- $(L/r_y)=(1920/26.4)=50<(9473/\sigma_y)+25=56.57$

Hence, the member would satisfy plastic section and lateral support requirements in the United States. Now, according to the procedure developed in this Section. the member cited would have an available rotation capacity of about 5.75 (Fig. 2.11) which is less than the minimum required rotation capacity of 7 required for fully ductile structures. Therefore, in both cases, the member would not be able to redistribute moments in accord with plastic design unless more stringent buckling limits were applied or interaction curves such as those in Fig. 2.11 were used.

We have seen, in Figs. 2.9-2.11, how the local buckling rules are highly influenced by the member lateral slenderness. Further, it was demonstrated through a simple example that the current local buckling limits may sometimes lead to an unconservative design. It is also seen how one can use the interaction curves to select a member with specified slenderness limits in order to achieve a chosen required rotation capacity. More details may be found in a recent paper by Daali and Korol (1994).

2.4 Summary

An approach which accounts for the simultaneous effects of plate slenderness in view of the required rotation capacity, at maximum moment, is proposed in Section 2.2 of this chapter. It has been shown that given some specific values for flange slenderness, α_f, and web slenderness, α_w, one can predict with acceptable accuracy the rotation capacity at maximum moment, i.e., when strength degradation is initiated. A tool is thus offered to choose higher than normal rotation capacities for seismic requirements and then to select the beam parameters needed for that application.

From the study done in Section 2.3, one can see that the member rotation capacity demands imposed by the seismic design codes cited are not always consistent with the classification of sections. It may be that member capacity values are more than ample in resisting the factored loads; however, the purpose of this study has not been to examine that issue. It was simply to accept code requirements and identify weaknesses in classification for design necessitating full ductility. An empirical expression, relating the plate slenderness with the member lateral slenderness, is used to develop ultimate rotation capacity and interaction curves for the selection of local buckling limits needed to achieve a specified required rotation capacity under monotonic loading.

An upper limit α_l of $(L/r_y)\sqrt{(\sigma_y/300)}=40$ is proposed as the critical limit for the flange lateral slenderness to be used with the Canadian buckling rules for beam sections required to develop a minimum rotation capacity of 6. Similarly, an α_l of 30 is suggested for beams required to achieve a minimum rotation capacity of 7 in the United States. Keeping in mind that the repeated cyclic effects were not accounted for in the above-mentioned, the suggested values of lateral slenderness appear to permit design for full ductility under monotonic loading. For greater values of the lateral slenderness, interaction curves are proposed to be used to reach a specified rotation capacity. The procedure can easily be applied to any standard of practice by simply replacing the buckling limits by the specified ones.

Table 2.1 Comparison of Predicted and Observed Values of the Stress Ratio.

Specimen # (Kuhlmann)	α_f^2	α_w^2	Estimated σ_y/σ_{cr}	Observed σ_y/σ_{cr}	Estimated over Observed
1	61.25	2235	.81	.819	0.99
2	69.2	2235	.83	.775	1.07
3	132	1832	.97	.943	1.03
4	95.92	1636	.88	.752	1.16
5	95.92	2240	.89	.769	1.16
6	95.92	3617	.93	.813	1.14
7	95.92	2637	.90	.763	1.18
8	95.92	2637	.90	.752	1.20
9	95.92	2619	.90	.733	1.22
10	89.04	2252	.87	.833	1.04
11	102.15	1832	.89	.781	1.14
12	111.39	1832	.89	.793	1.13
13	53.13	4479	.86	.833	1.02
14	62.65	4458	.88	.826	1.06
15	65.52	4392	.88	.819	1.07
16	68.45	1724	.81	.793	1.02
17	70.69	3129	.86	.757	1.13
18	72.2	5651	.93	.781	1.19
19	70.69	2498	.84	.757	1.11
20	70.69	2515	.84	.746	1.12
21	70.69	2515	.84	.751	1.11
22	80.0	2515	.86	.763	1.13
23	87.36	2510	.87	.787	1.12
24	95.92	2328	.89	.794	1.13

Table 2.2 Comparison of Predicted and Observed Rotation Capacity, R_m.

Specimen # (Lukey & Adams)	α_f^2	α_w^2	1	Predicted R_m	Observed R_m	Predicted over Observed
A-1	84.34	923	.1712	4.17	4.15	1.01
A-2	63.13	923	.221	6.05	5.1	1.18
B-2	60.84	2536	.181	4.53	3.24	1.39
B-3	82.57	2536	.129	2.87	2.78	1.03
C-2	61.03	3242	.161	4.46	4.9	0.91
C-3	82.86	3242	.1080	2.57	2.02	1.27
C-4	98.23	3242	.071	1.49	1.02	1.46
C-5	90.89	3242	.089	2.00	2.02	0.99

Table 2.3 Comparison of Predicted and Observed Values of Rotation Capacity, R_u.

Reference	Spec. #	α_f	α_w	α_l	Predicted R_u	Observed R_u
Kuhlmann (1989)	1	7.83	47.27	47.17	7.22	7.9
	2	8.32	47.27	47.7	6.56	7
	4	9.87	40.45	34.16	9.41	12.6
	5	9.87	47.33	34.25	8.07	8.6
	6	9.87	60.14	34.07	5.93	4.6
	7	9.87	51.35	23.63	10.44	13.4
	8	9.87	51.35	28.94	8.81	11.5
	9	9.87	51.17	34.16	7.41	7.8
	10	9.43	47.45	31.15	9.15	5.5
	11	10.11	42.80	42	6.85	8.9
	12	10.55	42.80	34.3	8.34	7.6
	13	7.3	66.92	46.91	4.59	5.1
	14	7.92	66.77	46.64	3.81	3.8
	15	8.09	66.28	47.17	3.52	3.6
	16	8.27	41.52	29.38	11.67	10.5
	17	8.41	55.94	29.11	9.29	9.5
	18	8.49	75.18	28.75	6.76	6.6
	19	8.41	49.98	28.14	10.46	12.0
	20	8.41	50.15	33.81	8.96	8.7
	21	8.41	50.15	39.47	7.64	7.2
	22	8.94	50.15	31.5	9.05	10.0
	23	9.34	50.10	29.91	9.12	6.7
	24	9.82	48.25	31.06	8.71	5.2

Table 2.4 Comparison of Predicted and Observed Values of Rotation Capacity, R_u.

Reference	Spec. #	α_f	α_w	α_t	Predicted R_u	Observed R_u
Lukey and Adams (1969)	A1	9.16	27.08	34.16	12.93	11.8
	A2	7.97	27.08	34.16	13.92	13.6
	B2	7.79	44.96	39.03	9.31	10.4
	B3	9.07	44.96	39.03	8.03	6.7
	C2	7.83	52.75	39.21	7.89	13.7
	C3	9.11	52.75	39.21	6.51	8.0
	C4	10.0	52.75	39.21	5.62	4.2
	C5	9.51	52.75	39.21	6.11	6.5

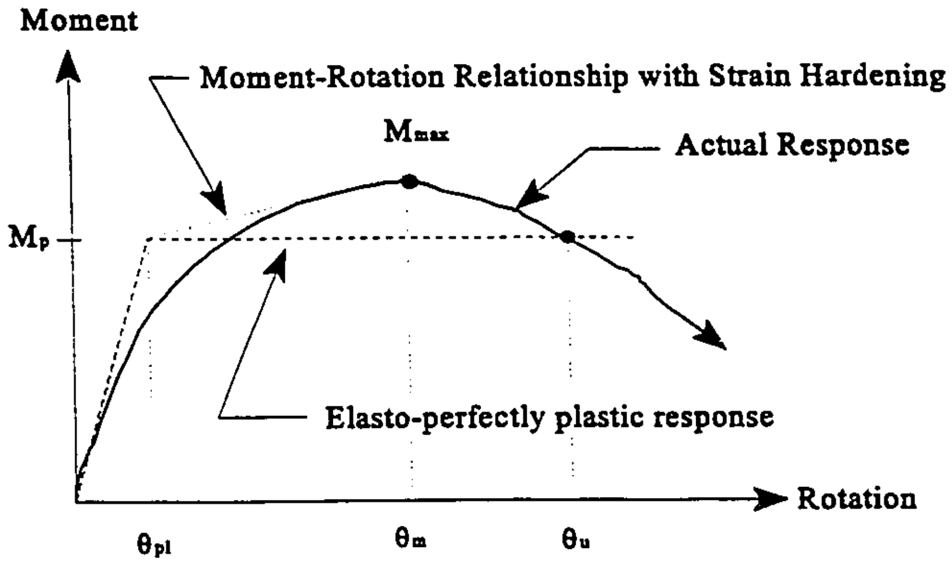

Fig. 2.1 Moment-Rotation Relationship

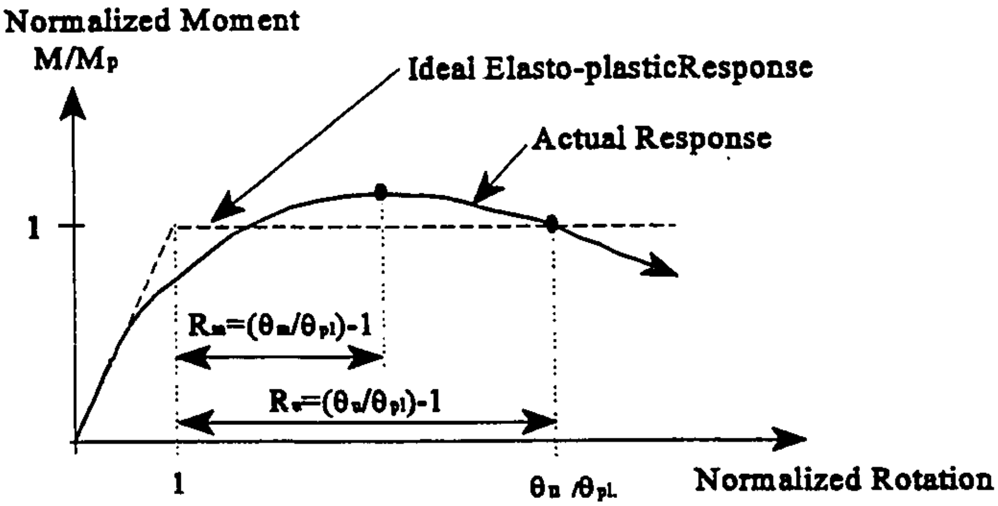

Fig. 2.2 Behaviour of Class 1 (Plastic Design) sections under monotonic loading

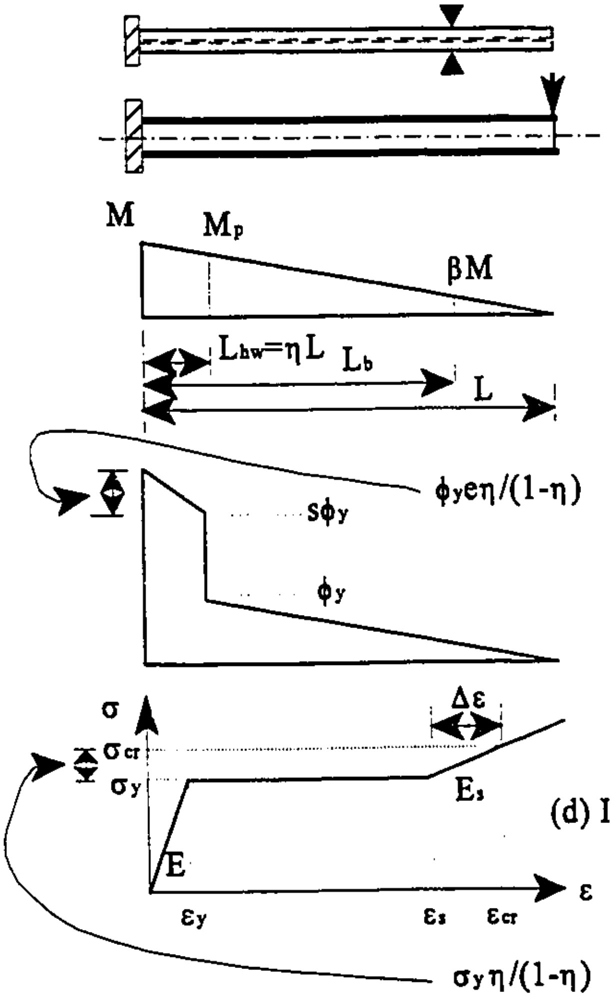

(a) Cantilever Beam

(b) Bending Moment

(c) Curvature Distribution

(d) Idealized Stress-Strain Relationshi

Fig. 2.3 Adopted stress-strain relationship

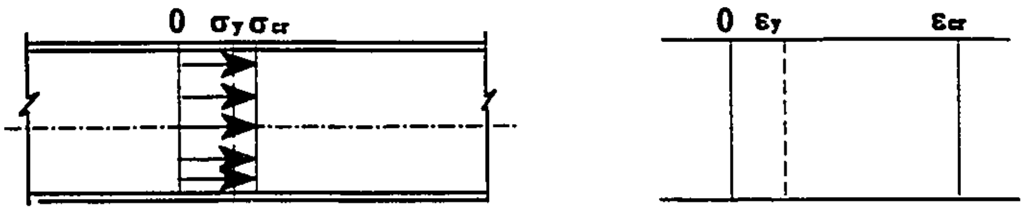

Stress Distribution **Strain Distribution**

a- Section under Axial Force

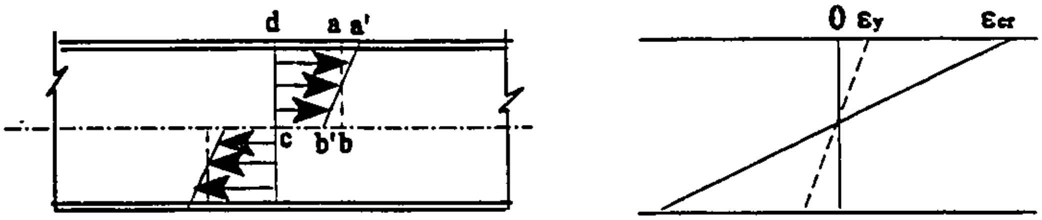

Stress Distribution **Strain Distribution**

b- Section under Flexure

Fig. 2.4 Stress and strain distribution

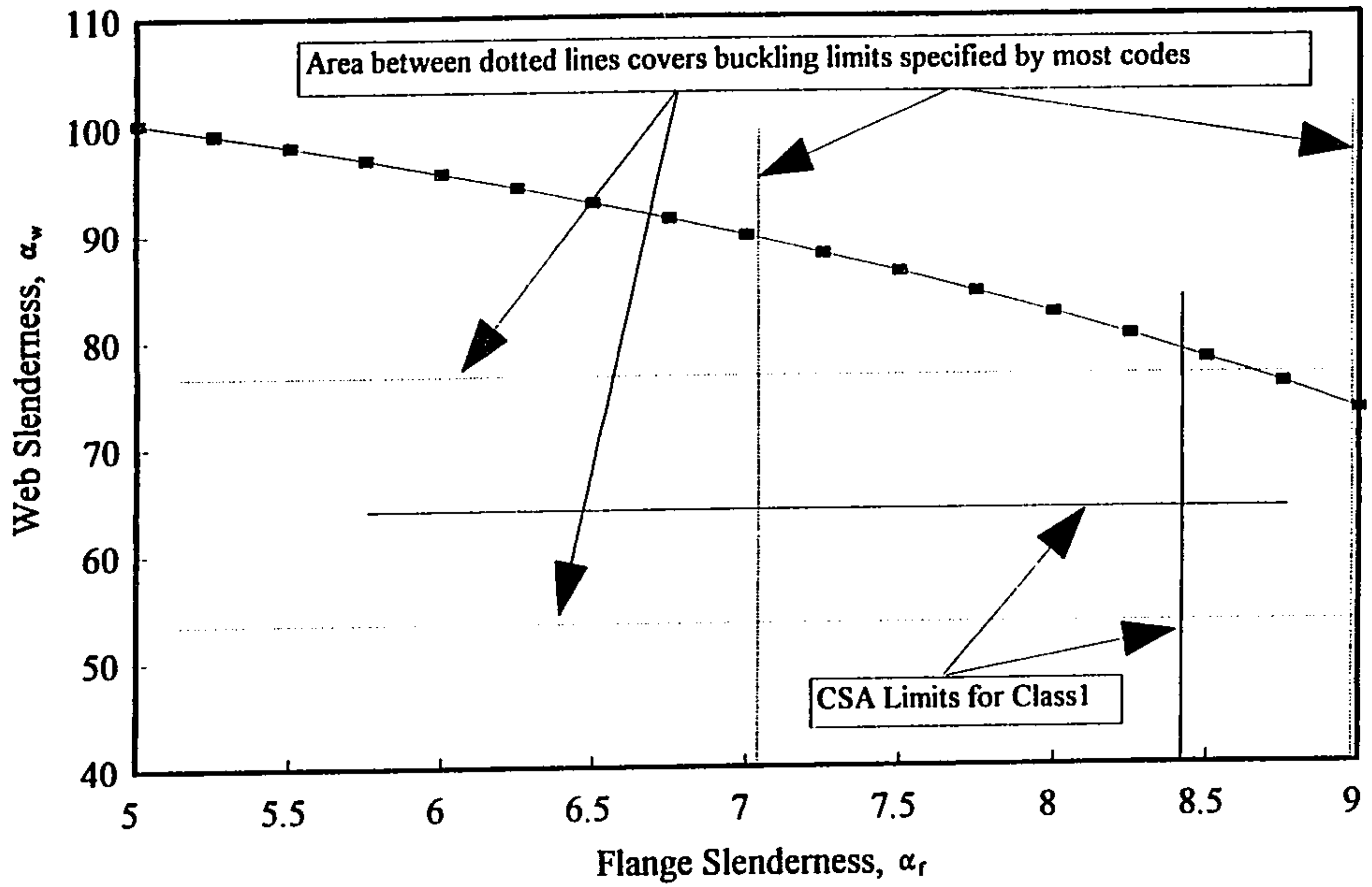

Fig. 2.5 Interaction Diagram for Rm=2

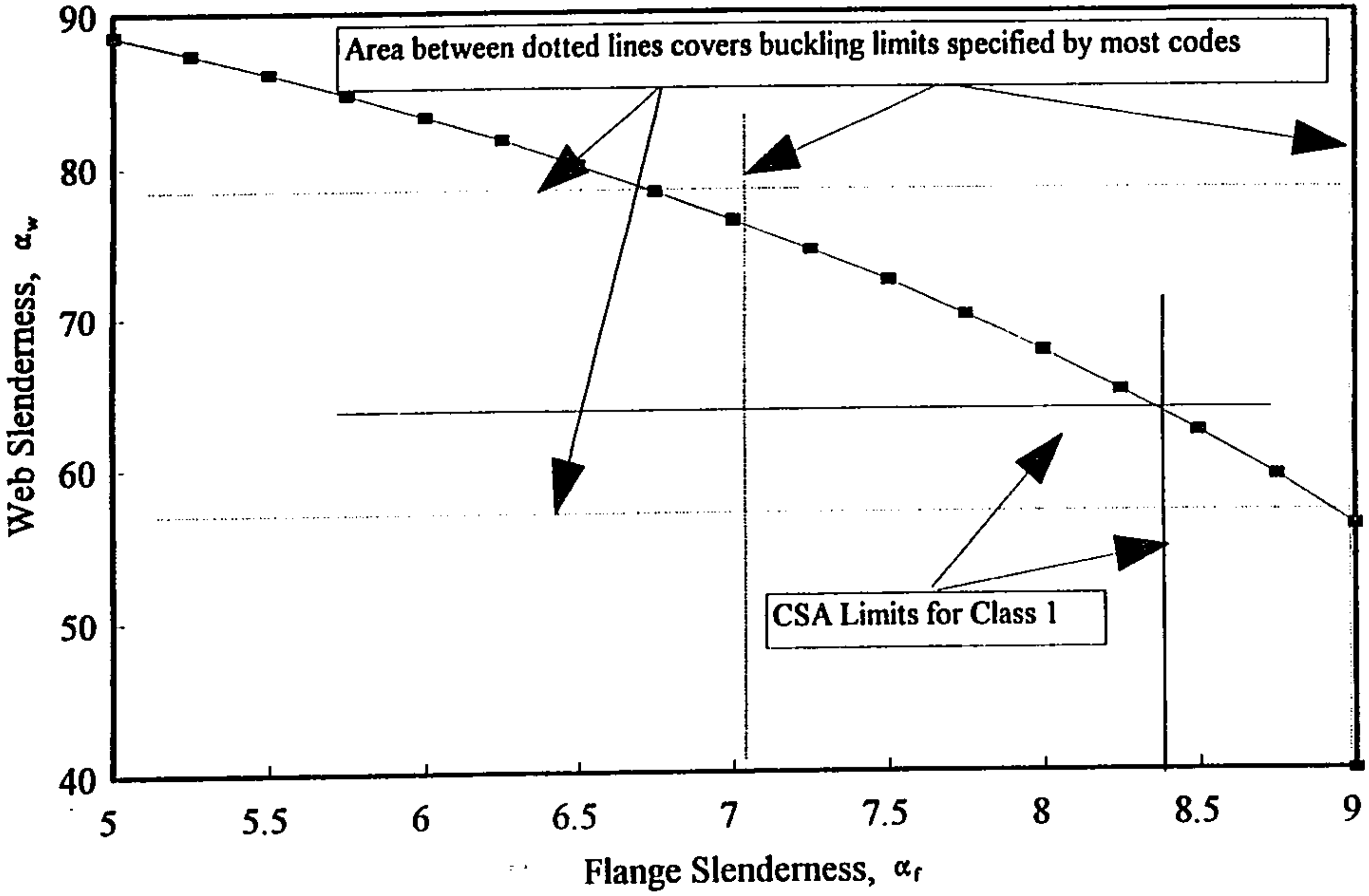

Fig. 2.6 Interaction Diagram for Rm=3

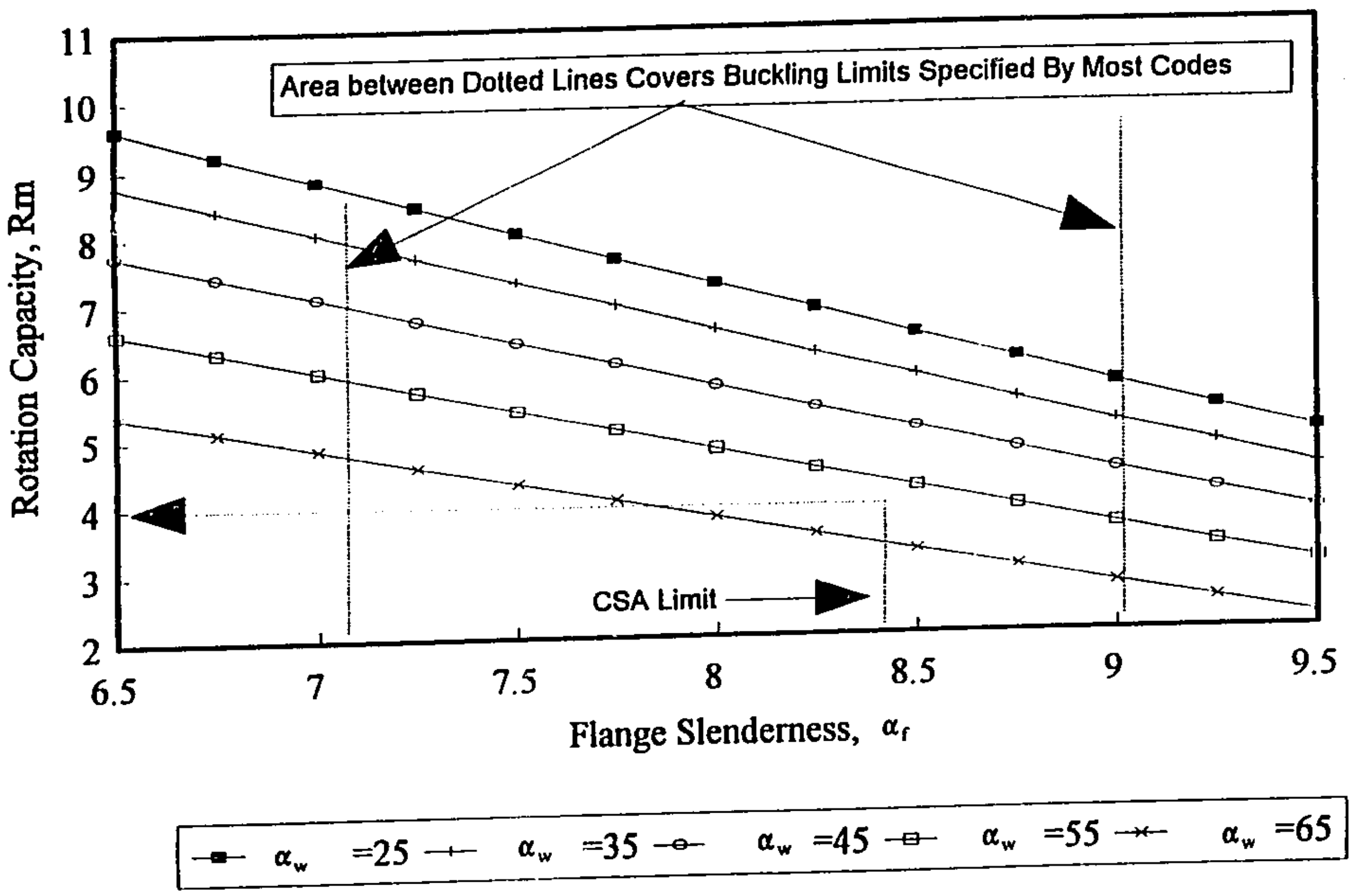

Fig. 2.7 Rotation Capacity at Maximum Moment

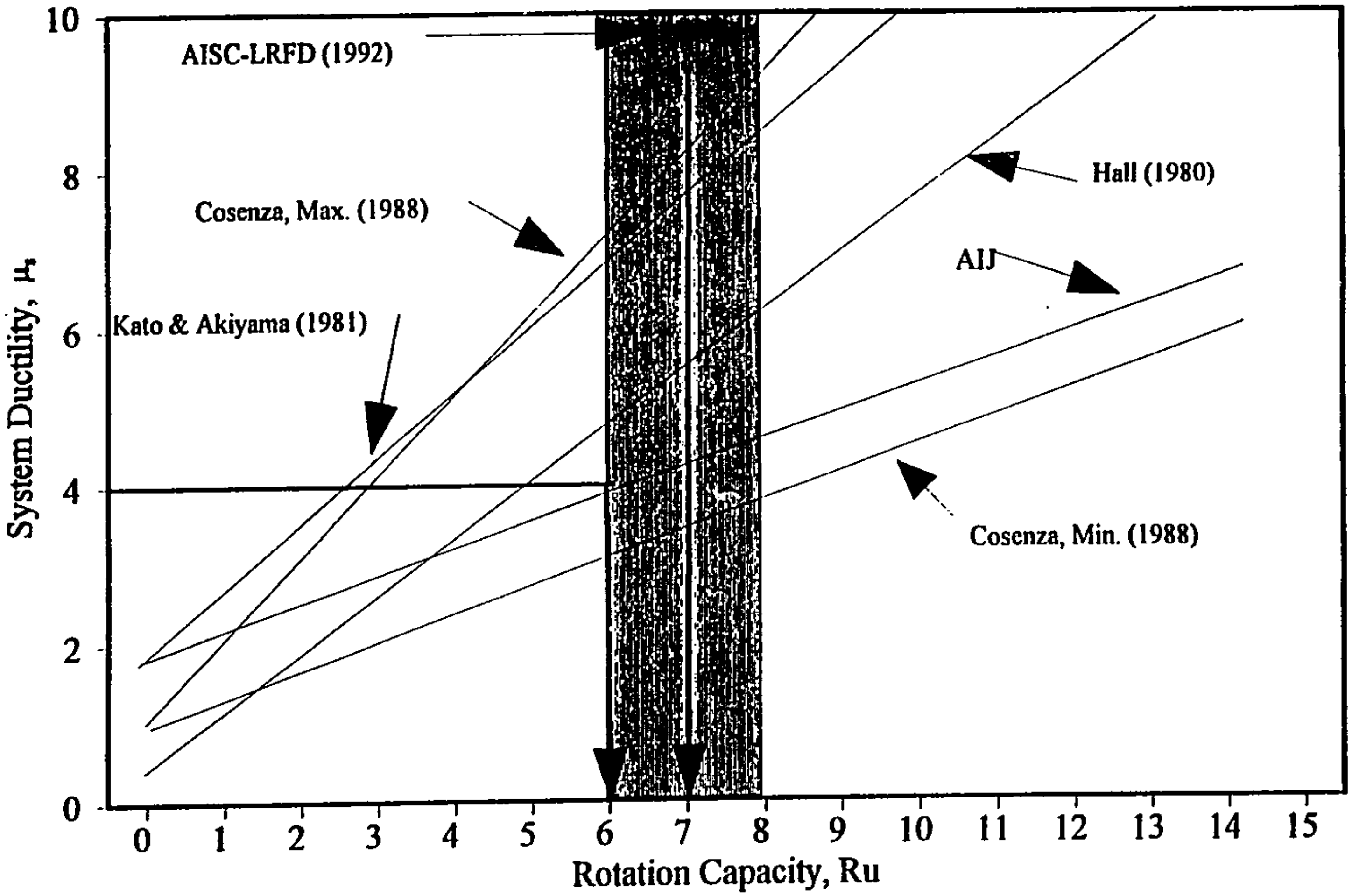

Fig. 2.8 System ductility- rotation capacity relationships.

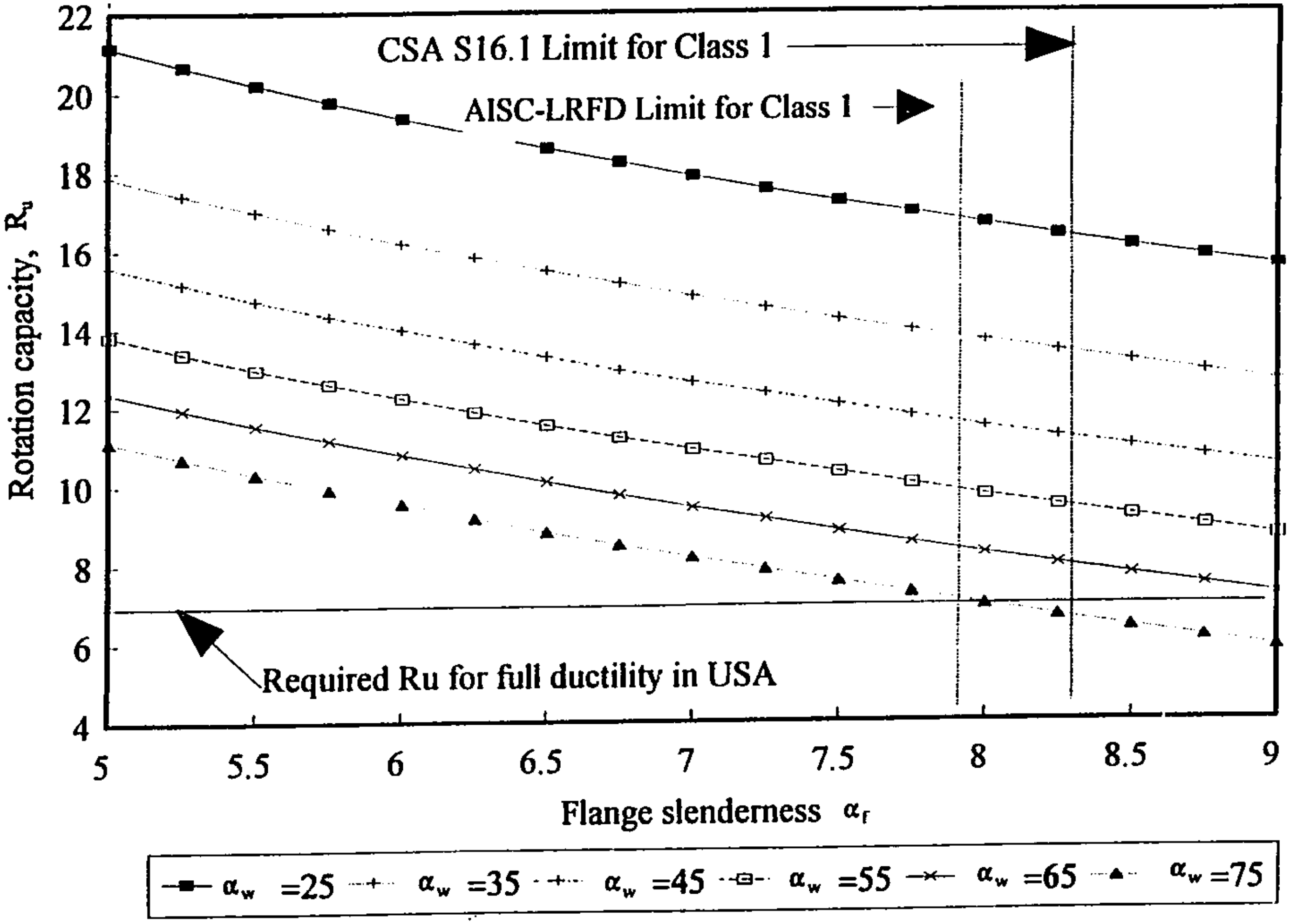

Fig. 2.9 Ultimate rotation capacity, Ru, for α_l =30

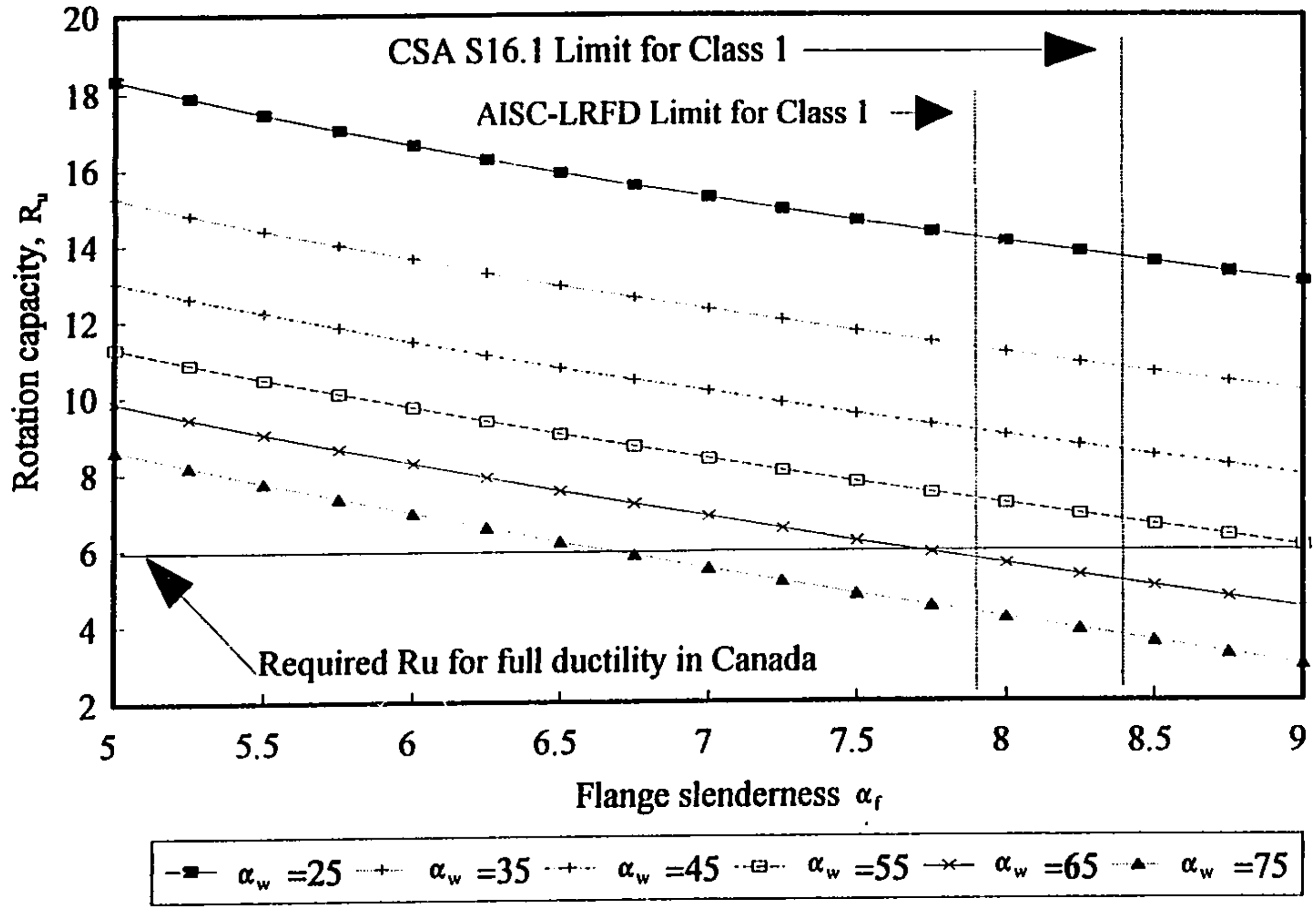

Fig. 2.10 Ultimate Rotation Capacity , Ru, for α_l =40

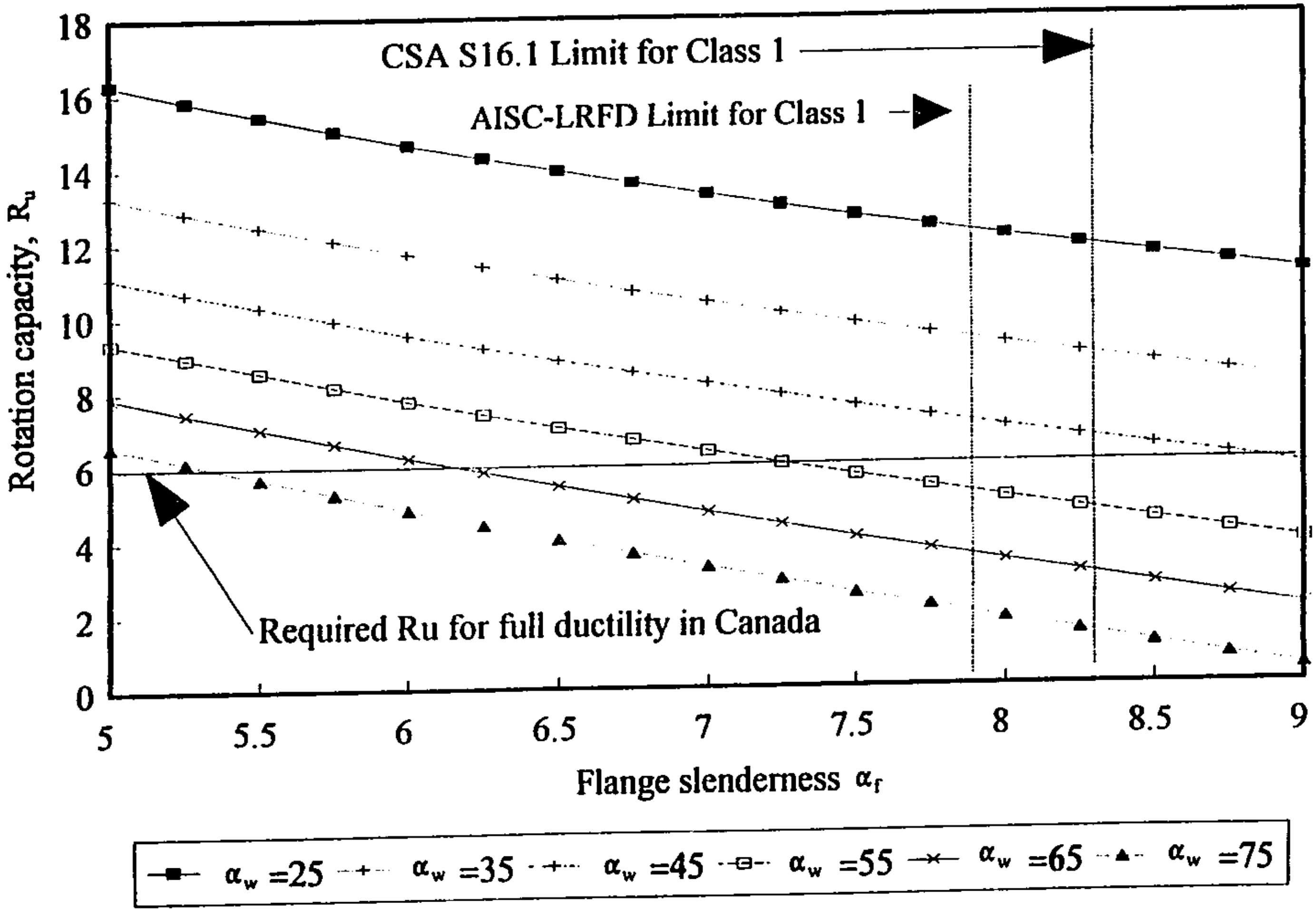

Fig. 2.11 Ultimate Rotation Capacity, Ru, for α_l =50

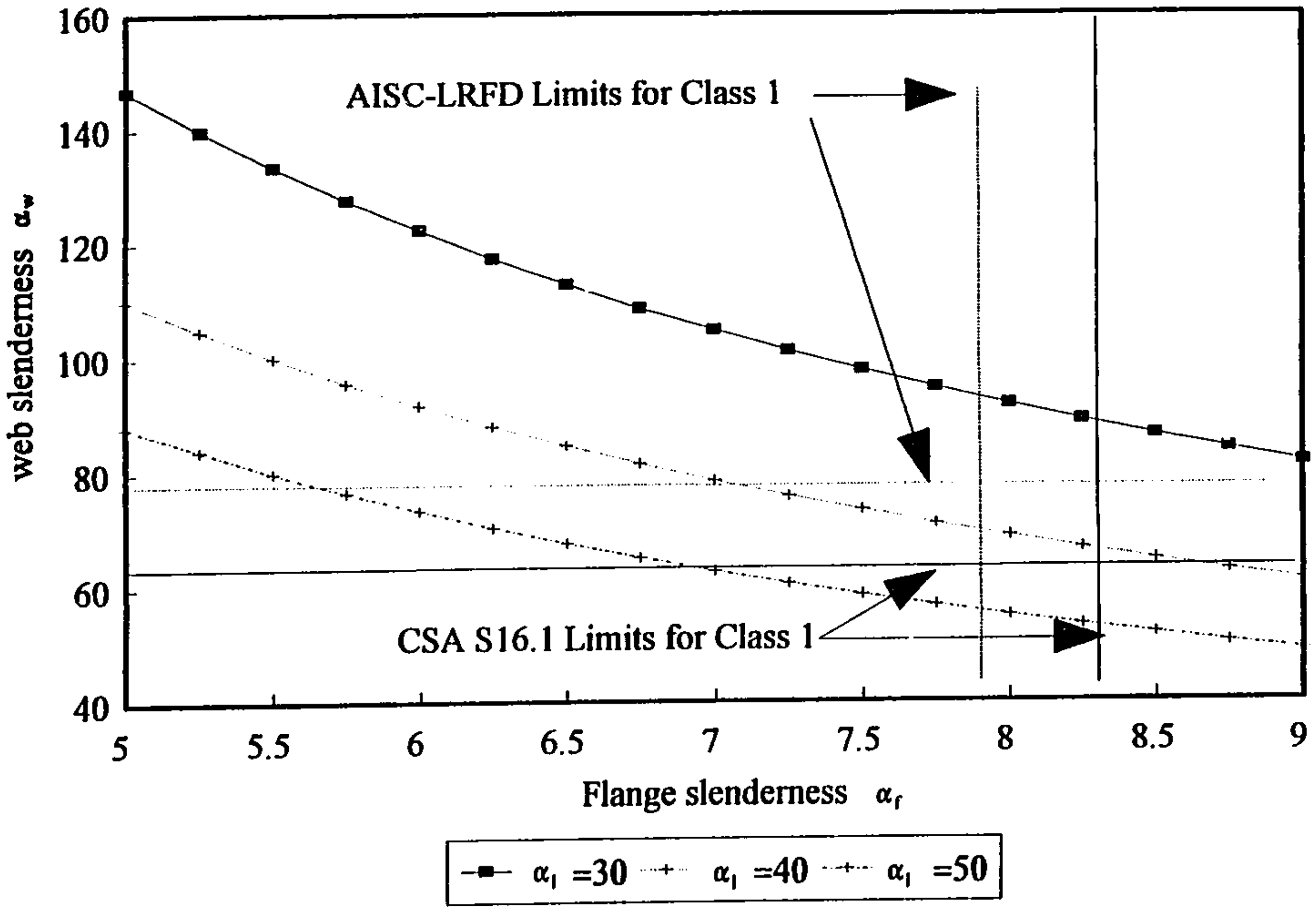

Fig. 2.12 Interaction Diagram for Ru=5

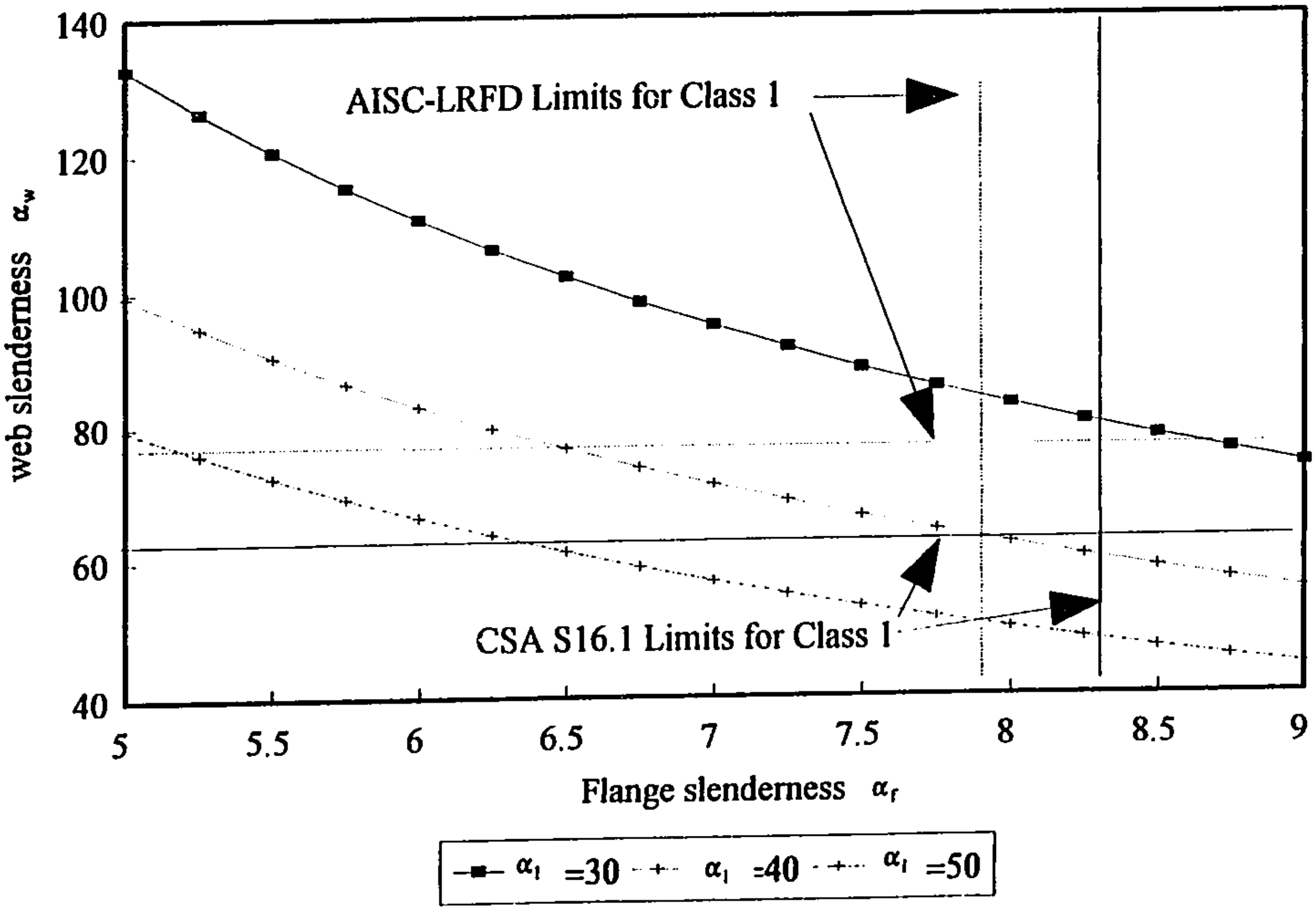

Fig. 2.13 Interaction Diagram for Ru=6

CHAPTER 3

PERFORMANCE ASSESSMENT AND DUCTILITY ENHANCEMENT OF CLASS 1 SECTION BEAMS

3.1 Introduction

Present-day plastic design and earthquake resistant design of fully ductile steel moment resisting frames rely heavily on the concept of plastic hinge formation and redistribution of forces to less stressed sections. This in turn implies that structural members in critical sections are expected to undergo severe deformations without a significant resistance fall-off. It has been and still is the usual practice to limit the slenderness of the plate elements and the lateral slenderness to values that enable the section to strainharden before any local or lateral buckling takes place.

In Chapter 2, it was demontrated that sections just meeting the plastic design rules of CAN/CSA-S16.1-M89 and subjected to monotonic loading barely deliver a rotation capacity value of 5, at ultimate. This may not be satisfactory, especially when load reversals occur during a structure's loading history.

Repeated cyclic loading applied to moment resisting frames is known to have detrimental effects that further lessens the capabilities of sections to deliver an adequate rotation capacity. In fact, Krawinkler et al. (1971) showed that load reversals superimposed on plate elements of beams having out-of-plane deformations adversely affects their performance. However, the added restraint offered by a flange/web stiffener would be expected to change the boundary conditions of the flange and web buckling pattern. This behavior would allow the beams that are locally stiffened to sustain substantially higher strains in the strain hardening range.

With the aforementioned in mind, the question of ductility and the associated required rotation capacity is first addressed. An experimental program on a series of 16 specimens was therefore conducted to assess the delivered rotation capacity and dissipated energy under cyclic loading. In addition, the effects of adding local stiffeners on the enhancement of rotation capacity and energy absorption in W-shaped beams are examined.

3.2 The experimental program

3.2.1 General

W-shaped beams with W310×39 and W310×21 sections were selected for 16 test specimens. The former section conformed to a steel grade of CSA-G40.21M-300 (σ_y=300 MPa, σ_u=450 MPa) while the latter complied with ASTM A36 requirements (σ_y=290 MPa, σ_u=415 MPa). The specimens were fabricated as cantilever beams (Fig. 3.1) and are representative of a half beam used in moment resisting frames subjected to earthquake loading or lateral loading in general.

The test specimens belong to three groups P, A and B. Specimens P1 to P3 of group P were cut from a W310×39 section. A0 to A6 specimens of group A and B0 to B5 specimens of group B were extracted from a lighter section W310×21. Series P and A employed beam lengths of 2125 mm, while the series B lengths were 1210mm. All specimens had the same end-plate and the same weld sizes connecting the rolled sections to the end-plate.

Since the prime focus of this study was on the beams and not the connecting devices, it was believed preferable to design the end plates to remain elastic during the test. Using Packer and Morris's (1977) yield line mechanism, a required thickness of 22 mm was calculated for the end plates for the beam ultimate moment. A 40 mm thick end plate was used for all specimens to ensure its elastic response; the result would thus minimize any absorption of energy by this connecting element. To avoid failure in the welds, all-around 6 and 4 mm fillet welds were used for fastening the flanges and the web respectively to the end plate. The welds were designed to develop a minimum of 1.4 times the nominal plastic moment of the section rather than the 1.2 factor as presently prescribed by CAN/CSA-S16.1-M89. All specimens were locally reinforced with 5 mm thick doubler plates at the point where they were pinned to the hydraulic reversible actuator.

3.2.2 Description of Specimens

It should be noted that the W-shaped beam sections W310×39 and W310×21 had half flange slenderness values of (b/2t)=8.25 and 8.85 and a web slenderness (h/w) of 48.33 and 57.18 respectively. These were close to the respective buckling limits $145/\surd\sigma_y$ and $1100/\surd\sigma_y$ required by the Canadian code (CSA 1989). Meanwhile, the plates constituting the stiffeners were 50×9 mm made from CSA-G40.21M-300W steel (σ_y=300 MPa, σ_u=450MPa), a standard grade. The locations of the stiffeners were such that they could offer out-of-plane restraint to the flanges and web at about 1.25 times the buckling wave length of the flanges, obtained using Kemp's (1986) formulation.

In Fig. 3.2, the bench mark specimens P1, P2, A0, A1, A2, B0 and B1 are shown along with those which were stiffened. Specimens P1 and P2 were made of a W310×39 section, while specimens A0, A1, A2, B0 and B1 were made of a W310×21 section as shown in Fig. 3.2-a. Specimen A3 was similar to A1, A2 and A3 except for a vertical web stiffener located at 110 mm from the face of the end plate; this detail is noted in Fig. 3.2-b. In Fig. 3.2-c are shown specimens P3, A4, A6, B3 and B5 which were similar to the ones in Fig. 3.2-a except that they were locally stiffened by a one sided Herring-bone stiffener detailed as follows: The stiffener of specimens P3, A4, A6 and B2 was oriented to meet the flanges at 110 mm from the face of the end-plate and fillet welded all-around. Specimen B3 was similar to the previous ones except that its stiffener extended a distance of 165 mm. Meanwhile, specimen B5's stiffener was positioned identically to the former group with welding intermittently all-around. In Fig. 3.2-d are shown specimens A5 and B4. Both specimens had Herring-bone stiffeners, one on each side of the web. While, the stiffeners of A5 were fillet welded all-around, those of B4 were fillet welded to the web and fitted to the flanges.

The end plates were 510×310×40 mm plates of CSA-G40.21M-300W steel (σ_y=300 MPa, σ_u=450MPa) grade, and had 12-26 mm diameter holes drilled to accomodate M24 high tensile strength bolts of grade ASTM A490. The bolts were tightened to the column stub using the "Turn-of-Nut" tightening method described in S16.1: (CSA 1989). Meanwhile, the column stub was designed to act rigidly and was a W310×179 section of grade CSA-

G40.21M-300W. To increase its rigidity further and eliminate rotation of the column stub flanges, additional stiffeners were welded at approximately 150 mm from each other on both sides of the web. This was done to insure plastic hinge formation exclusively in the beam at the junction with the column. For further information regarding fabrication details, the reader is referred to Fig. 3.2. Note that the weld sizes shown in Fig. 3.2-a were applicable to all specimens.

Tensile tests on standard size coupons were taken in the longitudinal direction from the flanges and the web of each of the specimens with the results shown in Table 3.1. Actual measurements of the thickness of the flanges and the web as well as measurements of the overall sizes of the section are listed in Table 3.2 along with the nominal values.

3.2.3 Test rig

A reaction frame was designed to accommodate the specimens so that the column stub would be securely bolted to the frame with 25 mm diameter high tensile strength bolts of ASTM A490 steel grade. The cantilever beam then projected horizontally from the column- stub. In a real structure, the presence of a deck slab and transverse steel beam framing would make lateral torsional buckling unlikely. In this test program, vertical rails attached to cross-beams were provided to serve as lateral supports to minimize lateral torsional buckling of the test beam (Fig. 3.3). The locations of the rails were at 1100 mm and 2200 mm from the face of end plate, thus conforming with the S16.1 (CSA 1989) design rule of 980 $r_y/\sqrt{\sigma_y}$ which prescribes 1180 mm for the critical unbraced length. To simulate the bending moment produced by alternating lateral loads in the part of the structure representing the beam, a reversible load was applied at the cantilever tip using a 50 mm diameter rod connected to a 250 kN capacity hydraulic actuator and clevis device. Fig. 3.3 shows diagrammatically the specimen test set-up.

3.2.4 Monitoring of the tests

Linear Voltage Displacement Transducers (LVDT's) and strain gauges were used to monitor the response of each specimen when subjected to cyclic loading while a standard load cell was used for measuring the load, P, transferred from the hydraulic reversible actuator to the tip of the beam. To detect initiation of local buckling of the flanges, pairs of strain gauges were applied opposite each other on the toes of the flanges at a distance of 125 mm from the face of the end plate. The onset of buckling was to be detected when measurements from pairs of gauges positioned on opposite sides of the flanges would begin to diverge. Similarly, to detect web buckling, pairs of strain gauges were applied opposite each other on both sides of the web, one set in the middle of the top part, and another in the bottom section. To monitor the deformations occurring in the flanges in the potential plastic hinge zone, a series of LVDT's, perpendicular to the top flange, was mounted on a special apparatus attached to the column stub. All told, a series of 4 LVDT's was used to monitor the rotation and longitudinal movements of the end plate. All specimens were whitewashed in the potential plastic zone to aid in observing the development of yielding. Meanwhile, a data acquisition system was used to transfer output to a computer for storage, plotting and other purposes.

3.2.5 Loading sequence

Under earthquake motion, a structure and its members exhibit a complex response history. Rather than simulate the actual load history and its rate of loading, it has been accepted practice to assess the ability of a member to perform satisfactorily with the use of quasi-static load histories. This is done on the basis of the work by Hanson (1971) and Almuti and Hanson (1973), in which was demonstrated the validity of using static hysteresis measurements to predict dynamic response.

Two different types of quasi-static cyclic load histories of progressively increasing amplitudes, governed by deflection control (see Fig. 3.4), originally used by Popov and Tsai (1989) and Castiglioni and DiPalma (1989), were used in testing the series of specimens. While this test method is somewhat extreme in the progression of loading, it has been the basis for comparing the performance of various sections to be used in seismic load cases. The load histories were applied in terms of actual initial yield displacements computed for the beams. Symmetric and non-symmetric load histories were evaluated. This was done in an attempt to answer at least partially whether or not ductility is load history dependent. Specimens P1, A0, A6 and B0 were tested under monotonic load while specimens A2 to A5 and B1 to B5 were tested under symmetric load history L2 (Fig. 3.4-b). Meanwhile, the non-symmetric load history, L1 (Fig. 3.4-a), was applied to P2, P3 and A1.

Specimen A1 was initially loaded with two loops of half yield displacement. This helped in checking if all measuring devices were working properly. The controlled displacement was then increased to the full yield value for two consecutive cycles. After that, the tip displacements were increased preferentially in the upward direction, the incremental amount being twice that of the downwards direction. At cycle 10, the downward displacements were stopped at about twice the calculated yield displacement. However, the upwards displacement continued to increase until the actuator reached its stroke limit of 150 mm representing about 8 times the yield displacement.

Specimens A2 to A5 and B1 to B5 were subjected initially to two loops of half yield displacement, then, to two loops of full yield displacement. Beyond this point, a continuous increase of half yield displacement per loop was applied. The load sequence was terminated for all tests by the stroke limit of the hydraulic actuator.

While the specimens were undergoing cyclic loading, data points were read, through the data acquisition system, at sufficiently close intervals to permit accurate monitoring of the specimen's response. Additional visual observations and measurements of flange and web buckling were recorded at each step of the load history.

3.3 Experimental results

3.3.1 General

Indeed the beam's response can be easily determined in several ways. It was decided to simply measure the rotation of the secant joining the tip to the support as an indication of overall beam-connection deformation. The deformation of the beam was isolated by simply subtracting the product of the connection rotation by the cantilever length from the overall beam-connection deformation. As such, the results to be described involve the applied forces versus beam tip-displacement and the applied moment M at the face of the end plate versus the overall beam rotation θ (elastic and inelastic), normalized by M_p (plastic moment based on a product of measured yield stress by nominal plastic section modulus) and θ_p (calculated rotation at M_p) respectively.

For a member subjected to bending moment that is laterally braced in accordance with the specification in use, the available ductility, Δ_u/Δ_p, or its rotation capacity, R_u, are ductility parameters that determine how effectively internal moments can be redistributed once the plastic tip load, F_p (or M_p) is reached. Here, ductility is defined as the ratio of maximum displacement, Δ_u, measured from the zero displacement intercept location, to the displacement, Δ_p, associated with F_p. Meanwhile, the rotation capacity defined as the amount of total rotation, beyond the plastic limit was earlier defined by Eqn. 2.9.

Following completion of the test series, the following observations were common for all tests: 1) The end plate did not show any visual distortion. 2) The welds connecting the rolled section to the end plate behaved satisfactorily up to the end of the loading histories. 3) Failure of specimens was always due to either local buckling or local buckling followed by lateral torsional buckling. 4) Once local instability set in, the flanges tended to buckle inwards on one side of the web and outward on the other during a full cycle of loading. Table 3.3 gives a concise overview of the test parameters as well as rotation capacity results.

3.3.2 Preliminary tests: series P

Specimen P1

The behavior of this specimen is shown by the force beam tip-displacement and the corresponding normalized moment-rotation curve given in Fig. 3.5, where the ratio of the maximum moment to the plastic moment M_p is plotted against the beam end rotation. The normalized bending moment continued to increase until a rotation of about twice the plastic rotation was reached. This rotation corresponds to the point where flange buckling was initiated. The load at which local flange buckling occurred was determined by using strain gages applied opposite each other on the outside and inside faces of the flange as shown in Fig. 3.6-a. Following flange buckling, the bending moment increased slightly to its maximum point, which corresponded to web buckling. The web buckling load was simply determined from the readings of an LVDT positioned as shown in Fig. 3.6-b. After reaching its maximum strength, the member started showing a load fall-off. At about a rotation capacity of 5.88, the resisting moment dropped below the plastic moment. The resistance kept decreasing with increasing inelastic rotations and the test was terminated because of the occurrence of lateral torsional buckling of the member at the plastic hinge location.

Specimen P2

This specimen was selected to illustrate cyclic behavior of beams. The force-displacement and corresponding normalized moment-rotation hysteretic loops for this specimen are shown in Fig. 3.7. The hysteresis loops displayed stable restoring force characteristics up to initiation of local flange and web buckling. With a further increase the of inelastic rotation, a resistance fall-off started to occur as a consequence of web buckling.

To investigate the low cycle fatigue effects on strength and energy dissipation, constant amplitude loops were conducted in the pre and post-buckling phase of the life of the stiffened specimen. The constant amplitude cycles conducted in the pre-buckling range show an insignificant change in the energy dissipation characteristics of the beam (Fig. 3.8-a). In the post-buckling range, the beam was cycled at a constant amplitude for two loops. In the first loop, the beam resisted a force of 120.3 kN and dissipated an amount of energy equivalent to 19.03 KN.m; in the successive loop, the beam resisted a force of 106.8 kN and dissipated an amount of energy of 17.62 kN.m as shown in Fig. 3.8. With further inelastic displacement, the beam resisting moment dropped below the plastic moment at a positive rotation capacity of 5.75 and a negative rotation capacity of 0.41. The test was terminated eventually because of lateral torsional buckling occurring in the plastic hinge zone.

Specimen P3

A Herring-bone style local stiffener was added to the web to investigate its effects on the rotation capacity. The hysteresis loops in Fig. 3.9 show that the stiffened beam delivered a positive full rotation capacity of about 9.38. In the first stage of the loading history, the beam displayed very stable restoring force characteristics. The first local buckle developed in the top flange at a tip load of about 130 kN or a moment of 1.3 M_p. The second buckle developed in the top web at a tip load of about 138 kN or a moment of 1.39 $M_{p.}$. Following flange and web buckling, the beam kept undergoing inelastic rotations without significant strength degradation up to a positive ductility of 6.5. In the last stages of the test, a second flange buckle developed on one side of the beam; this led to formation of a second buckle forming at the end of the stiffener hence precipitating lateral torsional buckling.

In this test, the stiffener showed no deterioration in its geometrical characteristics; the median lines of the Herring-bone stiffener remained straight even though the cross section of the beam underwent extensive distortions during the test.

Pre-buckling and post-buckling constant amplitude loops were conducted. From Fig.

3.10, it can be seen that there is an insignificant change in energy dissipation before buckling occurs. A slight strength and energy dissipation degradation occurred, however, in the post buckling range (Fig. 3.10-b).

3.3.3 Tests Series A

Specimen A0

In this test, loading was purely monotonic. The force beam tip-displacement and the corresponding normalized moment rotation curves of Fig. 3.11 show the behavior exhibited by specimen A0. After reaching its maximum force response, the member started degrading eventually losing its plastic strength at a ductility of 6.1 or a corresponding rotation capacity of 5.1.

Specimen A1

This specimen and others of the series to be described were cyclically loaded. For specimen A1, the experimental force versus beam tip-displacement and force versus beam displacement due to rotation of the end-plate are shown in Fig. 3.12. The normalized moment-rotation hysteresis curves are shown in Fig. 3.13. Note that the hysteresis loops were stable and maintained the same flexural stiffness up to cycle 8; from that point on, the elastic member stiffness started to degrade. At cycle 12, local buckling appeared in the flange followed by web buckling. As a result of the continuously increasing flange distortions, the member carrying capacity showed a gradual decrease after each cycle. At cycle 14, a second buckling wave appeared in the bottom flange and the web. Two cycles later, severe lateral torsional buckling precipitated failure at a moment of about 80% the plastic moment. The test was continued for an additional two cycles. At this point, the member resistance was found to be only about 50 % the plastic value. From Fig. 3.13, one can see that specimen A1 developed maximum positive and negative ductilities of 2.92 and 1.82 at cycles 13 and 14 respectively. Therefore, the rotation capacities for this case may be computed as 1.92 and 0.82 respectively.

Specimen A2

Figs. 3.14-a and 3.14-b show the tip force-displacement and force-displacement due to rotation of the end-plate respectively. Specimen A2 exhibited very stable hysteresis loops up to cycle 8. Examination of Fig. 3.15 shows that the beginning of local flange buckling and web buckling were in evidence during cycles 8 and 9 as indicated by the round and square symbols. Following local buckling of the flanges and the web, the load carrying capacity of the member started to gradually degrade with about a 6 to 10% rate from one cycle to the other. During cycle 11, a second buckling wave formed in the bottom flange. Although the rate of degradation of the member's resistance did not significantly change, flange buckling did however precipitate the formation of lateral torsional buckling in the bottom part of the cantilever beam at the plastic hinge location. In cycle 15, the resistance of the specimen was nearly 80% of the plastic moment with a corresponding ductility of about 8 observed. The test was terminated after another complete loop followed by a final push reached the stroke limit of the actuator. At that point, the resistance was about 52% of the plastic moment value. From Fig. 3.15, it is seen that the specimen delivered positive and negative ductilities of 3.44 and 2.69 at cycles 11 and 9 respectively.

Specimen A3

Specimen A3 was similar in all aspects to specimens A1 and A2 except that it had a vertical stiffener on one side of the beam. Local buckling within the stiffened zone started developing during cycle 9 in the top flange which was first compressed as shown by the experimental force versus beam tip displacement and normalized moment versus beam displacement hysteresis curves of Fig. 3.16. In cycle 11, web local buckling appeared at a distance equal to about the depth of the section. The combined flange and web local buckling caused an appreciable decrease in the member resistance. Symmetrical buckling of the top and the bottom flanges initiated the beginning of slight lateral torsional buckling in cycle 12. With a further increase in the amplitude of deformation, severe lateral buckling developed in cycle 13 causing another major drop in the load carrying capacity of the member. At that point the vertical stiffener slightly bent out-of-its plane (see Fig. 3.17). During the following cycles, fatigue effects led to the appearance of a crack opening on the top flange at the location where the stiffener was welded to the flange. This occurred with decreasing resistance. The member resistance at the final push was 50% of its plastic resistance. Fig. 3.16-b shows the member ductilities and rotation capacities determined from the experiment.

Specimen A4

Fig. 3.18-a shows that specimen A4 responded to the tip applied load with very stable

hysteresis loops up to cycle 9. Local flange buckling took place, in cycle 9, on the unstiffened side of the beam away from the stiffened zone. With a further increase in the deflection amplitude, (cycle 10), out-of-plane buckling developed in the web. The failure of the member was through local buckling of the flanges and the web evidenced by a sudden drop in the load carrying capacity with subsequent cycles as can be observed in Fig. 3.18-b. It is worth noting that for a ductility of about 10, (cycle 15), the specimen still had a resistance of about 80% of the plastic resistance. Due to fatigue effects, a crack developed at the connection of the herring-bone stiffener with the top flange (see Fig. 3.19). At the stroke limit, the load carrying capacity was nearly 65% of the plastic value. Though pushed to the stroke limit, the specimen did not show any appreciable amount of lateral torsional buckling. Note also that the stiffener as well as the flanges and the web of the stiffened area did not undergo any deformations whatsoever. Examination of Fig. 3.18 shows that the specimen delivered very high positive and negative ductility values of 4.51 and 4.17 at cycles 13 and 12 respectively.

Specimen A5

Examination of Fig. 3.20, shows that local buckling of the flange and the web clearly precipitated a sudden drop in the carrying capacity of the member during cycle 11. In fact, a slight local flange buckle started to appear in cycle 10. With a further increase of the controlled displacement in the following cycle, (cycle 11), flange local buckling clearly developed (see Fig. 3.21). This led, subsequently to an out-of-plane deformation in the web. In cycle 12, the resistance diminished to about the plastic resistance of the section. From then on, the deformations kept amplifying leading to lateral torsional buckling in cycle 13. At this point, the load carrying capacity of the member was about 85% the plastic resistance and the corresponding ductility was about 9. After three more inelastic cycles, the specimen was pushed to the stroke limit of the hydraulic actuator with the resistance of the member about 55% of M_p at that point. Note that, although the specimen suffered extensive damage in the flanges and the web away from the stiffened zone, the flanges, web and stiffeners kept their initial shape within the stiffened zone itself.

Specimen A6

After reaching the maximum strength at about a ductility of 4.7, specimen A6 started degrading in strength eventually, dropping below its plastic moment capacity at a ductility of about 8.25 (Fig. 3.22). With a further increase in the controlled displacement, the specimen kept losing strength. The test was stopped when the strength was about half the maximum.

3.3.4 Test series B

Specimen B0

Except for having about 55% the original cantilever length of earlier tests, specimen B0 was similar in all aspects to A0. Tested under a monotonic continuously increasing controlled displacement, the specimen reached a maximum force response at a ductility of about 4.5. After occurrence of flange and web buckling, the strength started degrading. At a normalized plastic moment of unity, the member developed a ductility value of 6.96 as shown in Fig. 3.23.

Specimens B1 t o B5

Figs. 3.24 to 3.28 show the behavior displayed by specimens B1 to B5. To an amateur's eye, the hysteresis loops exhibited by specimens B1 to B5 all look the same. However, a closer examination of the figures shows that initiation of strength degradation occurred at different amplitudes of deformation. Whereas specimen B1 showed initiation of strength degradation at about 18 mm (Fig. 3.24-a), that of B2 to B5 occurred at a much later point. For instance, B3 and B4 exhibited initiation of strength degradation at an amplitude of 33 and 31 mm, respectively.

To be noted as well is the strength deterioration from one reversal to the other. After the peak load was reached in specimens B1 and B2, there was a noticeable change in strength response, while specimens B3 to B5 exhibited a smooth strength deterioration from one reversal to the other.

3.4 Discussion of experimental results

3.4.1 General

By adding a herring-bone type of stiffener, the out-of-plane web deformations in the plastic hinge zone are reduced, flange buckling is delayed and the plastic hinge location displaced away from the face of the end plate; this results in a subsequent enhancement in the behavior of the specimens in terms of ductility and energy dissipation. For the specimens cited, the flanges and web were observed to buckle at slightly higher critical stresses than did the unstiffened equivalent specimens. This results in a member being able to develop plastification over a much wider zone and hence achieve greater ductility or rotation capacity.

A re-elaboration of the results already seen in the detailed description of the specimen results is shown in Table 3.3. An examination of the summary of the ductilities or rotation capacities shows that very good performance was obtained with the use of the herring-bone stiffeners. For monotonic tests, a comparison of the unstiffened specimen A0 with the stiffened one, A6, shows an increase of 30 to 40% in rotation capacity, as noted in Fig. 3.29. Comparing the positive ductility of the cyclically tested specimen P2 with P3, A2 with A4 and B1 with B3 shows an increase of 63, 31 and 99%, respectively. The beneficial role played by the stiffeners is perhaps best exhibited when the hysteresis loops of specimen B1 are plotted along those of B5. It is clearly shown that at a normalized plastic moment of unity, the ductility of the stiffened specimen is much larger than that of the unstiffened specimen. A similar observation holds true concerning the dissipated energy (see Fig. 3.30). Unlike A4, A5 and B2 to B5, specimen A3 did not show any noticeable increase in terms of ductility. This was due to flange and web buckling which occurred within the stiffened zone thus inhibiting any further increase in the member resistance. During the cycles of decreasing resistance, i-e, after local buckling took place, a comparison of the rate of resistance degradation for positive and negative bending moment from one cycle to the other shows, in Table 3.5, that specimens A4 and A5 underwent noticeably smaller rates of degradation than did specimens A2 and A3. This is an indication of the superiority of a herring-bone stiffener over a vertical one. A similar observation is equally applicable when comparing specimens B1 with B2 to B5 (Table 3.5). It can be gathered from Table 3.6 that while specimen B1 started showing signs of strength degradation, specimens B2 to B5 generally showed improved behavior for another 3 to 4 cycles before any evidence of strength degradation set-in.

3.4.2 Energy dissipation factors

To achieve economical design, ductile structures must dissipate large amounts of earthquake input energy through irrecoverable hysteretic energy dissipation. As such, structural members are required to undergo large inelastic deformations without significant loss of resistance and stiffness to enable them to dissipate the energy from the applied loading history. It is therefore clear that two factors are of paramount importance in earthquake engineering; these are namely: a) a member's ductility, i.e., its ability to deform and b) dissipate energy through inelastic excursions. The two above mentioned factors were found (Popov and Pinkney 1969; Popov and Bertero 1973) to yield two deterministic parameters used for the assessment of the response of a member or a structure subjected to dynamic loading. These are the ratio of the residual plastic deformation to the elastic deformation, denoted by the plasticity ratio π_d (Fig. 3.31-b), and the dissipation energy factor e_e, which is defined as the area under the half loop of the moment rotation curve to the elastic area defined as $0.5F_p\Delta_p$(Fig. 3.31). Note that F_p is the plastic load and Δ_p is the corresponding displacement. Thus to further comprehend the behavior of each of the specimens, use has been made of these two parameters to develop various diagrammatic relationships.

Of importance in resisting punishing cyclic forces is the normalized cumulated energy, Σe_e, defined as the sum of the normalized areas under half the hysteresis loops (positive or negative) that a member may experience. Figs. 3.32 and 3.33 show plots of this parameter and the corresponding values of the number of inelastic excursions experienced. It can be seen from these figures that the herring-bone stiffened specimens, A4 and A5 of group A and B2 to B5 of group B, dissipated noticeably more energy than the unstiffened specimens A2 and B1. Specimen A3, however, did not perform as anticipated as shown in Fig. 3.32-a. It behaved adequately up to the ninth inelastic excursion, but beyond that, the development of flange and web instability affected the energy absorption capabilities of the member.

A member under cyclic loading may follow three distinct behavioral paths (Fig. 3.34); these are as follows: a) If the member emulates an ideal elasto-plastic moment-rotation model, it will therefore follow path 3; consequently, there exists a unique relationship, of the type $e_e=2\pi_d$, between the normalized energy and the plasticity ratio. b) If the member exhibits strength deterioration, it will follow path 2. c) If it exhibits augmented strengthening, however, it will follow path 1.

With the above-mentioned in mind, the ratio, e_e, for specimens A2 to A5, and B1 to B5 is shown, in Fig. 3.35, in correspondence to each value of the plasticity ratio, π_d, defined earlier. A careful study of Fig. 3.35-a shows that all specimens in group A exhibited stable hysteresis loops up to a plasticity ratio of 4, as indicated by the straight line. In series A an appreciable change in the slope of specimen A2's curve occurred indicating plate instability. Specimen A3, meanwhile, behaved adequately up to a plasticity ratio of 4. After that a slight decrease in the slope continued to develop up to a plasticity ratio of 5.5 beyond which a sudden drop clearly occurred. Unlike the previous specimens, after maintaining its stability up to a plasticity ratio of 4.5, the e_e-π_d relationship of specimen A4 followed a rectilinear path up to the final loading. Specimen A5, in turn, behaved superbly up to a plasticity ratio of about 5. Its e_c-π_d relationship followed an almost horizontal path to the final stage. From Fig. 3.35-a, one can say that the herring-bone stiffened specimens A4 and A5 exhibited superior behavior throughout the tests compared to specimens A2 and A3.

From the series B test results (Fig. 3.35-b), observations made concerning series A, were clearly confirmed. It can be noted that the unstiffened specimen B1 started showing early signs of plate instability at about a plasticity ratio of 4, consequently deviating from path 3. Specimens B2, B4 and B5 continued to emulate an elasto-perfectly plastic behavior up to a plasticity ratio of about 6. However, specimen B3 showed signs of strain hardening from a plasticity ratio of 4 to 8. Afterwards, signs of plate instability started to set-in thus inhibiting a further increase in ductility. Overall, the herring-bone stiffened specimens B2 to B5 of group B displayed excellent behavior throughout the tests compared to the unstiffened specimen B1.

By normalizing the energy dissipated in every half loop to the energy absorbed by an elastic perfectly plastic member that undergoes the same plasticity ratio (Fig. 3.36), the normalized energy, e_p, can be obtained. A plot of the relationship of the normalized energy, e_p, with the corresponding values of the plasticity ratio is shown in Fig. 3.37. By examining Fig. 3.37-a, it appears that strain hardening effects are clearly evident up to a plasticity ratio of 4 to 5. Throughout the range of all plasticity ratio values, it will be noted that the herring-bone stiffened specimens, A4 and A5, dissipated about 15 to 25% more energy than the unstiffened specimen A2. Now, if a normalized energy of 0.8 in the early stage of loading for specimen A2 is taken as a reference value, then, we see that whereas specimen A2 developed a plasticity ratio of about 4.5, specimens, A4 and A5, yielded a plasticity ratio of about 6.5, i-e, an increase of about 45%. From Fig. 3.34-a it will be observed that specimen A3 exhibited an intermediate behavior up to a plasticity ratio of nearly 6. The trend exhibited by the stiffened specimens of series A is further magnified when examining at the test results of series B (Fig. 3.37-b). For instance, a comparison of the e_p-π_d curves shows that at a normalized energy reference value of 0.9, the plasticity ratio of specimens B2, B4 and B5 is about 60% more than that of B1. Meanwhile, the plasticity ratio of B3 is about double that of B1.

3.4.3 Remarks of a practical nature

Besides comparing the energy dissipation factors, a comparison was also undertaken with respect to ultimate strength and stiffness ratio at the ultimate state. Table 3.4 compares specimen response in terms of the normalized ultimate moment, M_u/M_p, and the normalized stiffness ratio, K_u/K_y, at ultimate deformation. These parameters are defined in Fig. 3.31. From the observations reported, an up-grade or retrofit of a ductile steel seismic moment resisting frame design may be achieved by simply introducing the herring-bone web stiffener only to critical regions. The same detail may indeed prove valid for relaxing b/2t and h/w slenderness ratios yet provide sufficient ductility, energy dissipation, joint strength and stiffness in a new design context. Also for reasons of: a) higher ductility, b) increased joint strength, c) higher dissipated energy and d) minimal joint stiffness loss, moment resisting frames utilizing herring-bone stiffeners at critical design locations are superior to regular ductile steel moment resisting frames.

A comparison of A4 with A5 shows that both specimens exhibited similar ductilities, resistance ratios and stiffness ratios; this is important since for the sake of minimizing construction and material costs, it is not necessary to use two sided herring-bone stiffeners. Single stiffeners of this type appear to be adequate. Another question which is of interest is whether it is necessary to fit or weld stiffeners to the flanges since there is the potential for cost savings. An alternate option would be to just use intermittently welded stiffeners on one side of the web only. Such details were investigated on specimens B4 and B5; a comparison of specimen B1 with B4 and B5 shows that these details can prove beneficial in terms of behavior.

Comparing the rotation capacity values of series A with those of series B (Table 3.3) suggests that the steepness of the moment gradient affects significantly the developed ductility. A beam with steep moment gradient, for instance B2, delivered greater ductility than one under a lesser moment gradient, as represented by specimen A4. Meanwhile, as only one section, subjected to two different moment gradients, has been used for purposes of comparison, the inference that the moment gradient affects significantly the delivered ductility is preliminary at best.

Let us reiterate that for a system ductility value, μ_s, of 4, we have suggested in Chapter 2 a member rotation capacity value of about 6 for plastic design. Examination of Table 3.3 shows that the unstiffened specimens either tested monotonically or cyclically did not deliver this required rotation capacity. The use of herring-bone stiffeners demonstrated that the stiffened beams can easily reach such a value under monotonic loading. Under cyclic loading, only specimens B3 to B5 delivered a rotation capacity of 6 or close to that value.

However, since the specimens were selected with slenderness ratios very close to those of Class 2, the results for a majority of class 1 sections would be improved even further. More may be found in papers by Korol and Daali (1994) and Korol and Daali (1995)

Last but not least, we have seen in Figs. 3.8 and 3.10 that local plate instability leads to significant strength and energy degradation from one cycle to the other. Clearly, low-cycle fatigue effects due to local buckling in the post-buckling range played a major role in the life of the specimen. These should, therefore, be accounted for in assessing the performance of structural beams when subjected to inelastic loading.

3.5 Finite element model

3.5.1 Introduction

From the study described earlier, it was observed that the maximum web out-of-plane deformations occur in the compression zone of the web, between the neutral axis and the inside of the flange. The location of the eventual plastic hinge and the corresponding out-of-plane deformations in the flanges and web have also been observed to occur within an approximate distance of a half web depth from the face of the end-plate connected to the column. Furthermore, studies (Rockey and Legget 1962) on the stability of longitudinally stiffened girder plates under static flexure had shown that the stiffener optimum location is at about one fifth of the depth of the web below the compression flange. To minimize or completely eliminate the out-of-plane deformations when reversal of loading is occurring, a local flange and web stiffener must therefore be located within a distance equal to the web depth from the face of the column. Because symmetry is of major importance when reversal of loading is present, the stiffeners must be located on both sides of the neutral axis.

Because of the complexities involved in optimizing the design of a stiffener, at the ultimate strength state, it was decided to use a finite element model (F.E.M.) to investigate the effects of employing a Herring-bone type stiffener on the behavior of locally stiffened beams. The aim was to use such results to propose some preliminary guidelines for the design of these stiffeners. The program initially developed by Koziey & Mirza (1993) uses a cubic-quadratic shell element with cubic approximations of displacements u, v and w at the corner nodes, one-third side nodes and the center node and quadratic approximations of rotations, α, β, ϕ and ψ at the corner nodes and mid-side nodes (Fig. 3.38). El Damatty et al. (1993) later extended the formulation to include material and geometrical non-linearities; the program was verified using a number of shell and plate structures in the non-linear range.

3.5.2 Validation of the F.E.Model

To show the validity of the finite element model, it was decided to compare the maximum load restoring characteristics achieved in the experimental tests with that obtained using the finite element model. Three specimens were used for the purpose of this comparison; these are namely: specimens P1, A0 and B0. To reflect as closely as possible the laboratory conditions experienced during the experiments, the finite element beam-model was fully fixed at one end, had lateral supports in accordance with the tested specimens and was loaded by an incremental tip load A mesh layout as shown in Fig. 3.39 was utilized.

In Table 3.8 is shown the comparison between the experimental and numerical results. It can be noted that the numerical finite element model reflected the laboratory results quite accurately. Percentage differences of 4, 8 and 13 were obtained for specimens P1, A0 and B0 respectively.

To further establish the validity of the results, the deformations resulting from the numerical study were also qualitatively compared to those observed in the experiments. The finite element results of the W-shaped cantilever beams under tip-loading showed that out-of-plane deformations in the flange and web occur mostly within a distance equal to the depth of the web from the face of the end-plate. For instance, Fig. 3.40 shows that local buckles in the flange under compression have apexes at about 250 to 300 mm from the face of the end-plate. Fig. 3.41 shows that deformations in the bottom part of web developed almost throughout the entire length of the beam; this may be the result of precipitation of lateral torsional buckling occuring in the plastic hinge zone. Schematic illustrations of these observations are shown in Fig. 3.42.

3.5.3 Employment of the F.E. Model to predict stiffener thickness requirements

The primary objective of the finite element analysis was to present design guidelines for the stiffener. To achieve it, a decision was made to fix the flange and web slenderness ratios as shown in Table 3.7 and vary the thickness of the stiffener. The subsequent load tip-displacement curves were then to be tracked up to the maximum moment. The optimum stiffener thickness would then be defined as the thickness at which no more additional displacement at maximum load is obtained, i.e., no more enhancement in terms of ductility is obtained. Note that this requirement is conservative because the unloading path that adds to ductility before falling below M_p is ignored.

For the problem at hand, a cantilever beam having a length of 2100 mm, a flange width of 160 mm and a center-line distance between flanges of 320 mm was used as a base element. A herring-bone stiffener was attached to the beam at 1.25 times the minimum half buckling wave-length, L_{hw}, of the flange. The thicknesses of the flanges and web were then varied to reflect different slenderness ratios of the plates (Table 3.7). Fig. 3.43 shows typical load tip-displacement response curves for the different stiffener plate thickness. It can be seen that increasing the stiffener thickness results in an improvement in terms of displacement at maximum moment. A ductility enhancement of the order of 20 to 30 % is generally obtained. Finally, from the results of the F.E.M. analysis, the obtained optimal stiffener thickness and the corresponding plate slendernesses were used to construct stiffener design graphs (Figs. 3.44 & 3.45) that reflect the interaction between flange and web slenderness ratios with the appropriate stiffener thickness or slenderness ratio. The design graphs suggest that with increasing flange slenderness and increasing web slenderness, the stiffener thickness should increase, or, correspondingly the stiffener slenderness should decrease.

From observations obtained in the test series undertaken and the finite element analysis, some design considerations will be addressed in the following section.

3.6 Design consideration for locally stiffened beams

3.6.1 Introduction

For plastic design (or Class 1) sections, two local buckling criteria were advanced by Lay (1965). These are as follows: 1) the section should be able to attain a fully yielded condition before local buckling. 2) For a beam under uniform moment, it is necessary that plastification extends sufficiently to allow for a half-wave length to be accommodated, termed the longitudinal buckling criterion. 3) In earthquake resistant design, a third requirement that reflects the ability of a member to deform well into the inelastic range without significant loss in strength is implicitly recognized in design codes and is termed "ductility".

Theoretical considerations of a cantilever beam under tip loading (Fig. 3.46) show that the rotation can be obtained by simply integrating the curvature distribution. Meanwhile, ductility, μ, is defined as the ratio of some rotation to the rotation corresponding to the plastic moment, i.e. θ/θ_p. Then referring to Fig. 3.46 one can show diagrammatically that a beam under no yielding in the plastic hinge zone would develop a ductility, at maximum moment, of $(0.5\phi_p L)/(0.5\phi_p L)=1$. When yielding extends over a finite length of the member, the ductility becomes:

$$\mu = \frac{\int \phi dx}{\theta_p} > 1$$

From this simple illustration, one can say that with an increase of the extent of yielding, the ability of a member to deform and exhibit additional ductility is also increased.

3.6.2 Longitudinal buckling criterion

Before discussing the design considerations for locally stiffened beams, let us first review how buckling initiates in beams generally. Understanding this phenomenon will allow the development of some provisions that may retard it.

For a beam under uniform moment, it is necessary that the yielded length in the flanges or web extends enough to allow for a half-wave length to develop and initiate local buckling (Fig. 3.47-a). However a beam under moment gradient requires a length equal to at least a full-wave length to yield before local buckling is initiated (Lay 1965). The difference in wave lengths is the result of different boundary conditions at the end of the yielded zones. Whereas in the beam under uniform moment, yielding may extend over the whole member, in the case of a beam under moment gradient, the yielded zone has ends that are well restrained or bounded. This is the result of restraint at the end of the yielded zone in the form of a point load or an elastic region as illustrated schematically in Fig. 3.47-b.

Using the torsional buckling equation of a flange restrained against buckling by a torsional spring, Kemp (1986) modified the assumptions of Lay and Galambos (1967) to obtain an expression for the yielded length that can accommodate a half-wave in order for local buckling to initiate. The expression is given by:

$$L_{hw} = \sqrt{\frac{C_f \pi^2 (2b)^2}{1.5 \epsilon_b (2b/t)^2 - 2}} \qquad \textbf{(3.1)}$$

where C_f is a parameter that reflects the level of restraint between the flange and the web. The value is 0.5 for the case of no web restraint and 1.0 when there is full web and warping restraint. The strain , ε_b in Eqn. 3.1 is the value obtained at the center of the yielded length and is given by:

$$\epsilon_b=\epsilon_y(s+e\frac{L_{hw}}{L-L_{hw}})$$

with $e=\frac{E}{E_s}$, $s=\frac{\epsilon_y}{\epsilon_{sh}}$

3.6.3 Stiffener configurations

In the context of framed structures subjected to lateral loading, beams will have bending moments that decrease (or increase) in value from one end of the beam to the other. Under such conditions, a beam under moment gradient would develop local buckling if the yielded length extends sufficiently to accommodate a full-wave length. If, however, in the potential plastic hinge zone a support that eliminates out of plane deformations is introduced (Fig. 3.48), the buckle would not initiate where it would have originally. Rather, it would be delayed until sufficient yielding spreads over the element and allows for a buckle to initiate in the adjacent zone. For instance, if a support is introduced at 1.25 times L_{hw} from the face of the end-plate, the extent of additional yielding would theoretically vary between about 0.65 times L_{hw} to 1.25 times L_{hw} depending on the level of rotational restraint provided by the stiffener to the flange or web. This subsequently would allow the beam to develop higher than normal ductility capacity.

One way to support the flanges and web of an I or a W-section is to provide a stiffener in the potential plastic hinge zone. Numerous configurations exist. For example, one may provide a longitudinal, a vertical, a diagonal stiffener or some other configuration which is deemed appropriate (Fig. 3.49).

As a consequence of the local buckling interactions, a Herring-bone style stiffener (Fig. 3.50) is advocated for several reasons: a) it has the advantage of distributing the material symmetrically about the neutral axis, b) it stiffens the web simultaneously in the vertical as well as the horizontal direction and c) it enforces nodal lines through the locations of maximum out of plane deformations in the flanges and the web.

3.6.4 Ductility enhancement at incipient buckling

If a one-sided herring-bone stiffener is used to locally stiffen a beam, then to have an appreciation of the increase in ductility at incipient buckling, the following methodology may be used. First, consider a curvature distribution of the type shown in Fig. 3.46. The ductility, μ, for this case may be written as:

$$\mu=1+\eta((2s-1)+e\frac{\eta}{1-\eta}) \qquad (3.2)$$

where $\eta=2L_{hw}/L$

Second, the half wave-length associated with the initiation of local buckling can be obtained by using Eqn. 3.1 which is repeated for sake of convenience as:

$$L_{hw}=\sqrt{\frac{C_f\pi^2(2b)^2}{1.5\epsilon_b(2b/t)^2-2}}$$

For an unstiffened beam, the ductility is obtained by simply substituting L_{hw} from Eqn. 3.1 into Eqn. 3.2. For a stiffened beam, assuming that the stiffener having rotational and translational restraints is located at 1.25 times L_{hw}, the term, $\eta=2L_{hw}/L$, in Eqn. 3.2 should be replaced by a maximum yielded length of $1.25L_{hw}+2\,L_{hw}=3.25L_{hw}$ (Fig. 3.48). For instance, if it is assumed that a cantilever unstiffened beam with material properties e=36, s=9 and having a yielded proportion $\eta=2L_{hw}/L=0.1$, the member would then have a ductility of 3.1. The same member with a stiffener delivering additional growth in the yielded zone of $3.0L_{hw}-2L_{hw}=1.0L_{hw}$ results in an η value of 0.15 (or a 50% increase) and a subsequent ductility, μ, of 4.5, i.e. a ductility enhancement of 45%. This is illustrated by path 1 and path 2 shown in Fig. 3.51. The same Figure shows additional curves having their associated increases in ductility and corresponding proportion of yielded lengths.

3.6.5 Design guidelines

The following preliminary suggestions are made on the basis of the above-described studies:

1) Since the predictions of the buckling half-wave lengths are at best approximate because of the unknown level of restraint between the flange and web, the stiffener should be located at a distance of 1.25 L_{hw} from the face of the end plate. Here the buckling half-wave length, L_{hw}, is obtained from Eqn. 1 using a parameter C_f of 0.5.

2) The stiffener ought to be attached to the flanges and web by intermittent fillet welds designed to resist 1.2 times 10% the compression yield force of half the flange and 1.2 times 10% the compression yield force of half the web depth respectively. The factor 1.2 reflects the possible strain-hardening that may be attained in the inelastic range.

3) The Herring-bone stiffener may be located on one side of the web only.

4) The stiffener may be designed using the design graphs shown in Figs. 3.44 & 3.45. Note that in practice, a stiffener thickness of less than about 4 mm would not be specified.

3.7 SUMMARY

From the study conducted in Chapter 3, the following summary-conclusions may be drawn:

1) The herring-bone stiffener definitely plays a beneficial role in enhancing the rotation capacity in beams where deficiencies in ductility and corresponding rotation capacity exist.

2) A one sided stiffener positioned at about 1.25 times the minimum buckling half wave-length of the flange and attached to the flanges and web by intermittent fillet welds seems to yield very good results.

3) A methodology for locating and designing the stiffener has been presented in section 3.5 of this Chapter. The location of the stiffener is simply obtained by calculating the natural buckling half wave-length of the flange of the beam in question; the thickness or slenderness of the stiffener may be selected from design graphs (Figs. 3.44 and 3.45) that relate the plates slenderness with the stiffener slenderness values.

4) The Herring-bone stiffening detail may be used not only to up-grade a ductile moment resisting frame design by adding this device to critical regions, but may also allow relaxation of the b/2t and h/w slenderness ratio requirements in CAN/CSA-S16.1-M89, without sacrificing needed ductility, energy dissipation, joint strength and stiffness.

Table 3.1 Tensile coupons test results

Specimen #	Flange		Web	
	Yield (MPa)	Ultimate (MPa)	Yield (MPa)	Ultimate (MPa)
P1	346	532	359	533
P2	-	-	-	-
P3	-	-	-	-
A0	300	444	313	456
A1	301	460	312	472
A2	300	465	314	450
A3	299	467	319	434
A4	296	450	312	475
A5	296	453	312	478
A6	326	487	348	501
B0	326	487	348	501
B1	323	485	344	498
B2	300	444	313	456
B3	322	488	345	496
B4	321	487	343	500
B5	322	488	331	494

Table 3.2 Comparison of actual and nominal dimensions of beam sections.

Spec. #	Flange Thickness (mm)		Web Thickness (mm)		Section Depth (mm)		Section Width (mm)	
	Nominal	Actual	Nominal	Actual	Nominal	Actual	Nominal	Actual
P1	9.7	9.6	5.8	5.6	310	311	165	166
P2	-	10	-	5.59	-	311	-	166
P3	-	9.8	-	5.7	-	311	-	165
A0	5.7	5.7	5.1	5.2	303	302	101	102
A1	-	5.6	-	5.2	-	304	-	103
A2	-	5.8	-	5.1	-	304	-	103
A3		5.6		5.1		304		103
A4	-	5.7	-	5.3	-	302	-	103
A5	-	5.6	-	5.2	-	304	-	101
A6	-	5.8	-	5.1	-	304	-	103
B0	-	5.8	-	5.1	-	304	-	103
B1	-	5.6	-	5.2	-	303	-	102
B2		5.6		5.2		304		102
B3	-	5.7	-	5.3	-	302	-	103
B4	-	5.6	-	5.1	-	303	-	102
B5	-	5.8	-	5.3	-	303	-	103

Table 3.3 Summary of experimental results: rotation capacity values

Specimen #	Specimen Description	Rotation Capacity, R_u, Measured from Zero Displacement Intercept		Rotation Capacity, R_u, Measured from Zero Force Intercept	
		+ve	-ve	+ve	-ve
P1	M- 310W39	5.88	-	5.88	-
P2	C- 310W39	5.75	0.41	5.75	5.34
P3	C- 310W39, V-stiffener	9.4	0.75	9.4	9.4
A0	M- 310W21	5.10	-	5.10	-
A1	C- 310W21	1.92	0.82	3.28	3.7
A2	C- 310W21	2.44	1.69	4.44	2.98
A3	C- 310W21, vertical Stiffener	2.69	2.49	4.89	4.5
A4	C- 310W21, V-stiffener	3.51	3.17	6.23	5.68
A5	C- 310W21, V-stiffener on both sides	3.15	3.16	6.1	5.78
A6	M- 310W21, V-stiffener	7.25	-	7.25	-
B0	M- 310W21	5.96	-	5.96	-
B1	C- 310W21	3.10	2.78	5.31	4.81
B2	C- 310W21, V-stiffener @ L_w	4.44	3.93	7.56	6.93
B3	C- 310W21, V-stiffener @ 1.5 L_w	6.19	7.37	9.18	12.49
B4	C- 310W21, V-stiffeners on both sides, welded to web and fitted to flanges	5.36	4.93	10.5	8.0
B5	C- 310W21, V-stiffener intermittently welded	5.79	5.46	9.3	8.79

where : $R_u=(\theta_{max}/\theta_p)-1$

M: Monotonic Load

C: Cyclic Load

L_w=110 mm

Table 3.4 **Summary of experimental results: Maximum resisting force and stiffness values.**

Specimen #	M_{max}/M_p	M_p (kN.M)	K_u/K_y	
			+ve	-ve
P1	1.13	211.1	0.15	-
P2	1.20	211.1	0.15	N.A.
P3	1.30	211.1	0.10	N.A.
A0	1.19	85.0	0.16	-
A1	1.118	89.4	0.34	N.A.
A2	1.17	89.4	0.29	0.37
A3	1.17	89.7	0.27	0.29
A4	1.21	88.6	0.22	0.24
A5	1.26	88.5	0.24	0.24
A6	1.19	87.12	0.12	-
B0	1.17	93.55	0.14	-
B1	1.19	92.7	0.24	0.26
B2	1.24	93.84	0.18	0.20
B3	1.25	92.4	0.14	0.12
B4	1.26	92.13	0.16	0.17
B5	1.23	92.4	0.15	0.15

Table 3.5 Resistance Deterioration beyond ninth Cycle for series A Specimens

Cycle #	M/M_n for +ve Bending				M/M_n for -ve Bending			
	A2	A3	A4	A5	A2	A3	A4	A5
10	1.12	1.17	1.20	1.26	0.95	1.11	1.15	1.22
11	1.06	1.15	1.14	1.25	0.87	1.06	1.02	1.17
12	0.95	1.06	1.02	1.13	0.79	0.93	0.96	1.01
13	0.89	0.91	0.98	0.97	0.72	0.82	0.92	0.90
14	0.84	0.78	0.94	0.87	0.66	0.74	0.87	0.80
15	0.76	0.67	0.86	0.79	0.60	0.65	0.82	0.72
16	0.68	0.58	0.84	0.73	0.53	0.57	0.76	0.66

Table 3.6 Resistance Deterioration beyond seventh Cycle for series B Specimens

Cycle #	M/M_p for +ve Bending					M/M_p for -ve Bending				
	B1	B2	B3	B4	B5	B1	B2	B3	B4	B5
7	1.18	1.22	1.21	1.21	1.17	1.12	1.23	1.23	1.21	1.19
8	1.16	1.24	1.24	1.23	1.21	1.05	1.24	1.24	1.20	1.21
9	1.04	1.24	1.25	1.25	1.23	0.99	1.21	1.25	1.24	1.20
10	0.96	1.17	1.25	1.26	1.22	0.94	1.07	1.26	1.16	1.16
11	0.94	1.04	1.24	1.26	1.13	0.92	0.99	1.25	1.08	1.06
12	0.91	0.99	1.22	1.23	1.05	0.90	0.94	1.24	1.02	1.00
13	0.89	0.95	1.19	1.18	1.01	0.85	0.91	1.23	0.97	0.98
14	0.86	0.91	1.10	1.10	0.99	0.80	0.87	1.21	0.93	0.96
15	0.82	0.87	1.00	1.02	0.97	0.74	0.83	1.19	0.92	0.94

Table 3.7 Sections characteristics and stiffeners location

Section #	Flange Slenderness Ratio, b/2t	Web Slenderness Ratio, h/w	span (mm)	Location of stiffener=1.25L_{hw}	Optimum Stiffener Thickness (mm)
1	6	30	2125	316	2.0
2	"	40	"	316	4.0
3	"	50	"	316	6.0
4	7	30	"	249	3.0
5	"	40	"	249	5.5
6	"	50	"	249	7.0
7	8	30	"	208	8.0
8	"	40	"	208	10.0
9	"	50	"	208	11.0
10	9	30	"	179	9.0
11	"	40	"	179	11.0
12	"	50	"	179	12.0

Table 3.8 Comparison of experimental and numerical results for P1, A0 and B0

Specimen	Section	Span, L (mm)	Maximum Load (kN)	
			Experimental	Numerical
P1	W310×39	2100	113.59	118.0
A0	W310×21	2100	48.16	52.00
B0	W310×21	1200	86.29	98.00

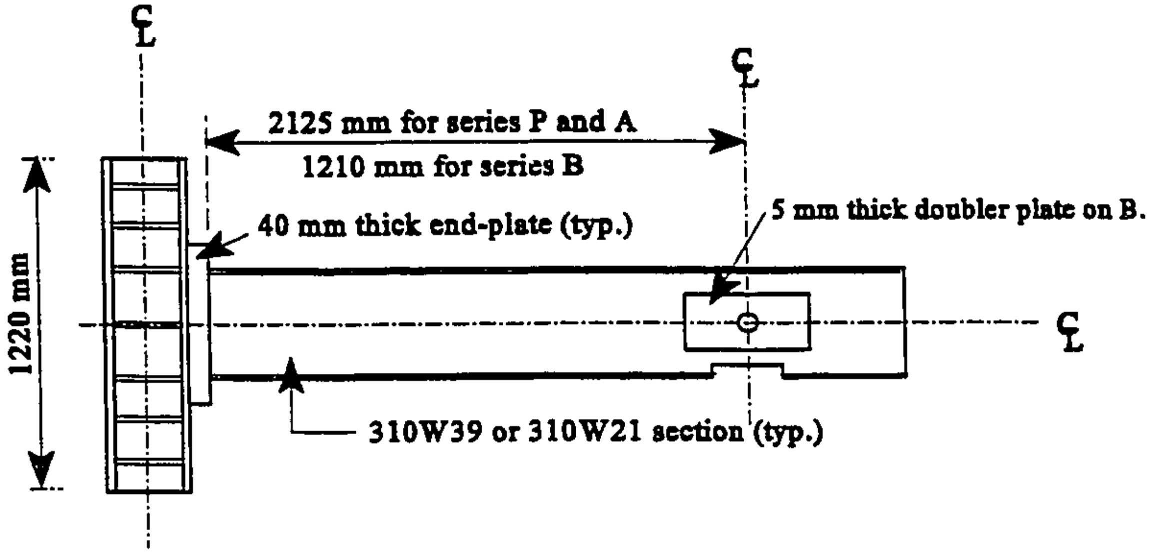

Fig. 3.1 A typical specimen with column stub

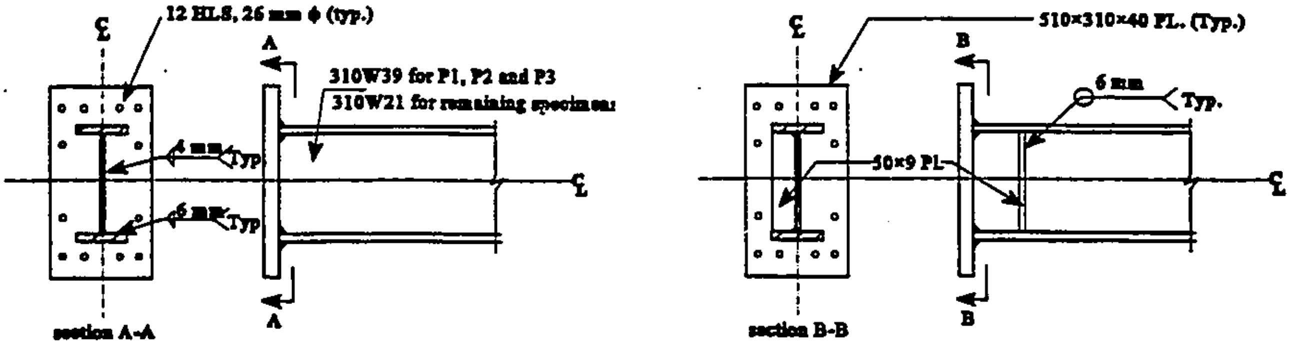

(a) - Specimens P1, P2, A0, A1, A2, B0 and B1

(b) - Specimen A3

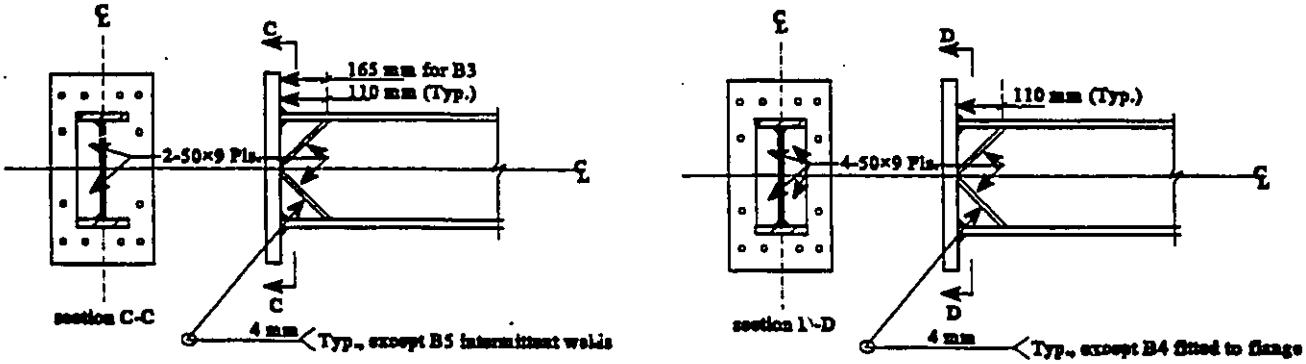

(C) - Specimens P3, A4, A6, B2, B3 and B5

(D) - Specimens A5 and B4

Fig. 3.2 Fabrication Details

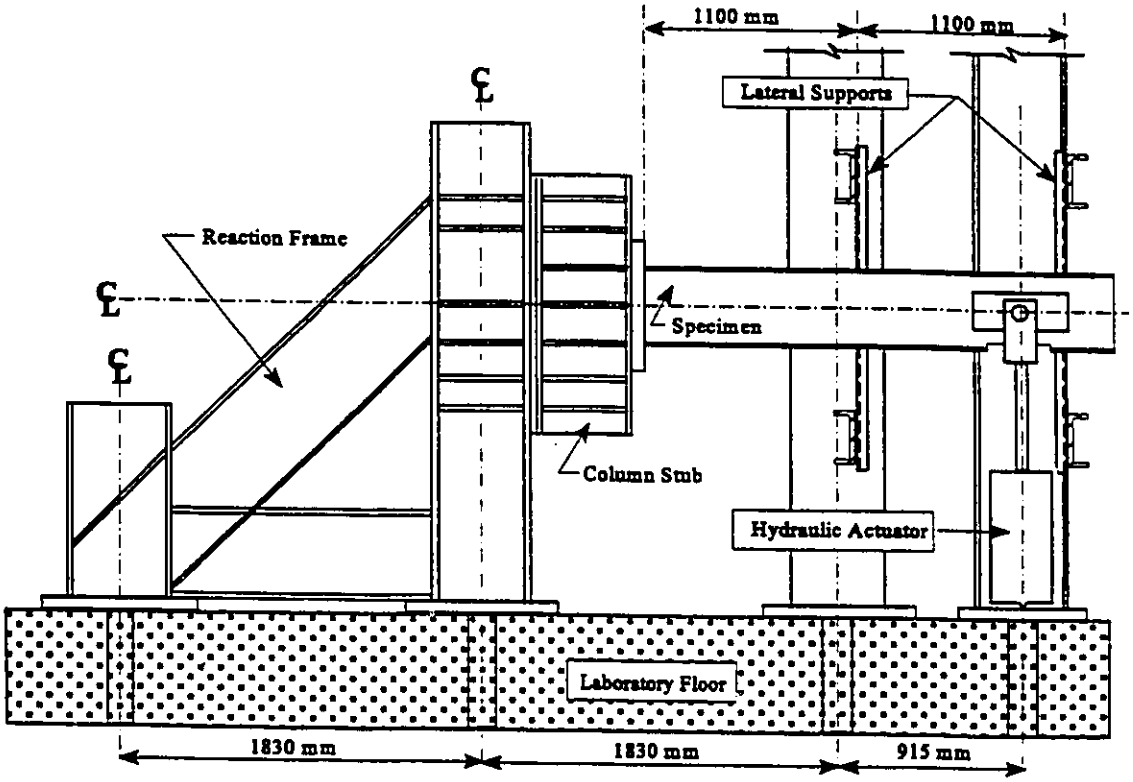

Fig. 3.3 Test Rig

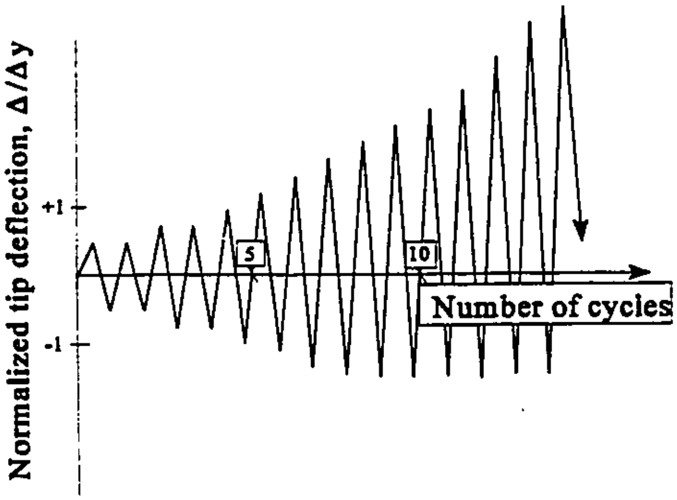

a- Non-symmetric load history, L1

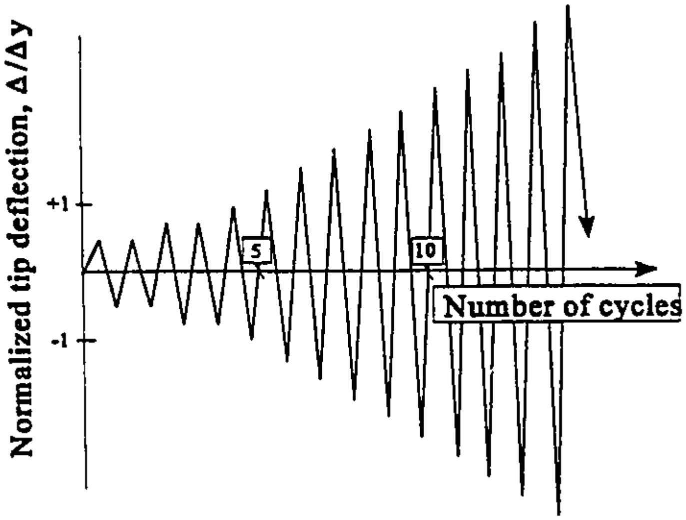

b- Symmetric load history, L2

Fig. 3.4 Load Histories

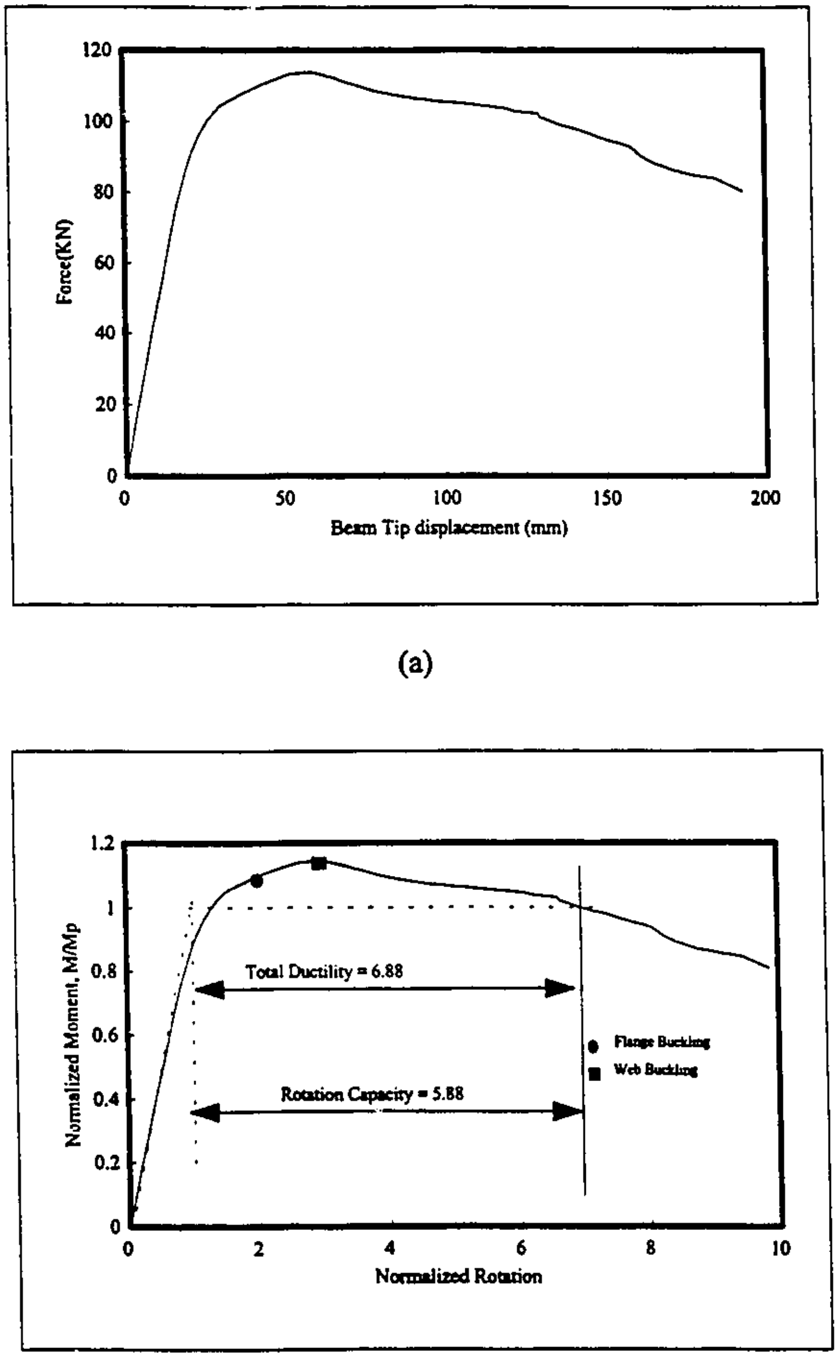

(a)

(b)

Fig. 3.5 Response of Specimen P1 under Monotonic Loading
(a) Force vs Beam Tip Displacement; (b) Normalized Moment-Rotation

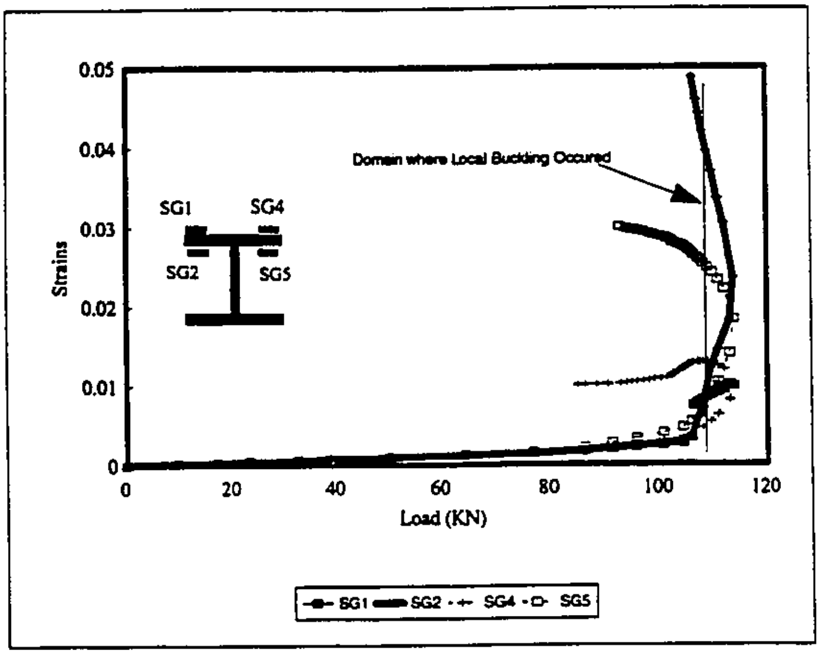

(a)

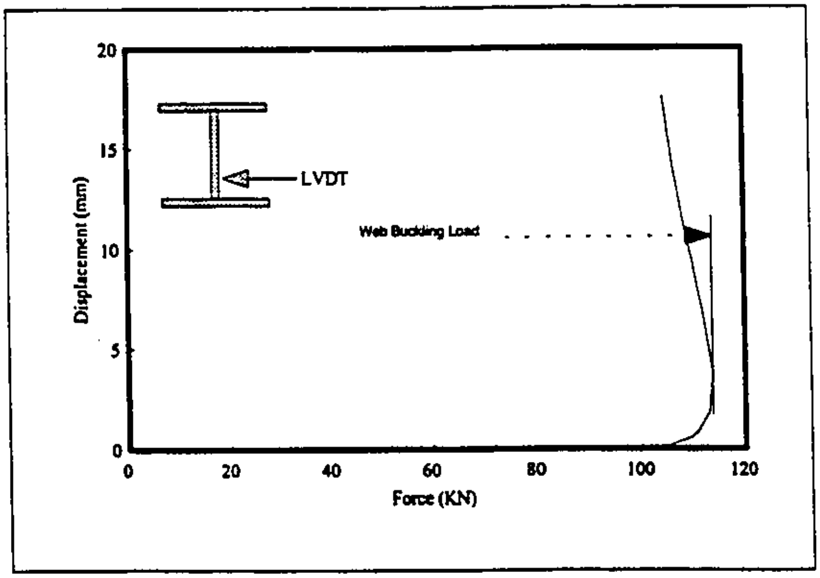

(b)

Fig. 3.6 Strains at Iniatiation of Buckling
(a) Flange Buckling; (b) Web Buckling

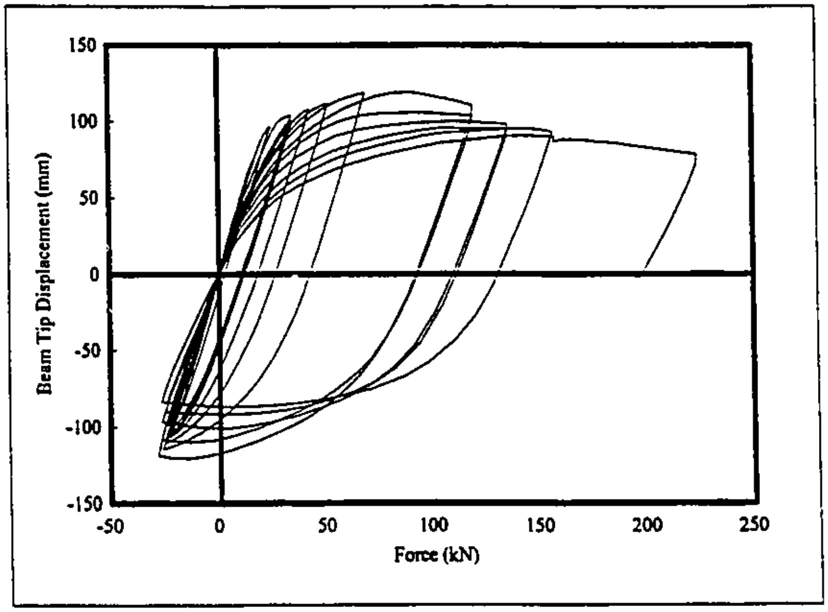

(a)

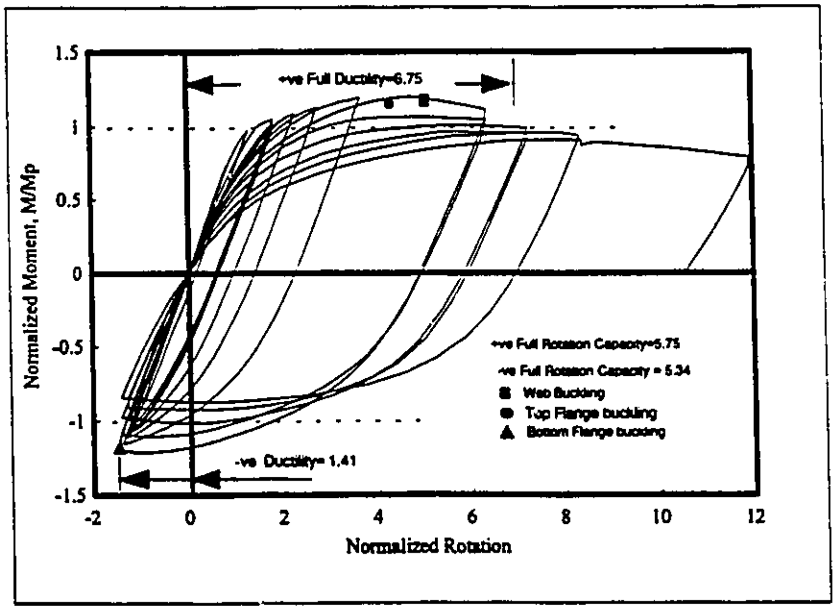

(b)

Fig. 3.7 Response of Specimen P2 under cyclic Loading
(a) Force vs Beam Tip Displacement; (b) Normalized Moment Rotation

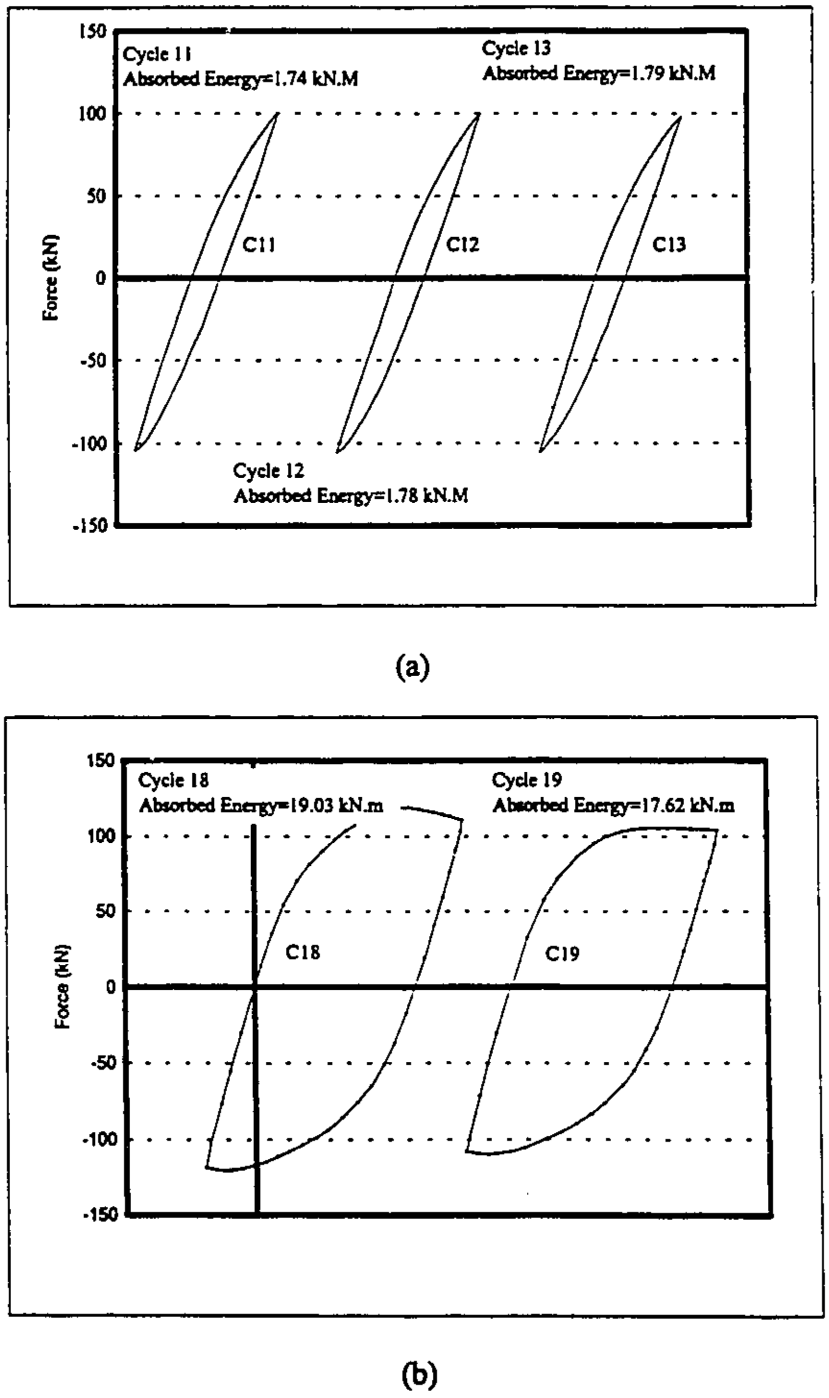

Fig. 3.8 Constant Amplitude Hysteresis Loops For Specimen P2
(a) Pre-Buckling Range; (b) Post-Buckling Range

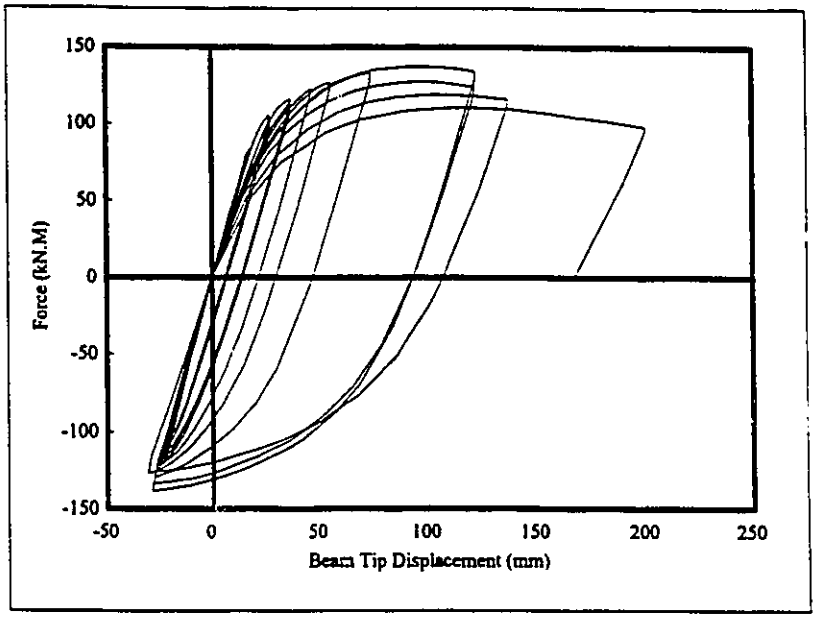

(a)

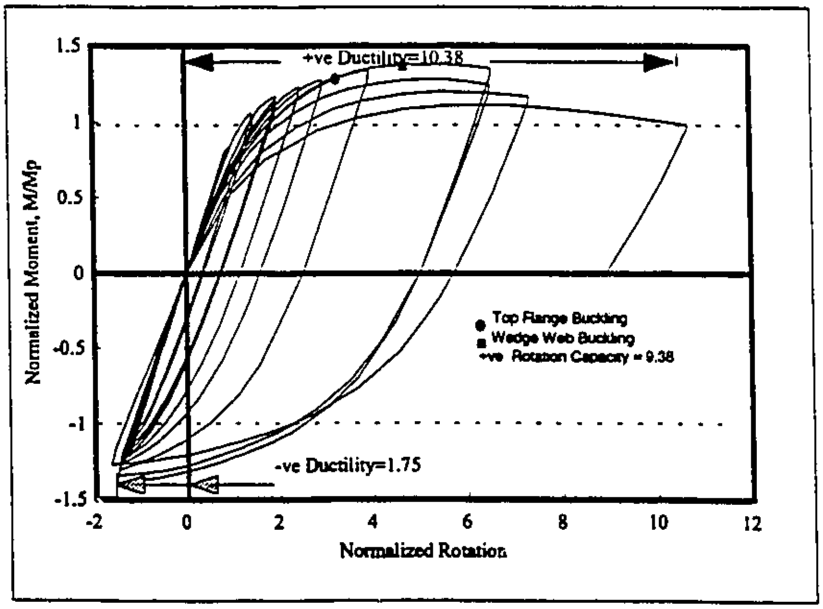

(b)

Fig. 3.9 Response of Specimen P3 under Cyclic Loading
(a) Force vs Beam; (b) Normalized Moment-Rotation

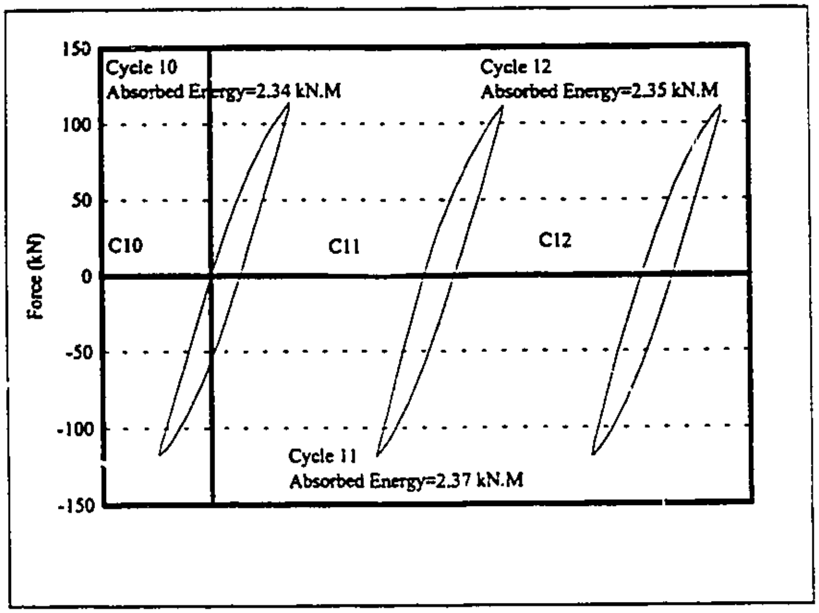

(a)

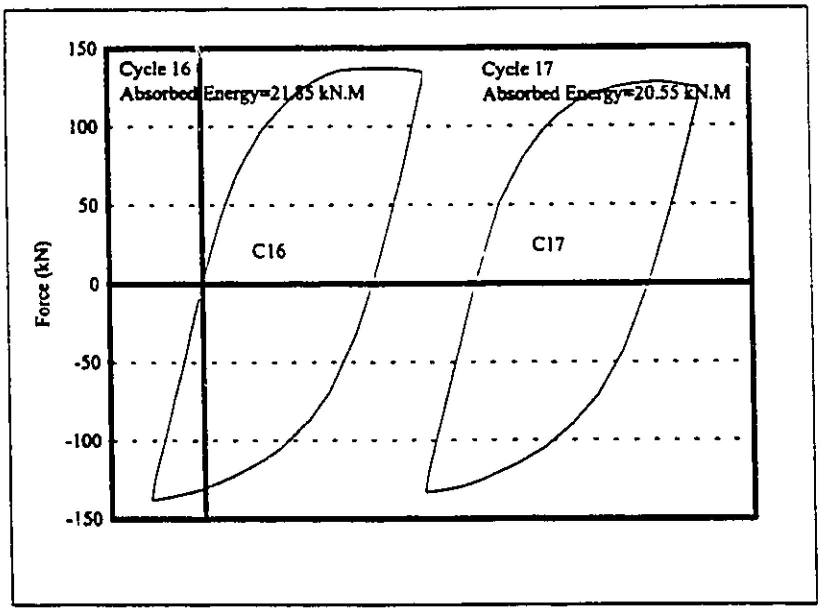

(b)

Fig. 3.10 Constant Amplitude Hysteresis Loops for Specimen P3
(a) Pre-Buckling Range; (b) Post-Buckling Range

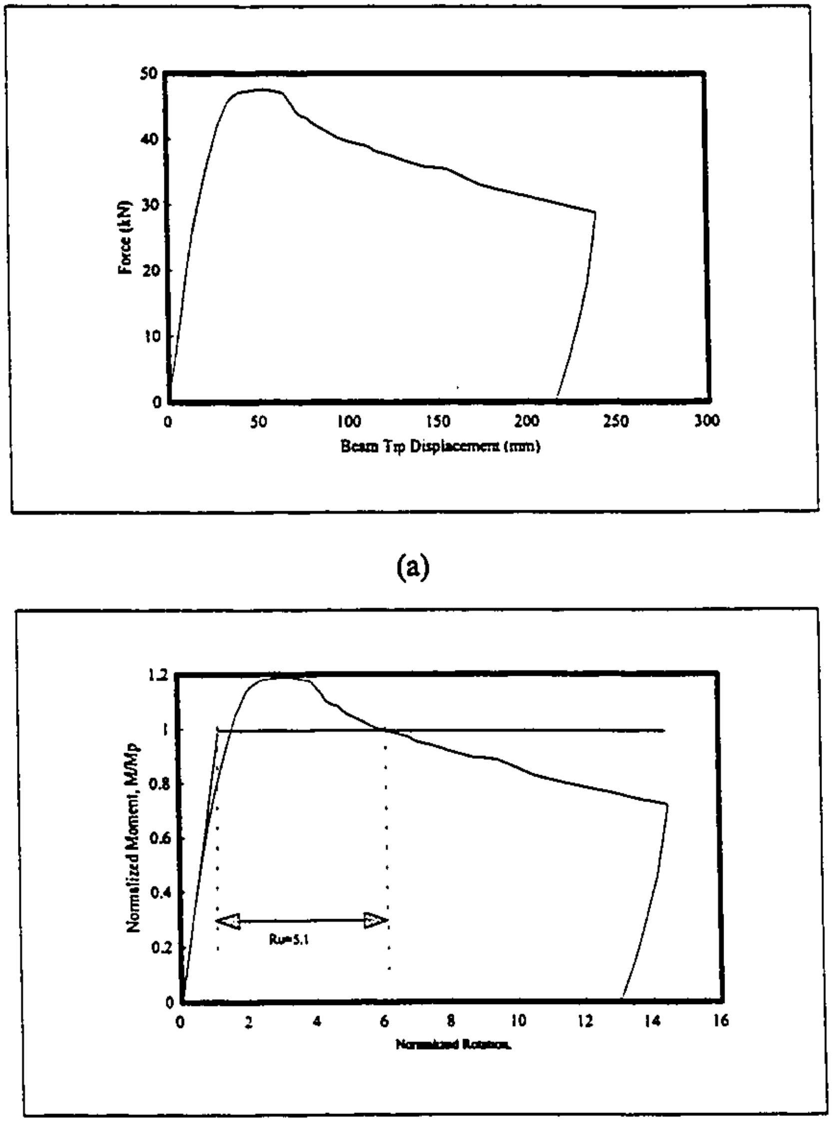

(a)

(b)

Fig. 3.11Response of Specimen A0 under Monotonic Loading
(a) Force vs Beam Tip Displacement; (b) Normalized Moment Rotation

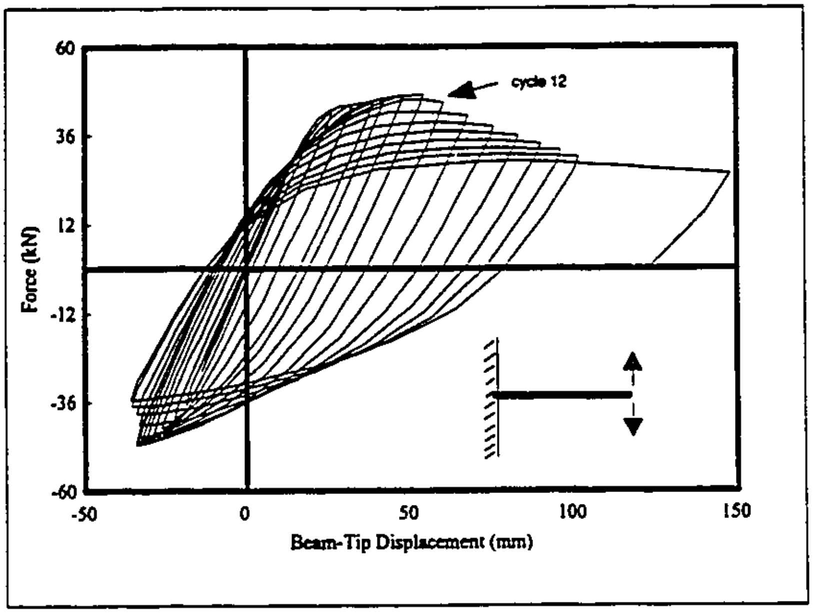

(a)

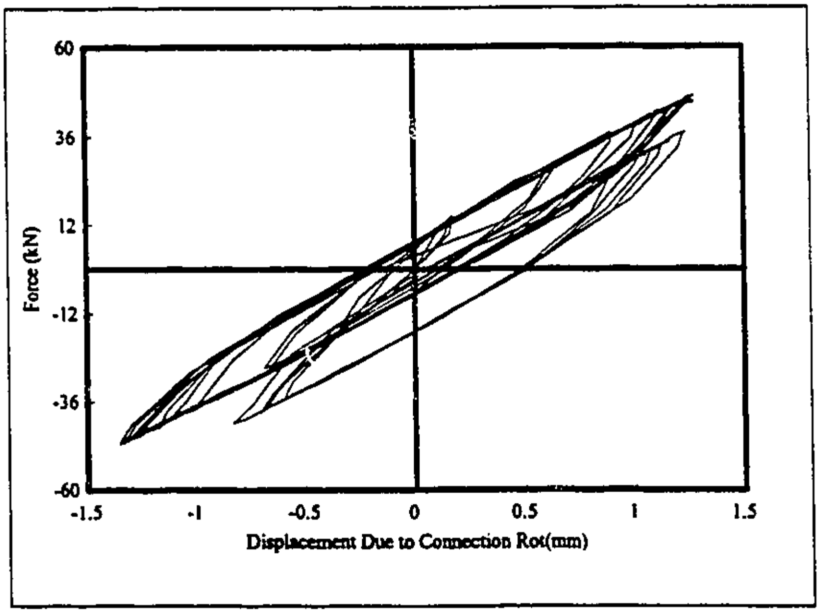

(b)

Fig. 3.12 Response of Specimen A1 Under Cyclic Loading
(a) Force vs Beam Tip Displacement;
(b) Force vs Beam Tip Displacement Due to Connection Rotation

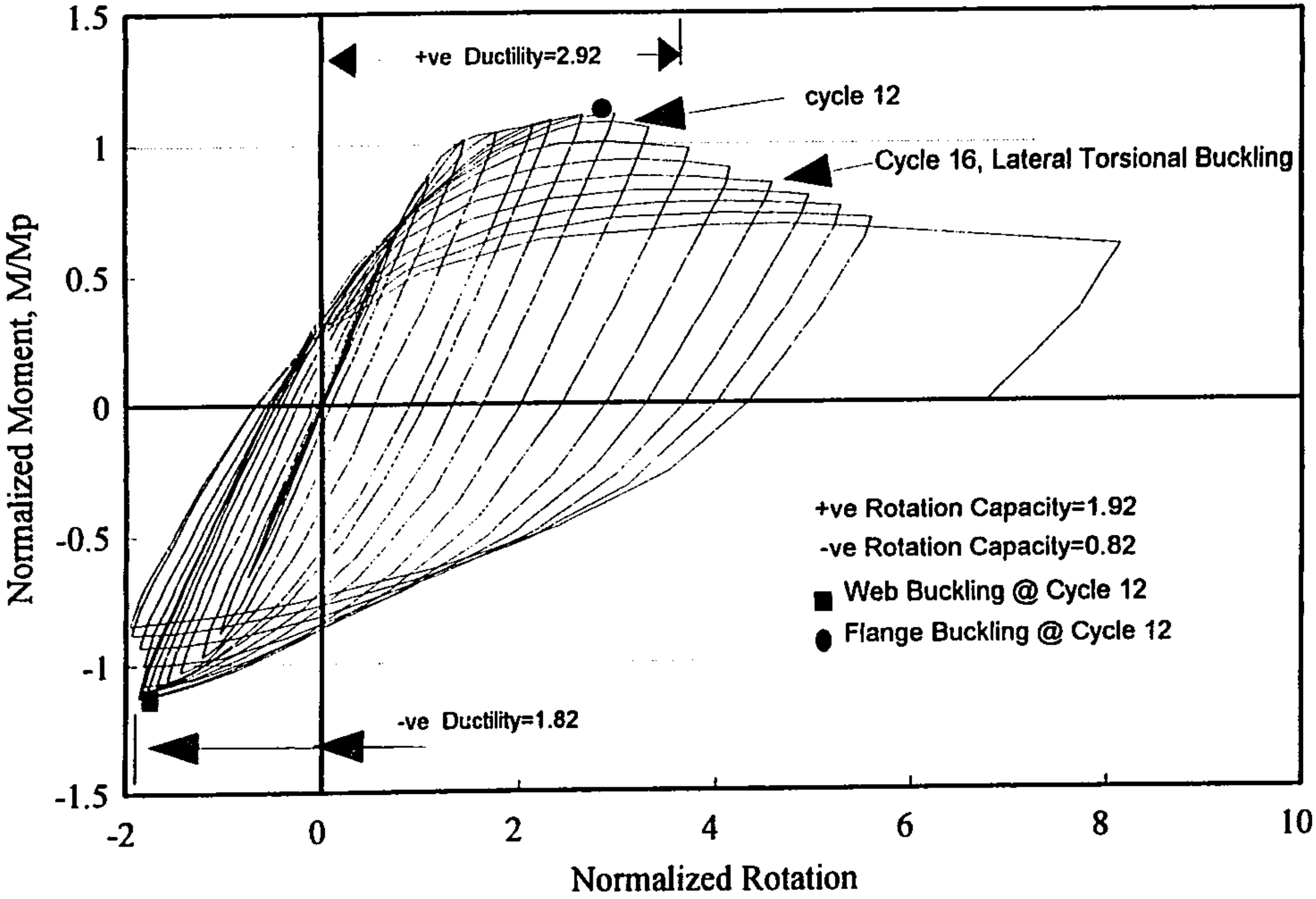

Fig. 3.13 Normalized Moment-Rotation Hysteresis Loops for Specimen A1

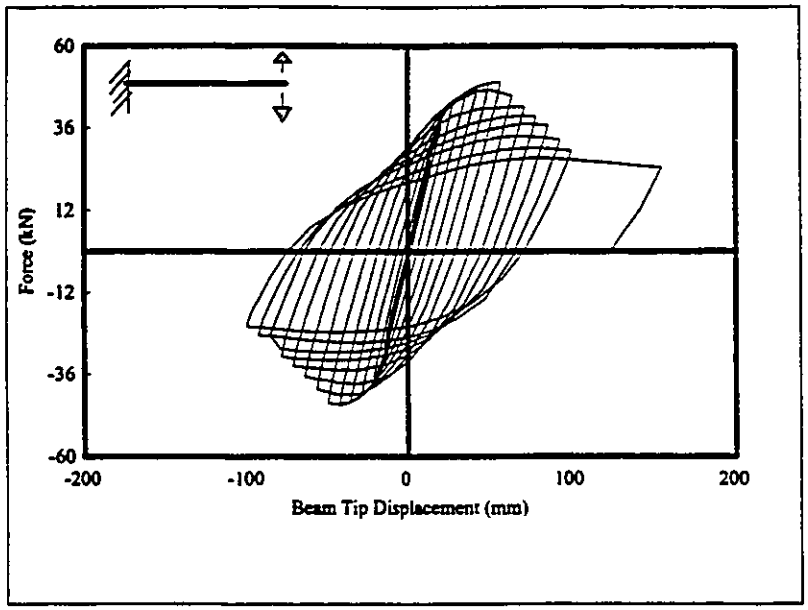

(a)

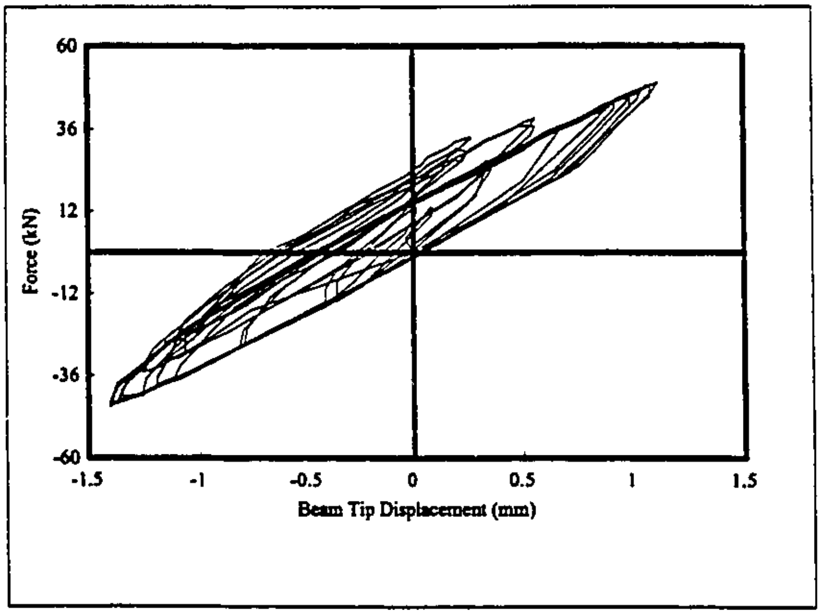

(b)

Fig. 3.14 Response of Specimen A2 Under Cyclic Loading
(a) Force vs Beam Tip Displacement
(b) Force vs Beam Tip Displacement Due to Connection Rotation

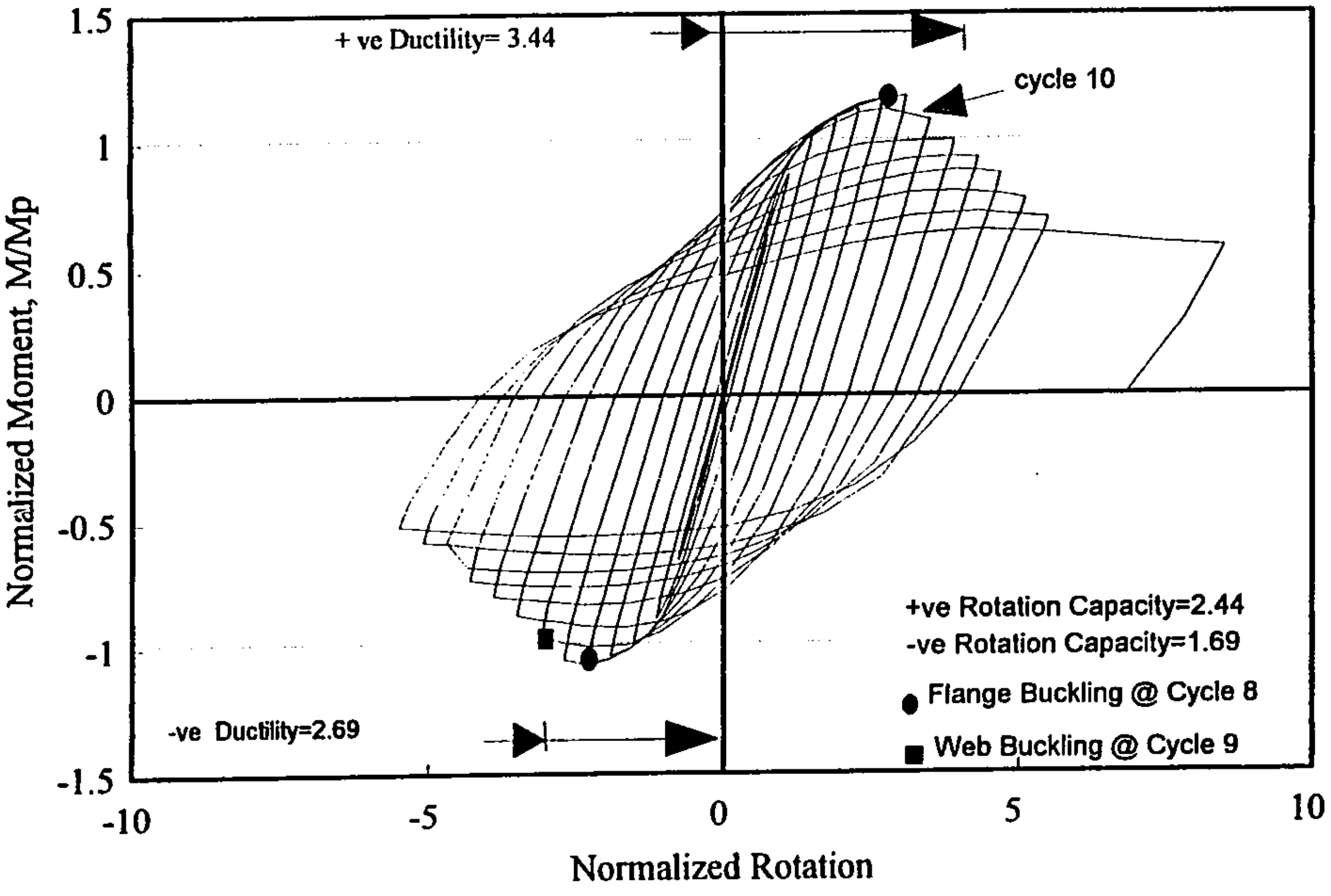

Fig. 3.15 Normalized Moment-Rotation Hysteresis Loops for Specimen A2

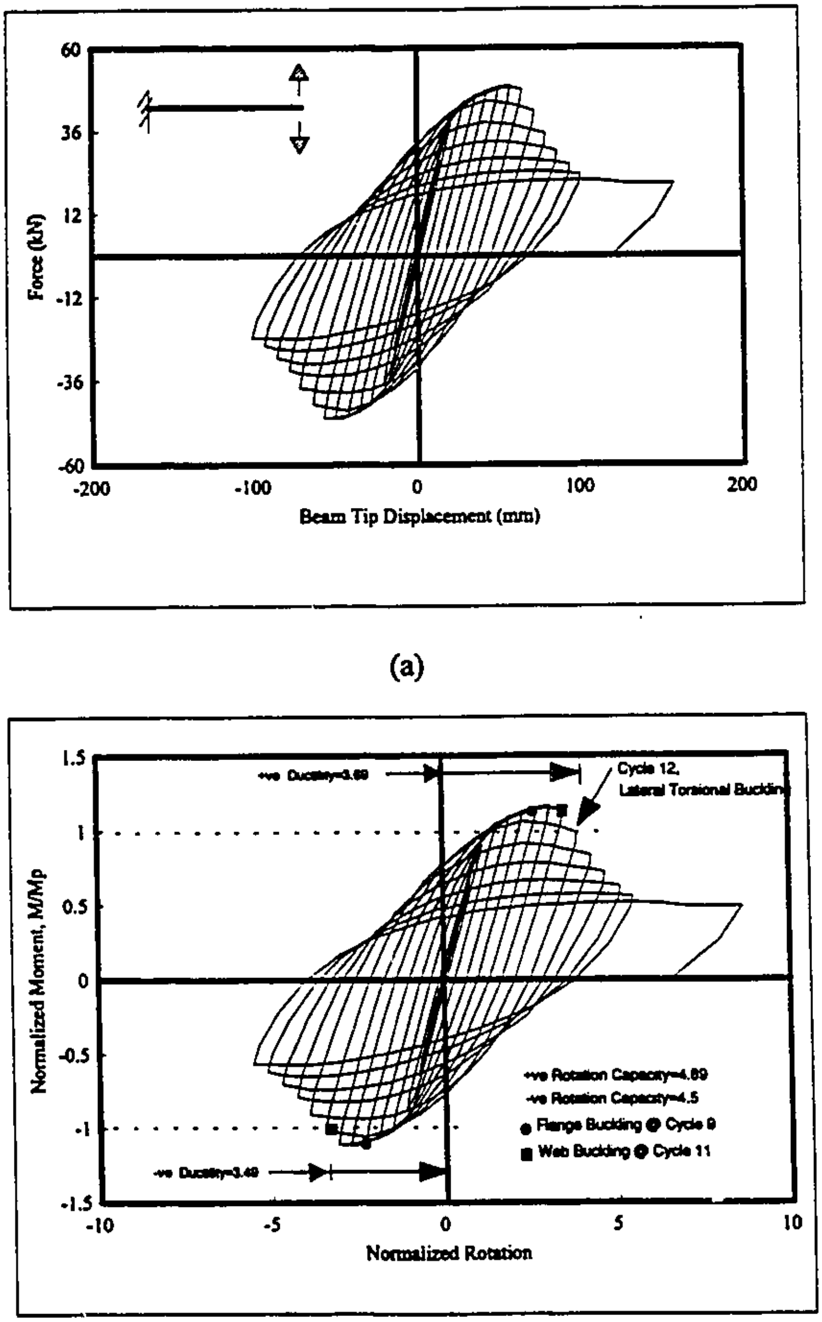

(a)

(b)

Fig. 3.16 Response of Specimen A3 Under Cyclic Loading
(a) Force vs Beam Tip Displacement; (b) Normalized Moment-Rotation

Fig. 3.17 Specimen A3 at failure

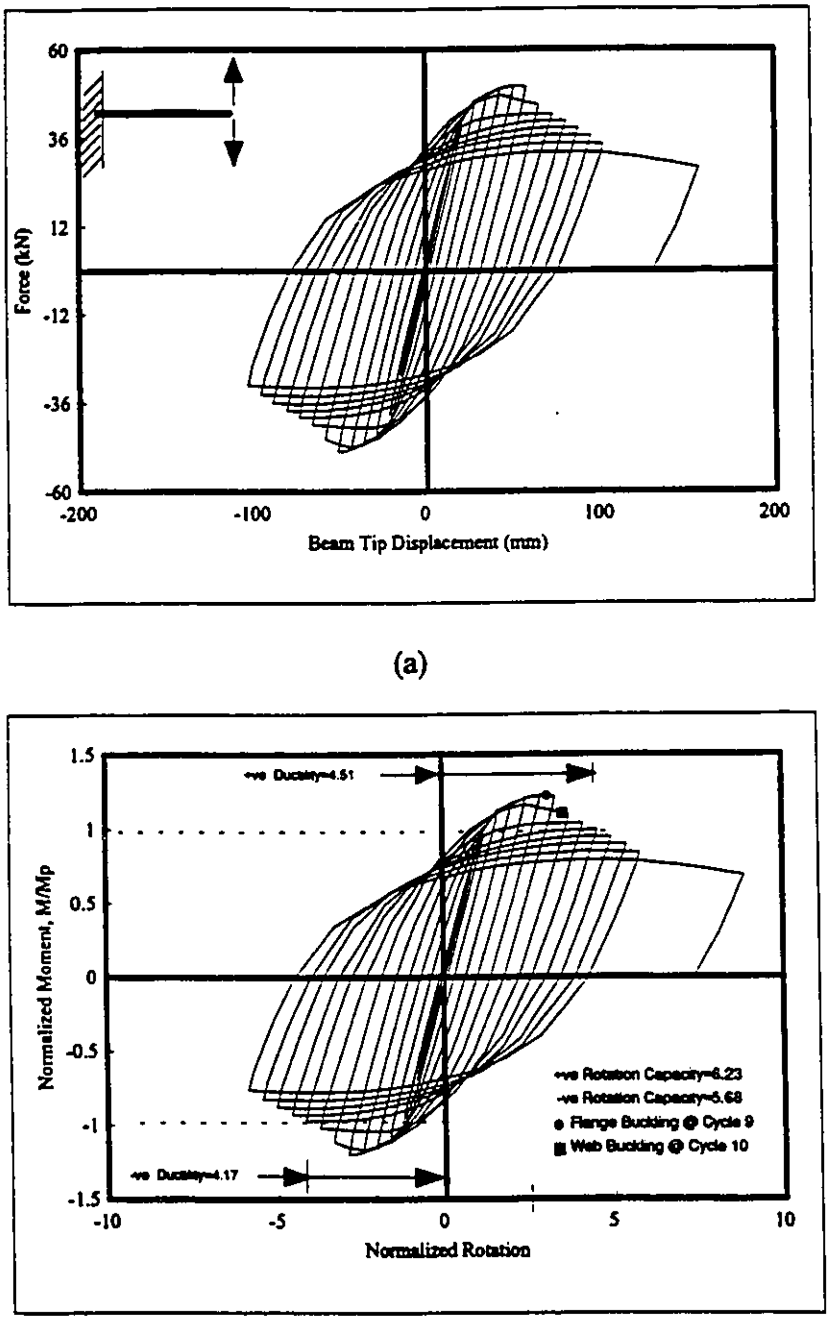

(a)

(b)

Fig. 3.18 Response of Specimen A4 under Cyclic Loading
(a) Force vs Beam Tip Displacement; (b) Normalized Moment-Rotation

Fig. 3.19 Specimen A4 at failure

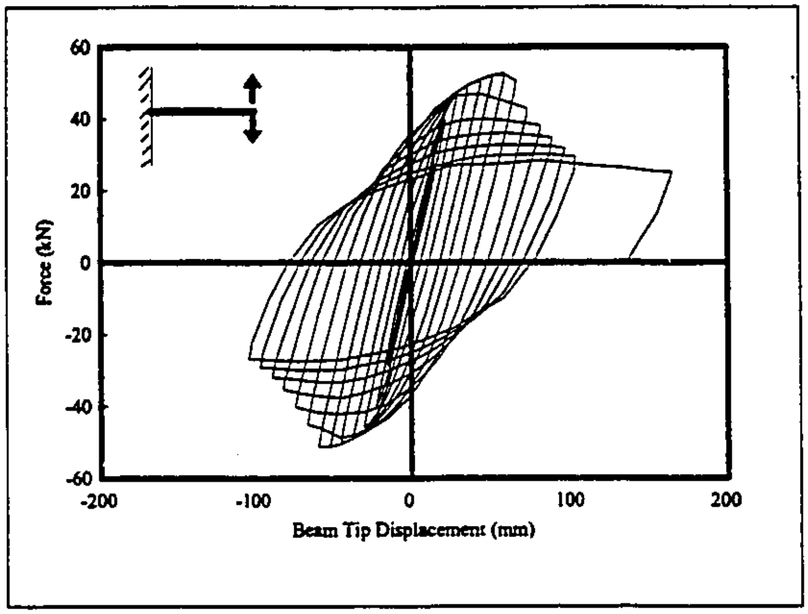

(a)

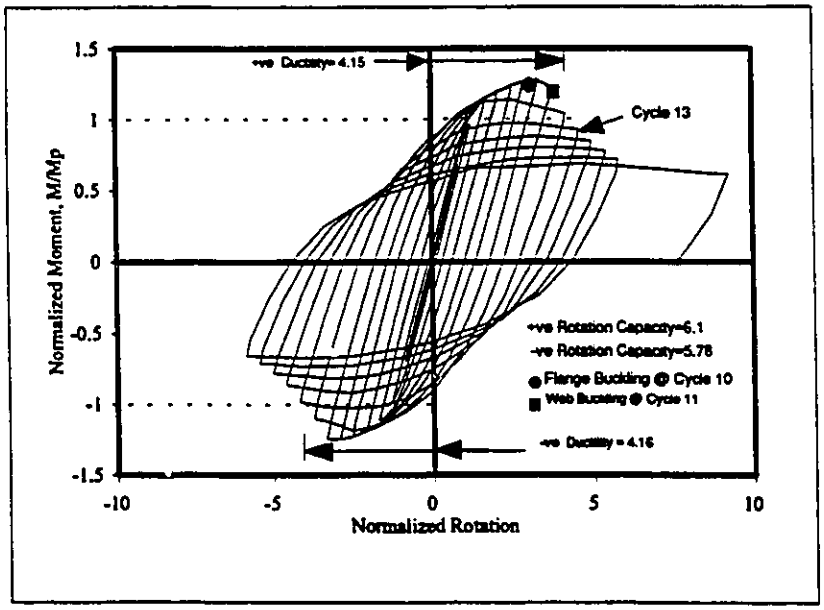

(b)

Fig. 3.20 Response of Specimen A5 Under Cyclic loading
(a) Force vs Beam Tip Displacement; (b) Normalized Moment-Rotation

Fig. 3.21 Specimen A5 at failure

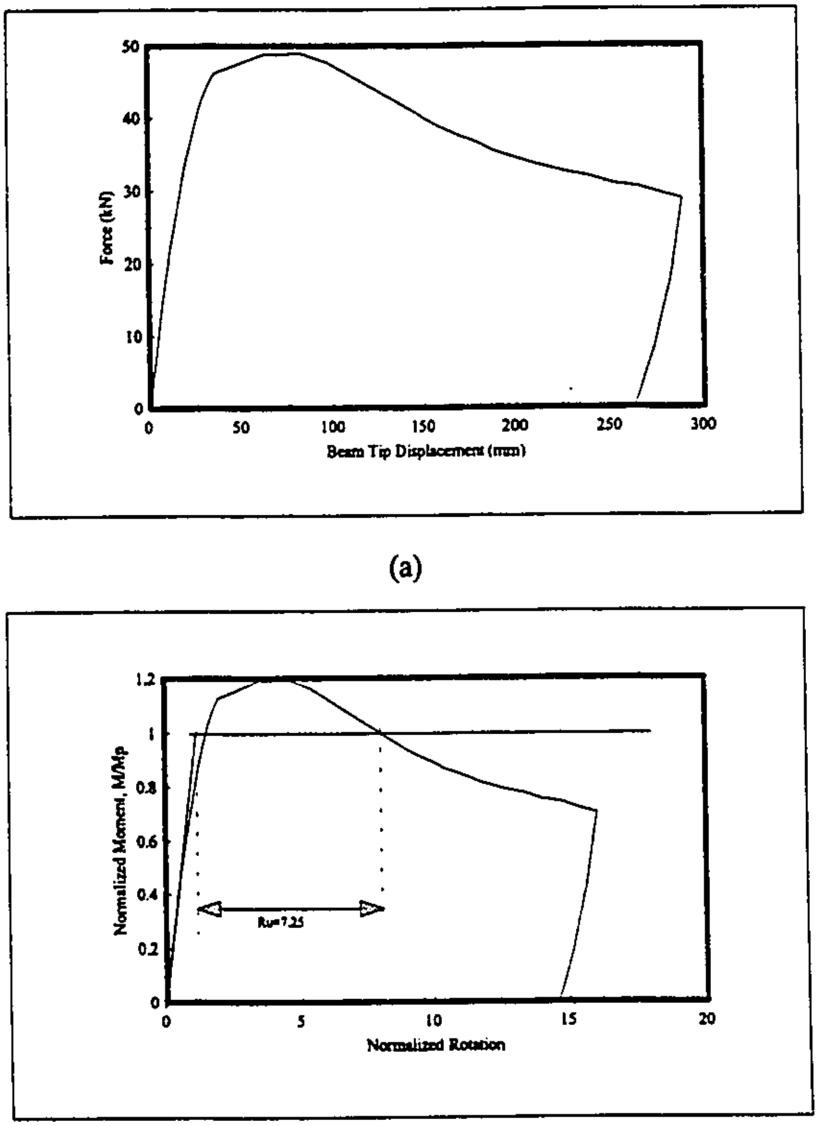

(a)

(b)

Fig. 3.22 Response of Specimen A6 under Monotonic Loading
(a) Force vs Beam Tip Displacement; (b) Normalized Moment Rotation

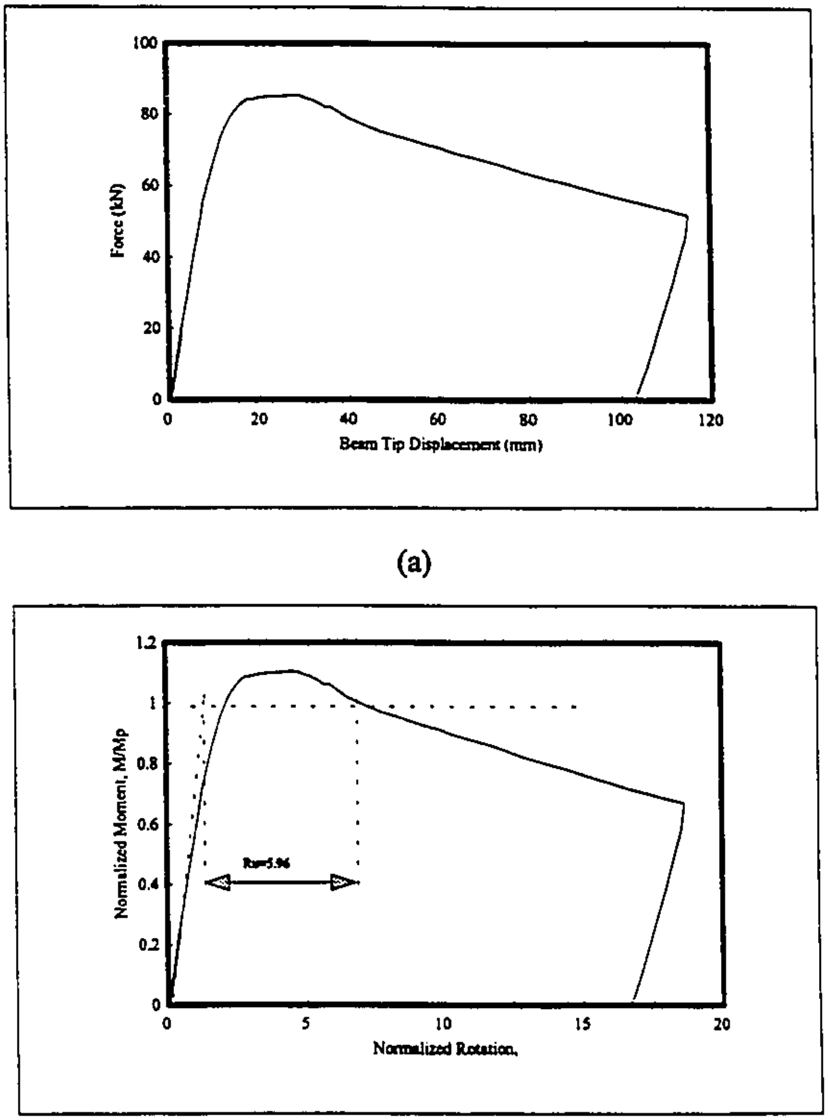

(a)

(b)

Fig. 3.23 Response of Specimen B0 Under Monotonic Loading
(a) Force vs Beam Tip Displacement; (b) Normalized Moment-Rotation

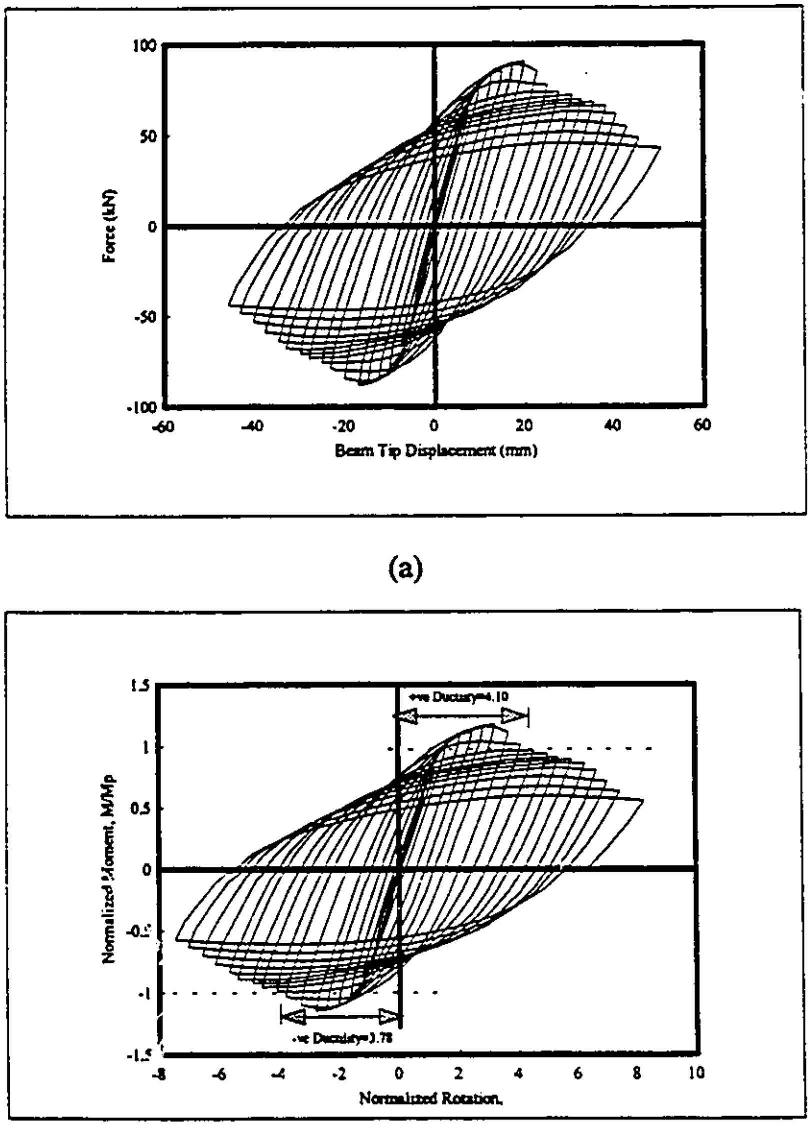

(a)

(b)

Fig. 3.24 Response of Specimen B1 Under Cyclic Loading
(a) Force vs Beam Tip Displacement; (b) Normalized Moment-Rotation

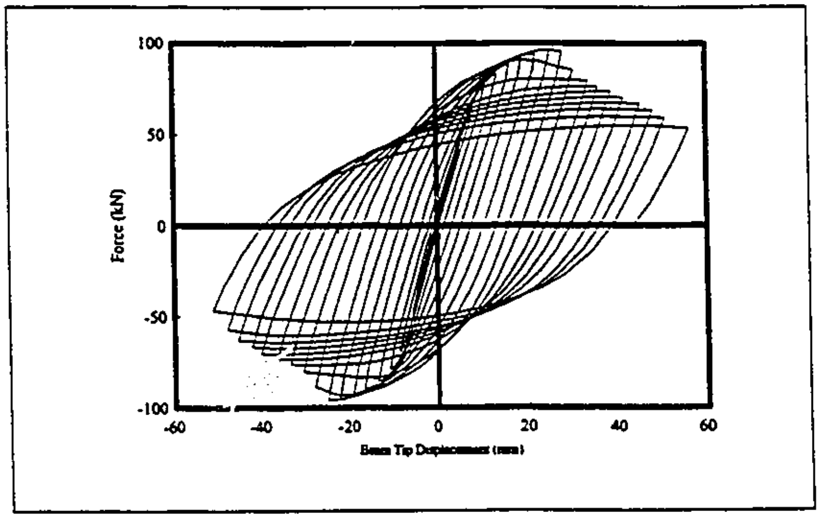

(a)

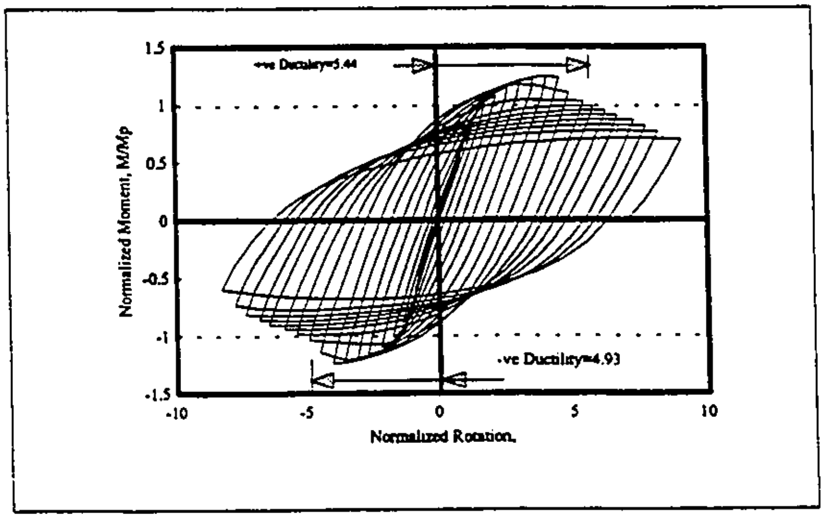

(b)

Fig. 3.25 Response of Specimen B2 Under Cyclic Loading
(a) Force vs Beam Tip Displacement; (b) Normalized Moment-Rotation

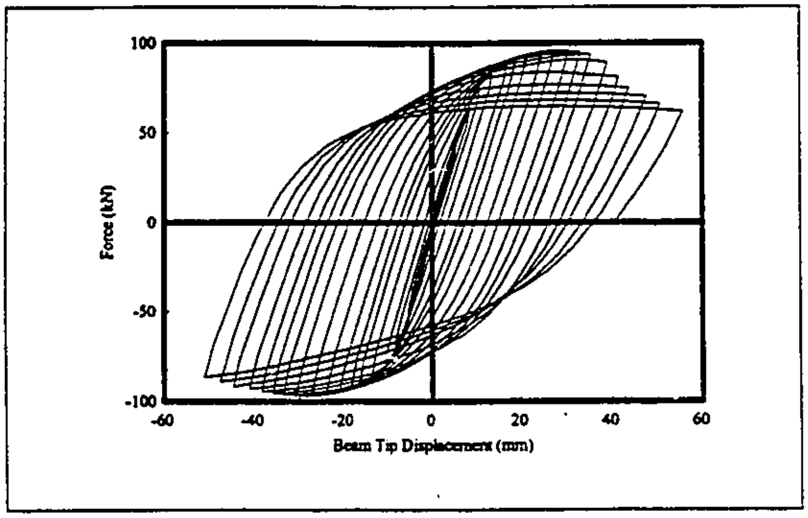

(a)

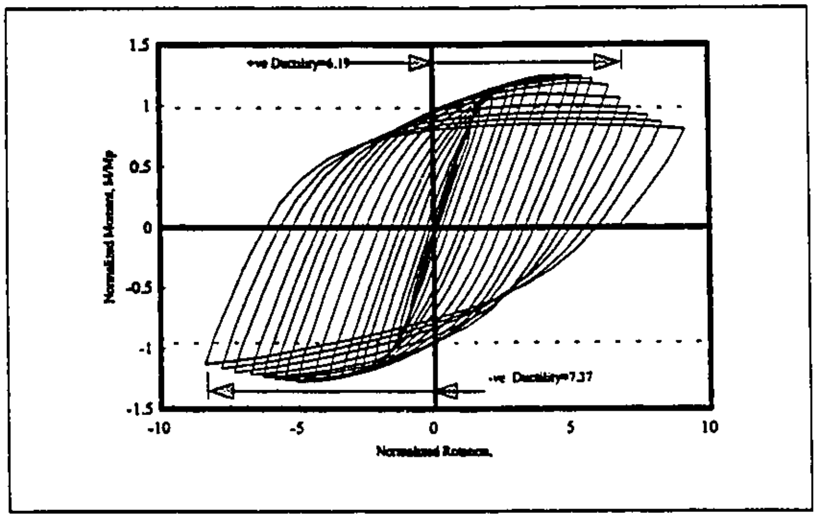

(b)

Fig. 3.26 Response of Specimen B3 Under Cyclic Loading
(a) Force vs Beam Tip Displacement; (b) Normalized Moment-Rotation

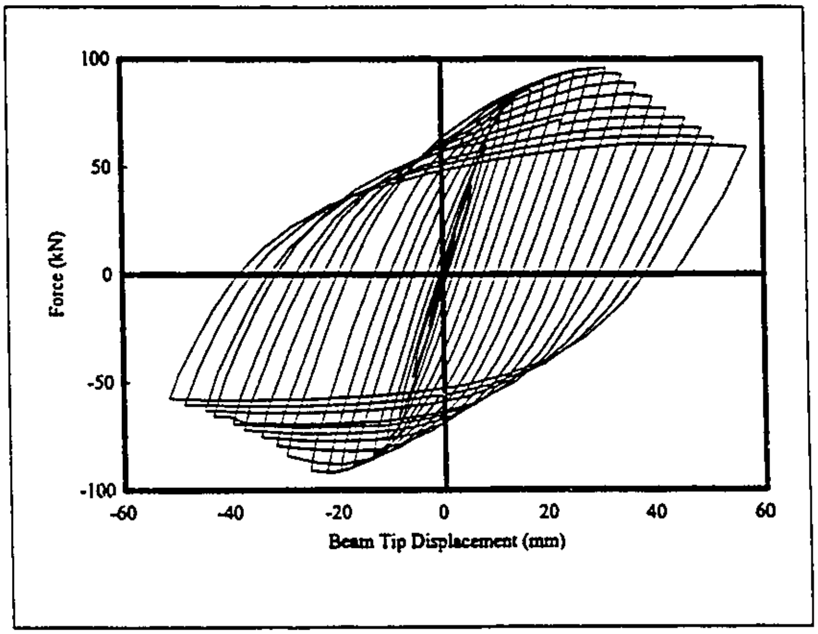

(a)

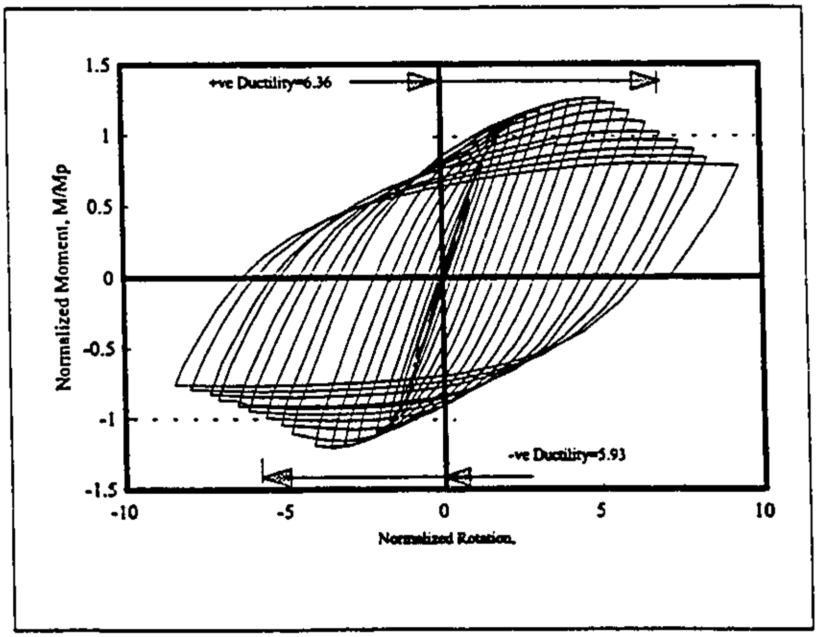

(b)

Fig. 3.27 Response of Specimen B4 Under Cyclic Loading
(a) Force vs Beam Tip Displacement; (b) Normalized Moment-Rotation

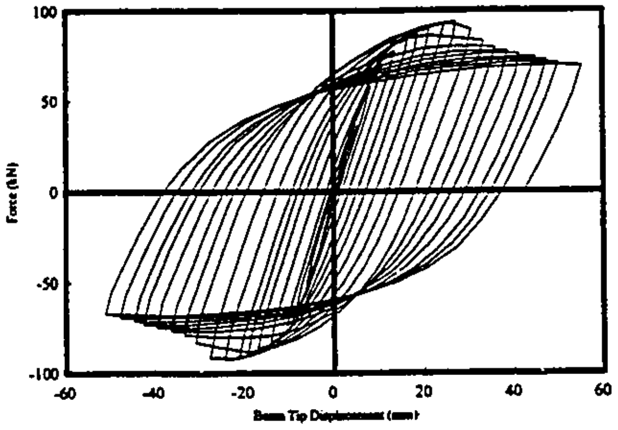

(a)

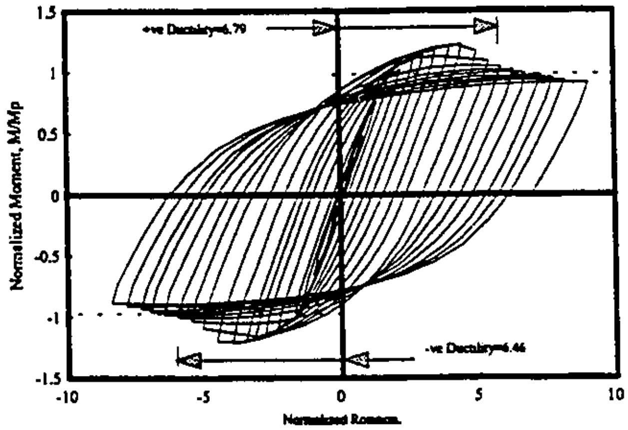

(b)

Fig. 3.28 Response of Specimen B5 Under Cyclic Loading
(a) Force vs Beam Tip Displacement; (b) Normalized Moment-Rotation

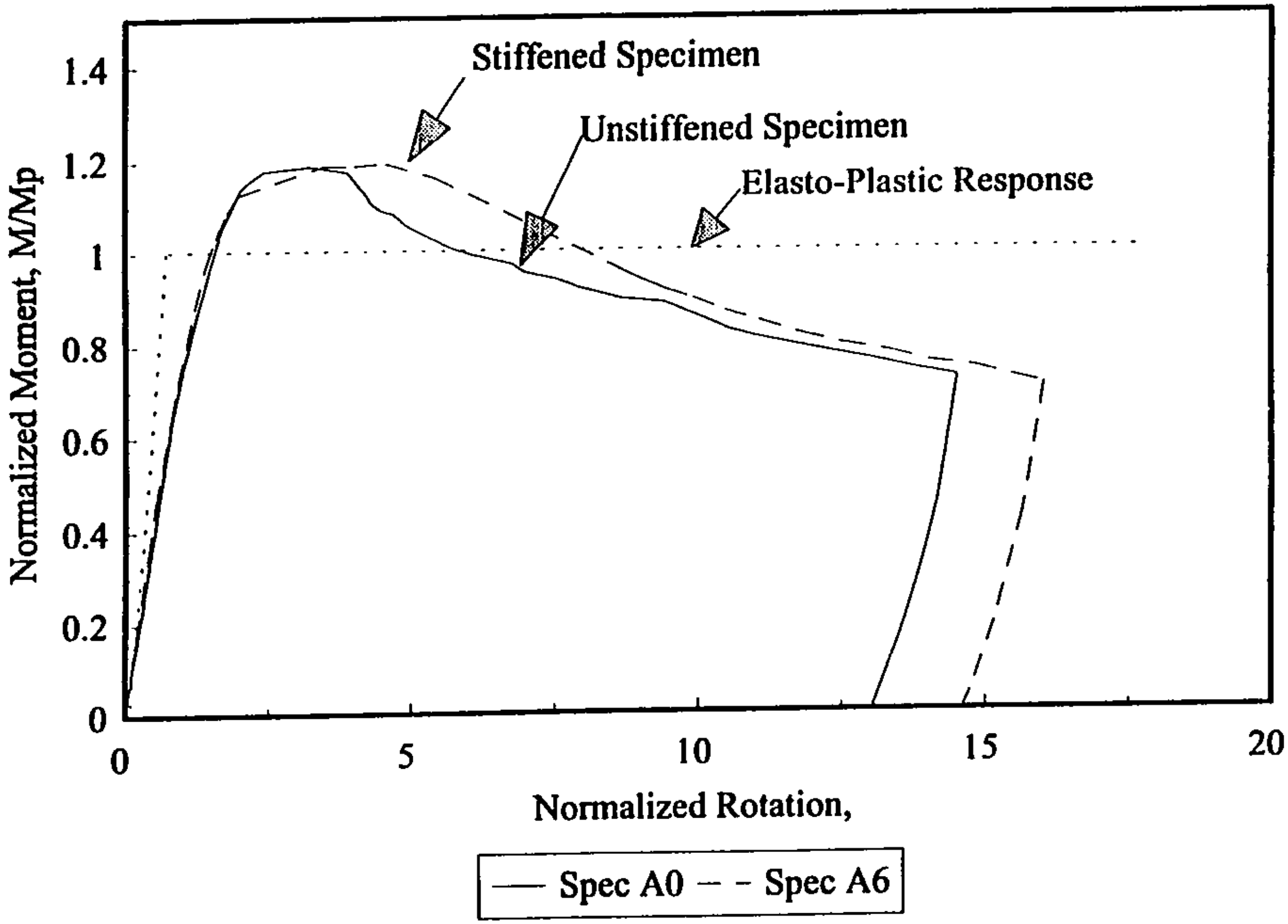

Fig. 3.29 Comparison of Specimens A0 with A6

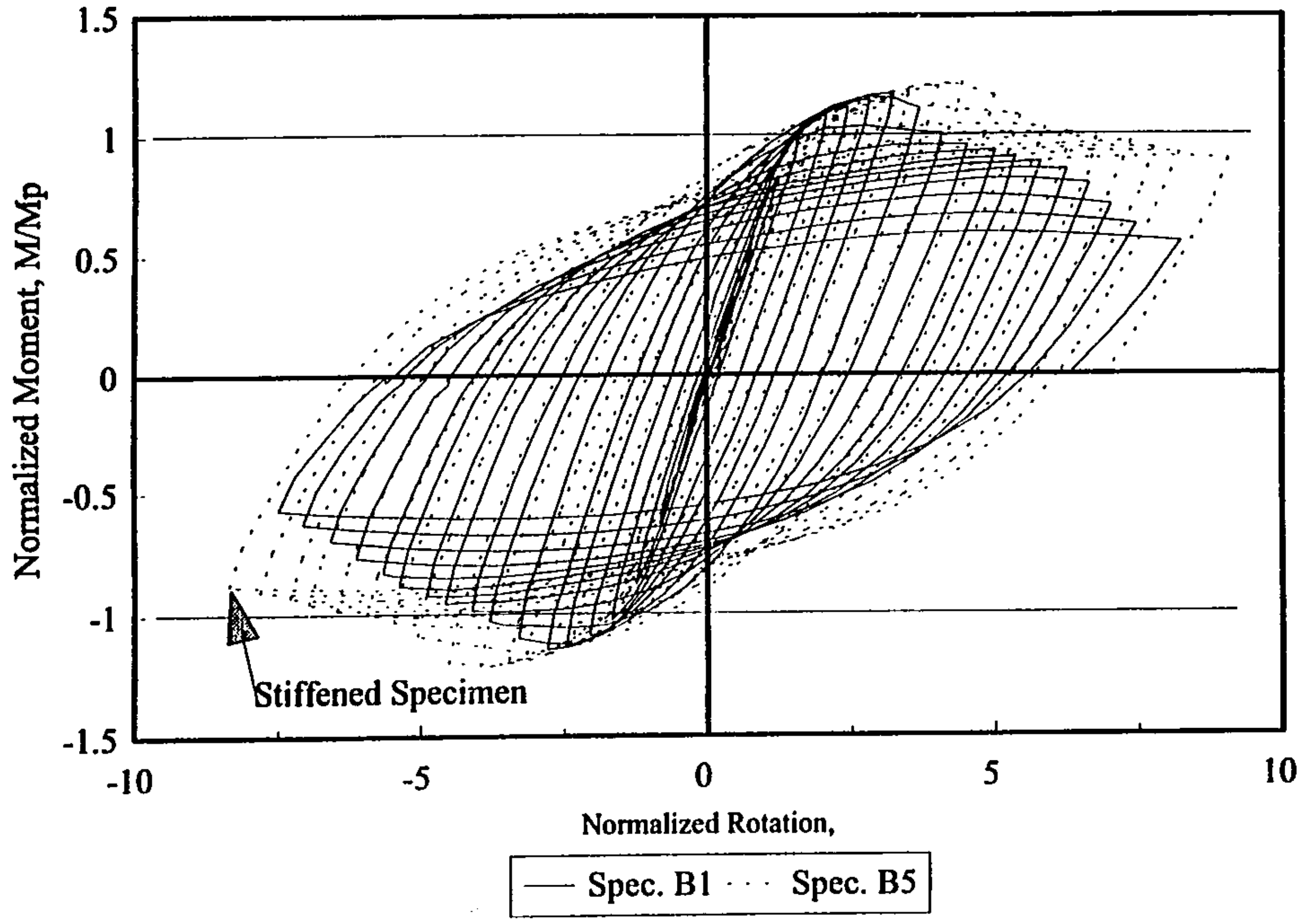

Fig. 3.30 Comparison of Specimen B1 with B5

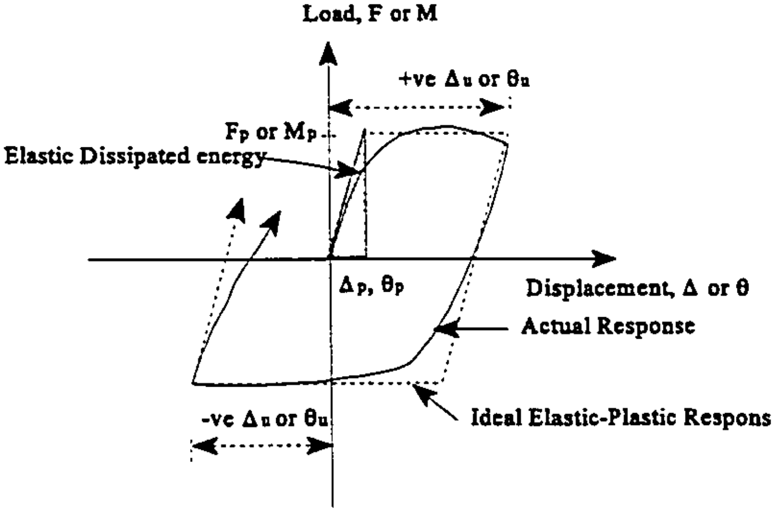

(a) First Cycle

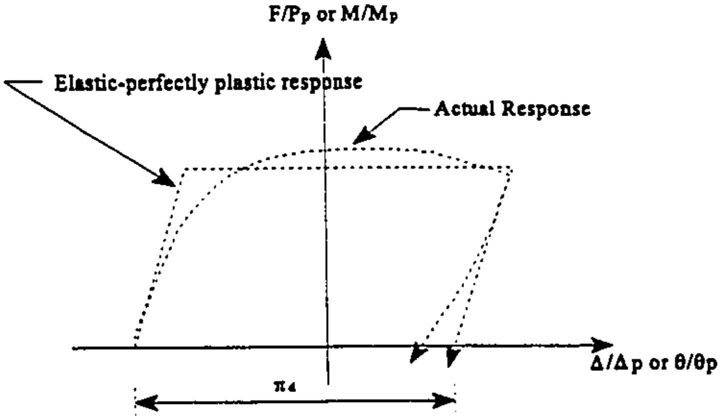

(b) Half cycle at peak load

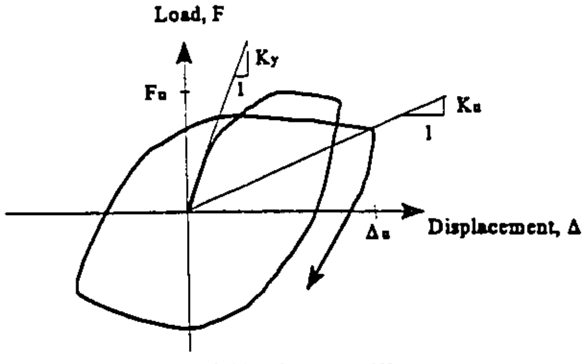

(c) Definition of yield and secant stiffness

Fig. 3.31Typical Response Curves

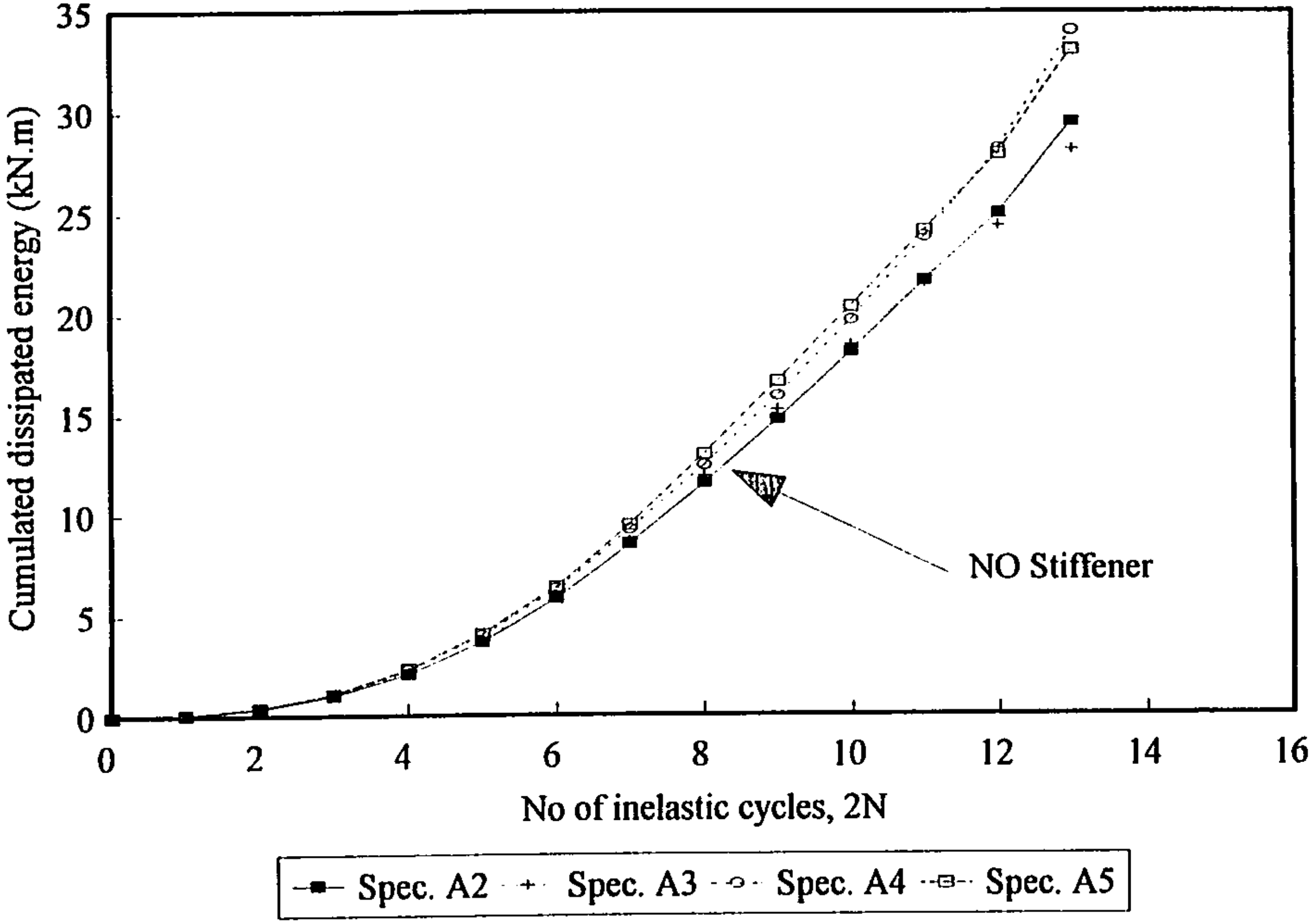

Fig. 3.32 Cumulated dissipated energy vs No of inelastic cycles for series A specimens

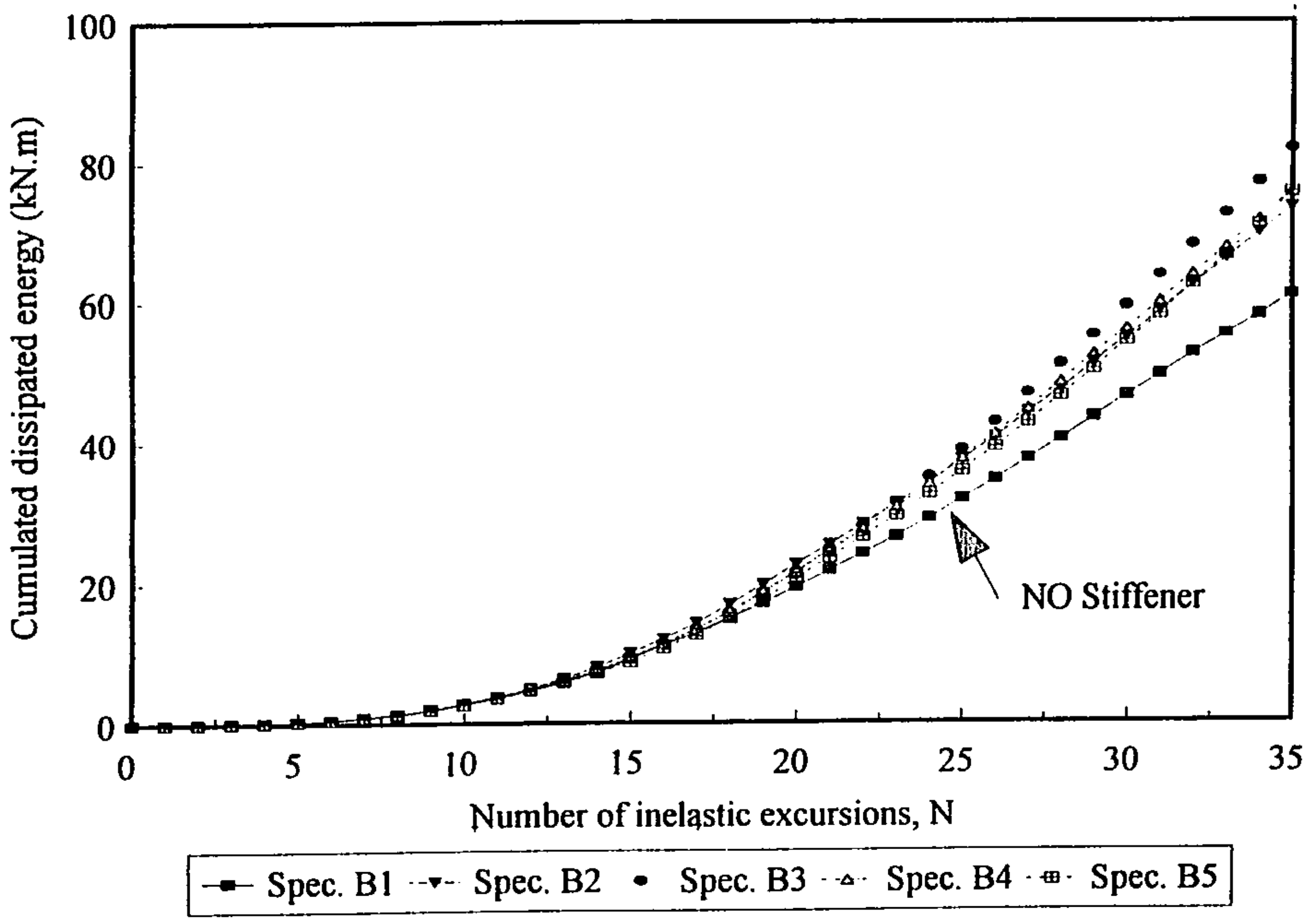

Fig. 3.33 Cumulated Dissipated Energy vs No of Inelastic Excursions for Series B Specimens

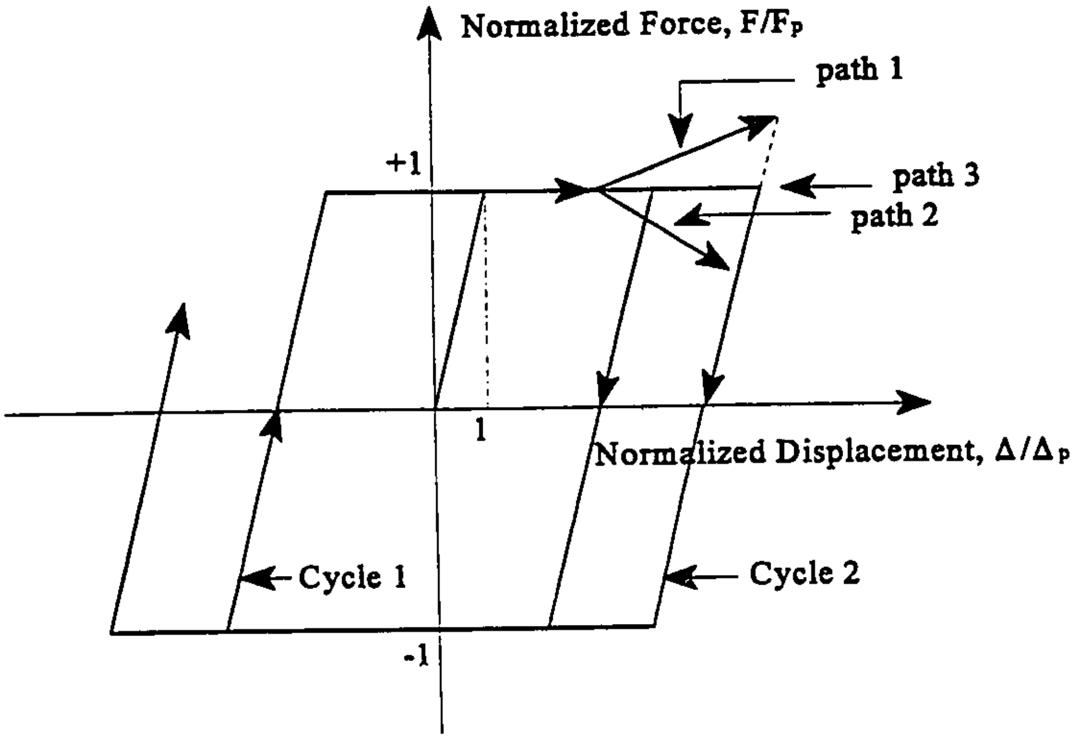

Fig. 3.34 Possible Behavioural Paths

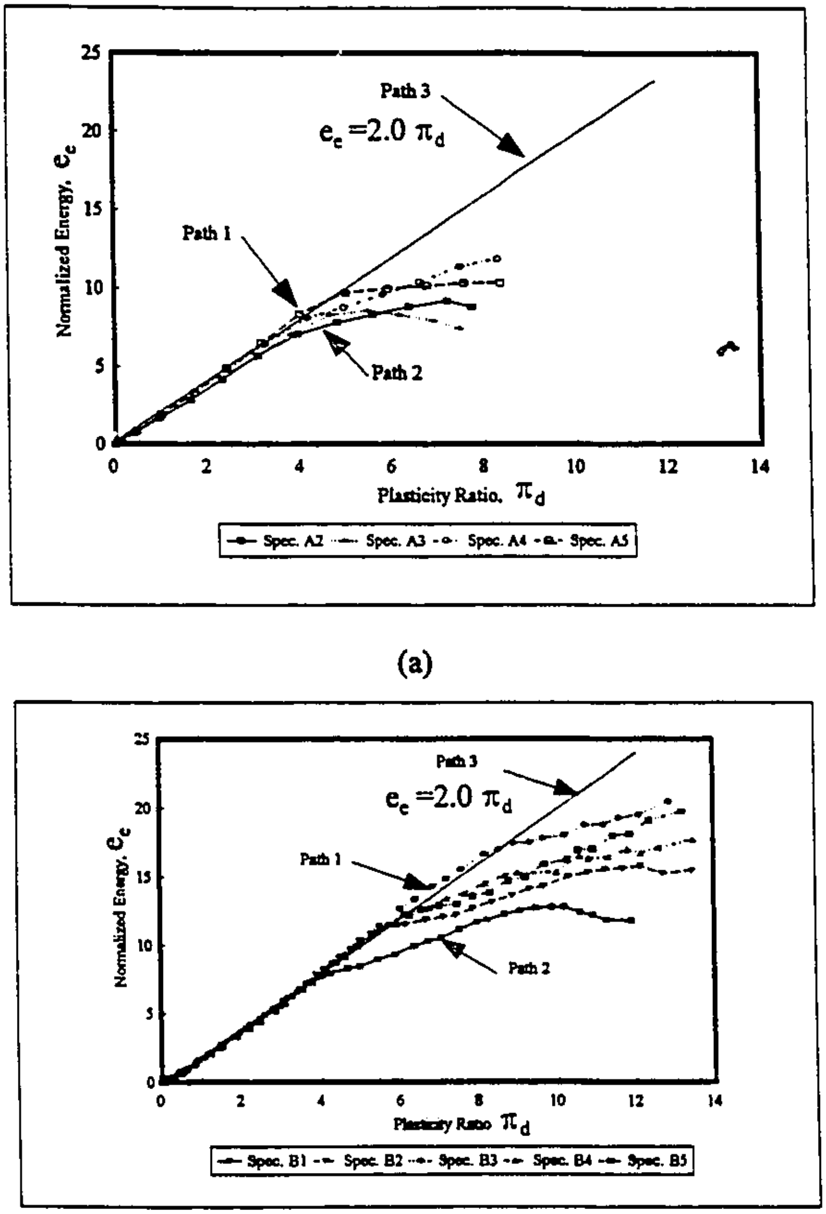

(a)

(b)

Fig. 3.35 Normalized Energy vs Plasticity Ratio:
(a) Series A Specimens; (b) Series B Specimens

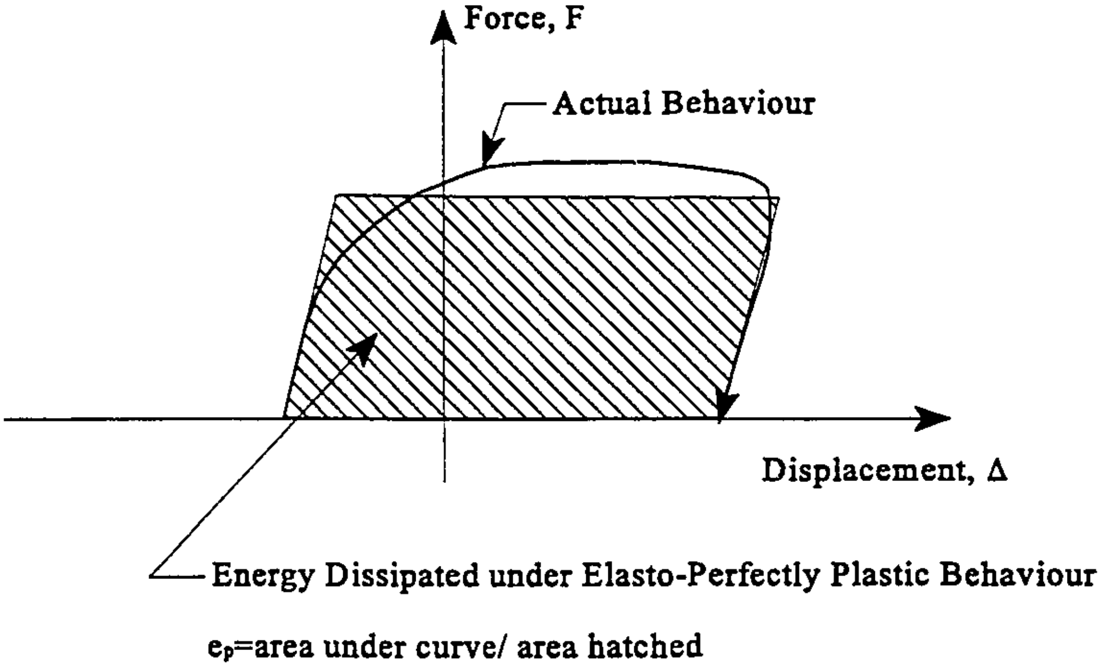

Fig. 3.36 Energy Dissipated under an Elasto-Perfectly Plastic Behaviour

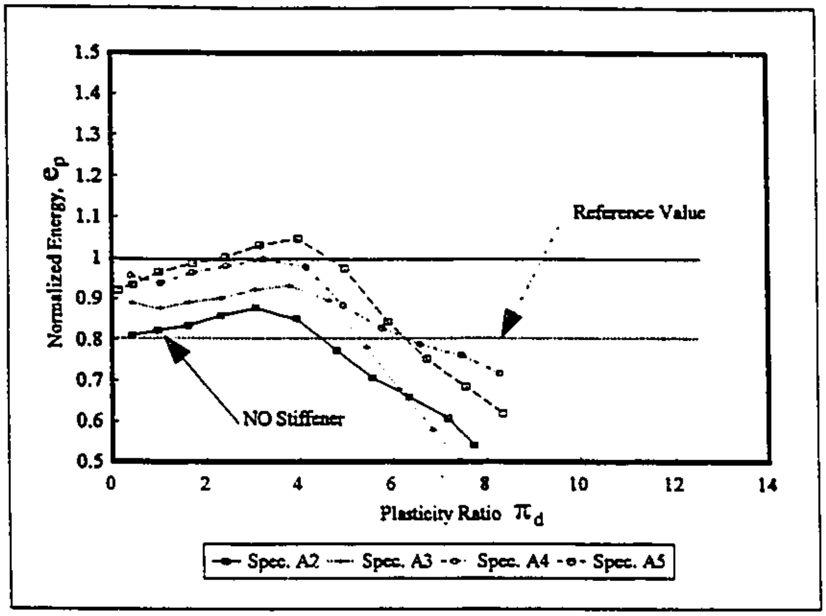

(a)

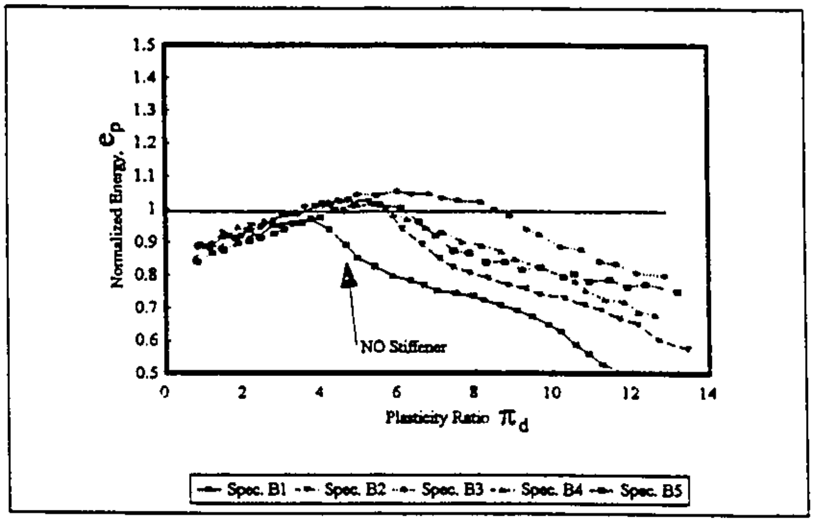

(b)

Fig. 3.37 Normalized Energy vs Plasticity Ratio
(a) Series A Specimens; (b) Series B Specimens

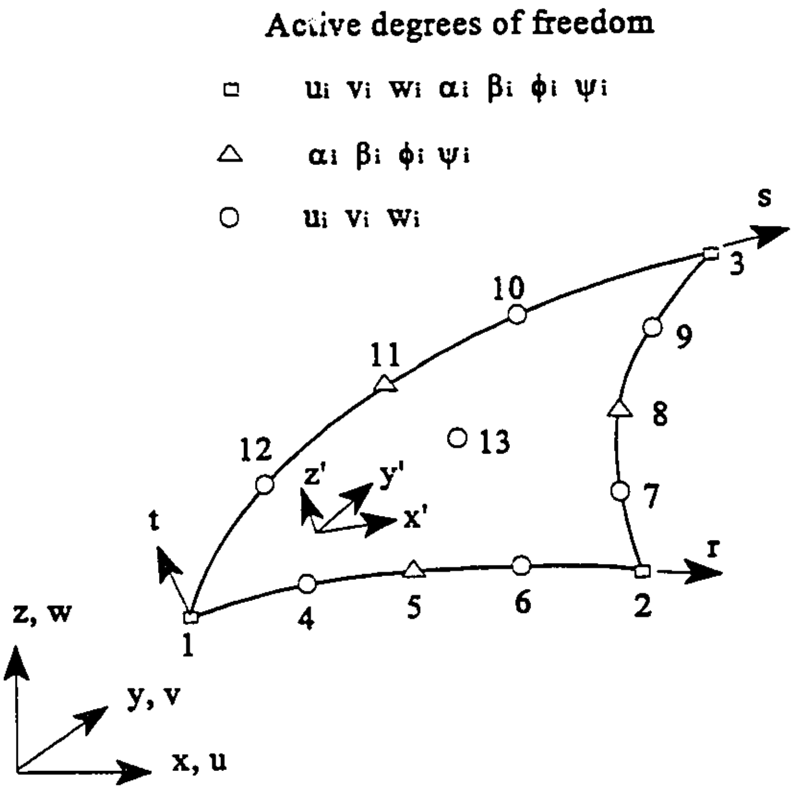

Fig. 3.38 Cubic-quadradic shell element.

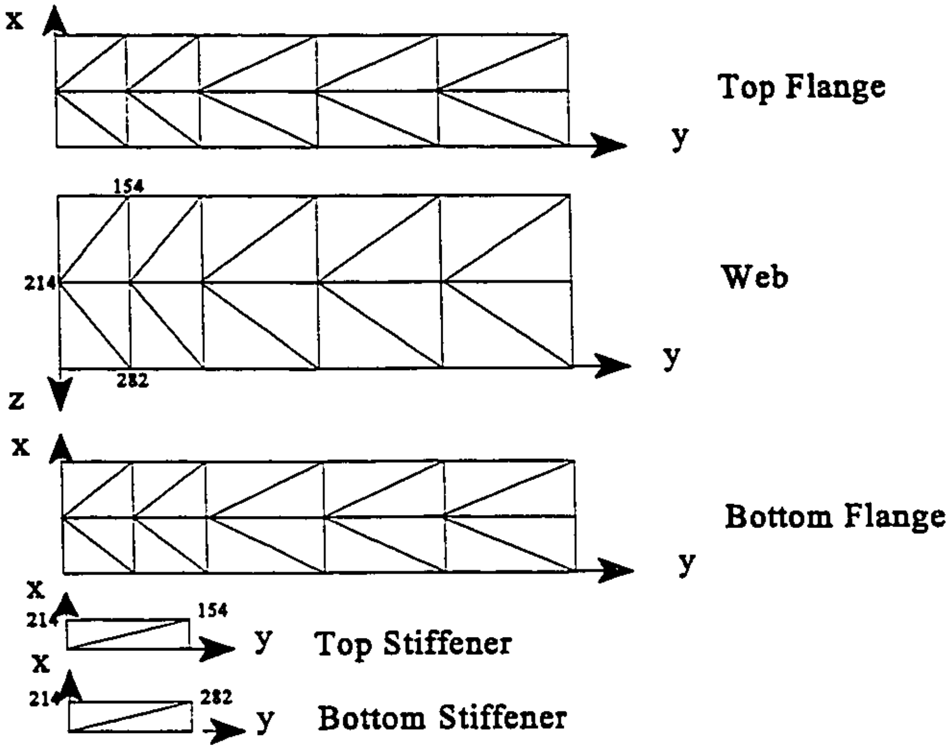

Fig. 3.39 Mesh Layout for Stiffened Beam

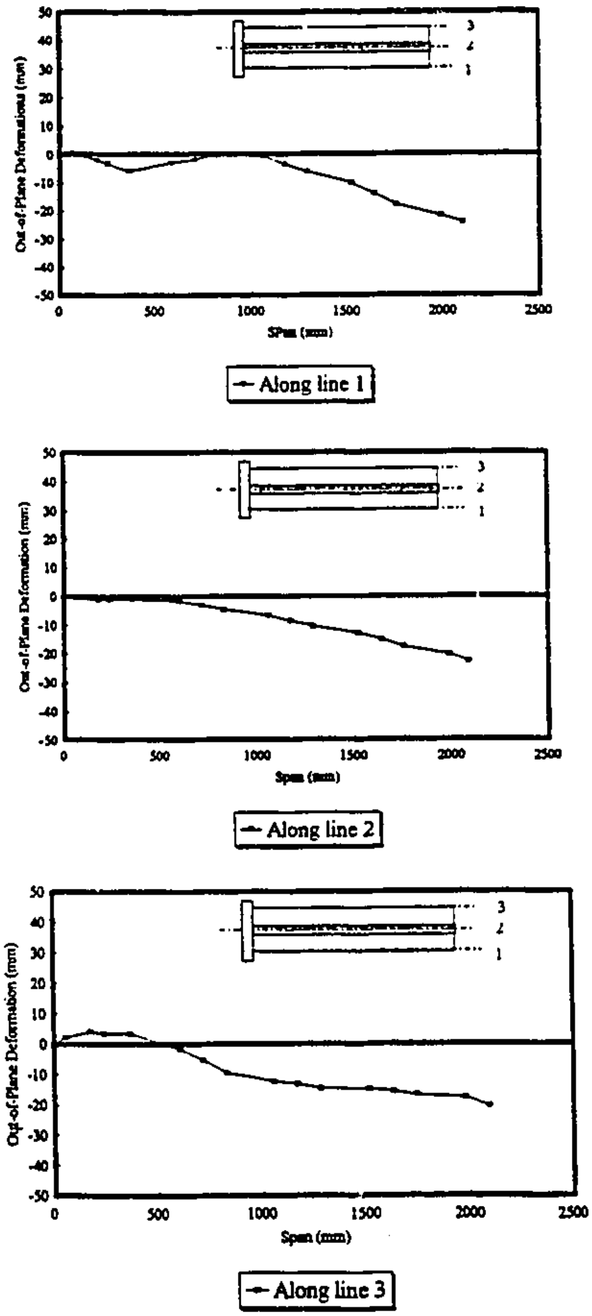

Fig. 3.40 Out-of-plane deformations in bottom Flange

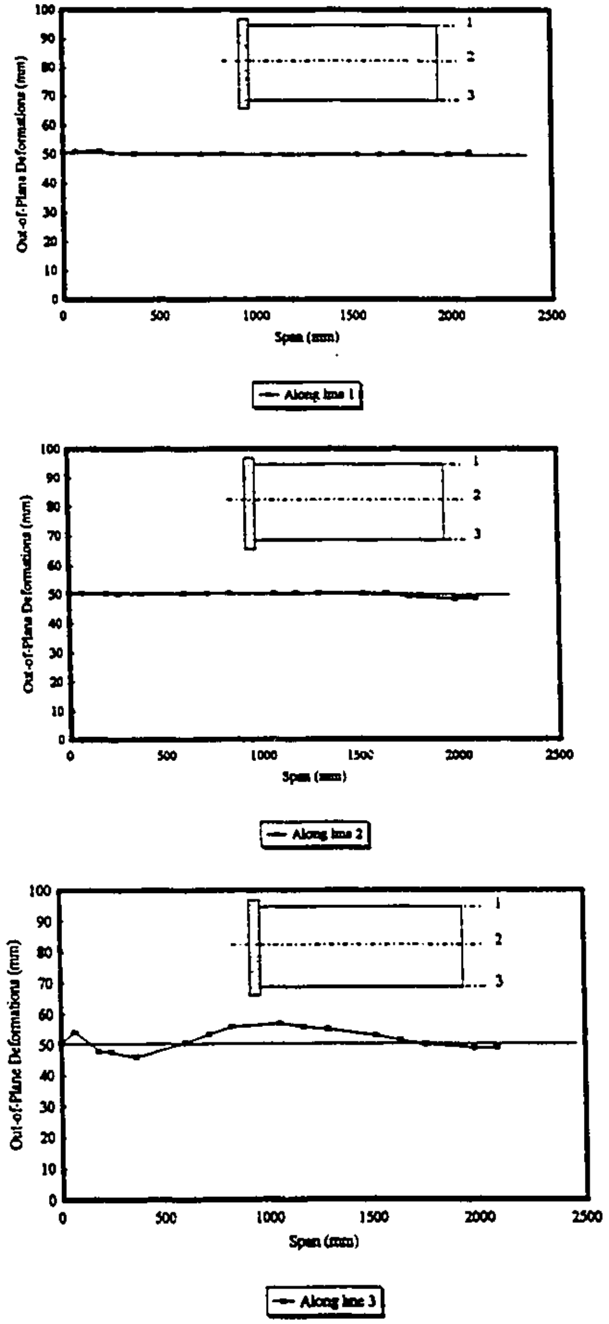

Fig. 3.41 Out-of-Plane Deformation in Web

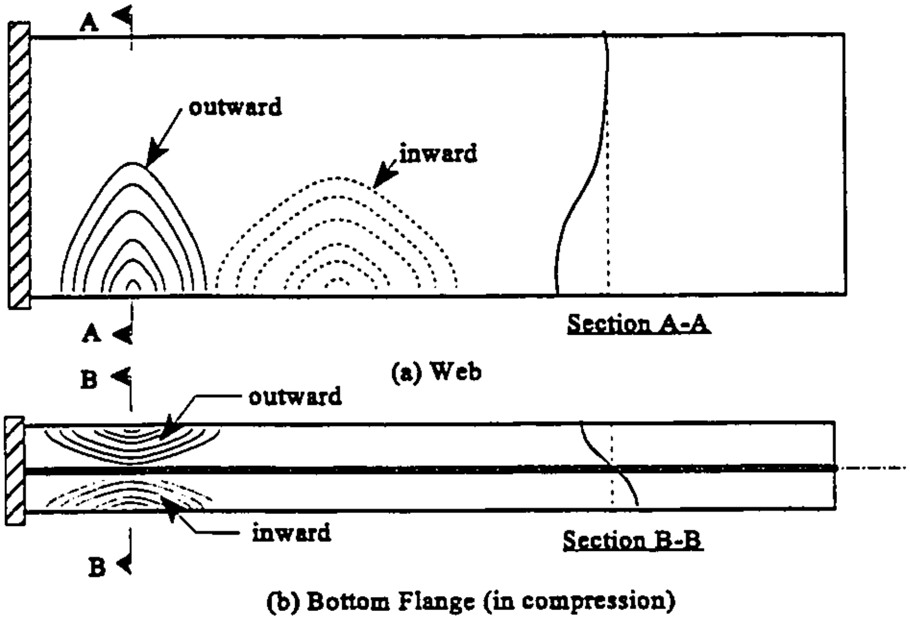

Fig. 3.42 Schematic Of Local Distortion: a) in Web; b) in Bottom Flange

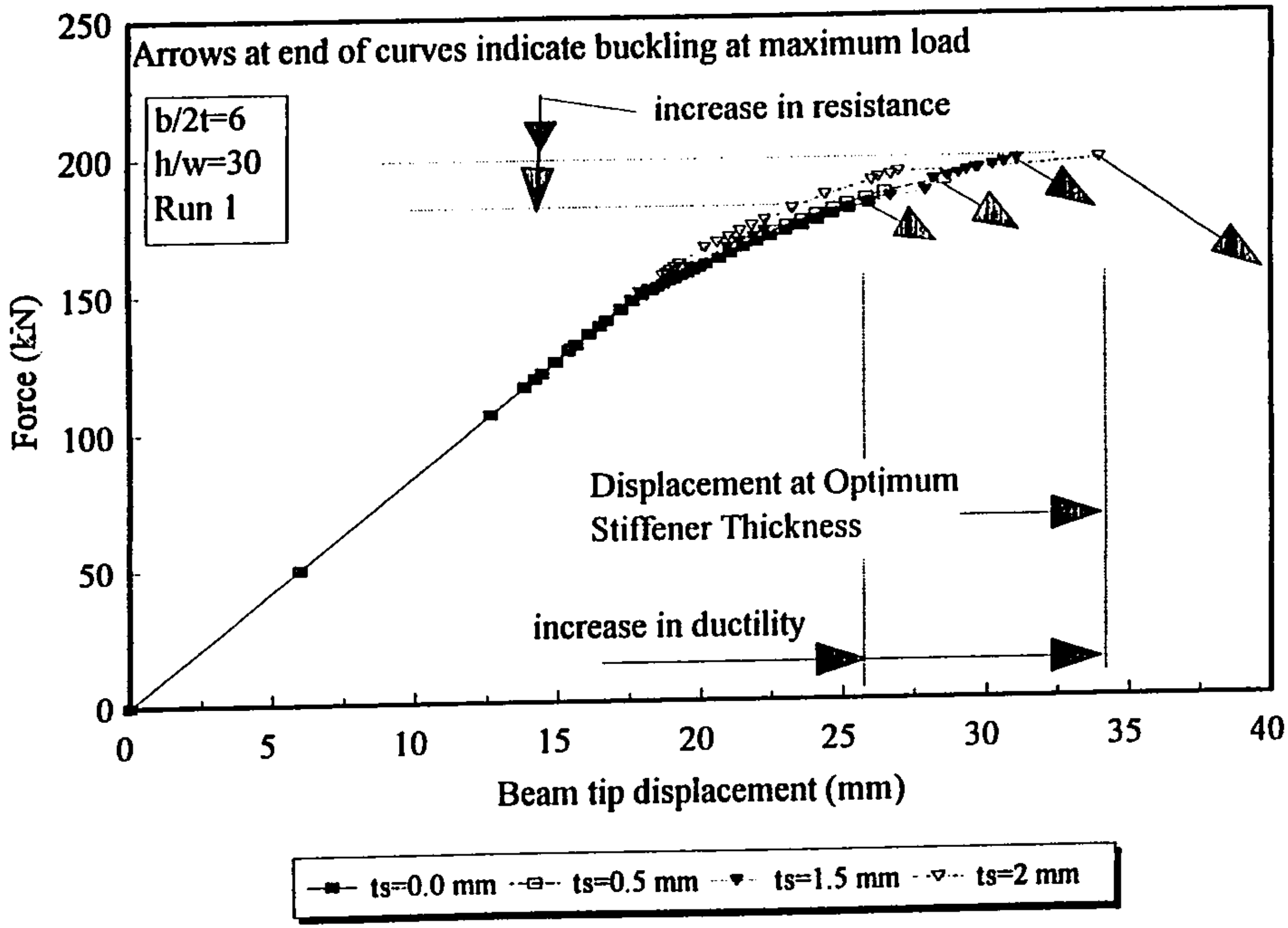

Fig. 3.43 Ductility enhancement at maximum resistance for case 1

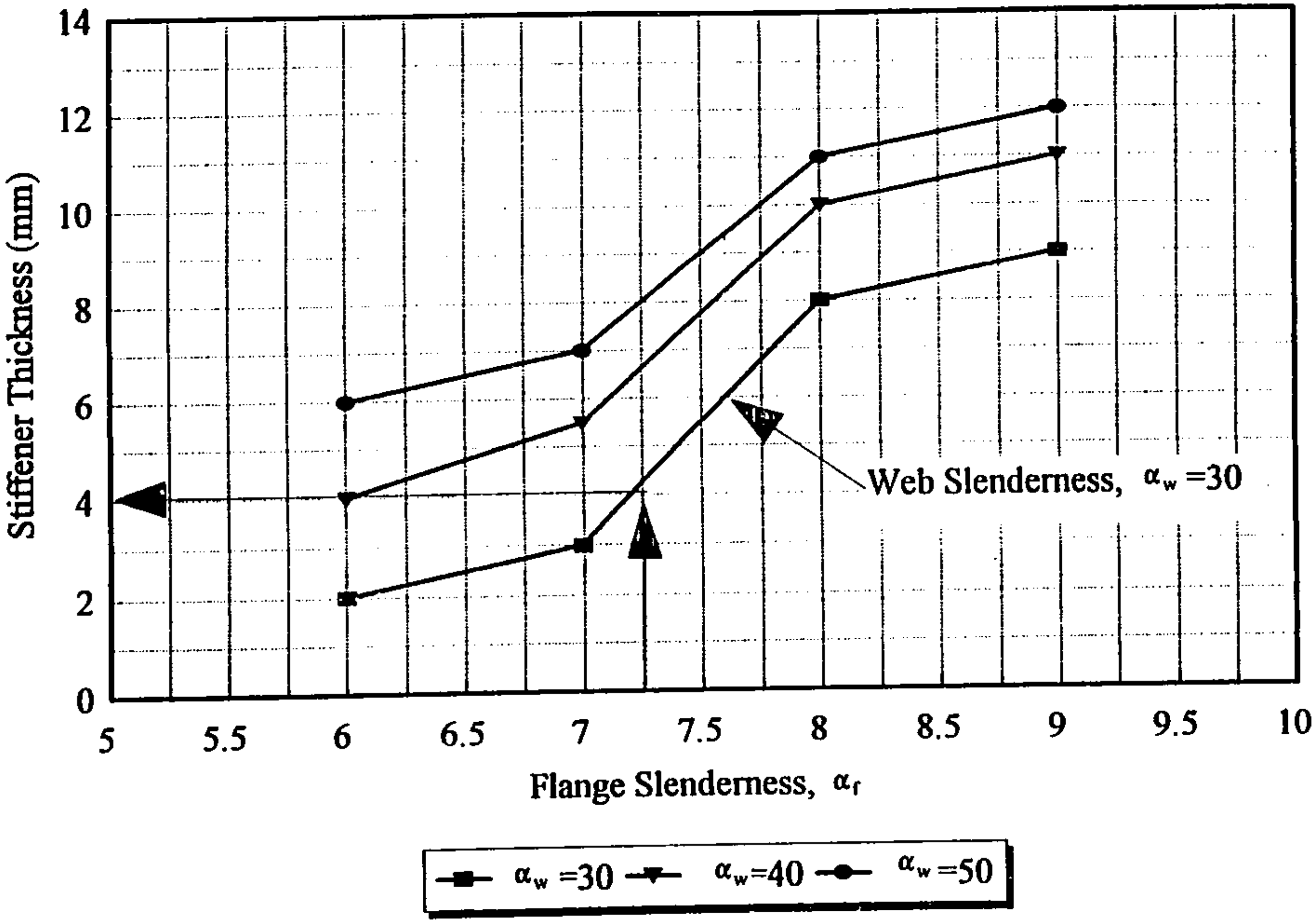

Fig. 3.44 Interaction between stiffener thickness and plates slenderness

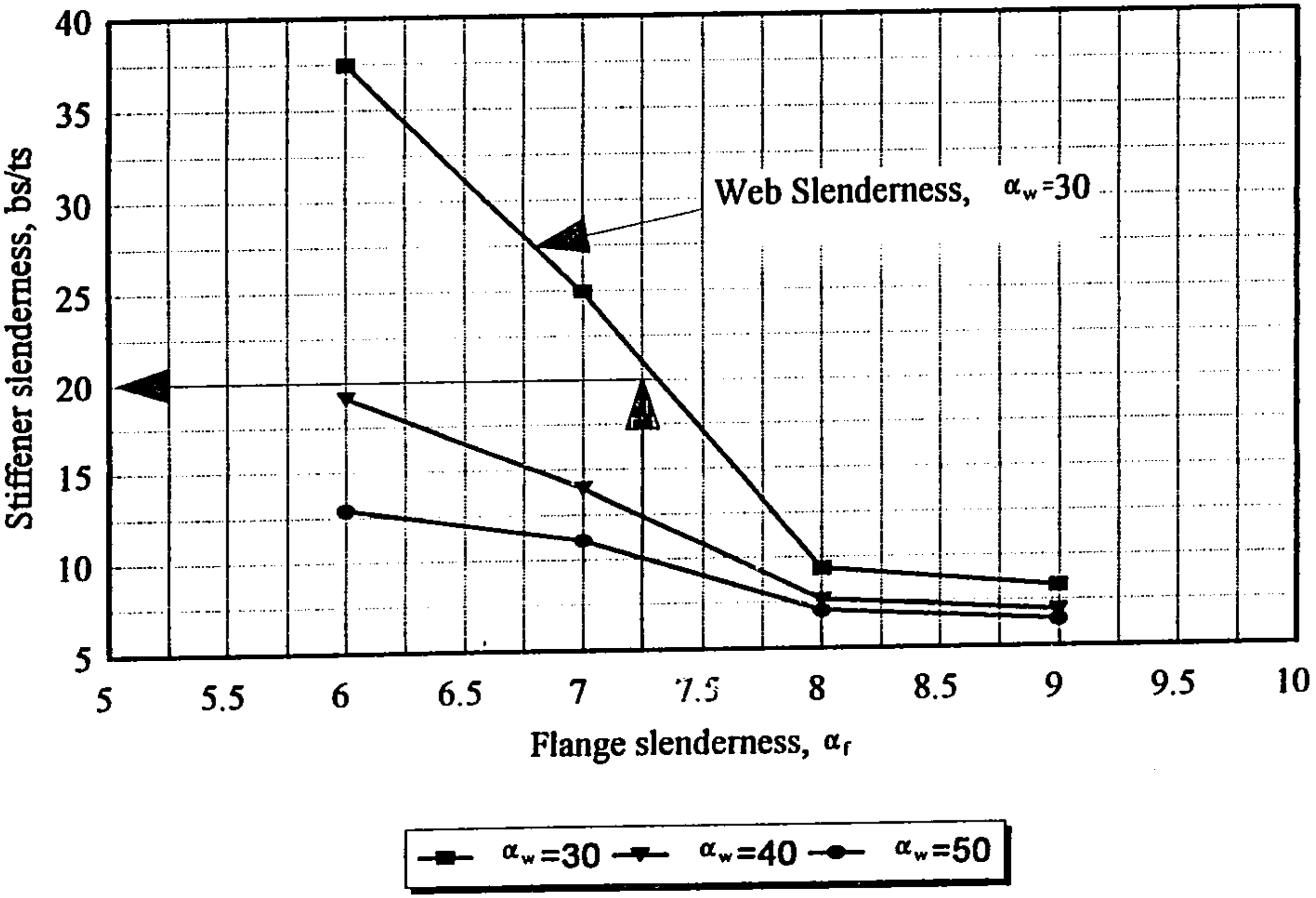

Fig. 3.45 Interaction between stiffener and plates slenderness

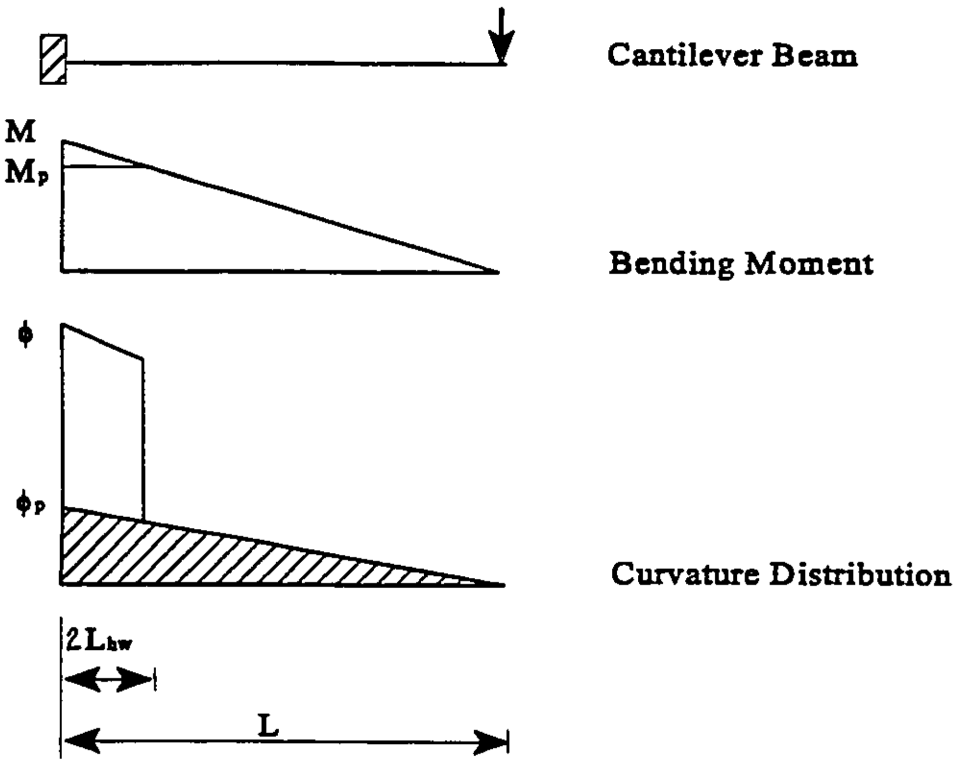

Fig. 3.46 Illustration of yielded length

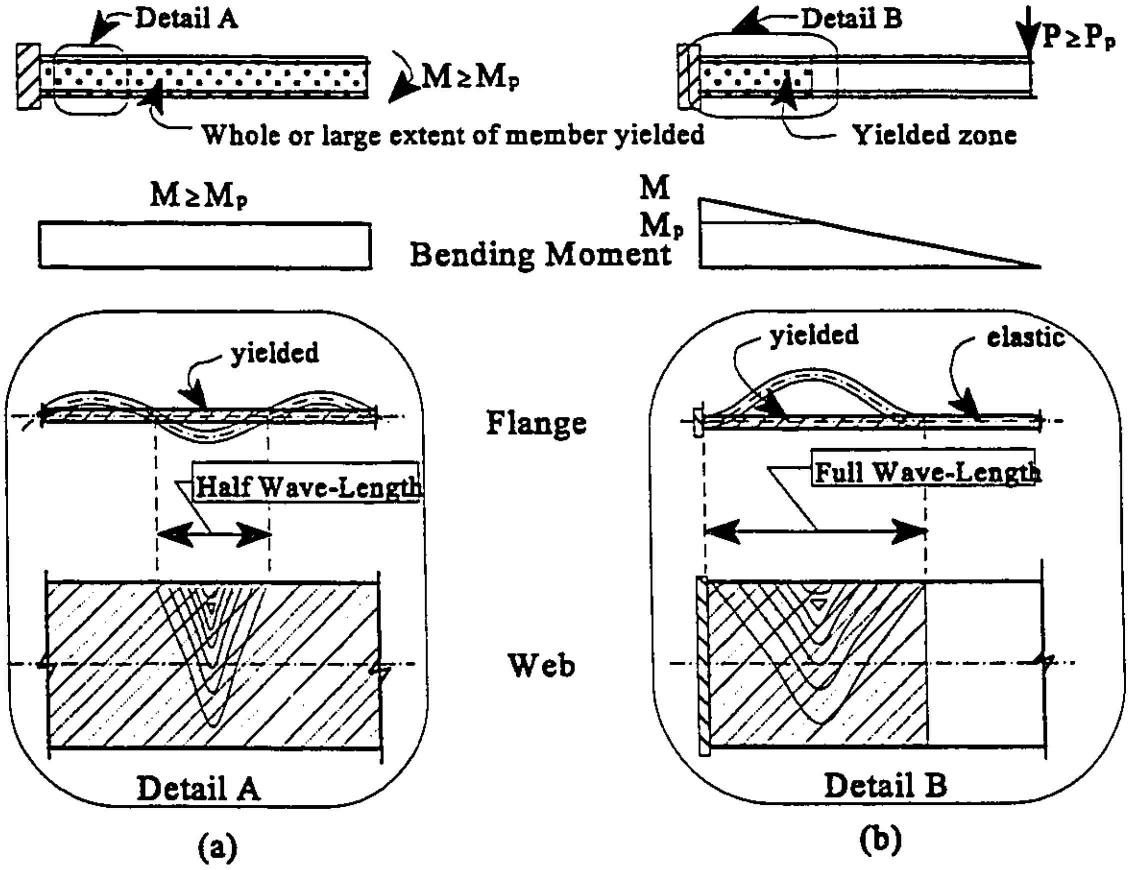

Fig. 3.47 Wave Length in a Beam Under:
(a) Uniform moment; (b) Moment gradient

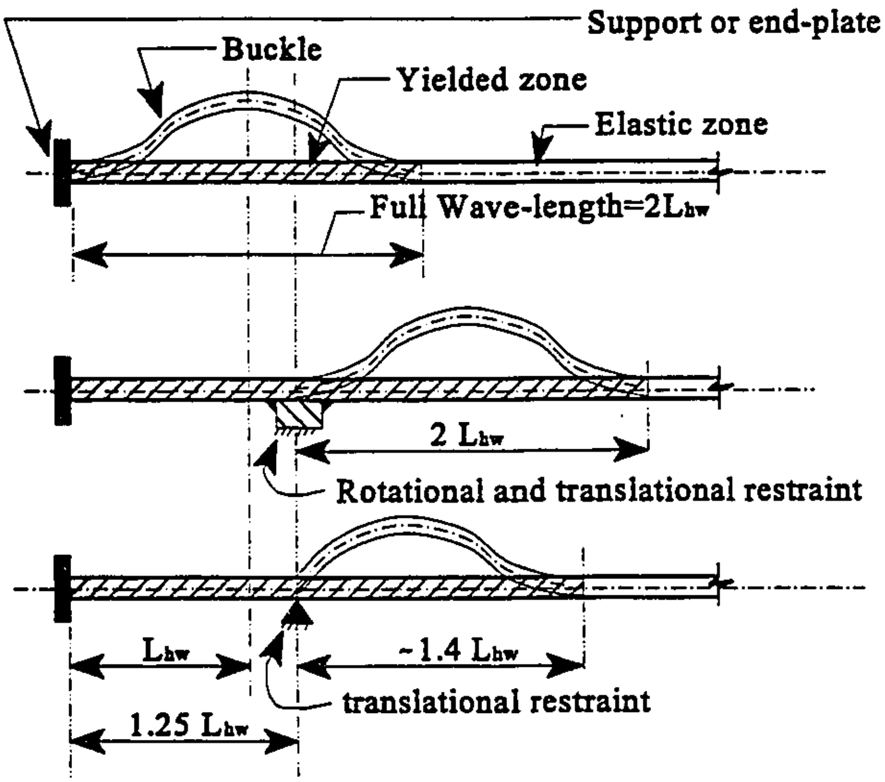

Fig. 3.48 Possible Location of Out-of-Plane Restraint in Flange

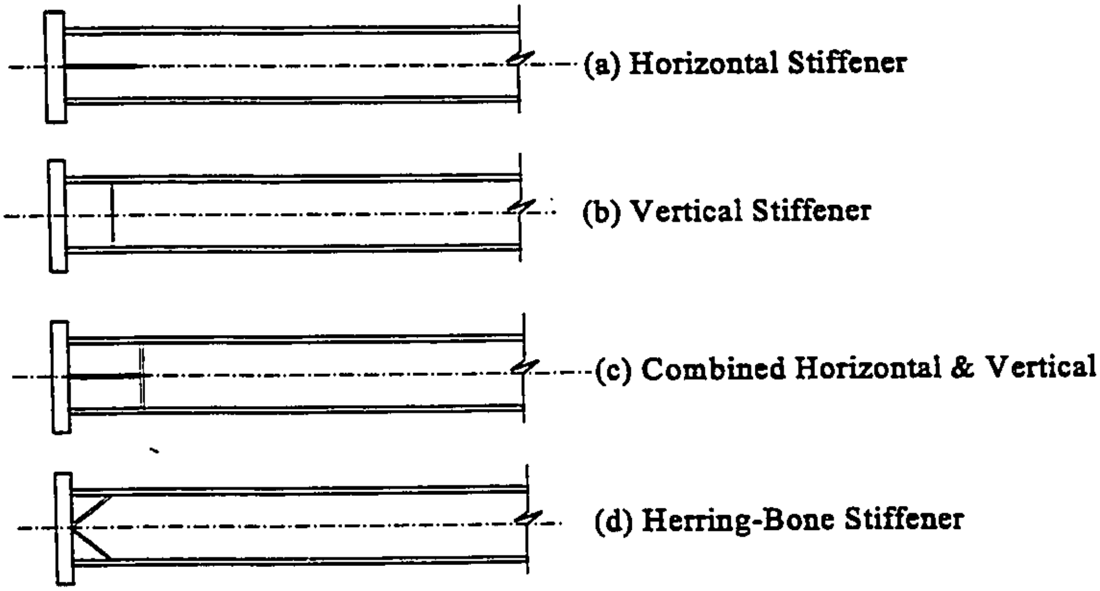

Fig. 3.49 Possible Stiffener Configurations

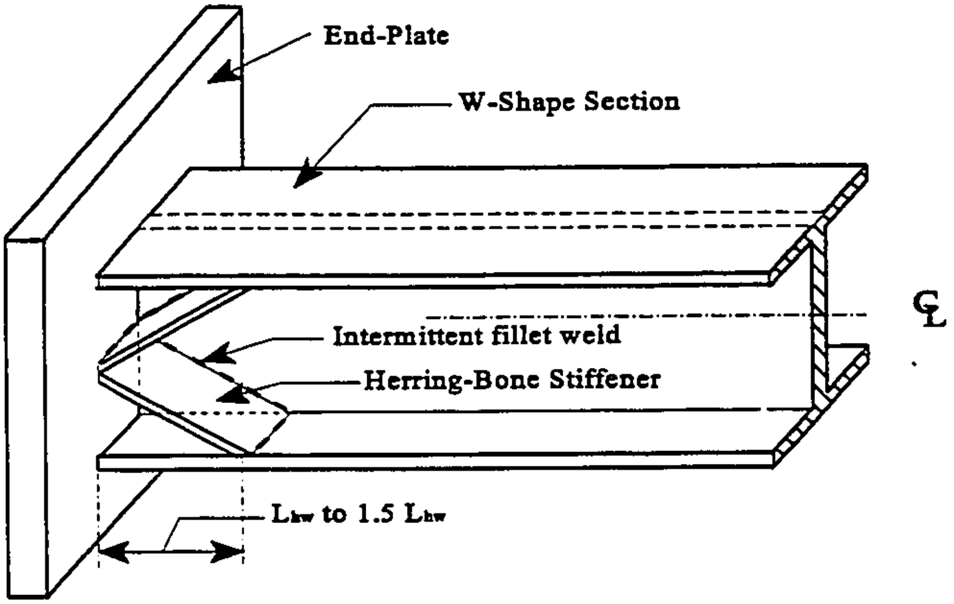

Fig. 3.50 Herring-Bone Stiffened Beam

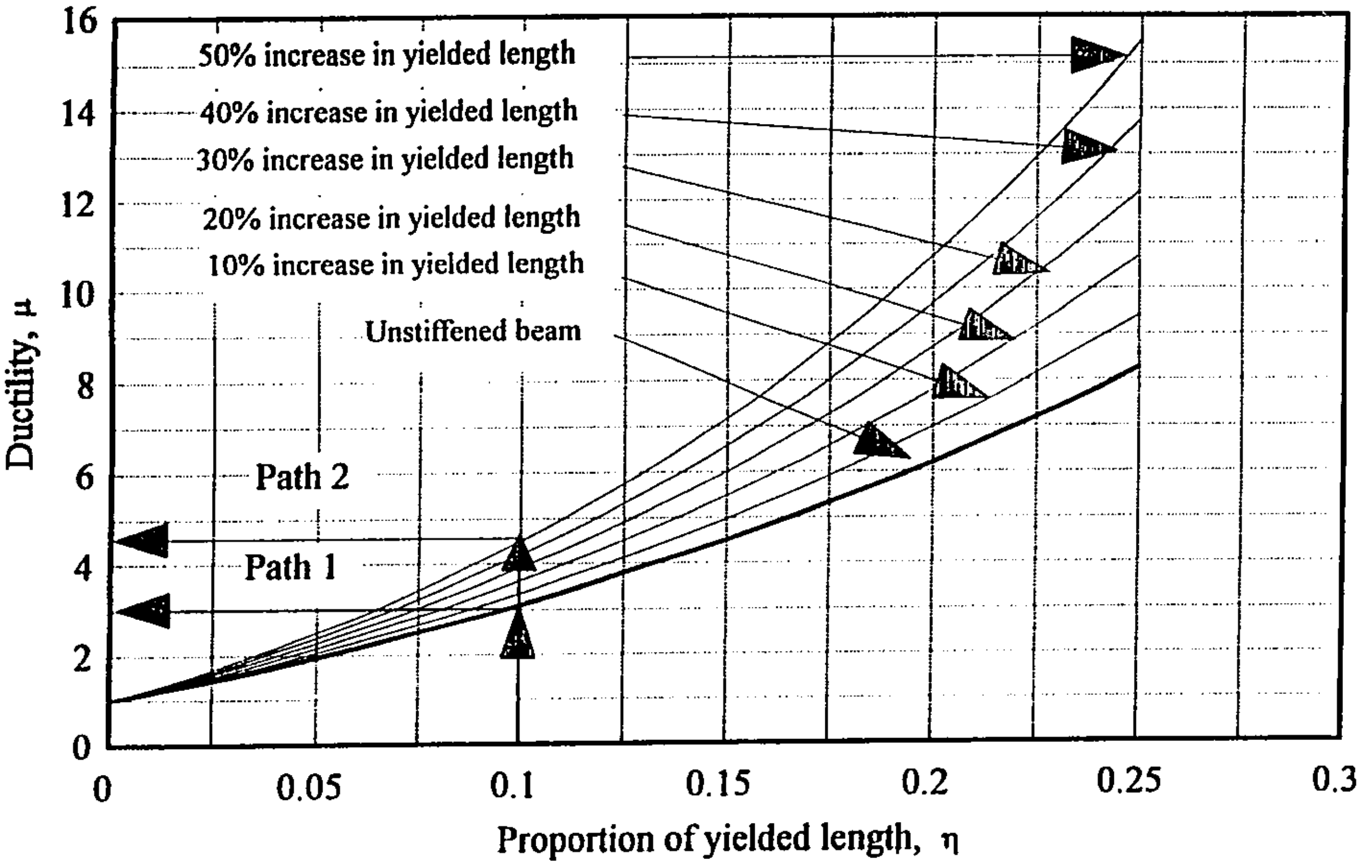

Fig. 3.51 Ductility enhancement due to increase in yielded length

CHAPTER 4

LOW CYCLE FATIGUE DAMAGE ASSESSMENT IN STEEL BEAMS

4.1 Introduction

The design of earthquake resistant structures requires, by necessity, allowance for some degree of damage during a seismic event in order to minimize construction cost. This can be achieved by providing both adequate ductility and sufficient strength to redistribute internal forces and thus absorb large amounts of energy.

Different modes of failure are possible in steel structures that may experience earthquake-type loading. These include excessive yielding, weld and plate-element cracking, panel joint collapse, distortional buckling, local buckling etc. Current earthquake design practice is primarily concerned with the maximum earthquake induced force or the maximum deflection that a structure might experience. Safety against total failure in moment resisting frames, for instance, is achieved through design rules limiting flange and web slenderness ratios. proper weld detailing and the provision of adequate lateral supports.

We have already mentioned in Chapter 3 some preliminary observations concerning low-cycle fatigue and its effects on resistance and dissipated energy. In this chapter, we shall further investigate this phenomenon, and in particular examine the behaviour of six specimens tested under constant amplitude loading. Three of the specimens were unstiffened cantilever beams, the remaining three being similar to the previous ones except that they were locally stiffened with a herring-bone style of stiffener. The results of the tests were used to generate a Coffin-Manson (Tavernelli and Coffin 1962) type of plastic rotation range to strength, or, rate of energy deterioration per reversal relationship; in addition, earlier experimental results have been used to generate a comprehensive model that can assess, in numerical simulations, the strength deterioration per reversal of loading for beams subjected to earthquake-type loading.

4.2 Prior research in low cycle fatigue

Most researchers have recognized that failure of a structural element could result from low cycle fatigue rather than maximum response, be it force or displacement. For instance, for macroscopic sized beams, Sherbourne (1963), Krishnasamy & Sherbourne (1968), Kasiraj and Yao (1969) and Gyoten et al. (1974) investigated low-cycle fatigue behaviour to provide insights into the behaviour of ductile structures under repeated loads; meanwhile, Neale and Schroeder (1971) considered instability under cycles of plastic deformation. On the element level, Yamada (1969) investigated experimentally the ductility-number of cycles to failure relationship for some steel and reinforced concrete beam-columns, while Mizuhata et al. (1977) investigated failure by crack propagation. Krawinkler et al. (1983) and Krawinkler (1982, 1987) addressed the question of damage accumulation due to local buckling in steel members subjected to earthquake ground motion; they presented some guidelines for the performance assessment of structural components. More recently, Castiglioni and Goss (1989), Castiglioni (1992) and Castiglioni and Losa (1992) examined the deterioration to number of cycles relationship in steel members under cyclic loading; at about the same time, Calado and Azevado (1989) and Calado (1992) addressed low cycle damage modeling at the fibre level of individual members and thence its application on the structural level.

Under constant amplitude cycling, steel members exhibit two different types of behaviour. If the amplitude of loading is sufficiently small, the steel members will be under a stationary state of response. The deterioration in strength and dissipated energy per reversal of loading is relatively small to justify being taken into account (Fig. 4.1-a). On the other hand, if the amplitude of loading is large enough to cause significant plasticity and local deformations, the strength and stiffness decrease with the number of load cycles. The behaviour exhibited by the element is now termed as "non-stationary". This is graphically illustrated in Fig. 4.1-b.

Because of the randomness of the load history during an earthquake, an early high reversal of inelastic deformation might lead to an initiation of local buckling in the flanges and web of a W-shaped section. Then, any secondary reversals of inelastic deformation would result in a further and continuous deterioration, (in strength, stiffness and energy dissipation), which would diminish most of its useful life. Damage caused by elastic reversals is negligible; however, those caused by inelastic ones need to be addressed. Thus, structures designed for earthquake loading can be weakened or damaged by a combination of reversals of inelastic deformations and high deformation excursions. It seems clear, therefore, that to properly assess the rotation capacity and energy dissipation performance of W-shaped beams, damage criteria are needed that account for the effects of repeated cyclic loading.

4.3 Experimental program

4.3.1 General

Two series of W-shaped beams with W310×21 sections having flange and web slenderness ratios, b/2t=8.85, and, h/w=57.18 respectively, were selected for six test specimens. These were fabricated as cantilever beams as shown in Fig. 3.1 and represent a half beam length in moment resisting frames subjected to earthquake loading.

The steel W310×21 sections were of grade ASTM 36 (σ_y=290 MPa, σ_u=415 MPa). The remaining components such as a column stub, end plates of the cantilever beams and fasteners used to fix the end plates to the column stub had the same characteristics already discussed in Chapter 3. Tensile coupons and section characteristics are given in Tables 4.1 and 4.2, respectively.

The test specimens had the following characteristics; in series SF, specimens SF1, SF2 and SF3 had lengths of 2125 mm. All-around 6 mm and 4 mm fillet welds were used to attach the flanges and web respectively to the end-plate. In the series SFS, specimens SFS1 to SFS3 were similar to the previous ones except that they had a one sided local herring-bone stiffener in the potential plastic hinge zone. The stiffeners were all-around fillet welded in the region between the end plate and 110 mm remote from it. Fabrication details of both series' specimens are shown in Fig. 4.2, while information concerning the test rig and instrumentation are given in Chapter 3.

In order to compare strength and energy deterioration of the stiffened and unstiffened specimens, three different constant amplitude load histories were applied to specimen groups SF1 and SFS1, SF2 and SFS2, SF3 and SFS3. These had constant amplitude values of ±52.5, ±79 and ±96 mm as represented by the load histories shown in Fig. 4.3.

The experimental objective was to obtain knowledge of the restoring force characteristics of beams subjected to constant amplitude loading. This would allow for an assessment of the strength and energy deterioration per reversal of loading and help in the formulation of damage models to be described in Chapter 5.

4.3.2 Test results

Specimen SF1

Specimen SF1 was tested at a constant reversible amplitude of ±52.5 mm corresponding to about three times the plastic displacement of the beam. In the first upward push causing the top flange to undergo compression, local buckling was initiated. Immediately thereafter, local web buckling was observed at a distance equal to about a half-depth of the section away from support. At maximum amplitude, the combined flange and web local buckling caused the specimen to undergo noticeable deterioration in strength and stiffness in the first reversal (Fig. 4.4). In the following few reversals, the specimen continued to sustain an appreciable amount of deterioration in strength and dissipated energy until about 10 reversals of constant amplitude, at which point the rate of deterioration slowed. This is clearly identified by the closeness of the hysteresis loops shown in Fig. 4.4.

Specimen SF2

Typical force-displacement curves show the behaviour of this specimen in Fig. 4.5. The specimen was cycled at a constant amplitude value of ±79 mm, corresponding to 4.5 times the beam plastic displacement of the beam. After suffering flange and web buckling, during the first reversal, the beam continued to sustain significant resistance up to its maximum amplitude. In the following reversal, and then the subsequent ones, it is seen that the beam section endured an major load fall-off from one reversal to the other. The test was eventually terminated because of initiation of cracks in the plastic hinge zone.

Specimen SF3

Typical hysteretic loops for specimen SF3 are shown in Fig. 4.6. Repeated constant amplitude values of ±96 mm were applied to this beam. It can be observed that with high inelastic displacement, resistance drop-off started to occur well before the displacement limit was reached. Again, this occured because of flange and web buckling. Examination of Fig. 4.6 shows that following the first reversal the load carrying capacity of the member started to significantly degrade. The test was terminated because of large cracks developing in the flanges.

Specimen SFS1

This specimen was tested with a load history identical to that of SF1; it was found that a slightly higher restoring force was exhibited than in its counterpart specimen. Following the first few reversals during which noticeable deterioration was taking place, a slow down in the rate of damage was exhibited as observed by the closeness of the hysteretic curves (Fig. 4.7).

Specimens SFS2 and SFS3

Unlike their unstiffened counterparts these displayed an almost constant rate of deterioration in strength from one cycle to the other. In Figs. 4.8 and 4.9 is shown the behaviour exhibited by SFS2 and SFS3. Both tests were eventually terminated when the restoring force was about 50% of ultimate. At that stage, fatigue effects led to the appearance of large crack openings in the top flange of both bcam sections .

4.4 Discussion

4.4.1 Rates of deterioration

Constant amplitude tests are useful because they provide information on the fatigue performance parameters of sections meant to resist dynamic loading and are easily comparable with the work of others. As described earlier, three groups of specimens were tested at different constant amplitudes. A specimen's hysteresis loops are especially useful. In this case, data obtained from the two series of tests were used to yield information on the rates of deterioration of strength and dissipated energy. Plots were prepared involving normalized positive and negative forces, F, at peak displacements against the number of reversals the specimens underwent. As well, the normalized energy, E_d/E_u, is plotted against the number of reversals, N, where E_u is the dissipated energy during the first full reversal of loading.

Results of the SF series specimens are shown in Fig. 4.10 to 4.12. For example, Fig. 4.10-a shows the deterioration in strength versus the number of reversals, N, for specimen SF1. It is clearly seen that after undergoing a high rate of deterioration, the loss in strength considerably stabilized between reversals 20 and 90. Once cracking developed in the bottom flange, the specimen again showed increased deterioration. Similarly, after undergoing initially high deterioration in the dissipated energy, the deterioration rate stabilized between reversals 20 and 90 as shown in Fig. 4.10-b. Test results of specimens SF2 and SF3 were treated in a similar manner and are shown in Fig. 4.11 and 4.12. The SF2 specimen showed significant change in strength and associated crack propagation at reversal 50 while SF3 demonstrated more regular behaviour. In general, it can be observed that three ranges of response can be identified by their different rates of deterioration both in strength and dissipated energy. This is not so, however, for specimen SF3 where it is readily observed that only two distinct rates of deterioration were identified (Fig. 4. 12).

In contrast, Series SFS specimens showed somewhat different behaviour. For instance, specimen SFS1 exhibited only two distinct rates of deterioration until reversal 100. Note, also, that the rates of deterioration in range I of specimen SFS1 are slightly lower than those of its equivalent specimen SF1 (Fig. 4.13). Similar observations are equally applicable to specimens SFS2 and SFS3 for range I of the tests as shown in Figs. 4.14 and 4.15 when compared with their unstiffened counterparts(Figs. 4.11 and 4.12).

To simplify an interpretation of the data, regression analysis was used to yield straight lines to fit the experimental results. The slopes of these lines represent the rates of deterioration per reversal for each range. For example, the strength of specimen SF1 degraded in the first few reversals at a rate of 0.015 given by the slope of the line (Fig. 4.10); in the following reversals, the rate of degradation of the resisting force diminished to a value of 0.0012. After that, deterioration increased again to a value of 0.0027 until failure. From figures 4.10 to 4.15, one can note that the initial rate of degradation in strength and dissipated energy changed after about the first ten to fifteen reversals both in terms of loss in strength and accompanying energy. The second point of transition when it occured, was less well defined for the specimens tested occurring between 40 and 90 reversals.

4.4.2 Modeling of damage due to local buckling

An important parameter for measuring bending deformation in a member is the plastic rotation range, Θ_p, experienced by a member during inelastic cyclic loading. For one event of loading, Θ_p is obtained by dividing the total inelastic tip displacement at successive zero load states by the member length. Fig. 4.16 shows a typical plot of such a response in a constant amplitude test. From the experimental results, it is seen that if the value of the plastic rotation range (or amplitude of inelastic deformation) increases, the number of reversals to failure decreases. A log-log plot of the plastic rotation range values versus the rates of deterioration values in both strength and dissipated energy is shown in Figs. 4.17 and 4.18 for each of the SF and SFS-series specimens. The specimens' behaviour is very suggestive of a linear pattern-type distribution. If a straight line were to be fitted to the experimental results, we obtain a Coffin-Manson type of equation (Tavernelli and Coffin 1961) of the form:

$$\Delta d = a(\Theta_p)^b \qquad (4.1)$$

where Δd is the deterioration per reversal and "a" and "b" are experimental parameters that reflect the properties of the member under a constant amplitude test. The above equation suggests a relationship similar to the stress level-number of cycles (S-N) relationship found in high cycle fatigue.

For the W310×21 section under consideration, a least square analysis of the differences of the test results and predicted results yields the following relationships for strength and energy deterioration values.

$\Delta d_s = 8.69(\Theta_p)^{1.80}$ for strength deterioration per reversal in SF-series **(4.2-a)**

$\Delta d_s = 1.17(\Theta_p)^{1.28}$ for strength deterioration per reversal in SFS-series **(4.2-b)**

$\Delta d_e = 1.26(\Theta_p)^{1.11}$ for energy deterioration per reversal in SF-series **(4.3-a)**

$\Delta d_e = 0.83(\Theta_p)^{1.08}$ for energy deterioration per reversal in SFS-series **(4.3-b)**

Fig. 4.17 and 4.18 clearly prove the superiority of stiffened specimens. From Fig. 4.17, it can be seen that for a plastic rotation range value of 0.05, one obtains a rate of deterioration per reversal of 2.5% for series SFS and 3.5% for series SF. Similar observations hold true in considering dissipated energy. At a plastic rotation range of 0.05, series SFS specimens suffered 3% deterioration in energy per reversal versus 4.5 % for the SF series.

Since the damage in strength or dissipated energy is Δd_s or Δd_e, then the total number of reversals to failure for a constant amplitude test will be written in general form as $n=1/\Delta d$. If Miner's rule (Miner 1945) of linear damage accumulation were used, then for variable amplitude tests the cumulated damage, d, and the total number of reversals, N, of different magnitudes Θ_{pi} are given by:

$$d=a\,\Sigma(\Theta_{pi})^{b} \tag{4.4-a}$$

and

$$N=a^{-1}\,\Sigma(\Theta_{pi})^{-b} \tag{4.4-b}$$

Note that Θ_{pi} is simply Θ_p during the ith positive or negative reversal.

If x is introduced as a limit of damage acceptability (10-20% say), then the total number of reversals to failure is given by:

$$N= x\,a^{-1}\,\Sigma(\Theta_{pi})^{-b} \tag{4.5-a}$$

and the cumulated damage is:

$$D=x^{-1}a\,\Sigma(\Theta_{pi})^{b} \tag{4.5-b}$$

So far, all relationships expressing the rate of deterioration have been expressed in terms of plastic rotation range, Θ_p. Note however that instead of the plastic rotation range, one can use parameters such as displacement, curvature, ductility, etc. For instance, the rate of deterioration in dissipated energy may be expressed in terms of ductility as:

$\Delta d_e = 0.0064(\mu-1)^{1.15}$ for energy deterioration per reversal for the SF-series specimens **(4.6)**

where μ is a dimensionless parameter defined as the ratio of ultimate displacement to the plastic displacement measured from zero load intercept.

4.4.3 Empirical model for damage assessment in beams

Numerous expressions for the Coffin-Manson relationship have been presented in the literature. It is unfortunate to note, however, that not all of them compare to each other. The reason is that while, for instance, Yamada (1969) and Mizuhata et al. (1977) give a relationship between amplitude of deformation and number of cycles, Castiglioni (1992), Castiglioni and Losa (1992) and Castiglioni and Goss (1989) present relationships between the normalized total amplitude (positive and negative) and the number of cycles. Krawinkler (1982), on the other hand, suggests relationships between the rate of deterioration in strength or energy and the plastic rotation range.

Strength deterioration models of three different rolled steel sections, (Krawinkler 1983 and Daali and Korol 1994), are shown in Fig. 4.19. Added to these are the experimental results obtained by Castiglioni and Guiliana (1989) and processed by the author to be comparable to the others. It is clearly seen that although showing a similar trend, the sections yield different strength deterioration rates per reversal of loading. Since in practice, it is common to at least indirectly select beams according to their flange slenderness, web slenderness and lateral slenderness ratios, it was decided to try to predict empirically the member parameters, "a" and "b", according to these slenderness ratios.

Values of the parameters "a" and "b" from strength deterioration models are given in Table 4.3 with their corresponding slenderness ratios. Plots of the parameters "a" and "b" versus the modified flange slenderness value, $\alpha_f(=\frac{b}{2t}\sqrt{\frac{\sigma_y}{300}})$, the modified web slenderness, $\alpha_w(=\frac{h}{w}\sqrt{\frac{\sigma_y}{300}})$, and the modified lateral slenderness, $\alpha_l(=\frac{L}{r_y}\sqrt{\frac{\sigma_y}{300}})$, show no clear pattern; however, those of the same parameters versus the effective slenderness, α_e, expressed as a normalized product of the three above-mentioned slendernesses, i.e. $\alpha_f \alpha_w \alpha_l / 30072$, clearly shows a trend. With increasing values of the effective slenderness, α_e, the value of the parameter "a" increases, while that of "b" is relatively stable maintaining an average value of 1.648 (Fig. 4.20). In Fig. 4.19, section 310W21 having an effective slenderness, α_e, of 0.71 is shown to exhibit a noticeably greater deterioration rate than does section HE220B whose effective slenderness, α_e, is 0.115. Using the least squares method, parameter "a" was expressed in terms of the effective slenderness, α_e, as follows:

$$a = -1.98 + 14.3\,\alpha_e \tag{4.7}$$

Here, parameter "b" was taken as 1.648, the average value for the specimens listed in Table 4.3. In a study by Krawinkler (1987), it was suggested that unlike parameter "a" believed to be of a random nature, parameter "b" was noted to be a much more stable parameter between 1.5 to 2.0. Note that good agreement is shown to exist between the observed values of the parameters "a" and "b" and those empirically predicted.

Eq. 4.1 along with Eq. 4.7 were then used to generate a comprehensive model for the prediction of strength deterioration per reversal of loading (Fig. 4.21). Such a model, then, has the potential to be used in numerical nonlinear analyses of ductile moment resisting frames along with the rain-flow cycle counting method (Downing and Socie 1982) to yield information on the level of deterioration in strength or dissipated energy sustained in a structural member during a prescribed load history such as an earthquake record. Practical implications of the model can be seen in the evaluation of damage accumulation in members belonging to Class1 sections. It should be noted however that since the method described is based on limited data, the actual expressions for determination of the parameters "a" and "b" may not be as accurate as a broad set of experiments could provide. Nonetheless the approach is deemed to be a reasonable way of predicting damage in steel beams under cyclic loading.

4.4.4 Example of application

The prediction of strength deterioration for a particular application follows. Consider the inelastic rotation response of a W610×125 beam section belonging to a seven-storey building subjected to a strong motion earthquake record history as shown in Fig. 4.22. The beam section has the following characteristics:

$\alpha_f = 7.65$, $\alpha_w = 54.57$ and $\alpha_l = 56.58$.

As such, the effective slenderness, α_e, is 0.7854 and using Eq. 4.7 we obtain:

a= 9.25, with parameter " b" equal to 1.65.

To be able to apply the knowledge derived from the constant amplitude tests, one needs to convert the random response in an equivalently ordered response expressed in terms of closed loops of constant amplitude deformation. For that, we need to apply the rain-flow method or any other equivalent approach. (For more details the reader is referred to Bannantine et al. (1990) where an excellent summary of such methods is covered). A rain-flow algorithm written by Downing and Socie (1982) was modified by the authors and used to identify the constant amplitude deformation closed loops and their corresponding ranges. Using Eq. 4.5-b, the cumulated deterioration in strength is obtained as:

$d_s=(9.25)(2)[0.003796^{1.65}+0.0007592^{1.65}+0.0094^{1.65}+......]$

where the values within the square bracket are obtained from Fig. 4.23 and represent the plastic rotation range values. Note that the number "2" reflects the fact that there are two reversals per complete cycle.

In the above example, the cumulated deterioration in strength, d_s, is 9.1% of the maximum resisting force. This value however is not normalized and is not directly related to a known failure mode. Furthermore, it should be noted that within this class of damage models there is no definite damage acceptability limit upon which there is agreement. For instance, while Krawinkler (1982) suggests a 10% to 15% reduction from the maximum restoring force, Calada and Azevedo (1989) and Calado (1992) suggest a 50 % reduction in dissipated energy from the first full cycle of loading. Such differences of opinion exist, perhaps, because of the complexity existing between the reserve of strength of structural elements on the one hand and that of the structure as a whole. Nonetheless, d_s is considered to be a reliable damage indicator that can be used in a diagnosis of a structural element if a damage acceptability limit is set and agreed upon a-priori. More details concerning this topic may be found in Daali and Korol (1995)

4.5 Summary and conclusions

Under strong earthquake motion, structural elements may undergo a high inelastic excursion followed by several inelastic reversals that will eventually affect their restoring force characteristics.

To shed some light on the low cycle fatigue effects due to local buckling, results of three groups of specimens tested under three different constant amplitude tests were used to yield a Coffin-Manson type of equation, giving the deterioration (in strength, dissipated energy) per reversal of loading. It is shown that specimens with herring-bone type stiffeners exhibited slower rates of deterioration both in strength and dissipated energy. Furthermore, Miner's rule can be used to obtain the cumulated damage as a function of the number of reversals. Finally, the experimental results of the constant amplitude tests of this study along with the results of earlier work were used to propose a strength damage assessment model for beams. Indeed, the model uses the plate and lateral slenderness of the beam to predict the strength deterioration per reversal of loading and the cumulated damage after a given number of reversals, N.

To follow in the subsequent Chapter, is a treatment on damage models suitable for use as damage criteria.

Table 4.1 Tensile coupons test results

Specimen #	Flange		Web	
	Yield (MPa)	Ultimate (MPa)	Yield (MPa)	Ultimate (MPa)
SF1	323	485	344	498
SF2	322	488	345	496
SF3	323	490	345	499
SFS1	322	488	331	494
SFS2	321	487	343	500
SFS3	320	490	336	496

Table 4.2 Comparison of actual and nominal dimensions of beam sections.

Spec. #	Flange Thickness (mm)		Web Thickness (mm)		Section Depth (mm)		Section Width (mm)	
	Nominal	Actual	Nominal	Actual	Nominal	Actual	Nominal	Actual
SF1	5.7	5.6	5.1	5.2	303	303	101	102
SF2	"	5.7	"	5.3	"	302	"	103
SF3	"	5.8	"	5.1	"	304	"	103
SFS1	"	5.8	"	5.3	"	303	"	103
SFS2	"	5.6	"	5.1	"	303	"	102
SFS3	"	5.6	"	5.2	"	304	"	101

Table 4.3 **Observed and predicted section parameters.**

Reference	Sections	α_f	α_w	α_l	α_e	Observed		Empirically obtained	
						a	b	a	b
1	W310*21	8.85	57.71	41.88	0.711	8.69	1.81	8.19	1.648
2	W6*9	9.43	32.17	30.89	0.311	3.05	1.69	2.48	1.648
3	HE220A	10	26.8	25.59	0.228	0.61	1.5	1.28	1.648
3	HE220B	6.9	19.8	25.23	0.114	0.50	1.55	-0.33	1.648
3	IPE300	7	39.2	42.15	0.384	2.29	1.69	3.52	1.648

1: Authors

2: Krawinkler (1983)

3: By Authors from experimental data of Castiglioni and Guiliana (1989)

Note: a and b are parameters defined in Eqn. 4.1

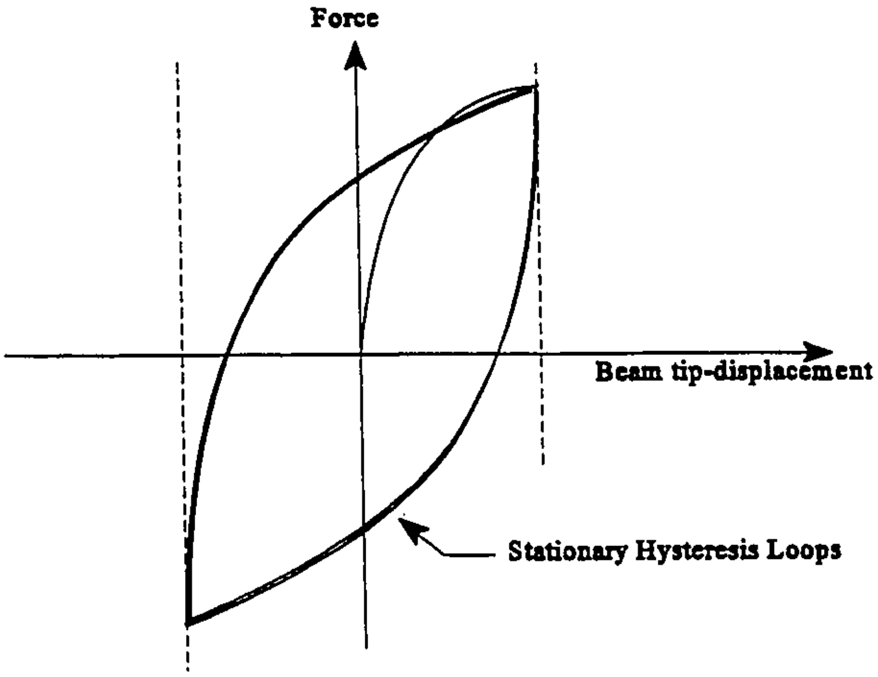

(a) Stationary hysteresis loops

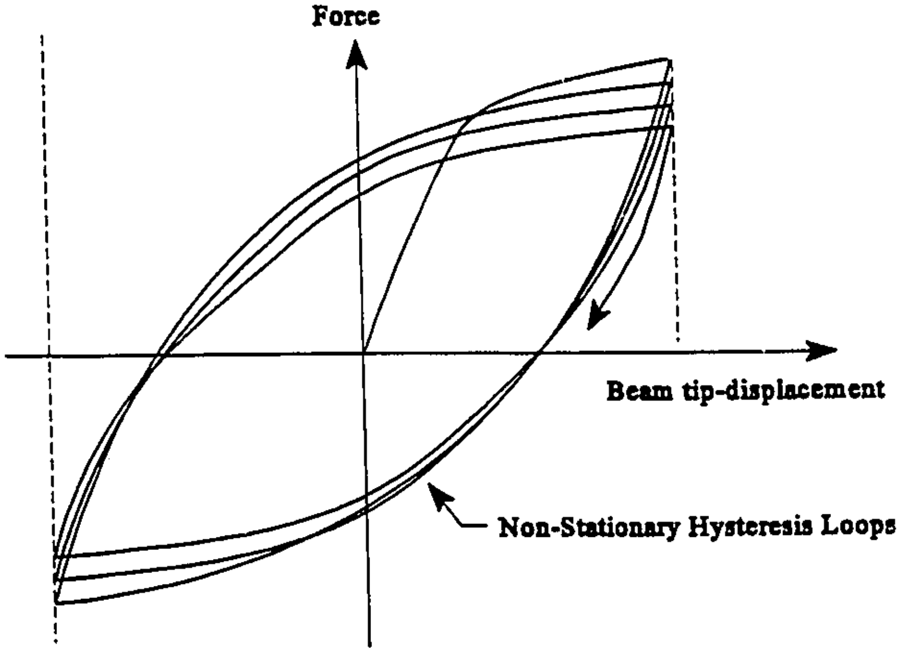

(b) Non-stationary hysteresis loops

Fig. 4.1 Behaviour under small and large constant amplitude loading

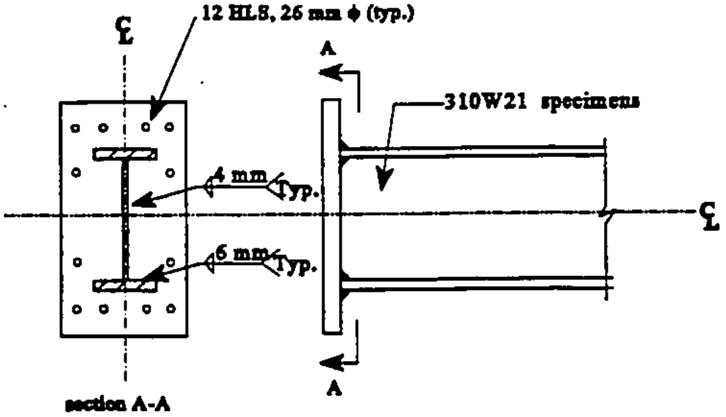

(a) Series SF Specimens

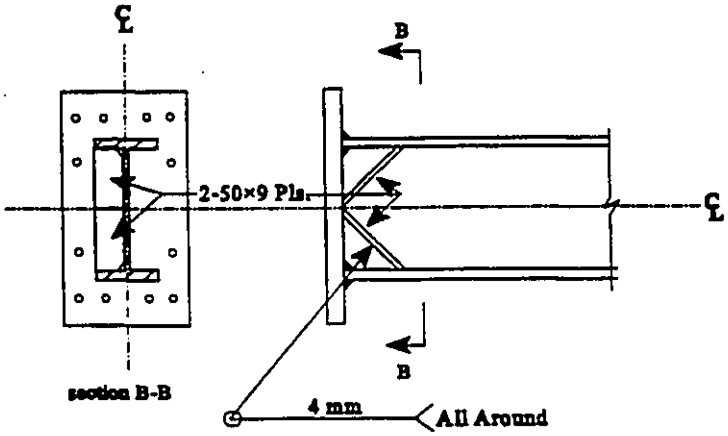

(b) Series SFS Specimens

Fig. 4.2 Typical Fabrication Details

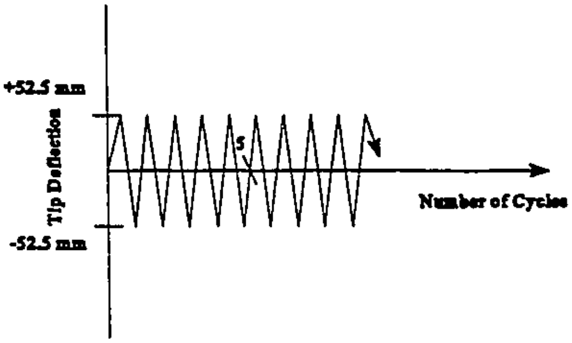

(a) Load History for SF1 and SFS1

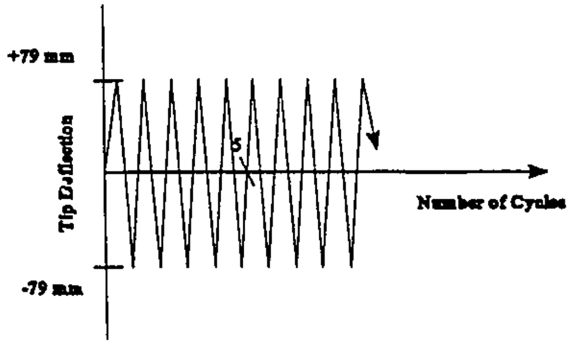

(b) Load History for SF2 and SFS2

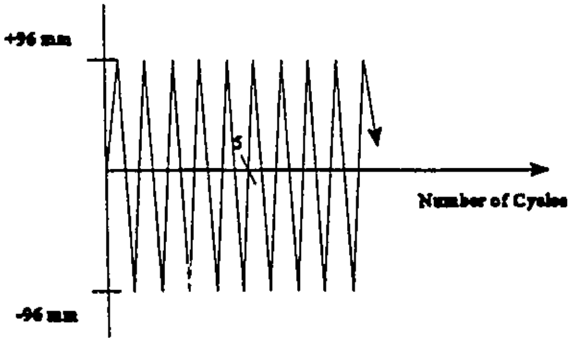

(c) Load History for SF1 and SFS1

Fig. 4.3 Load histories

Fig. 4.4 Response of Specimen SF1 under Constant Amplitude Deformation

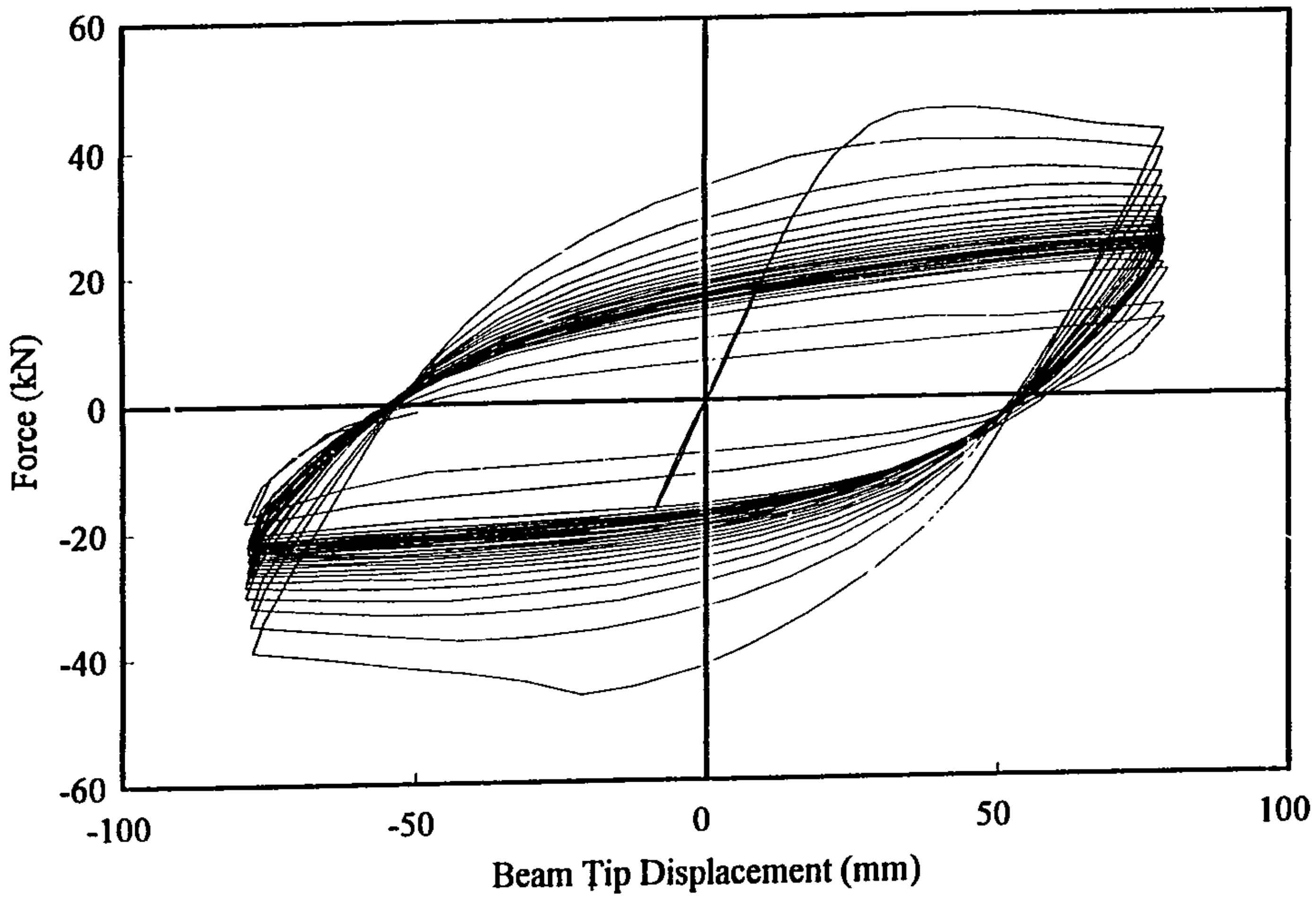

Fig. 4.5 Response of Specimen SF2 under Constant Amplitude Deformation

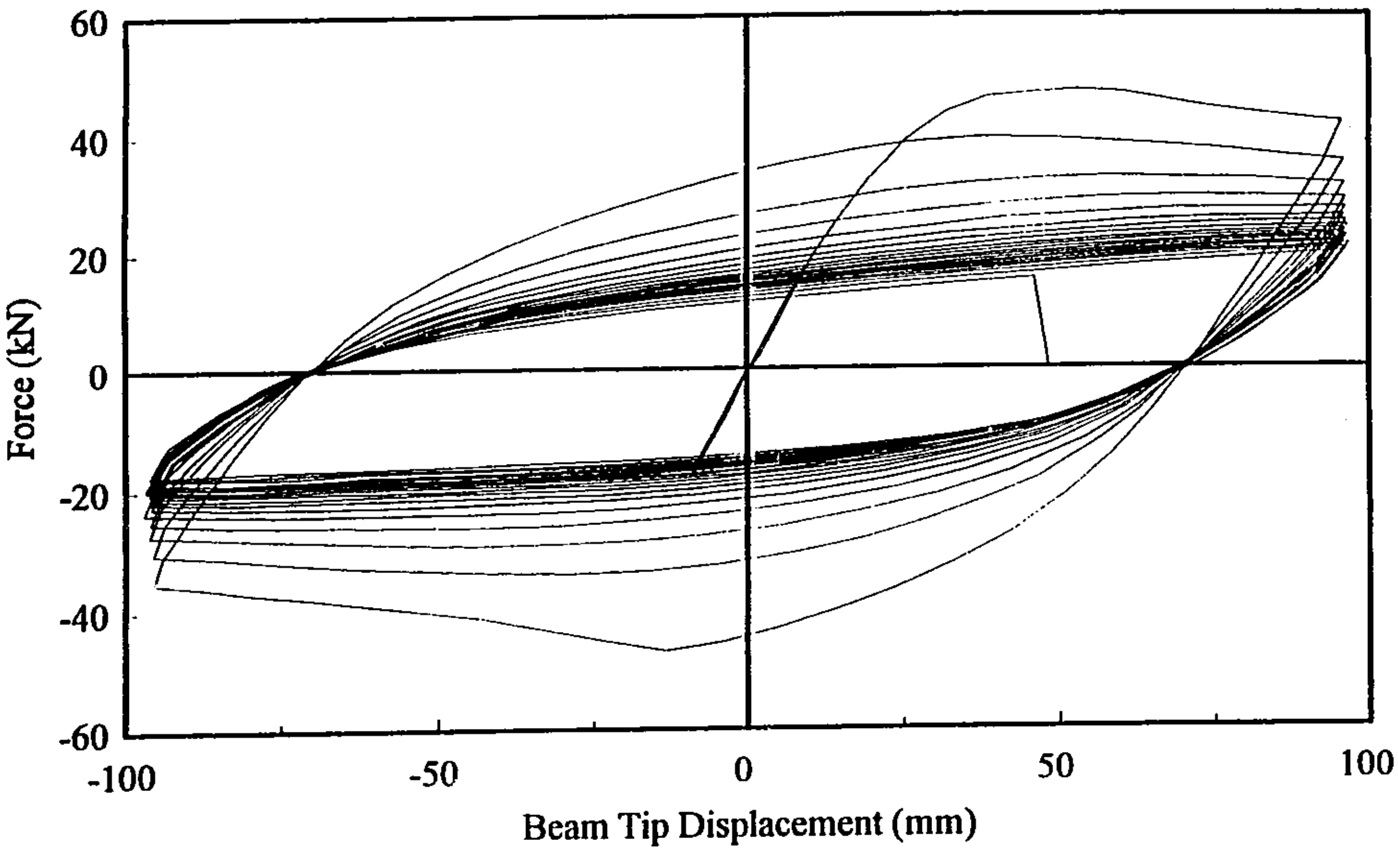

Fig. 4.6 Response of Specimen SF3 Under Constant Amplitude Deformation

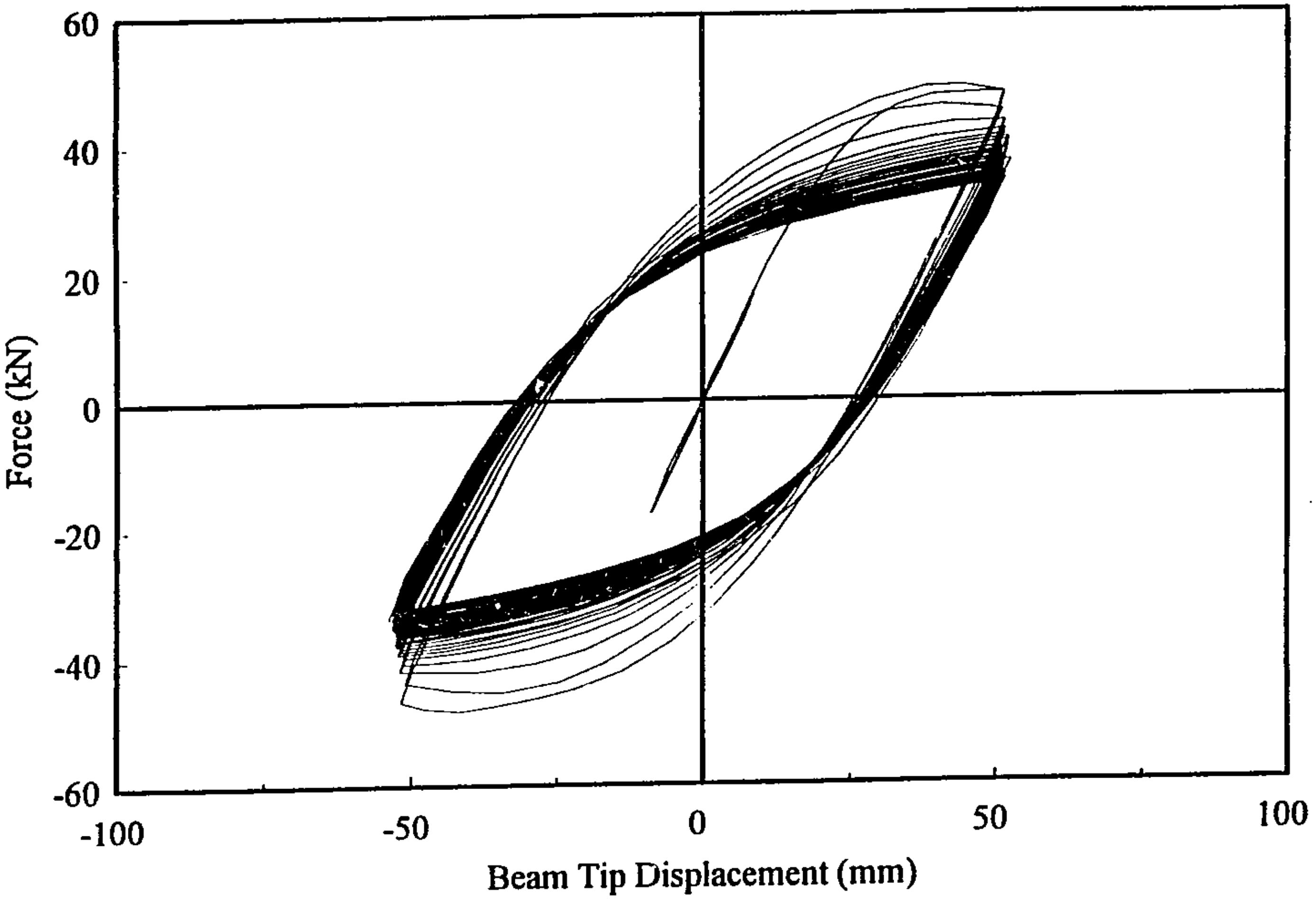

Fig. 4.7 Response of Specimen SFS1 under Constant Amplitude Deformation

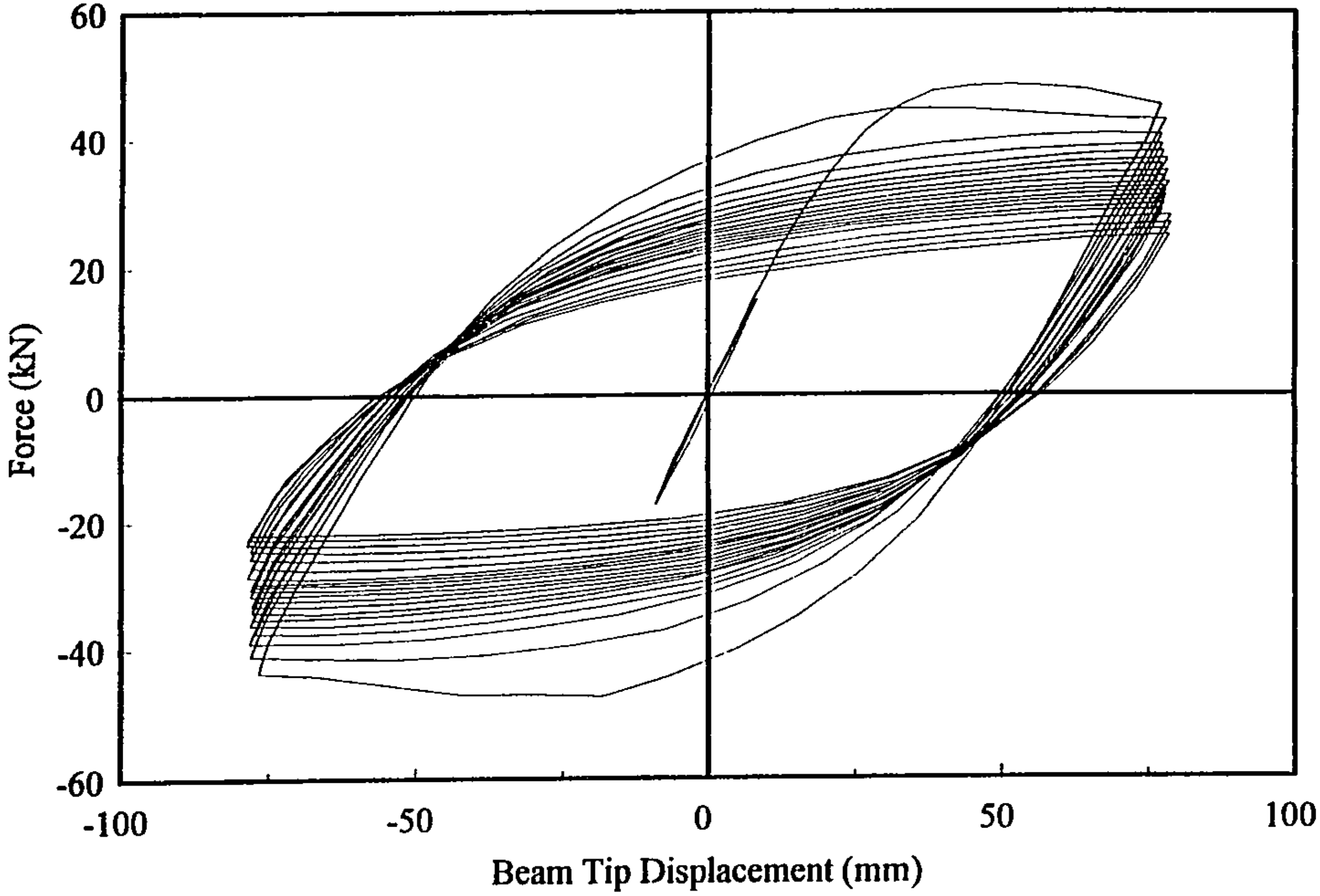

Fig. 4.8 Response of Specimen SFS2 Under Constant Amplitude Deformation

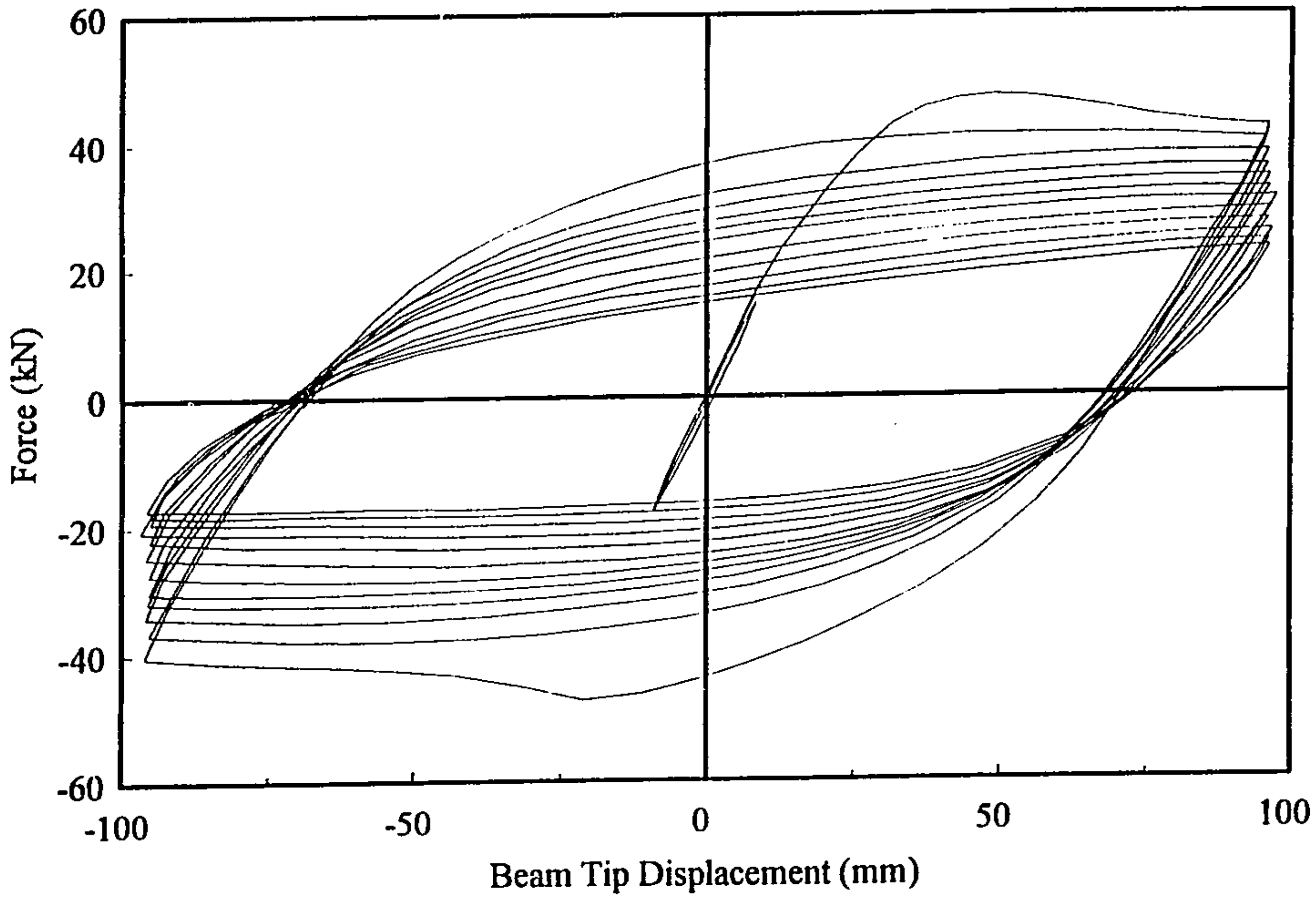

Fig. 4.9 Response of Specimen SFS3 Under Constant Amplitude Deformation

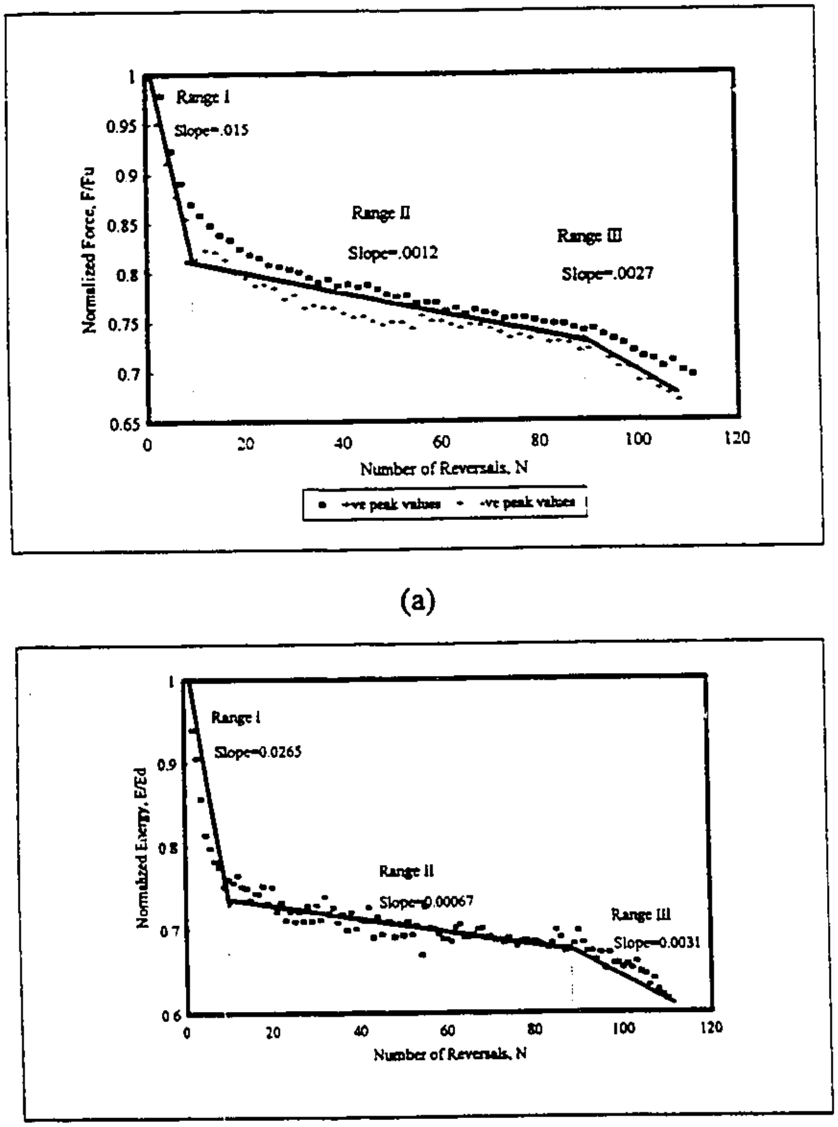

(a)

(b)

Fig. 4.10 Specimen SF1 Deterioration in:
(a) Strength; (b) Dissipated Energy

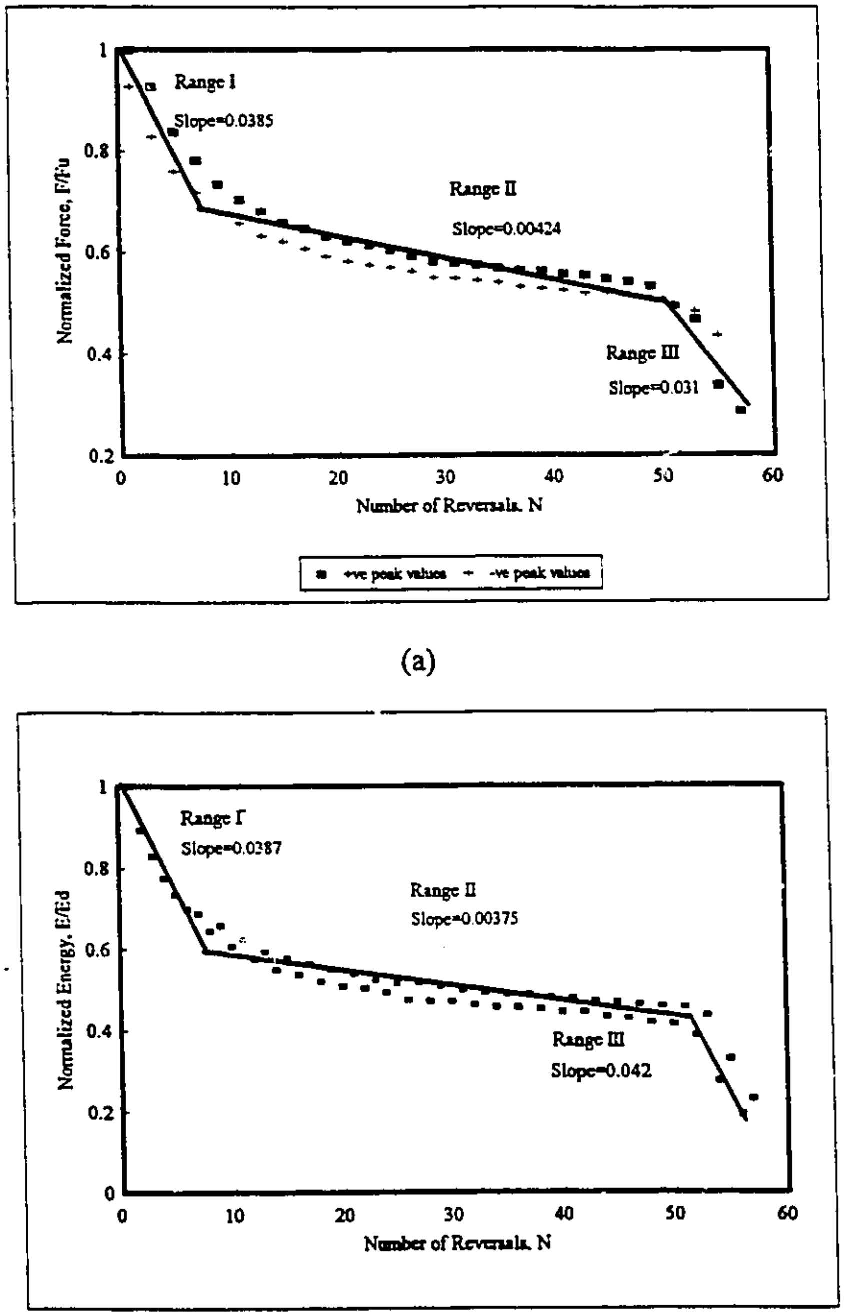

(a)

(b)

Fig. 4.11 Specimen SF2 Deterioration in:
(a) Strength; (b) Dissipated Energy

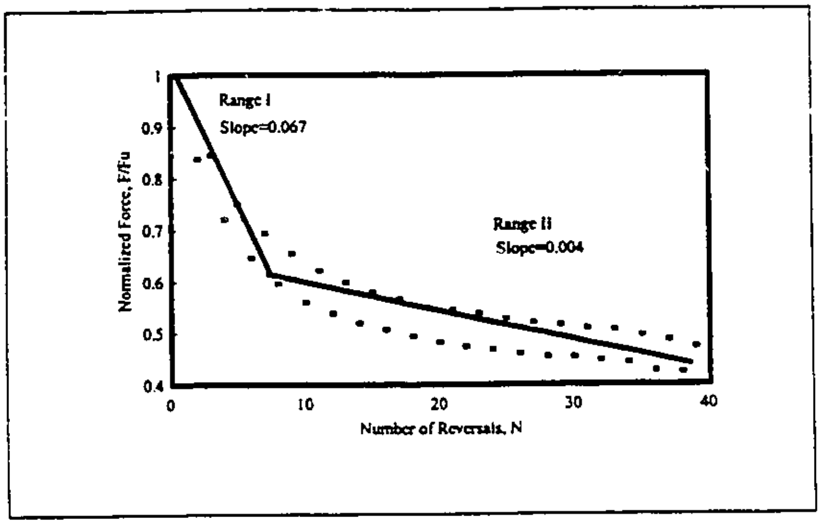

(a)

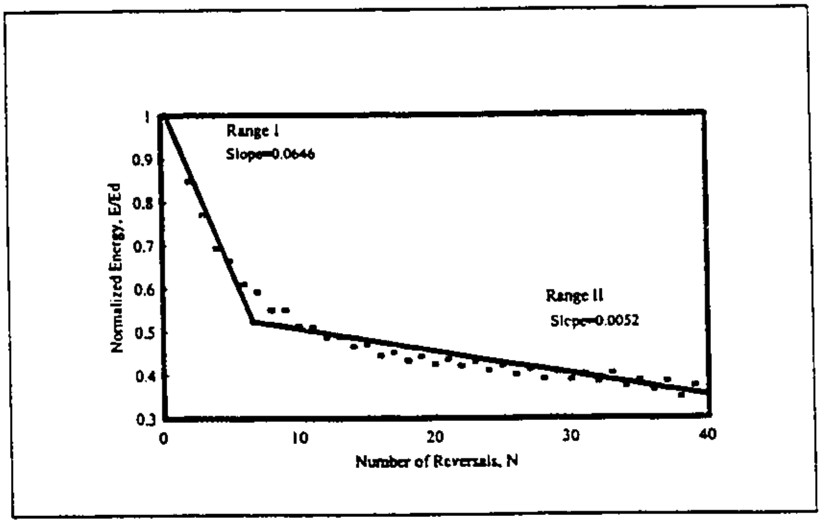

(b)

Fig. 4.12 Specimen SF3 Deterioration in:
(a) Strength; (b) Dissipated Energy

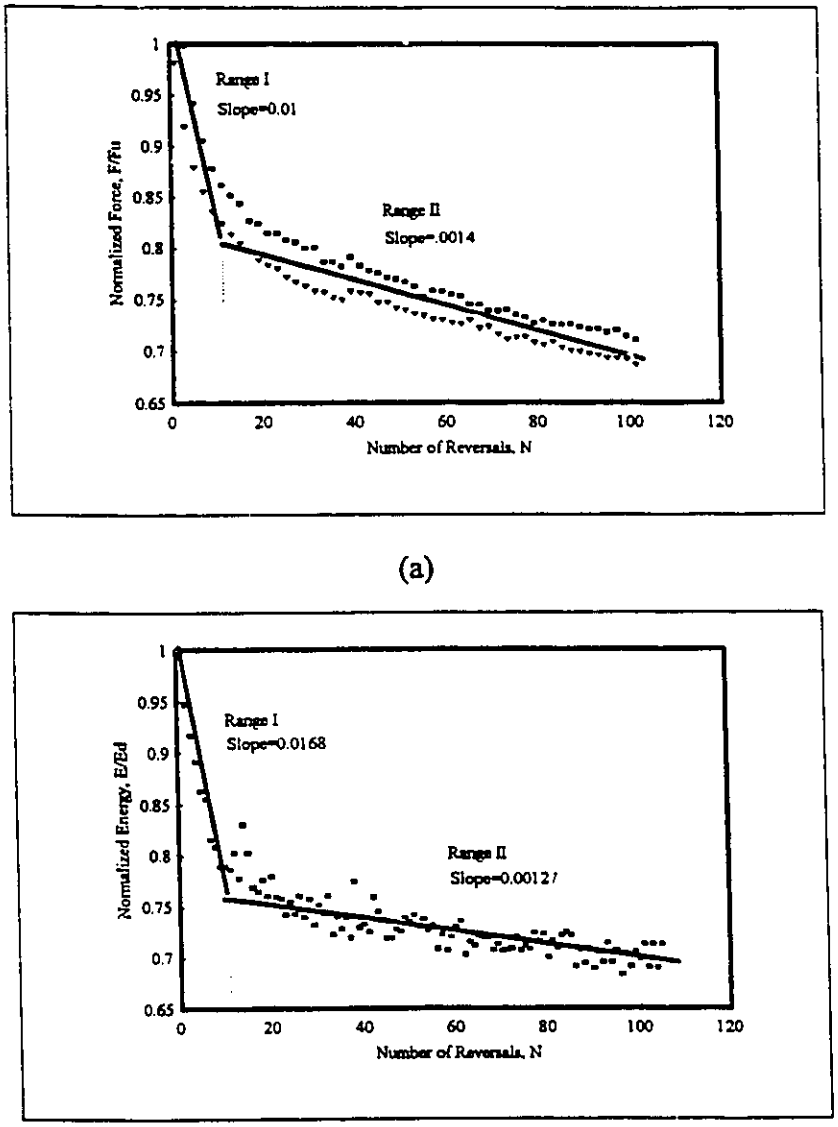

(a)

(b)

Fig. 4.13 Specimen SFS1 Deterioration in:
(a) Strength; (b) Dissipated Energy

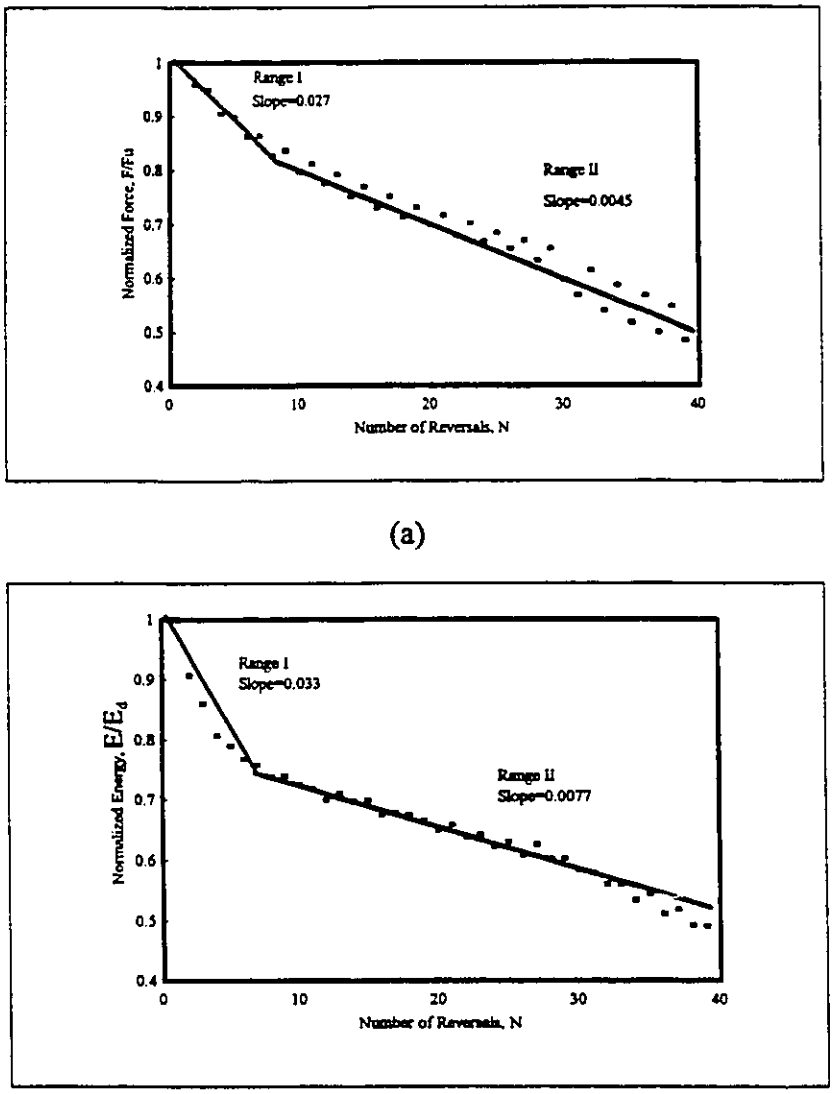

(a)

(b)

Fig. 4.14 Specimen SFS2 Deterioration in:
(a) Strength; (b) Dissipated Energy

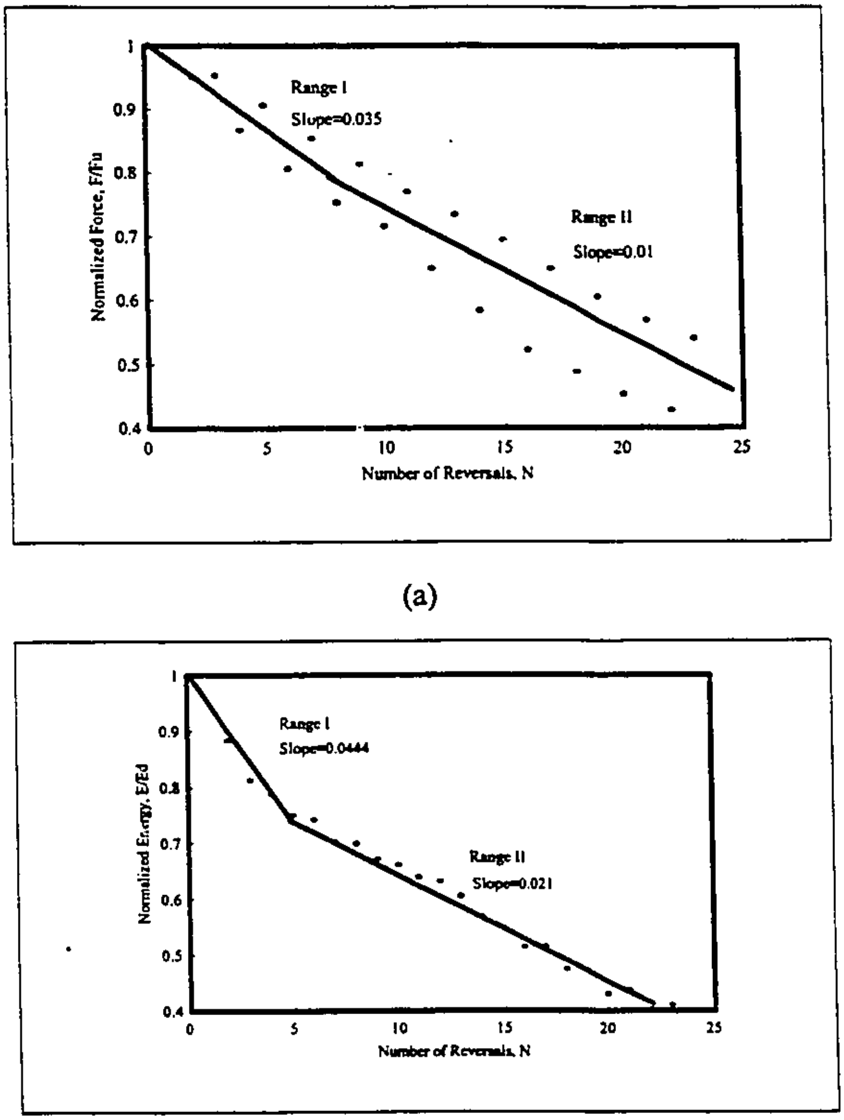

(a)

(b)

Fig. 4.15 Specimen SFS3 Deterioration in :
(a) Strength; (b) Dissipated Energy

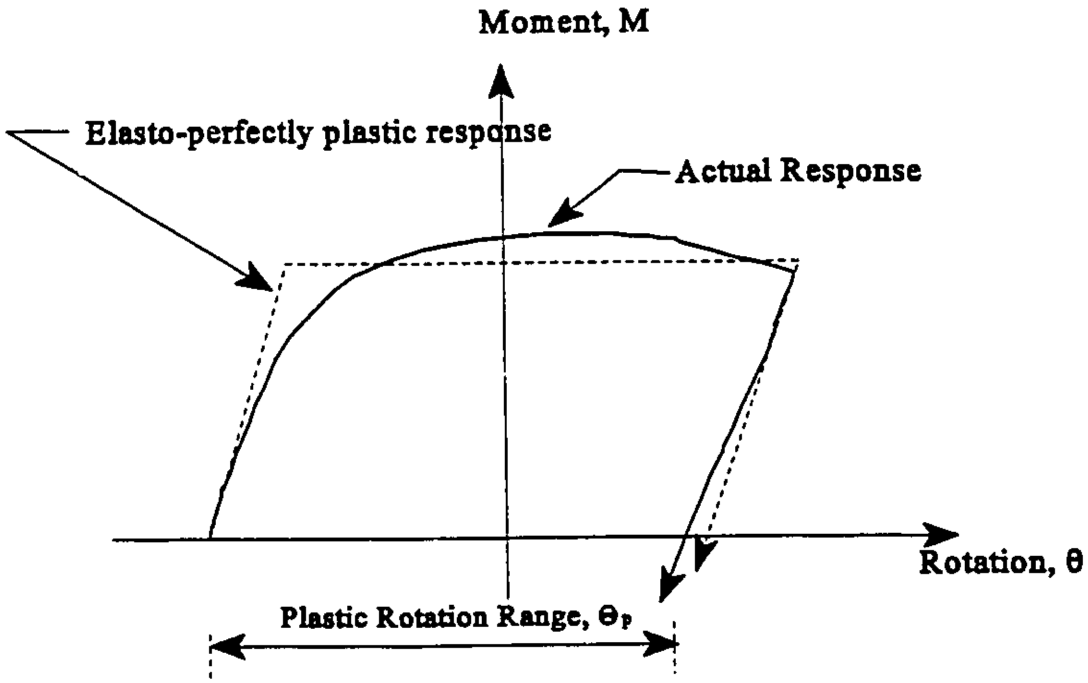

Fig. 4.16 Definition of plastic rotation range

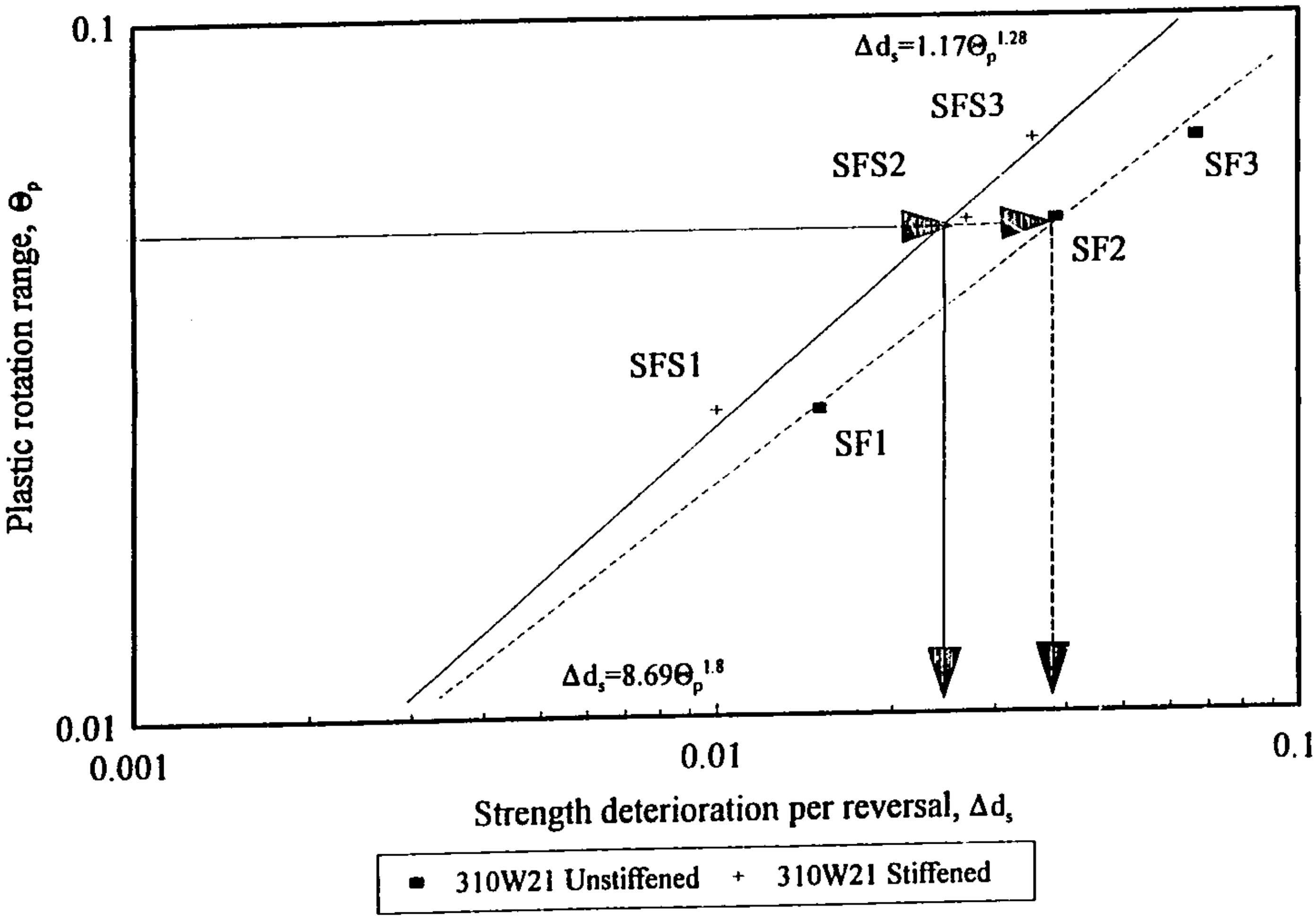

Fig. 4.17 Strength deterioration per reversal for series SF and SFS

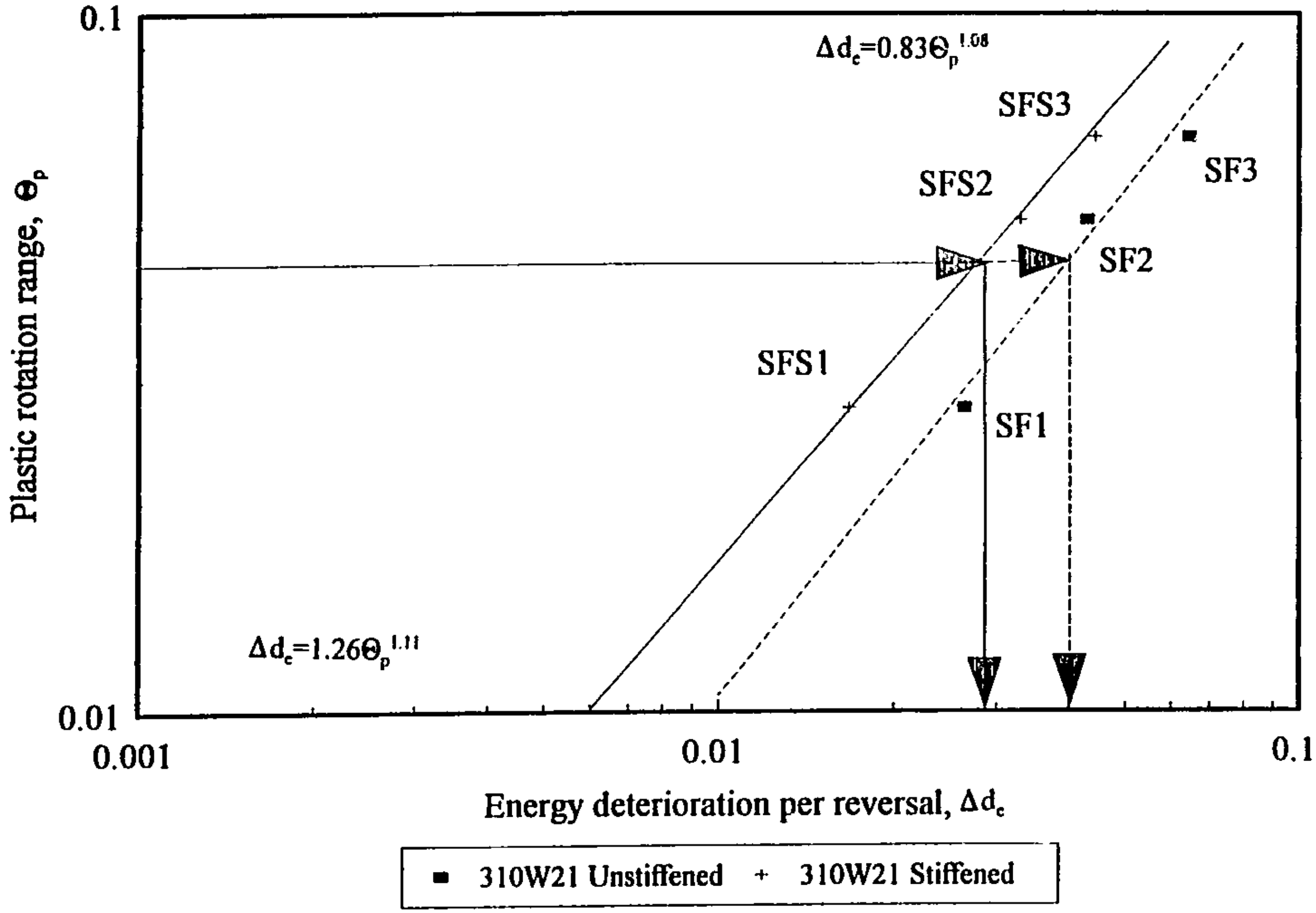

Fig. 4.18 Energy Deterioration per Reversal for Series SF and SFS

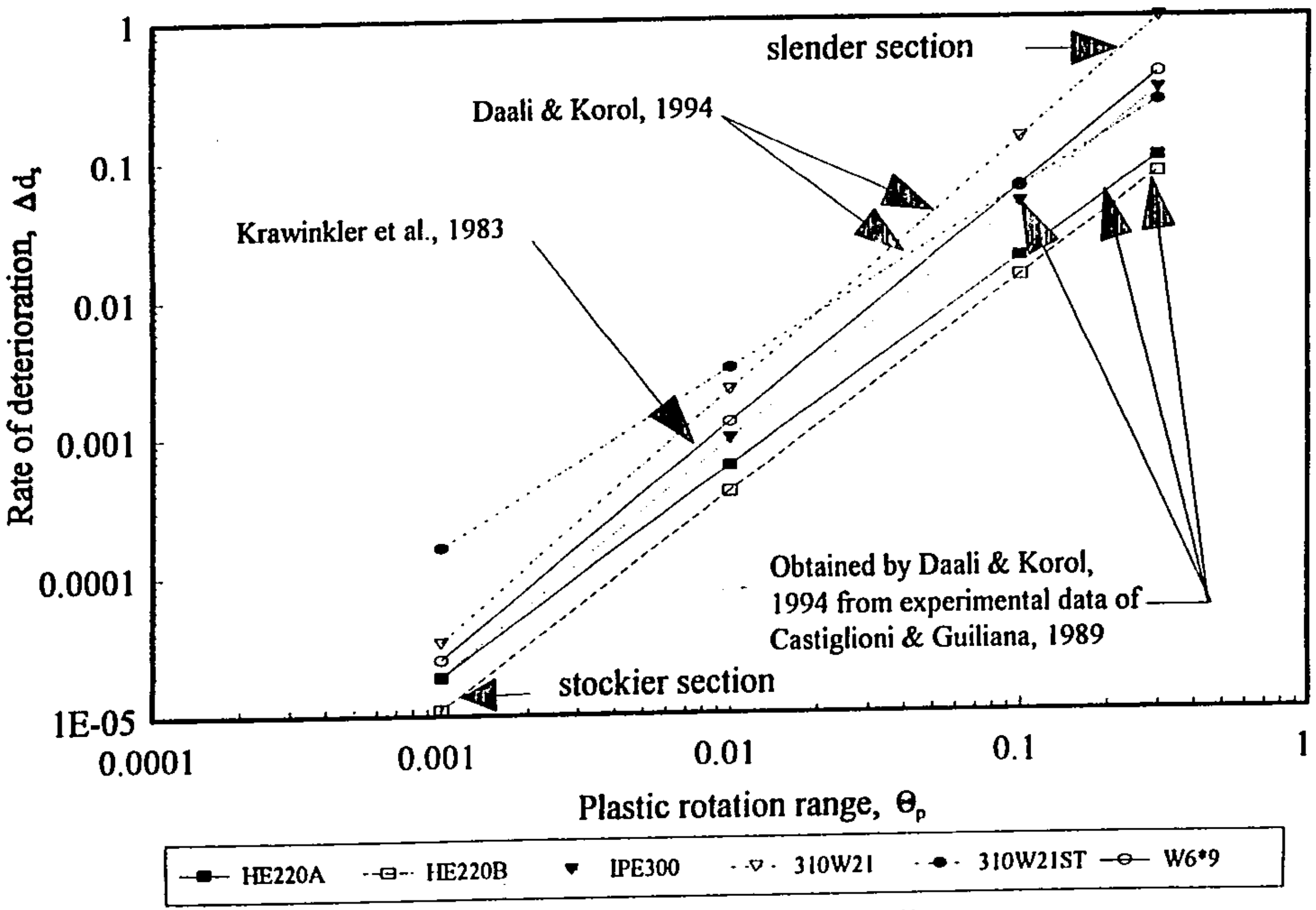

Fig. 4.19 Strength deterioration models in the literature

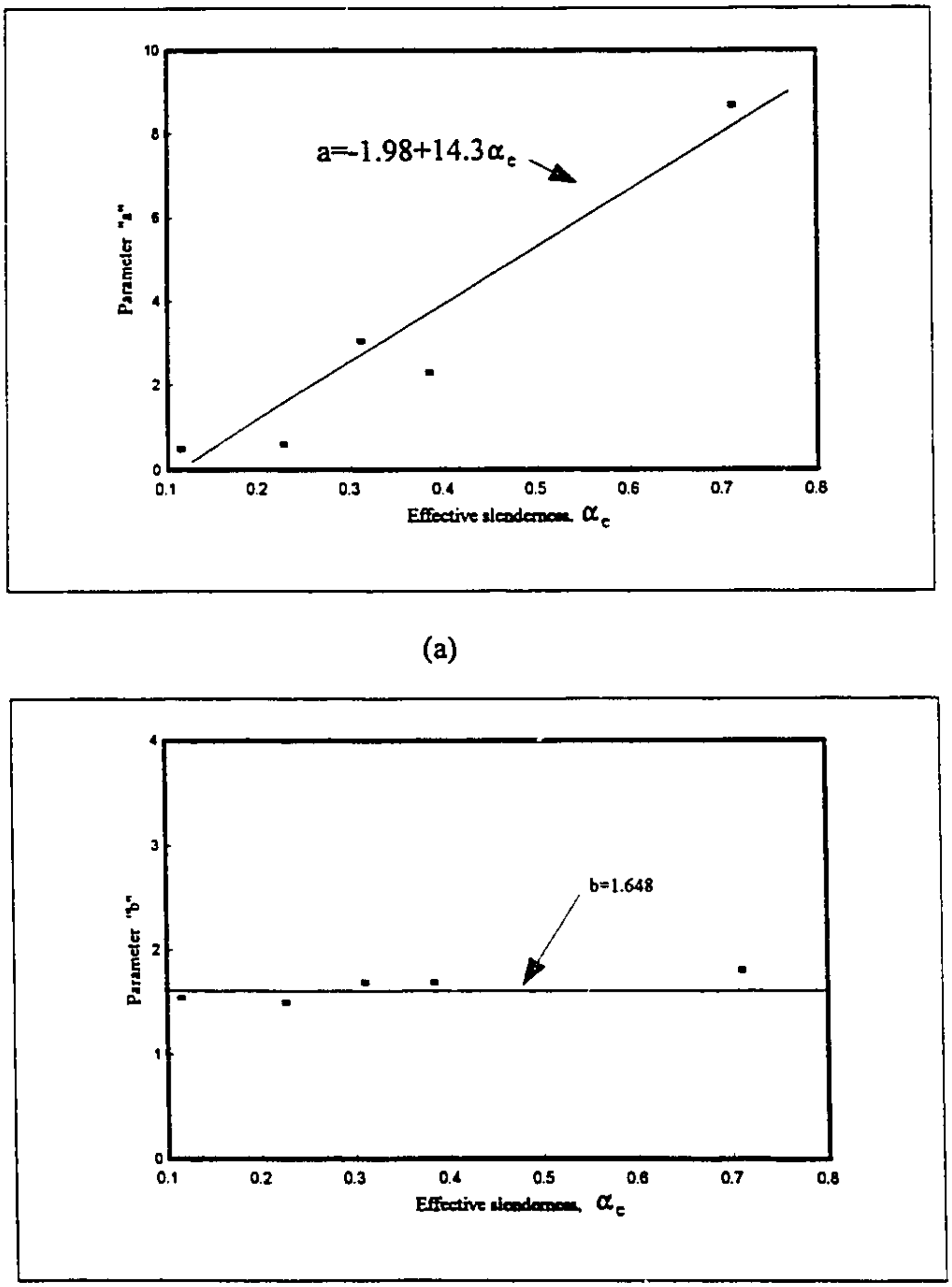

(a)

(b)

Fig. 4.20 Effective slenderness, α_e , vs parameters "a" and "b"

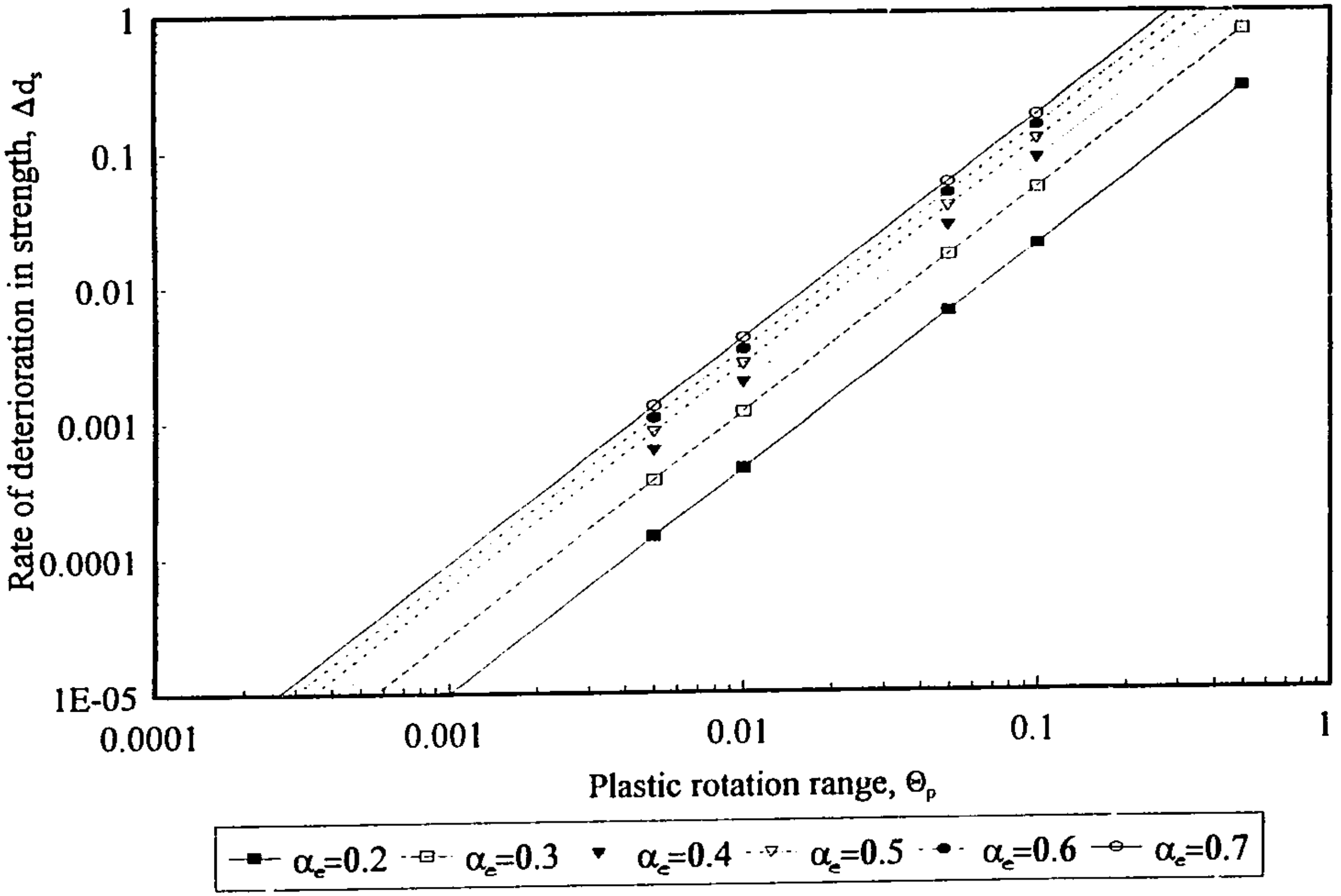

Fig. 4.21 Model for prediction of strength deterioration

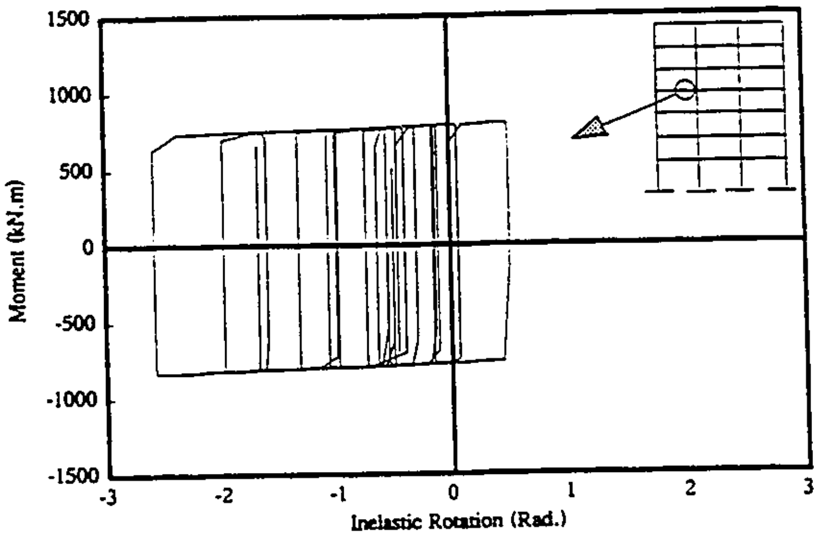

(a) Moment- Inelastic Rotation Response in a beam end

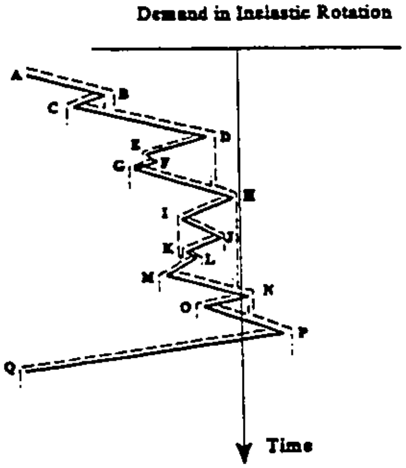

(b) Deformation History

Fig. 4.22 Strong motion response of a beam in a seven storey building

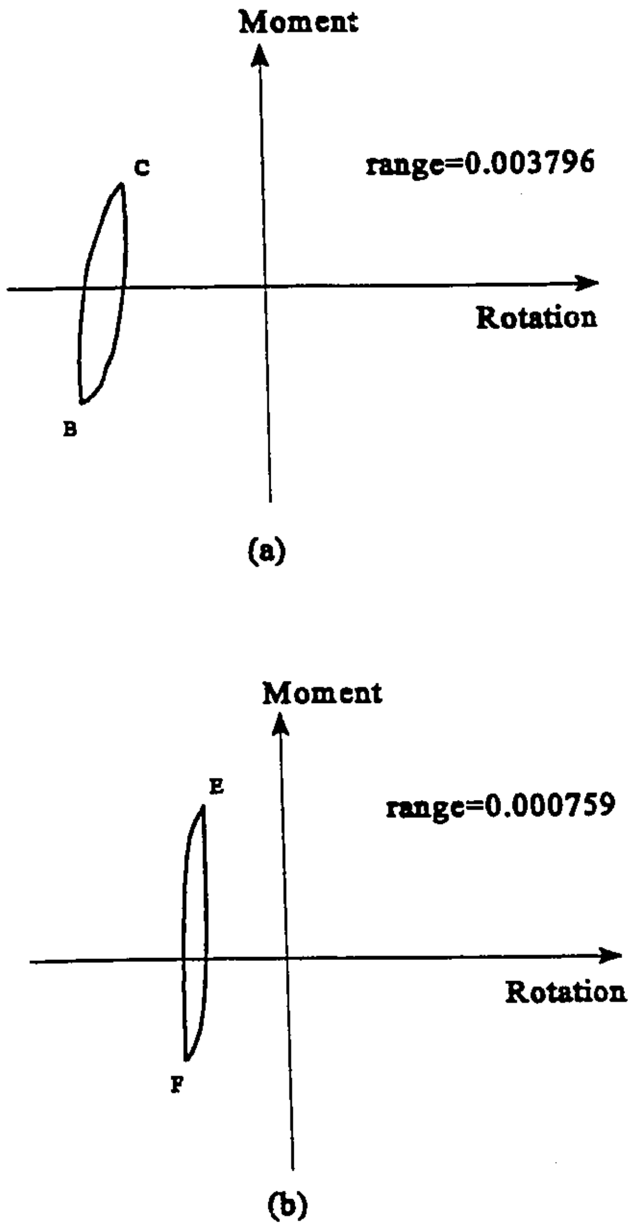

Fig. 4.23 Identification of closed loops:
(a) Range B-C; (b) Range F-E

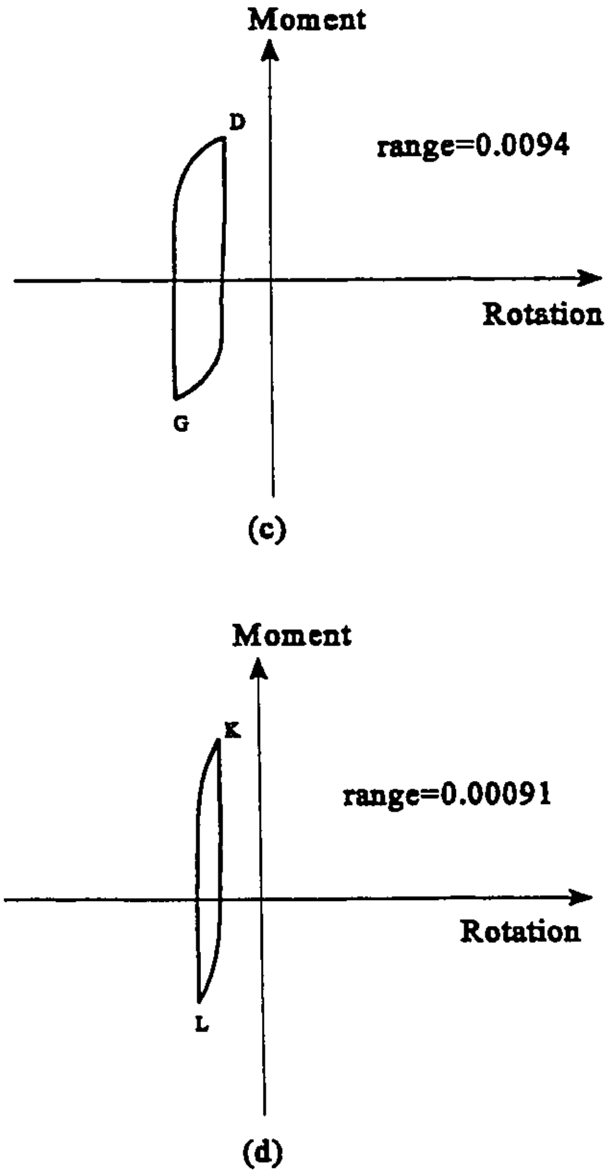

Fig. 4.23 Identification of closed loops:
(c) Range D-G; (d) Range K-L

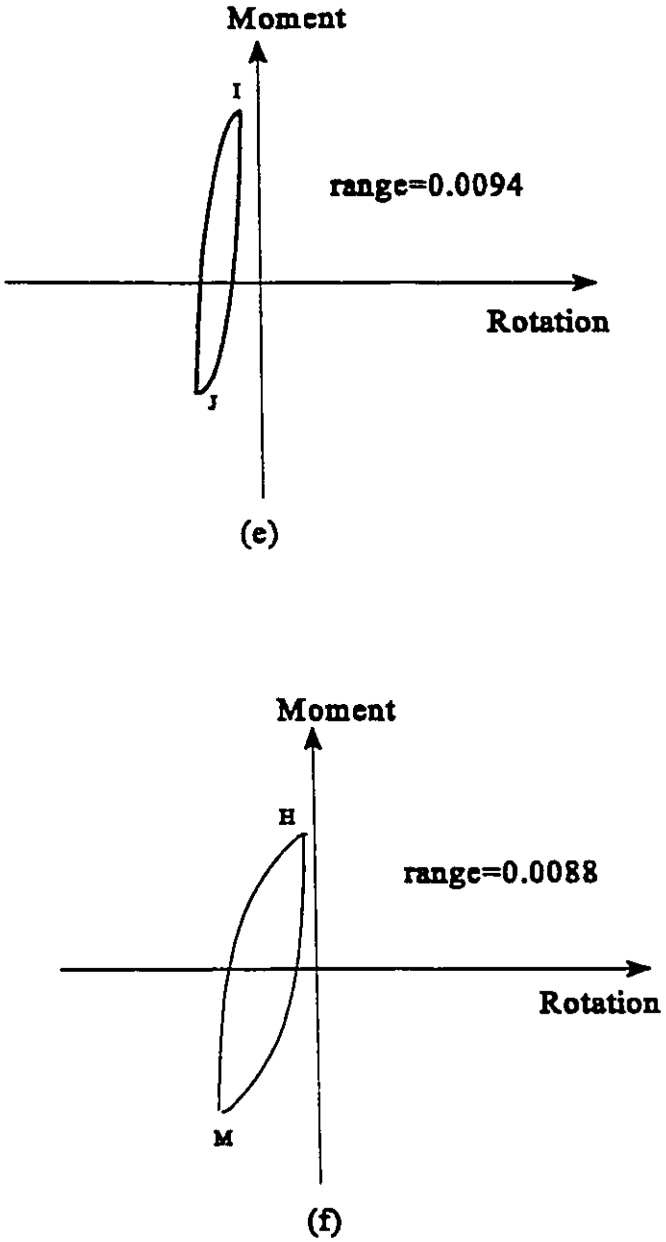

Fig. 4.23 Identification of closed loops:
(e) Range I-J; (f) Range H-M

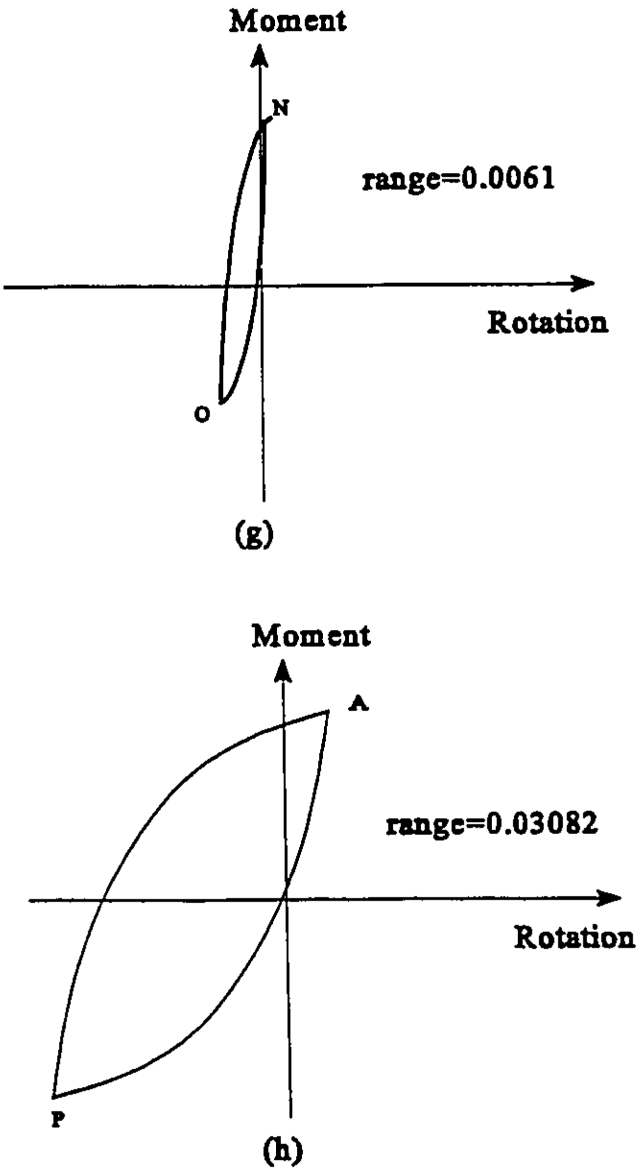

Fig. 4.23 Identification of closed loops:
(g) Range N-O; (h) Range A-P

CHAPTER 5

DAMAGE MODELS FOR STEEL BEAMS SUBJECTED TO EARTHQUAKE TYPE OF LOADING

5.1 Introduction

Under severe ground motion, elements of a ductile structure may sustain a high number of inelastic excursions. The members might, subsequently, be subjected to repeated alternating bending or high inelastic tensile and compressive forces and sometimes a combination of the two. Column or beam plate elements are therefore not only subjected to inelastic reversals of loading but continuous geometrical changes that are locally important and which lead to local or lateral torsional buckling. Indeed, the interaction of plastic deformations and local or global destabilizing effects is probable under certain circumstances. For example, if sufficiently large, inelastic excursions can cause significant damage in the form of low cycle fatigue magnified by local buckling or cracking. Under such conditions, the capacity in energy dissipation of the elements designed or selected on the basis of maximum displacement only will be smaller than required. Thus a possibility of failure due to low-cycle fatigue and excessive displacements can become a higher probability than is deemed acceptable.

The purpose of this Chapter is first to review some simple and more advanced mathematical models for damage assessment, and then to advance two different approaches for the prediction of damage assessment in steel beams when repeated loads together with low cycle fatigue effects are taken into account. The first approach is based on a linear combination of maximum response and low-cycle fatigue; the second one is based on Park and Ang's model (1985), described in the next section. Finally, using a simple criterion, the two approaches are used in Chapter 6 to yield deterministic values of the available adequate ductility that should be used for beams subjected to earthquake type loading.

5.2 Damage models in the literature

Within the context of earthquake design, the philosophy is to accept some repairable local damage but prevent the collapse of the structure as a whole, when subjected to moderate and strong motion earthquakes of low probability of occurrence. Large inelastic excursions frequently lead to a considerable amount of damage in structural members. This, therefore, demands a detailed consideration of the potential damage and remediation in beams, columns, beam-to column connections and in bracing members and their corresponding connections.

Low cycle fatigue damage due to either cracking or local buckling has been for some time of academic interest only. The Northridge earthquake with a 6.8 Richter intensity proved to the contrary that low cycle fatigue damage is indeed a problem that researchers should deal with in practice. After an initial period where only a handful of structural damage assessments had been reported, over sixty steel moment resisting frames built in the mid to late 1980s were later found to be seriously damaged (Degenkolb, 1994). A good example of damage due to earthquakes may also be found in the work of Nonaka and Iwai (see Wierzbicki and Jones 1989).

So far, design codes rely solely on implicit design requirements to control the level of damage in steel members, in particular, and steel structures in general. These design requirements are, however, insufficient or inadequate when addressing the above-mentioned problem. This is further complicated by the fact that the prediction of damage is a matter that requires ample knowledge and qualification in the usage of nonlinear dynamic analysis programs, mathematical damage models and some basic knowledge in the selection of earthquake records or spectra.

Damage in a structural member or the structure as a whole has usually been predicted in terms of ductility demand parameters that may depend on displacement, rotation, stiffness or even dissipated energy limits, and, sometimes a combination of the above. While some are applicable to a section level, others are used at the element level and others still are used at the overall structural level. For instance, curvature ductility, defined as the ratio of maximum ductility to ductility at yield, is always used at the section level. At the element level, the most commonly used damage indicator is either the rotation ductility or displacement ductility. Numerous other damage indicators may be found in the literature; some are expressed in terms of the ratio of initial to reduced secant stiffness, while others are in terms of ratio of demand to capacity in dissipated energy or in the form of cumulative damage theory. Fig. 5.1 illustrates some of these damage indicators. The subject of damage indicators may be found in numerous papers such as in Banon et al. (1982), Powell and

Allahabadi (1988), Chung et al. (1987) and Meskouris and Kratzig (1990).

Before attributing any limitations to the above-mentioned damage indicators, let us first reiterate that maximum response by itself is not sufficient in assessing damage in a structure. The duration of a strong motion event is the other parameter that should be addressed in the form of number of excursions or perhaps more importantly, the dissipated energy. The reason for the latter proposition is that under severe earthquake loadings, structural elements undergo large inelastic displacements accompanied by a substantial number of smaller inelastic excursions. Based on the experimental investigations discussed in Chapter 4, we have seen that damage in a member is a cumulative process. With every excursion (or amplitude of loading), the member will suffer and show strength or energy deterioration in its exhibited behaviour. Thus any damage model should reflect the maximum response as well as the repeated inelastic effects which appear in the form of low-cycle fatigue symptoms.

Most of the damage indicators mentioned above are deficient in one way or another. The class of ductility damage indicators lies on the unconservative side because, simply put, the repeated cyclic effects are not accounted for. Meanwhile, the class of normalized dissipated energy damage indicators is overly conservative because cummulative damage due to numerous small amplitude deformations is attributed the same importance as damage under one large amplitude deformation (Powell and Allahabadi, 1988).

Though simple to use, these damage indicators are however insufficient or inadequate because of the reasons highlighted above. Consequently, a number of advanced mathematical models for damage assessment have recently been proposed in the literature. Some involve a combination of normalized maximum displacements and normalized dissipated energy (Banon and Veneziano, 1982, Park and Ang, 1985); still others are based on cumulative damage theory in the form of low-cycle fatigue relationships (Krawinkler and Zohrei, 1983, and Daali and Korol, 1994). In the following, we shall discuss some of the more advanced damage models.

Banon and Veneziano (1982) developed a damage indicator, for reinforced concrete members, which makes use of the effects of maximum displacement and dissipated energy. Their damage asssessment model is given by:

$$D=\sqrt{(D_1^*)^2+(D_2^*)^2} \quad \text{, where} \quad D_1^*=\frac{K}{K_r}-1 \quad , \quad D_2^*=1.1\left(\frac{E_h}{\frac{1}{2}M_y\theta_y}\right)^{0.38} \quad ,$$

where K is the initial stiffness, K_r the reduced secant stiffness, E_h the dissipated energy, while M_y and θ_y are the yield moment and associated rotation, respectively. A criticism attributed to this model was that it was calibrated by few experimental data (Cosenza, 1990).

Meanwhile, Krawinkler and Zohrei (1983) conducted experimental tests on cantilever beams cyclically loaded and proposed an experimental low-cycle fatigue damage accumulation model for steel components of the Coffin-Manson type:

$D=a\sum(\Theta_p)^b$,

where Θ_p is the residual plastic deformation and "a" and "b" are parameters that were defined in Chapter 4 and reflect the properties of the tested sections.

Park and Ang (1985) took Banon and Veneziano's (1982) work a step further by developing a damage index for reinforced concrete members and defined it as a linear combination of the normalized maximum deformation and the normalized dissipated energy.

Some of the criticisms attributed to most of these damage models are that their value range is not normalized; for instance, a displacement ductility ($\mu=\Delta/\Delta_p$) or a stiffness ratio ($\mu=K_E/K_S$) as shown in Fig. 5.1 would still not give sufficient insight into how the member or the structure is damaged. Furthermore, their inability to give a zero value of damage at the yield state results in an ambiguous interpretation of their predicted damage values.

5.3 Models for damage assessment in steel beams

Damage models that account for maximum deformation and repeated load or low-cycle fatigue effects have been applied recently by a number of researchers to practical applications. For instance, McCabe and Hall (1989) and Cosenza et al. (1990) used such damage models in the construction of modified spectra that reflect inelastic behaviour. Meanwhile, Fajfar and Fischinger (1990) and Fajfar (1992) furthered this concept to develop modified spectra and equivalent global system ductilities that account for cumulative damage effects in the form of low-cycle fatigue.

Of course, it is preferable to limit the number of parameters that can be used to assess damage in a member or a structure to only those deemed important. Moreover, the damage parameters that should be used must be those response quantities that are easy to obtain or directly obtainable from results of a structural dynamic nonlinear analysis. Furthermore, before formulating any new damage model, the term "failure" must be clearly defined and understood. By now, we know that in ductile steel structures strength and ductility are two very important characteristics that permit structures to resist and redistribute forces in the course of an earthquake event. It is, therefore, logical only to define failure of a Class 1 section at the point where it is no longer able to reach its plastic strength (Fig. 5.2). At this stage, damage in the member is associated with a damage index value ranging from zero to one. In this case, zero would mean no damage has occurred in the member, i.e., member has been loaded elastically or slightly beyond (without suffering any form of deterioration). A value of unity would mean that the member is fully damaged and can no longer sustain the plastic limit force.

In the following two approaches, we shall show how the combination of maximum response and cyclic load effects can be used to derive damage assessment models for steel beams under earthquake types of loading.

5.3.1 First approach:

It seems clear that any damage model should, as a minimum, combine the maximum response with repeated cyclic load effects. As such, the simplest damage model that seemingly can be used is of the form $D=D1+\beta\ D2$ where $D1$ is the damage under maximum response, β is a calibration factor and $D2$ is the damage under low-cycle fatigue effects. For damage due to maximum response, one can use a linear relationship of the form:

$$D1=\left(\frac{\mu-1}{\mu_{mono}-1}\right)\ngtr 1.0 \qquad \textbf{(5.1)}$$

where μ is the amount of ductility (Δ/Δ_p) having a maximum experienced value μ_{max} as shown in Fig. 5.3, and μ_{mono} is the maximum ductility under monotonic loading. Note that under monotonic loading, this model gives the value of zero damage at yield ductility and 1 at a ductility value equal to the monotonic limit, μ_{mono}.

To account for low-cycle fatigue effects, a series of experiments on full size steel members was undertaken, and described in Chapter 4, to assess and model the rates of deterioration in dissipated energy per reversal of loading. For the specimens under consideration, a least squares analysis of the differences of the test and predicted results gives, as illustrated in Fig. 5.4, a relationship between the rate of deterioration in dissipated energy, Δd_e, and the displacement capacity values, (μ_i-1) as follows:

$\Delta d_e = 0.0064(\mu_i-1)^{1.11}$ for energy deterioration per reversal in range I (Fig. 4.10 to 4.15)

If Miner's (1945) rule of linear damage accumulation is used, then for variable amplitude tests the cumulated damage, D2, after N reversals of different ductility magnitudes is given by

$$D2=a\,\Sigma(\mu_i-1)^{1.11} \qquad \textbf{(5.2)}$$

where μ_i is the ductility measured from the zero load intercept and experienced during the ith reversal as shown in Fig. 5.3. To determine the value of "a", the monotonic loading case is considered with unloading halted at $F=F_p$ followed by one reversal of loading only. Here, the damage maximum value is unity, and hence the relationship is given by:

$1=a(\mu_{mono}-1)^{1.11}$, thus $a=(\mu_{mono}-1)^{-1.11}$

where μ_{mono} is the maximum monotonic ductility at which the member is still maintaining its plastic resistance.

Substituting parameter "a" into Eqn. 5.2 yields the following for N reversals:

$$D2=\Sigma\left(\frac{\mu_i-1}{\mu_{mono}-1}\right)^{1.11} \tag{5.3}$$

Eqn. 5.3 yields the value zero at μ_i=1, i.e., no damage is presumed to result provided that the maximum displacement equals but does not exceed the yield displacement. This means that the initiation of damage has not started so long as the member is not strained inelastically. A linear combination of the damage index of the maximum deformation (Eqn. 5.1), with that of the low-cycle fatigue expression (Eqn. 5.3), gives the damage model shown in Fig. 5.5 and is expressed as:

$$D=\left(\frac{\mu_{max}-1}{\mu_{mono}-1}\right)+\beta_1\Sigma\left(\frac{\mu_i-1}{\mu_{mono}-1}\right)^{1.11} \tag{5.4}$$

where D is a Damage Index, β_1 is a calibration factor and μ_{max} is the maximum ductility. As noted in Fig. 5.3 it is less than the maximum monotonic ductility μ_{mono}. Note that, unlike the mathematical models proposed by the afore-mentioned researchers, the proposed model of Eqn. 5.4 gives the expected value of zero at a ductility equal to the yield ductility, while at failure, the value of damage index is assumed to just reach unity, the limiting value. Fig. 5.5 is a graphical representation of the two components.

5.3.2 Second approach:

For this approach, Park and Ang's (1985) damage model is considered; the expression for damage is given by:

$$D=\frac{\mu_{max}}{\mu_{mono}}+\frac{\beta_2}{F_p\delta_p\mu_{mono}}\int dE \tag{5.5}$$

where D is a Damage Index, F_p is the plastic limit load, dE is the increment of dissipated energy and β_2 is perhaps a different calibration factor from β_1 that can be expressed in terms of section and member characteristics. Clearly expression 5.5 is potentially desirable because experimental results are often given in terms of hysteresis loops exhibiting the behavior of the specimens. It is however tedious to integrate the area under the curves in order to obtain the total dissipated energy.

The aim of this section is to try to simplify Park and Ang's (1985) damage model to yield a simpler expression. As such, let the sum of the normalized energy under every reversal of loading defined by the ratio of the total dissipated energy to the elastic energy be given by :

$$\Sigma e_e=\frac{\int dE}{(\frac{1}{2})F_p\delta_p}$$

which simplifies Eqn. (5.5) to

$$D=\frac{\mu_{max}}{\mu_{mono}}+\beta_2\frac{\Sigma e_e}{2\mu_{mono}} \tag{5.6}$$

To be of value in practice, it is particularly desirable to replace the numerator of the second term in Eqn. 5.6 by a factor based on cyclic test results. Although focussing on the effects of local buckling of beam plate elements, tests done by Popov (1970) on Class 1 members subject to cyclic loading showed that a linear relationship exists between the normalized energy, e_e, and π_d, the latter defined as the ratio of the residual plastic deformation to the plastic deformation. With increasing beam tip deflection (or residual plastic deformation), it was shown that the dissipated energy per reversal of loading increases in a linear fashion. The relationship found is given by $e_c=1.77\ \pi_d$. In 1973 Popov performed more tests, this time suggesting $e_c=2.1\ \pi_d$. Recently, Korol and Daali (1994) performed twelve tests on specimens under cyclic loading and confirmed this latter result. From the above, it seems that the relationship between the normalized energy, e_c, and the plasticity ratio, π_d, is largely independent of section characteristics and load history. Irrespective of the section characteristics and the nature of the load history, one can therefore suggest for simplicity that the normalized energy be related to the plasticity ratio by $e_c=2.0\ \pi_d$.

So long as initiation of instability is not significant, one can show that the linear relationship existing between the normalized energy, e_c, and the plasticity ratio, π_d, is also applicable to the cumulated energy, $\sum e_c$, and the cumulated plasticity ratio, $\sum \pi_d$. This suggests that at any time during the loading history, the cumulated normalized energy is linearly related to the cumulated plasticity ratio. This was confirmed from the experiments reported in Chapter 3. For example the cumulated normalized energy and the cumulated plasticity ratio values of specimen B3 throughout its load history is shown in Fig. 5.6. Note that a linear relationship was found between the two parameters, with the constant =2.0 providing very good correlation. Experimental results of tests by Popov and Pinkney (1969) and Popov and Bertero (1973) (Figs. 5.7 and 5.8) have also shown that the cumulated energy is approximately related to the cumulated plasticity ratio by:

$$\sum e_c=2\ \sum \pi_d \tag{5.7}$$

Now, recall that a member's ductility demand at a point in time is defined as $\mu_i=(\Delta_i/\Delta_p)$ where δ_i is the deflection at some characteristic location such as a load point or joint at the ith reversal. At the point where the member resistance drops below its plastic resistance (Fig. 5.2), the ultimate deformation at failure equals the sum of the residual plastic deformation, Δ_{rp}, and the plastic deformation, Δ_p, as:

$$\Delta_i=\Delta_{rp}+\Delta_p$$

Substituting the ultimate deformation in the ductility expression gives the following:

$$\mu_i=\frac{\Delta_{rp}}{\Delta_p}+1=\pi_d+1 \tag{5.8}$$

Combining Eqns. 5.7, 5.8 and 5.6, gives:

$$D=\frac{\mu_{max}}{\mu_{mono}}+\beta_2\frac{\Sigma(\mu_i-1)}{\mu_{mono}} \tag{5.9}$$

where the term $\Sigma(\mu_i-1)$ may be interpreted as the cumulated positive and negative residual plastic deformation the member has undergone. An example of the elasto-plastic type response for four load reversals is given in Fig. 5.9.

5.3.3 Determination of the monotonic ductility μ_{mono}:

For the purpose of predicting monotonic ductility, an empirical expression of the rotation capacity at ultimate, R_u, developed in Chapter 2 is used. The expression is repeated here for sake of completeness and is given by:

$$R_u=-9.2\alpha_e+10.71\alpha_e^{-.293} \tag{5.10}$$

where α_e is the effective slenderness of the member defined by Eqn. (2. 10)

The ductility under monotonic loading may therefore be expressed by:

$$\mu_{mono}=R_u+1=1-9.2\alpha_e+10.71\alpha_e^{-.293}$$

5.3.4 Determination of the calibration parameter:

For the purpose of determining the calibration factor, either β_1 or β_2, one can use the definition of failure advanced earlier requiring the damage index, D be equal to unity. Using the damage models of Eqns. 5.4 and 5.9 along with Eqn. 5.10, values of the calibration factor can be obtained. For this purpose, cyclic loading data from the results of four tests by Korol and Daali (1994), three tests by Korol et al. (1990) and eleven tests by Castiglioni and Di Palma (1989) were used. Observations from the experiments done by Daali and Korol (1994) and others suggest that damage in beams depends not only on the flange slenderness, but on the web slenderness and the lateral slenderness as well. However because of the limited number of experiments used for this study, it was only possible to identify a clear trend between the flange slenderness and the calibration factor. Therefore, it was decided to relate the calibration factor to flange slenderness only. The least squares method was used to obtain expressions that fit the experimentally obtained values of the calibration factors, while the following expressions with coefficients of variation of 0.27 and 0.31 were obtained respectively for the two approaches:

$\beta_1=0.11(\alpha_f/8.37)^{1.6}$ for Daali and Korol's model **(5.11-a)**

$\beta_2=0.085(\alpha_f/8.37)^{2.26}$ for the approach based on Park and Ang's model **(5.11-b)**

Predicted values of the calibration factor using Eqns. 5.11 are plotted with experimental points and are shown in Fig. 5.10. It is noted that there is a considerable degree of scatter between the observed and predicted values of the calibration factors for both models. The reason is that there is not a very tight ensemble of data points found in the literature. Note that the determination of the calibration factors is only preliminary at this stage and that the mathematical form of this parameter can further be refined with use of more experimental data to include parameters such as web slenderness and lateral slenderness.

5.3.5 Discussion:

If use is made of Eqns. 5.4 and 5.9 along with Eqns. 5.10 and 5.11, one can assess the damage suffered by a member under a given load history. This concept was applied to generate values of damage for the specimens tested by Korol and Daali (1994), Korol et al. (1990) and Castiglioni and Di Palma (1989). It is noted, in the last columns of Table 5.1, that very good agreement is obtained for both approaches between the predicted Damage Index values and the expected Damage Index value of unity. On average, a coefficient of variation of 0.11 is obtained for both approaches. These findings will be shortly published in a paper by Daali and Korol (1995).

5.4 Summary

Damage assessment in structural elements can be modelled as a linear combination of maximum response and either repeated effects in the form of low-cycle fatigue or dissipated energy. Two completely different approaches for damage quantification have been presented in this Chapter. The first approach is based on experimental results of tests performed by the authors; the second approach is a modification of Park and Ang's damage assessment model. Though simple and deterministic in nature, the techniques have been shown to yield predicted damage values in good agreement with experimental data. Despite the randomness of any earthquake load event, results achieved with this methodology may be considered quite acceptable. It is therefore believed that the proposed damage models should prove very useful in non linear dynamic analyses. To follow in the next Chapter, is the application of the damage models developed in this Chapter and the concept of adequate ductility that is necessary in designing or retroffiting members subjected to earthquake type loading.

Table 5.1 Summary of predicted and observed values of damage.

Reference	Specimen #	α_f	α_m	α_l	monotonic ductility μ_{mon}	measured maximum ductility μ_{max}	predicted damage, D at failure	
							1st approach	2nd approach
Korol and Daali (1994)	P2	8.86	45.82	33.56	10.33	6.17	0.99	1.12
	A1	8.43	52.83	47.20	6.46	2.92	0.93	0.87
	A2	8.42	52.74	47.12	6.51	3.44	0.82	0.96
	B1	8.42	52.74	47.12	6.51	4.10	0.90	1.03
Korol et al. (1990)	A1	8.70	43.34	26.93	12.61	3.93	0.86	0.72
	A2	8.77	43.69	27.15	12.43	6.41	0.91	1.20
	A4	8.70	43.34	26.94	12.61	3.64	0.73	0.74
Castiglioni and Di Palma (1989)	HE220A 1	9.45	25.33	24.35	16.54	7.82	1.21	1.24
	HE220A 2	9.53	25.51	24.53	16.38	6.14	1.17	1.06
	HE220A 3	9.48	25.42	24.44	16.46	5.21	1.05	0.95
	HE220A 4	9.45	25.33	24.35	16.53	5.43	1.01	0.94
	HE220B 1	6.70	19.23	24.68	20.71	13.59	1.28	1.28
	HE220B 2	6.76	19.40	24.90	20.52	9.85	1.07	1.10
	IPE300 1	8.43	47.26	51.14	6.76	3.20	1.04	0.82
	IPE300 2	8.42	47.20	51.09	6.79	2.57	0.96	0.87
	IPE300 3	8.30	46.49	50.32	7.23	3.95	1.06	1.02
	IPE300 4	8.28	46.38	50.20	7.30	5.35	1.25	1.26
	IPE300 5	8.31	46.54	50.38	7.20	5.20	1.20	1.07

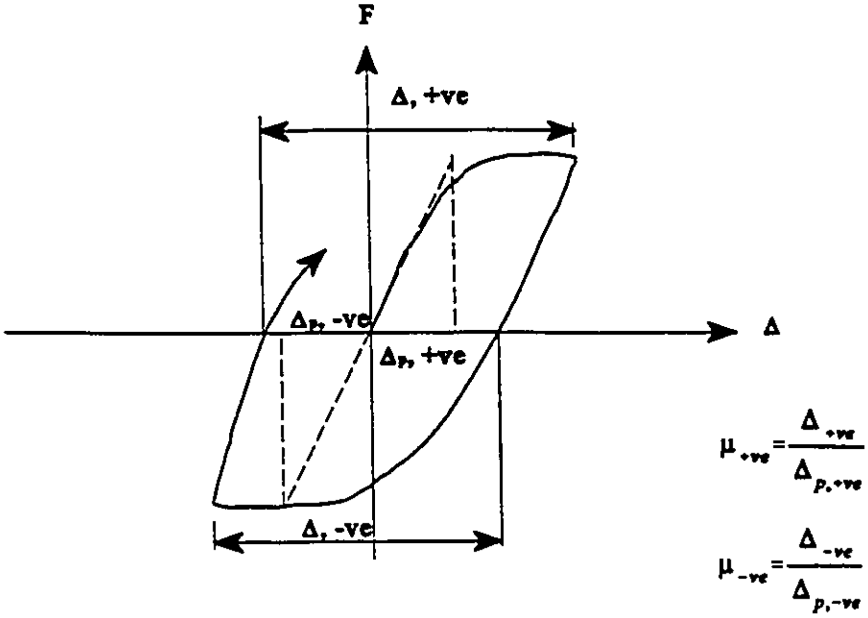

(a) Cyclic Ductility

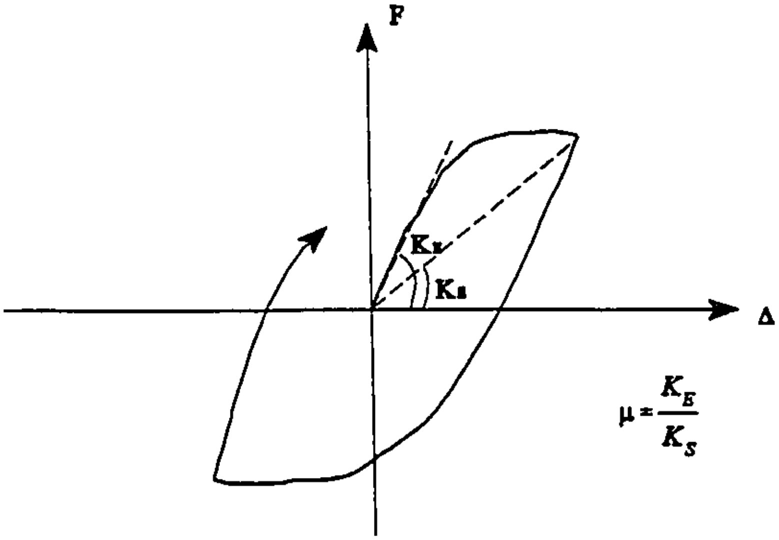

(b) Stiffness Ratio

Fig. 5.1 Examples of Damage Indicators

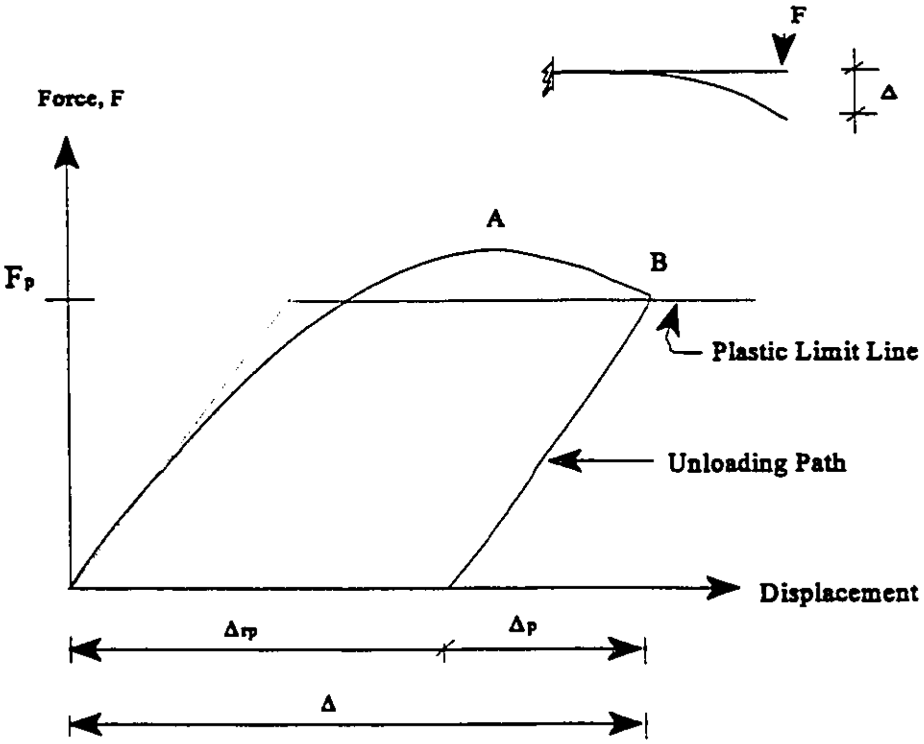

Fig. 5.2 Definition of residual plastic and yield displacements

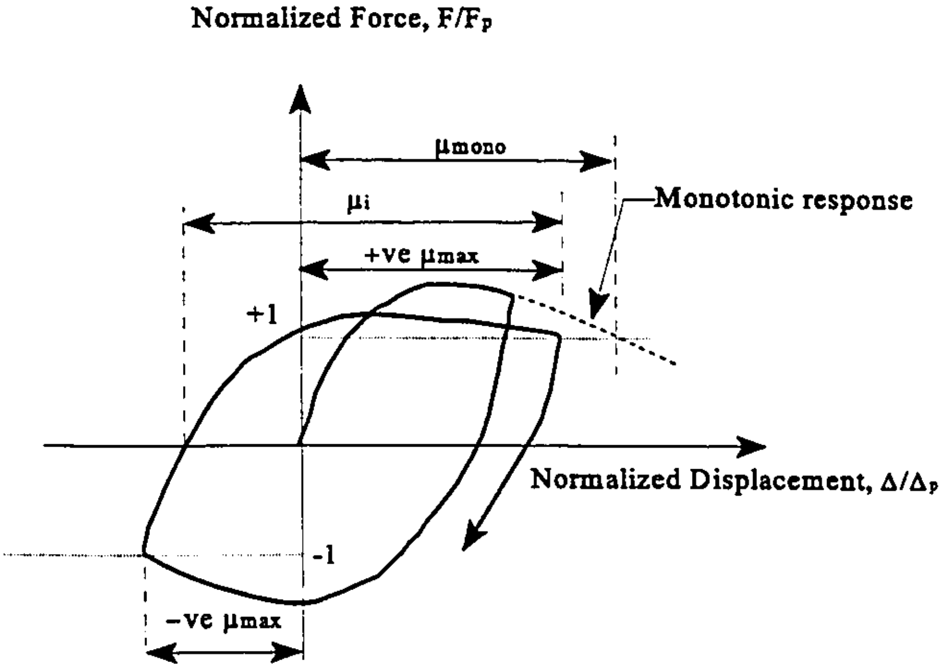

Fig. 5.3 Typical Hysteresis Loops

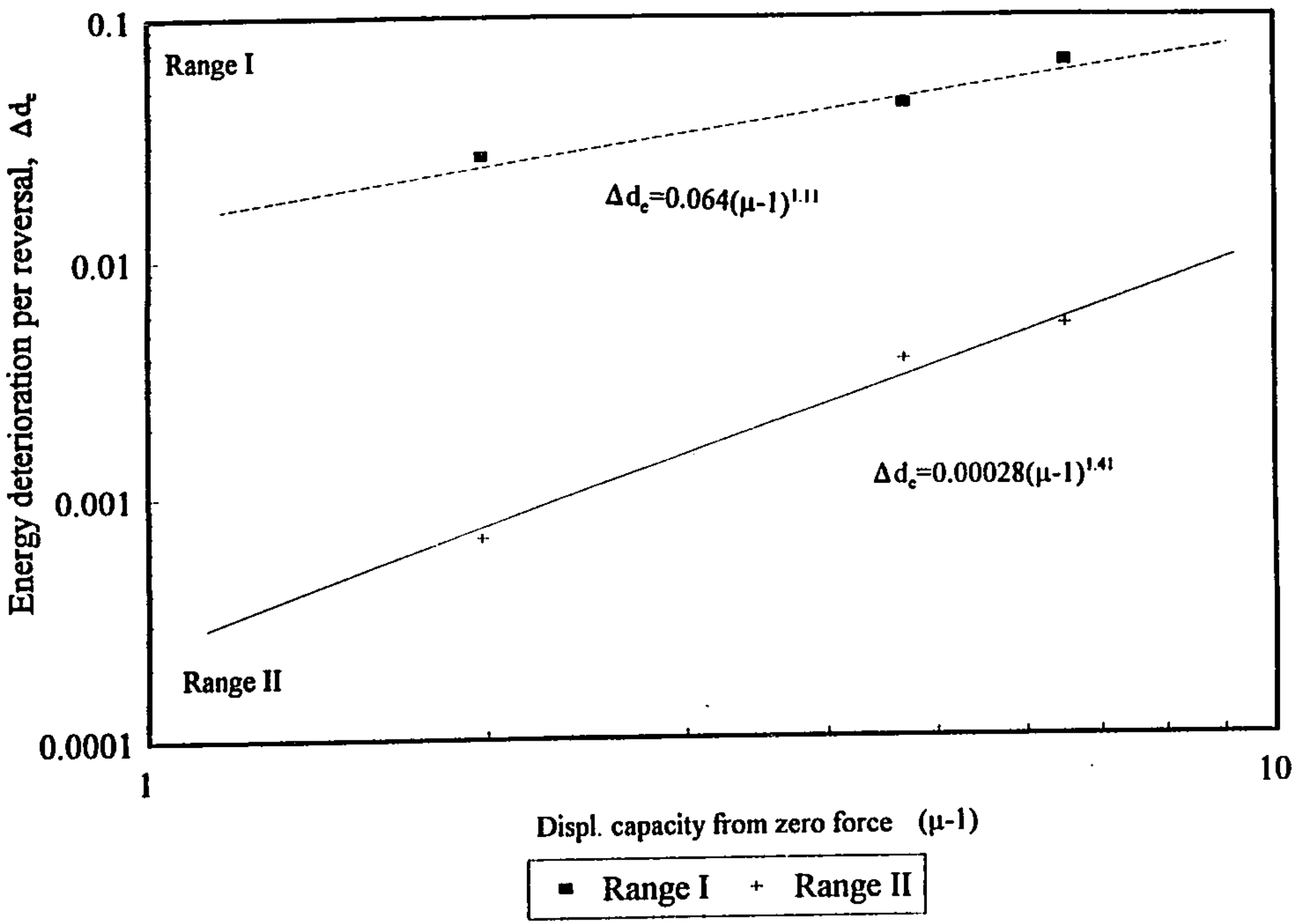

Fig. 5.4 Displacement capacity as a function of energy deterioration per reversal of loading

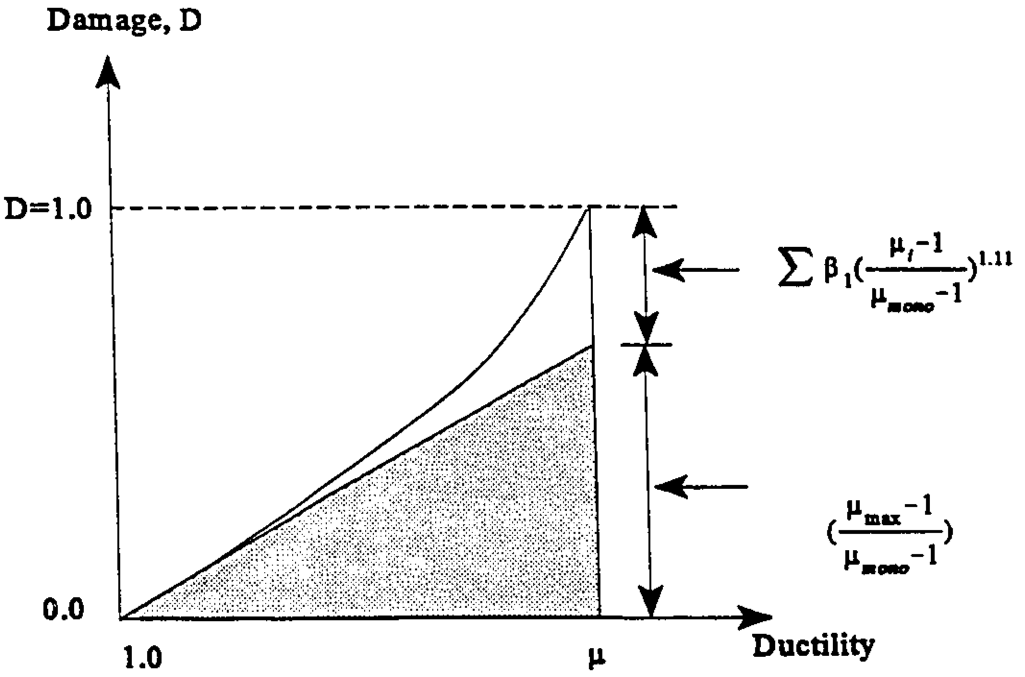

Fig. 5.5 Assumed damage model for a cyclic case

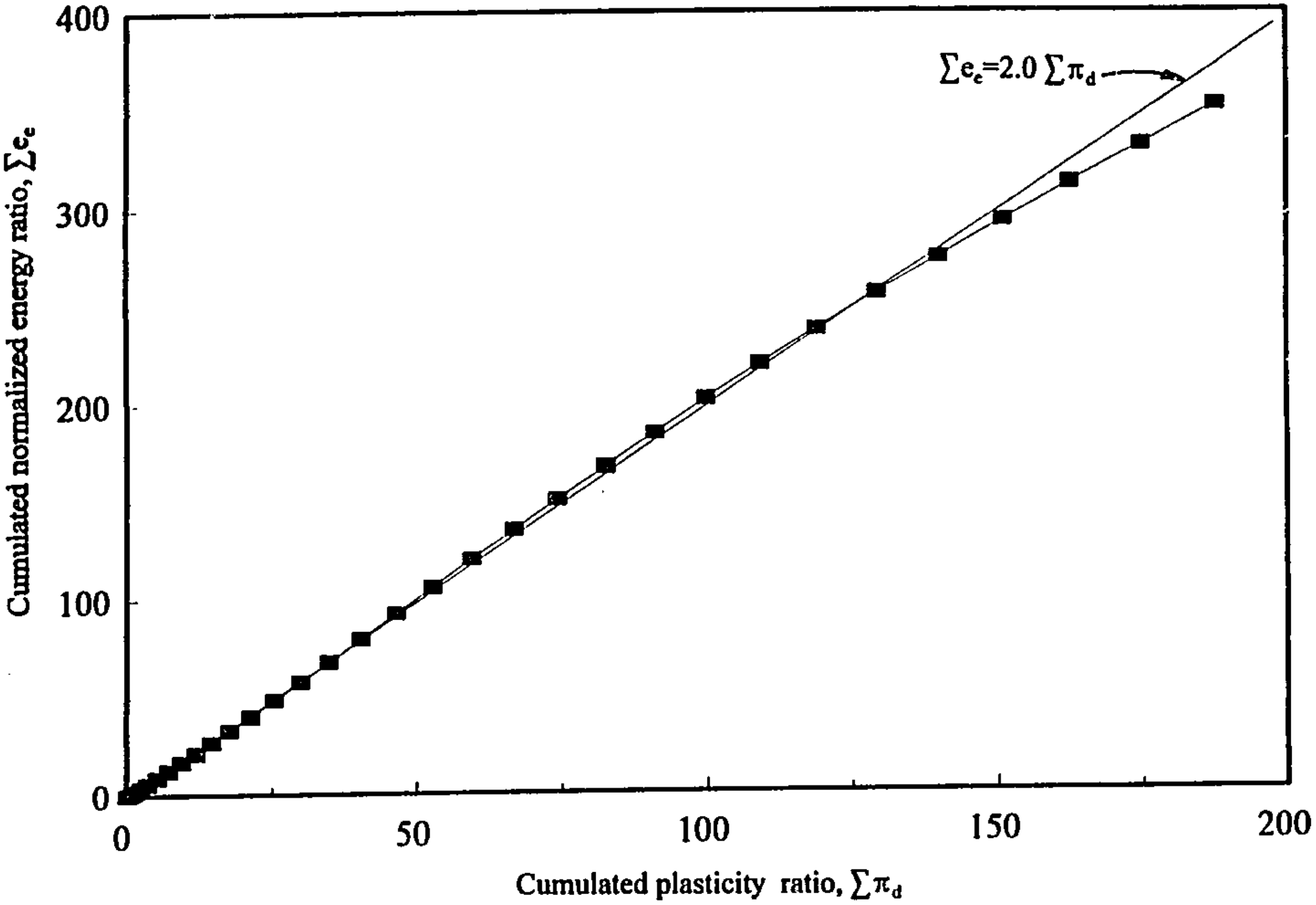

Fig. 5.6 Cumulated normalized energy vs cumulated plasticity ratio for specimen B3

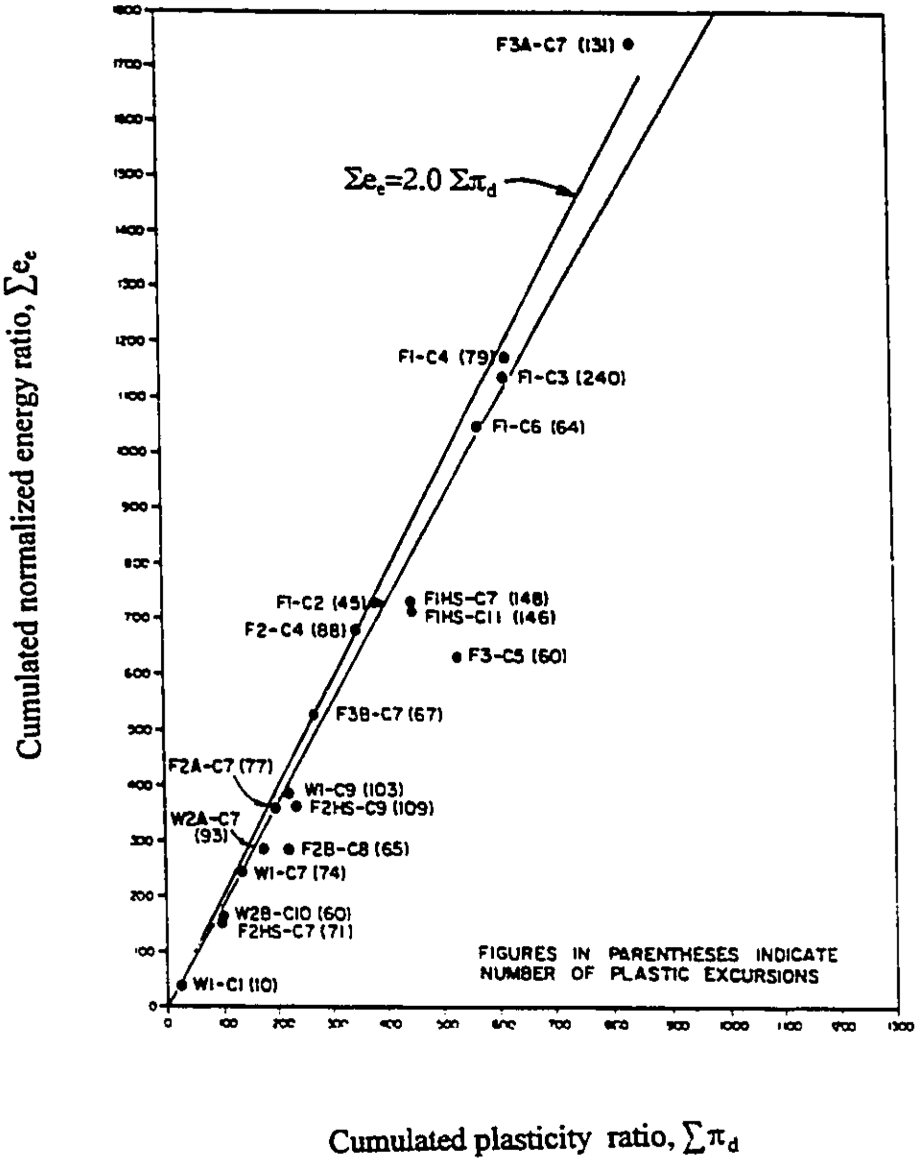

Fig. 5.7 Cumulated normalized energy vs cumulated plasticity ratio (Adapted from Popov and Pinkney 1969)

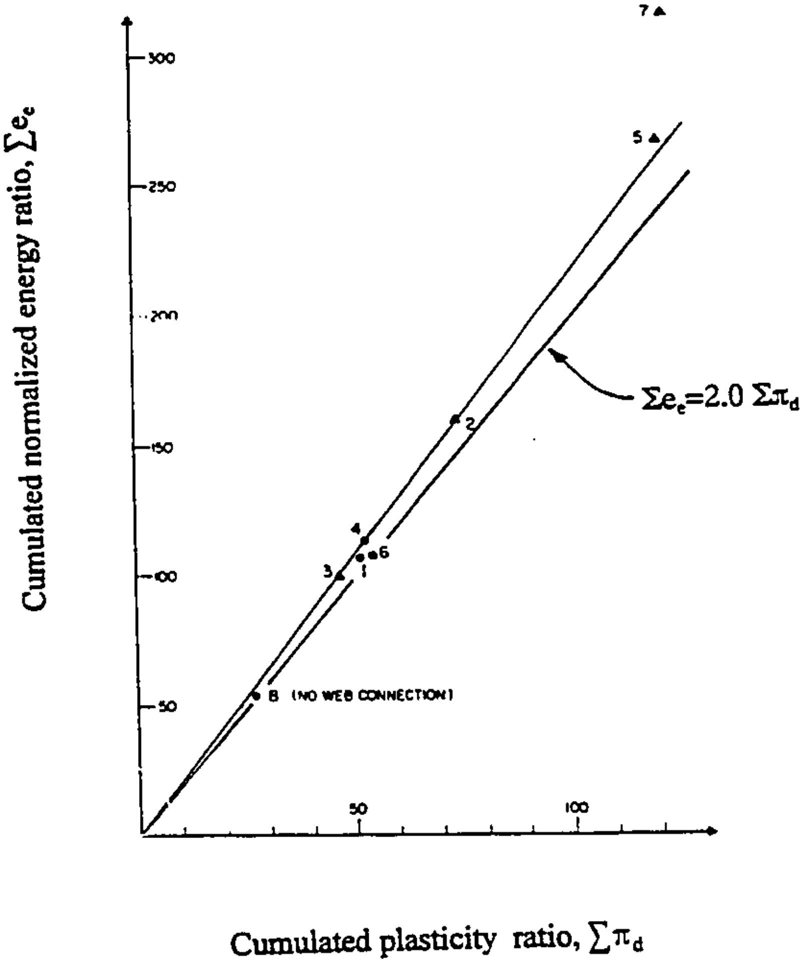

Fig. 5.8 Cumulated normalized energy vs cumulated plasticity ratio (Adapted from Popov and Bertero 1973)

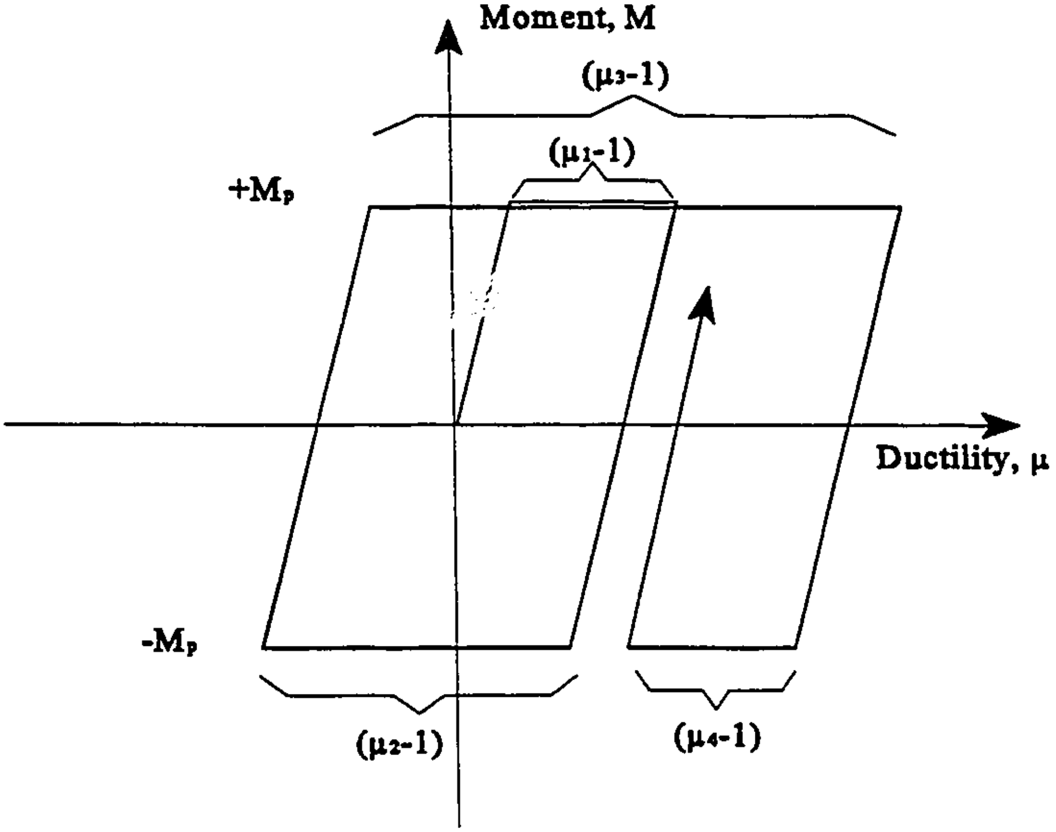

$$\sum(\mu_i-1)=(\mu_1-1)+(\mu_2-1)+(\mu_3-1)+(\mu_3-1)+(\mu_4-1)$$

Fig. 5.9 Cumulated residual plastic deformation

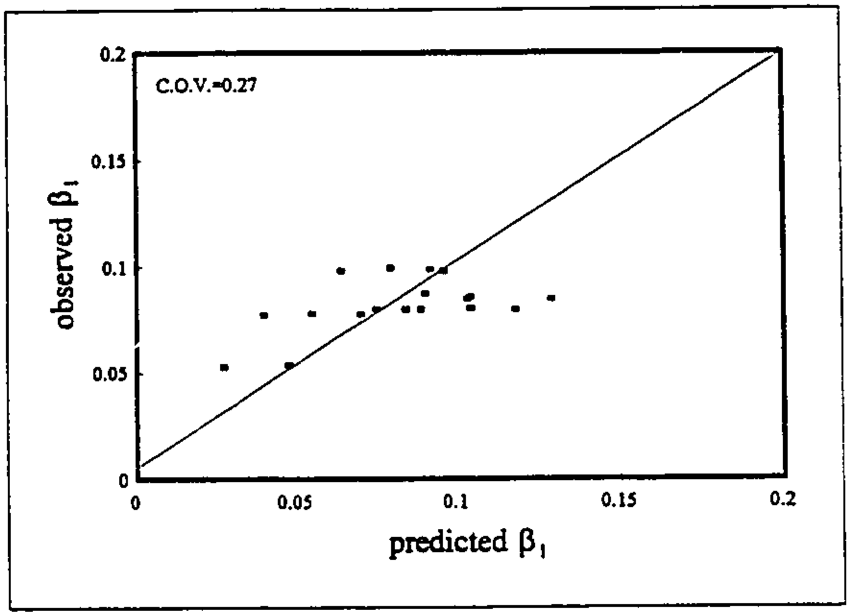

(a)

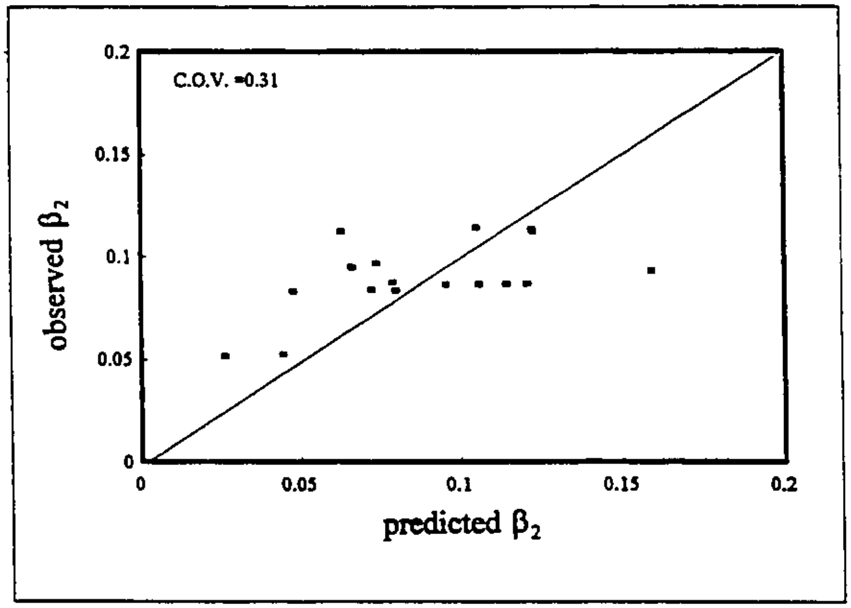

(b)

Fig. 5.10 Predicted vs observed values of the calibration parameters.
(a) Daali and Korol's approach, (b) Park and Ang's model based approach

CHAPTER 6

ANALYSIS OF A SEVEN-STOREY BUILDING

6.1 Introduction

In general, the main objective of design codes is the safeguard of human life against possible failures. The basic philosophy adopted by several seismic codes throughout the world (NBCC, 1990, NEHRP, 1992 and NZS 4203, 1984) is that: a) Structural and non-structural damage is tolerated during major earthquakes, b) Non-structural damage is permissible during moderate earthquakes and c) No damage is accepted during a minor shake.

The design of earthquake-resistant structures rely on the ability of the engineer to adequately estimate the energy demand of a given earthquake and the corresponding supply of strength, stiffness, structural ductility and member ductility of the designed structure. To accomplish the above, it has been accepted practice to satisfy: a) Serviceability conditions by providing sufficient strength and stiffness, and b) Energy demands that result from cyclic lateral forces in the form of large inelastic excursions. The latter expresses the ability to absorb and dissipate the energy input from an anticipated earthquake or an anticipated magnitude of earthquake.

Because of the complexities involved in the selection of earthquakes record histories or earthquake spectra, the associated non-linear dynamic analysis and the subsequent design phase, engineers usually use code simplified design procedures that employ equivalent static lateral loads (NBCC 1990). Among the number of basic assumptions that are used in the latter procedure, two are cited here: a) That the structure be designed to withstand design storey shears resulting from a distribution that emulates the dominance of the first lateral mode, and b) That the resulting storey drifts be less than some code prescribed value.

Design code requirements have been, in general, partly based on past performance of structures and partly on research conducted in university laboratories. It is therefore expected that these code requirements will be continually refined with new knowledge. The advent of recent unsatisfactory performance of buildings in the Northridge earthquake (Degenkolb, 1994) suggest some very relevant questions that form the basis of this Chapter. The questions are as follows: is the duration of a strong earthquake motion of relevance in the performance of a moment resisting steel frame or not? Is this performance similar to that expected by most modern codes? If an unsatisfactory performance results, is there a way of improving the simplified design method and its associated clauses?

To try to answer some of the questions phrased above, the National Building Code, of Canada (NBCC, 1990), was used as a basis for the design steps of a seven-storey fully ductile steel building having a square area floor plan three by three bays.

6.2 Design procedure

The hypothetical building has moment resisting perimeter frames in one direction and is braced frames in the other. Fig. 6.1 shows a plan view of the sample structure and Fig.

6.2 shows an elevation of the lateral resisting MRF. The building has a surface area of 576.0 m^2 and an overall height of 29.0 m consisting of one mechanical floor in the top storey and office floors for the remaining. The building's location was assumed to be in Victoria, B.C.

6.2.1 Design loads

Gravity loads:

The building is assumed to have an all-around metal curtain wall system and insulation weighing 1.75 kPa. All levels except the mechanical floor have a 75 mm wide-rib steel deck with 65 mm normal density concrete cover (2350 kg/m3) resulting in a 2.55 kPa distributed load. The mechanical floor has a 75 mm steel deck with 90 mm concrete cover resulting in a load of 3.15 kPa. A load of 0.75 kPa is assumed for the floor finish, insulation and ceiling and a 4 ply asphalt and gravel roof, giving a load of 0.32 kPa, is assumed for the uppermost level.

NBCC (1990) design live loads of 2.4 and 3.6 kPa were selected for the office floors and the mechanical floor, respectively. The partitions were assumed to have a 1.0 kPa live load, while a uniformly distributed snow load of 1.0 kPa is prescribed for Victoria.

Lateral loads:

Two types of lateral live load are usually used in the design process of a building. These are the lateral live loads from earthquake and those from wind. It may be that one or the other governs the design with respect to serviceability and strength. It is therefore, the purpose of the following sections to evaluate the magnitude of each one of these, and use them in the design process.

a) Earthquake loads:

Most structures have a build-in strength that exceeds that prescribed by codes. This is termed over-strength, and is the result of a number of contributing factors among which, one may cite the redundancy, oversizing of members, material strength that exceeds the nominal one and finally the non-structural elements that contribute in the lateral resisting system. Ductility is another factor that is, in general, an integral part of materials used for structural steel. However, it may be present at the member level, and to a lesser extent at the structural level. North American codes having provisions for earthquake design take these aspects into account in an indirect way through the use of force reduction and overstrength factors.

In Canada, the elastic base shear, V_e, is divided by a force modification factor, R, and multiplied by a calibration factor, U=0.6, to give the minimum design base shear, V as:

$$V=(V_e/R)U \tag{6.1}$$

The force modification factor reflects the ductilite nature of the structure, whereas U, reflects the inverse of the overstrength factor. The elastic base shear is given by:

$$V_e=vSIFW \tag{6.2}$$

in which,

v is the zonal velocity ratio having a 10% probability of exceedance in 50 years.

S is the seismic response factor.

I is the importance factor.

F is the foundation factor and

W is the weight of the building.

For the building at hand, the following have been used: v = 0.30, I = 1.0, F = 1.3 and W = 144485 kN. To calculate S, the seismic response factor, knowledge of the fundamental period of vibration is required. This was first estimated as 0.1N, i.e., 0.7 sec., according to NBCC (1990), where N is the number of storeys. Later, a modal analysis on the preliminary frame design gave a period of 1.85 seconds for the first mode of vibration. However, this value was not used since NBCC (1990) restricts the maximum period of vibration to 1.2 times the former one. This resulted in a seismic response factor, S, of 1.37 which in combination with the other parameters gave a design base shear of 1193 kN.

The design base shear was later distributed to each floor according to the NBCC (1990) formula:

$$F_i=(V-F_t)\left(\frac{W_i h_i}{\sum W_i h_i}\right) \qquad \textbf{(6.3)}$$

where

F_i is the a force at ith floor,

F_t is the a force at the top floor, equal to 0.07 T V and zero if T<0.75 seconds,

W_i is the weight at the ith floor, and,

h_i is the height at the ith floor.

b) Wind loads:

Reference velocity pressures, q, of 0.45 kPa and 0.55 kPa corresponding to 10% and 30% probability of exceedance for Victoria were used in the design process. The variations of the wind pressure along the height and other factors such as the gust and shape factor were also included. The resulting base shear acting on each of the perimeter frames was evaluated at 530 kN. Thus, a comparison of the earthquake base shear with the wind base shear shows that the former governs the strength aspect of the design process.

6.2.2 Proportioning of the sample structure

Unlike other codes of practice where the concept of strong column-weak beam is explicitly advocated, NBCC (1990) uses the concept of capacity design wherein the critical element or elements are identified and designed accordingly. The ranking of members at a connection is done by firstly, comparing the member's factored resistance with the nominal resistance of the other members and secondly by assuming that every one of the members reaches 1.20 times the nominal resistance, where the 20% reflects a possible overstrength (more may be found in a paper by Redwood et al. 1990 on this subject). Once a critical element or elements are identified, these are then chosen such that their section and member characteristics permit ductile behaviour. For instance, if a beam is identified as the critical element, it should then satisfy all the conditions of Class 1 sections. For the sample building under consideration, the above methodology along with other code requirements was followed in the design process. The end result was a building having the member sizes shown in Fig. 6.3.

6.3 Computer modeling

a) Modeling:

A general purpose computer program, DRAIN-2DX, developed by Prakash and Powell (1992) was used for the non-linear static and dynamic analysis. The sample building was analyzed using beam-column elements with bi-linear moment-curvature and moment-rotation relationships and yield interaction surfaces specified at the ends of the beams and beam-columns. Besides having the ability to calculate the usual member end forces, storey shears at each time step, displacements and rotation envelopes, the program calculates mode shapes, frequencies, cumulated inelastic rotations, and cumulated energy quantities as well. The latter are of relevance here since they can be directly used in the damage assessment models developed in Chapter 5.

b) Analysis response spectra:

In general, earthquake records have a large number of parameters that may influence their shape and contents and subsequently lead to a difference in structural response of the buildings. These parameters range from the location of an earthquake to the nature and conditions of the soil, the frequency content, the duration of strong shaking and numerous others not cited for the sake of brevity. One major factor among all these can however be singled out since it seems to have a significant role on the structural responses of buildings. This is termed the frequency content of the record and is commonly referred to as the ratio of peak ground acceleration to peak ground velocity, A/V. It is customary to associate a high A/V ratio with strong and close proximity earthquakes while a low A/V ratio is associated with large and distant earthquakes (Naumoski et al. 1993).

For the purpose of the computer analysis and because Victoria is anticipated to experience an intermediate, A/V, ratio of peak ground acceleration to peak ground velocity (NBCC, 1990) it was decided to generate an artificial time history from an averaged response spectra of a group of 15 intermediate ones (Naumoski et al., 1993). The averaged response spectrum (Fig. 6.4) was first scaled at a ground velocity of 0.3 m/s as given by NBCC (1990) for the city of Victoria, B.C. The computer program SYNTH (Naumoski, 1984) was then used to generate an artificial acceleration time history record (Fig. 6.5) that has a response spectrum compatible with the selected target response spectrum (Fig. 6.4). The artificial acceleration time history record was finally used as input into DRAIN-2DX to assess the response of the sample building.

6.4 Analysis of the seven storey building

a) Static Analysis:

To check the adequacy of the designed building, an elastic analysis was performed at the end of the design stage. The purpose of this was to check the storey drift under wind, earthquake and gravity loads. The drifts calculated over the seven storeys were within the deflection limits specified by NBCC (1990). These are 0.002 times the storey height for wind based on a velocity pressure, q, having a probability of being exceeded in any one year of 1 in 10; and (0.02/R) times the storey height for earthquake (where R is the force modification factor). Fig. 6.6 shows the maximum lateral deflections along with the code specified limits while Fig. 6.7 shows a comparison of the calculated values of storey drifts and the Canadian code's specified limits. Subsequent to the above, an inelastic quasi-static lateral load to failure check was performed on the sample structure to assess its strength adequacy. The program DRAIN-2DX was used to this end; the gravity service loads were kept constant while the design base shear was increased in a step wise manner. As shown in Fig. 6.8, the structure developed its first plastic hinge at a lateral load equal 1.1 times the design base shear. Afterwards, numerous other plastic hinges developed throughout the structure. Appreciable levels of lateral loads were sustained past the maximum inelastic drift permitted by the code, indicating development of an adequate over strength capability were however sustained past the maximum inelastic drift permitted by the code.

b) Dynamic analysis:

We have seen in the above that the steps followed in the design process led to an acceptable behaviour of the moment resisting frame under lateral equivalent static loads and gravity loads. The overall strength was greater than the nominal one and the lateral deflections under specified wind and earthquake equivalent static loads were smaller than the code prescribed ones. In the present section, we shall see how the same building behaves under an anticipated earthquake.

The envelopes of maximum lateral deflections, drift ratios and inelastic rotations at the end of the members are shown in Figs. 6.9 to 6.11. Comparing Figs. 6.6 with Fig. 6.9, it can be seen that the lateral deflections under the anticipated earthquake are, on average, of the order of five to six times the elastic allowable lateral deflections under the equivalent lateral static loads, and of the order of 25% to 50% more than the inelastic allowable deflections. The earthquake induced story drifts can be seen in Fig. 6.10 to exceed the 2% story drift ratio allowed by NBCC (1990) under inelastic behaviour. From the envelope of inelastic rotations, it can be seen that plastic hinges formed exclusively at the column bases and the beam-ends (Fig. 6.11). This signifies that the behaviour exhibited by the MRF of the sample building was of the strong column-weak beam type. Of course, this kind of behaviour is ideal since the distribution of plastic hinges is distributed uniformly throughout the structure. Note that the strong column-weak beam type of behaviour is desirable in some jurisdictions but is not the only response permitted by NBCC (1990); indeed, mixed forms and locations of energy dissipation are also permitted as long as the structure is designed properly.

c) Damage assessment:

The objective of this section is to make use of the damage assessment models developed in Section 4 of Chapter 5. The analytical study is restricted to the application of the damage assessment models to the beams only. No attempt has been made to apply the present damage models to the beam-column elements since the effects of the axial force were not incorporated in the damage models. This would necessitate a major experimental and analytical study that is not within the scope of this research program. The damage assessment models developed earlier and given by Eqns. 5.4 and 5.9 were used. A detailed example of the application on the left and right plastic hinges of the beam of the central bay on the fourth floor of the MRF is shown in Fig. 6.12. In Figs. 6.13 is shown the damage distribution in the whole frame. The results given by the top numerals were obtained using the Daali and Korol's damage assessment model; the results given between parentheses are those obtained using the modified Park and Ang model. Comparing the results of the two models, it can be seen that for high levels of damage, the two models yield similar results. For a low level of damage, the modified Park and Ang model yields D values that are significantly greater than the Daali and Korol model. This difference is because the mathematical formulation of the original Park and Ang model does not converge to a zero damage value under no inelastic deformation. A study of Fig. 6.13 shows that damage is significantly greater in the first and fourth storey than the remaining ones. This may be due to a combination of effects such as the selection of the sections and the P-Δ effects.

d) The use of Herring-bone stiffeners as an alternative to improve the response of the building.

A procedure that permits the quantification of improvement in ductility of an unstiffened beam versus a stiffened one was proposed in Section 3.6.4 of Chapter 3. Herein, we shall show how the concept of the Herring-bone stiffener can be used to our advantage to improve the behaviour of a given member and subsequently reduce the damage inflicted upon it.

Consider the W610x101 beam used in the fourth storey of the seven storey building (Fig. 6.3). The section has a yield stress of 300 MPa and is laterally supported according to CAN/CSA-S16.1-M89. Furthermore, it has a half-flange width, b=114 mm, a web depth, h=603 mm, a flange thickness, t=15 mm and a web thickness, w=11 mm.

Using Eqns. 3.1 and 3.2 with e=36 and s=9, one obtains a value for the half wave-length equal to 340 mm. The expected ductility is subsequently equal to 5.15. If a Herring-bone is introduced at 1.25 times the half wave-length of the unstiffened beam, then the ductility value of the stiffened beam is 6.68, i.e., an improvement of the order of 30%. If a stiffened beam were used instead of an unstiffened one in the central bay of the fourth floor, then the damage values employing Daali and Korol's model for that beam would be 0.66 for the left end and 0.86 for the right one (Fig. 6.12). Note that a considerable improvement is achieved when the latter values are compared to those obtained for the unstiffened beam i.e. 0.88 and 1.14 respectively.

6.5 Adequate ductility in steel members

The damage models that were employed in the previous section have proven to be very useful in numerical analyses where the deformation history is available. It is difficult, however, to use them in their present form in a design process since the load history is not known a priori. Furthermore, non-linear dynamic analyses are still the privilege of only a few design offices. For these reasons, it was decided to make use of the concept of adequate ductility given in the New Zealand building code (1988). It is stated, in Section 3.2 of that standard, *that structural systems intended to dissipate seismic energy by flexural yielding shall have "adequate ductility"*. This term is furthermore defined such that the building as a whole shall be able to sustain eight load reversals of loading having the same ductility without a strength loss of more than 20%.

However, instead of applying the criterion in its present form, let us rather state that " *for steel beams, an adequate ductility is defined such that the member shall be able to sustain eight load reversals of loading, having the same required ductility, without strength* *loss below the plastic limit*". This likely represents a more conservative requirement since it essentially excludes the strain hardening benefits that are often ignored anyway. Applying this modified criterion to the damage models (Eqns. 5.4 and 5.9) developed previously yields the following expressions at failure:

$$1=\left(\frac{\mu_{max}-1}{\mu_{mono}-1}\right)+8\beta_1\left(\frac{\mu_i-1}{\mu_{mono}-1}\right)^{1.11}$$ for Daali and Korol's approach **(5.4-a)**

and

$$1=\frac{\mu_{max}}{\mu_{mono}}+8\beta_2\frac{(\mu_i-1)}{\mu_{mono}}$$ for the approach based on Park and Ang's model **(5.9-a)**

where $\mu_i=2\mu_{max}-1$

Equations 5.4-a and 5.9-a relate in a unique manner the monotonic ductility, μ_{mono}, to the maximum ductility, μ_{max}, if the calibration factor is known. Equation 5.9-a can be rearranged to read:

$$\mu_A=\mu_{max}=\frac{\mu_{mono}+16\beta_2}{1+16\beta_2} \tag{6.4}$$

where μ_A is defined as Adequate ductility. This value is important since it denotes the amount of ductility that is needed in order for an element to withstand the cyclic load history that may have to be experienced by the member. A plot of the adequate cyclic ductility using Eqn. 6.1 (Fig. 6.14) shows that the flange slenderness dictates how much deterioration a section can sustain under repeated effects or low-cycle fatigue. For instance, if the flange is very slender, then the effect of the repeated loads accelerates and accentuates any instability which already appeared in the early stages of loading. This subsequently leads to a rapid deterioration in the behavior of the section. On the contrary, a stockier flange develops flange instability under severe inelastic deformations only. Thus the deterioration in behavior will be noticeably smaller than in the previous case. Consequently, it may be said that adequate ductility of a beam with a stocky flange is much closer to the monotonic value than is the case for a slender flange (Fig. 6.14). Note that the above mentioned does negate in any way the importance of the web slenderness and its effects on the strength deterioration. The small number of experimental data did not permit to include such effect in the mathematical model.

To exemplify the use of the concept of adequate ductility, calculations addressing the monotonic and adequate ductilities of a specific section are undertaken in the following example.

6.6 Example

Consider the W610×101 beam section used in Section 6.4-d. Since the yield stress, σ_y, has a value of 300 MPa, then the plate slenderness values, lateral slenderness and the monotonic ductility are given according to Eqn. 5.10:

$$\alpha_f=\frac{b}{2t\epsilon}=\frac{114}{15}=7.6 \quad , \quad \alpha_w=\frac{h}{w\epsilon}=\frac{603}{11}=54.6 \quad , \quad \alpha_l=\frac{L}{r_y\epsilon}=56.58 \quad , \quad \alpha_e=\frac{\alpha_f\alpha_w\alpha_l}{30072}=0.78$$

and

$$\mu_{mono}=1-9.2\alpha_e+10.71\alpha_e^{-0.293}=1-(9.2)(0.78)+(10.71)(0.78)^{-0.293}=5.27 \qquad \Leftarrow$$

According to Eqn. 5.11, the calibration factor, β_2, is:

$$\beta_2=0.085(\frac{\alpha_f}{8.37})^{2.26}=0.085(\frac{7.6}{8.37})^{2.26}=0.069$$

and from Eqn. 6.1, the adequate ductility, μ_A, is:

$$\mu_A=\frac{\mu_{mono}+16\beta_2}{1+16\beta_2}=\frac{5.27+(16)(0.069)}{1+(16)(0.069)}=3.03 \qquad \Leftarrow$$

From this simple exercise, one can see that a member having a monotonic ductility of 5.27 would have an adequate ductility of 3.03 after undergoing eight reversals of loading. The deterioration in strength and dissipated energy is reflected in the reduction of the ductility capabilities of the member.

Now that the concept of damage assessment and the idea of "Adequate ductility" have been introduced, it would be interesting to determine whether the beams selected during the design process of the building are satisfactory based on the adequate ductility criterion. A comparison, in Fig. 6.15, of the maximum ductility demand values with the adequate ductility values calculated with Eqn. 6.4 show that the ductility demand in the first, fourth and fifth levels are greater than the available adequate ductility. This result therefore suggests that the selected members would probably not perform in a satisfactory manner unless they were properly strengthened with Herring-bone or other types of stiffeners. On the other hand, the ductility demand in the second, third, sixth and seventh levels is lower than the available adequate ductility thus signifying that the members at these levels would perform satisfactorily.

6.7 Summary

An adequate design of ductile steel MRF's in earthquake prone zones is normally achieved by satisfying appropriate stiffness and strength requirements specified in the code having appropriate jurisdiction. However, the response of a building designed according to such standard may not necessarily respond to an anticipated earthquake in the same manner as would be expected. Indeed, drift ratios and the corresponding lateral deflections may be larger than the code specified limits if non structural components are excluded from the analysis. Furthermore, damage, in the form of diminished ductility may result perhaps in unacceptable losses in strength.

From the non-linear dynamic analysis, the application of the approaches developed in Chapter 5 for the prediction of damage in steel beams under cyclic loading has been demonstrated. Despite the randomness of any earthquake load event, results achieved with this methodology may be considered quite acceptable.

Finally, a criterion for the selection of sections on the basis of adequate ductility rather than the usual buckling rules has been proposed. It is believed that the use of this criterion will prove beneficial in limiting the damage under earthquake-type loading.

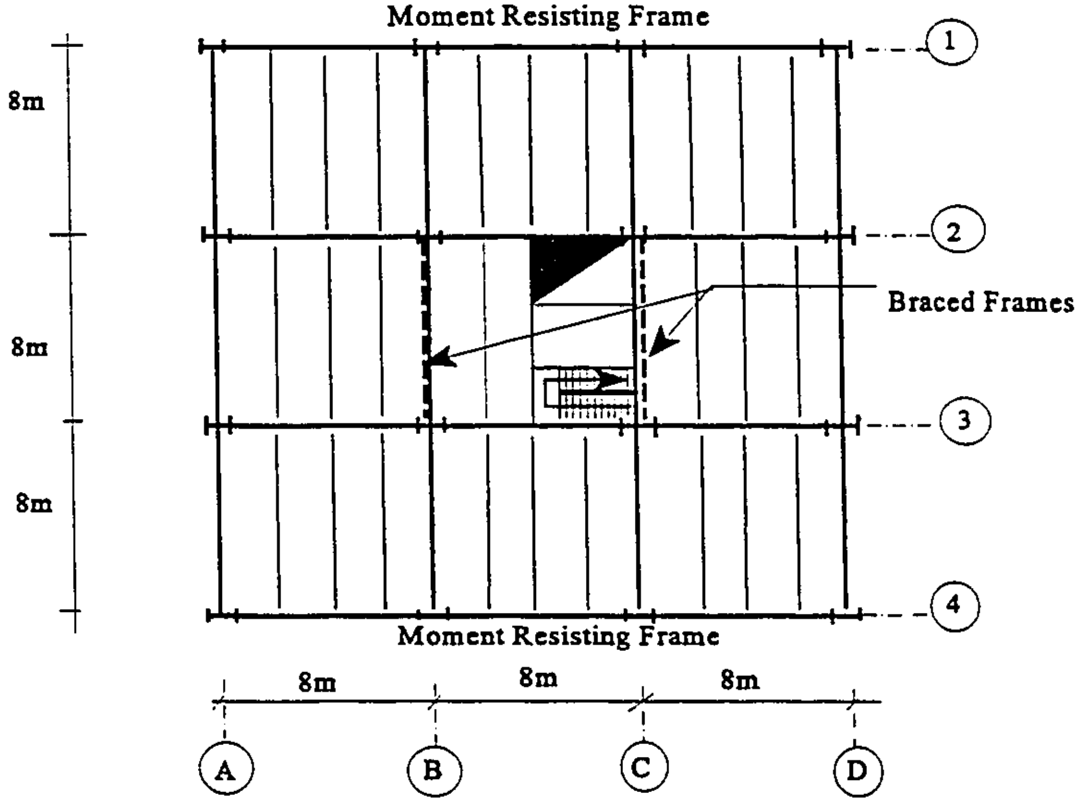

Fig. 6.1 Plan view of sample building

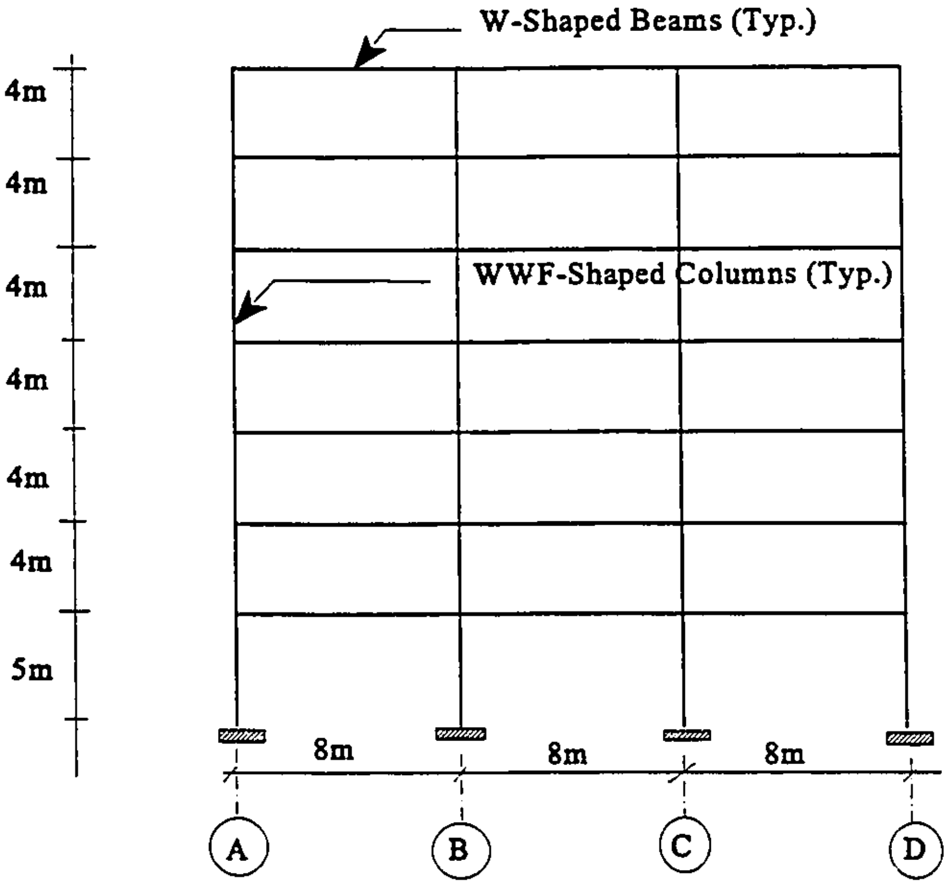

Fig. 6.2 Elevation of moment resisting frames on column lines 1 & 4

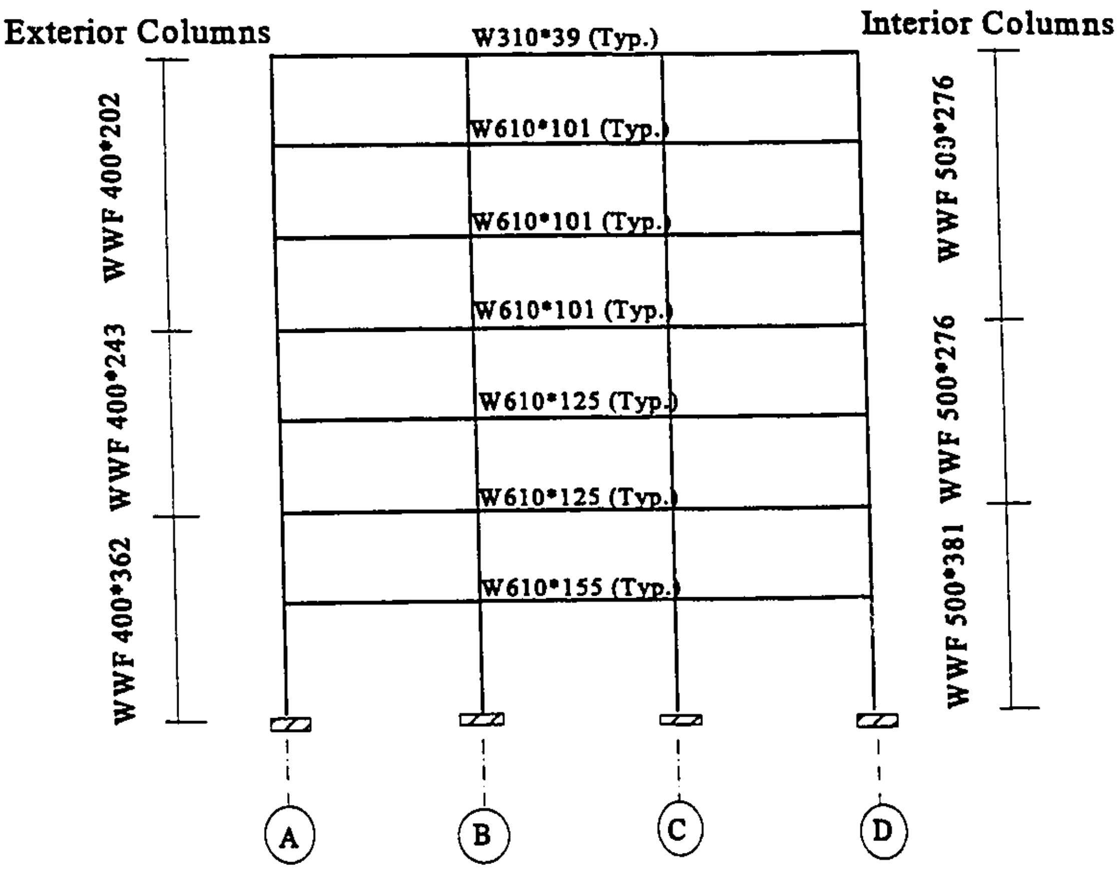

Fig. 6.3 Selected members in sample building

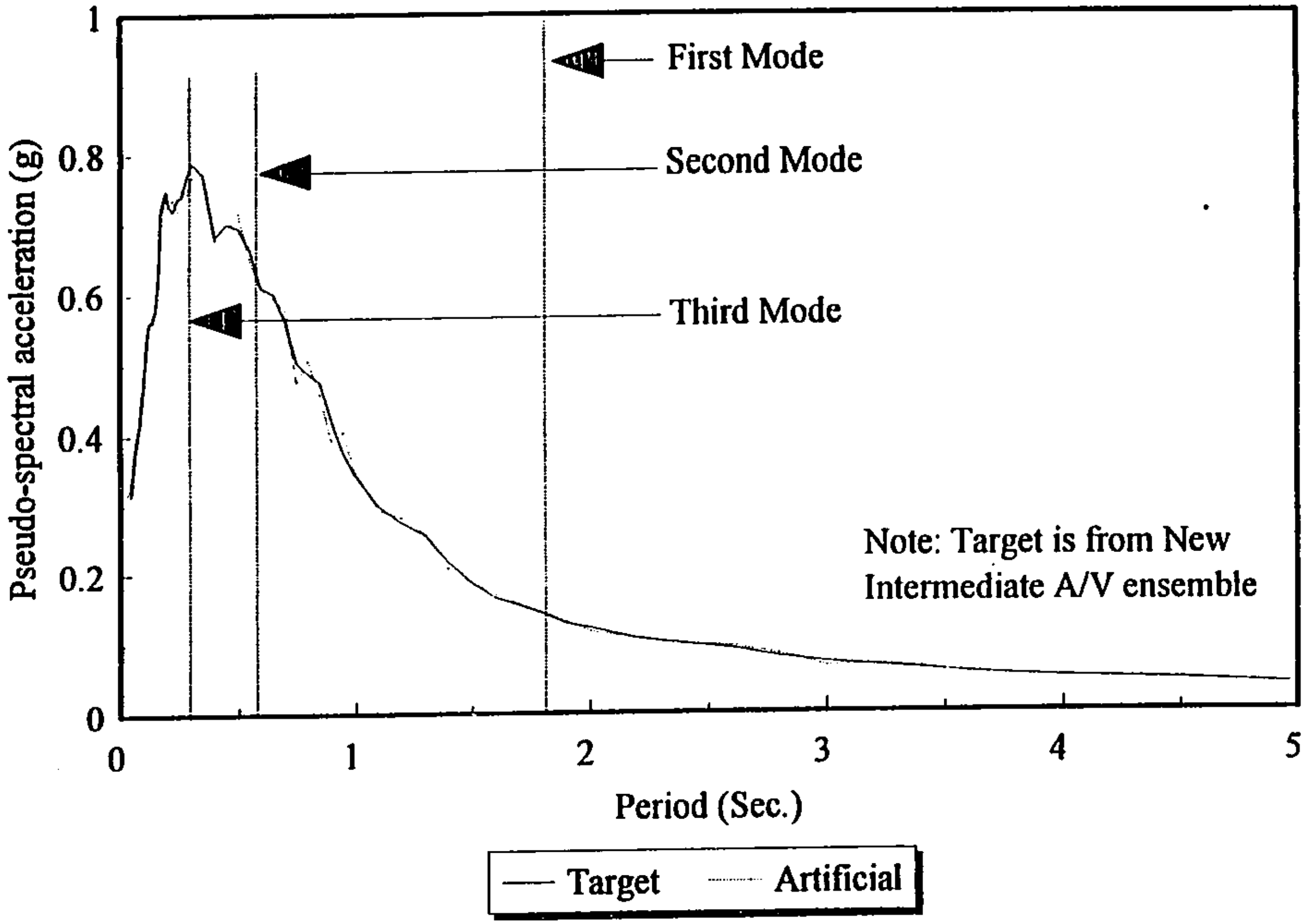

Fig. 6.4 Artificial and new intermediate A/V averaged spectral acceleration

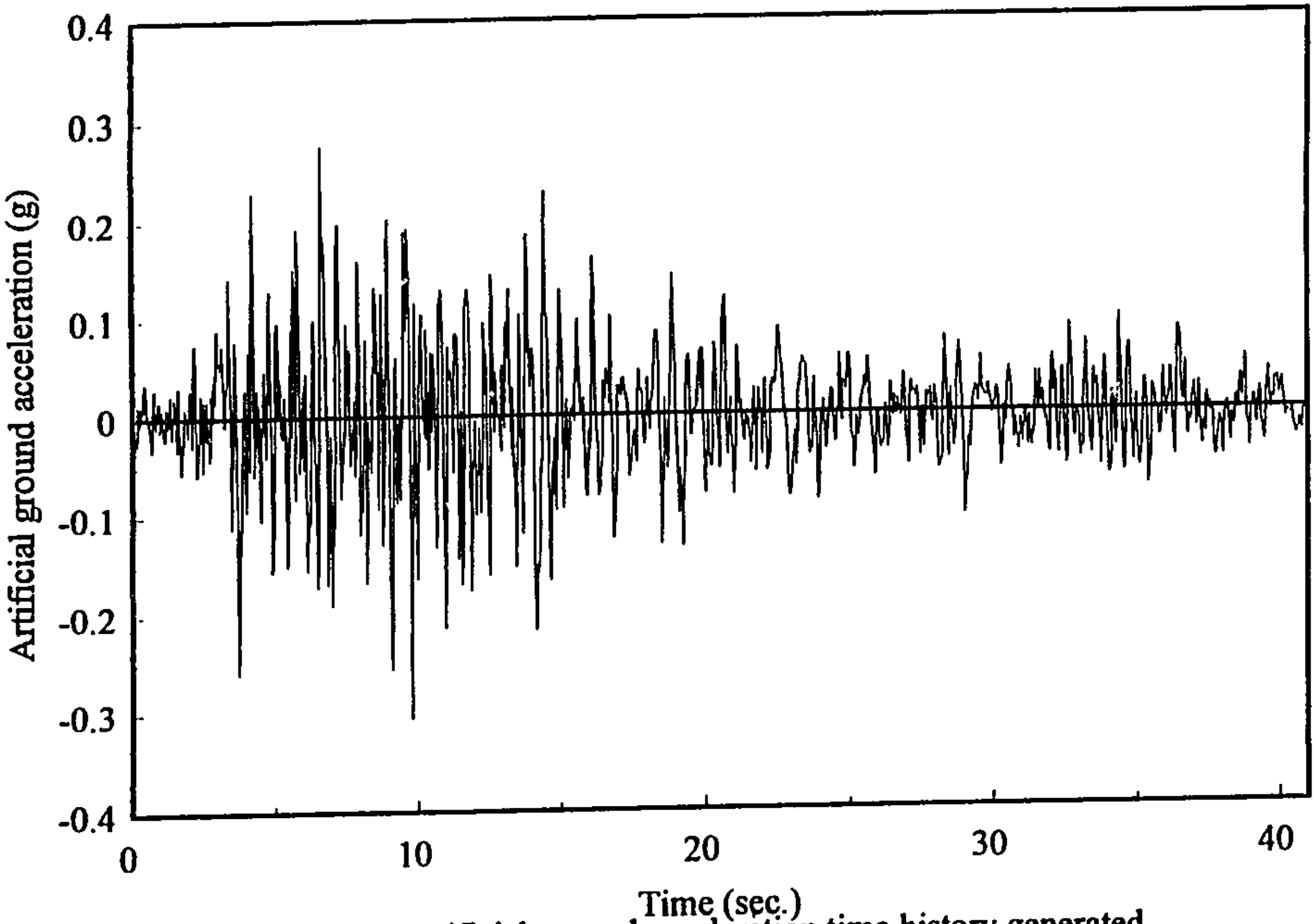

Fig. 6.5 Artificial ground acceleration time history generated from the new intermediate A/V ratio ensemble

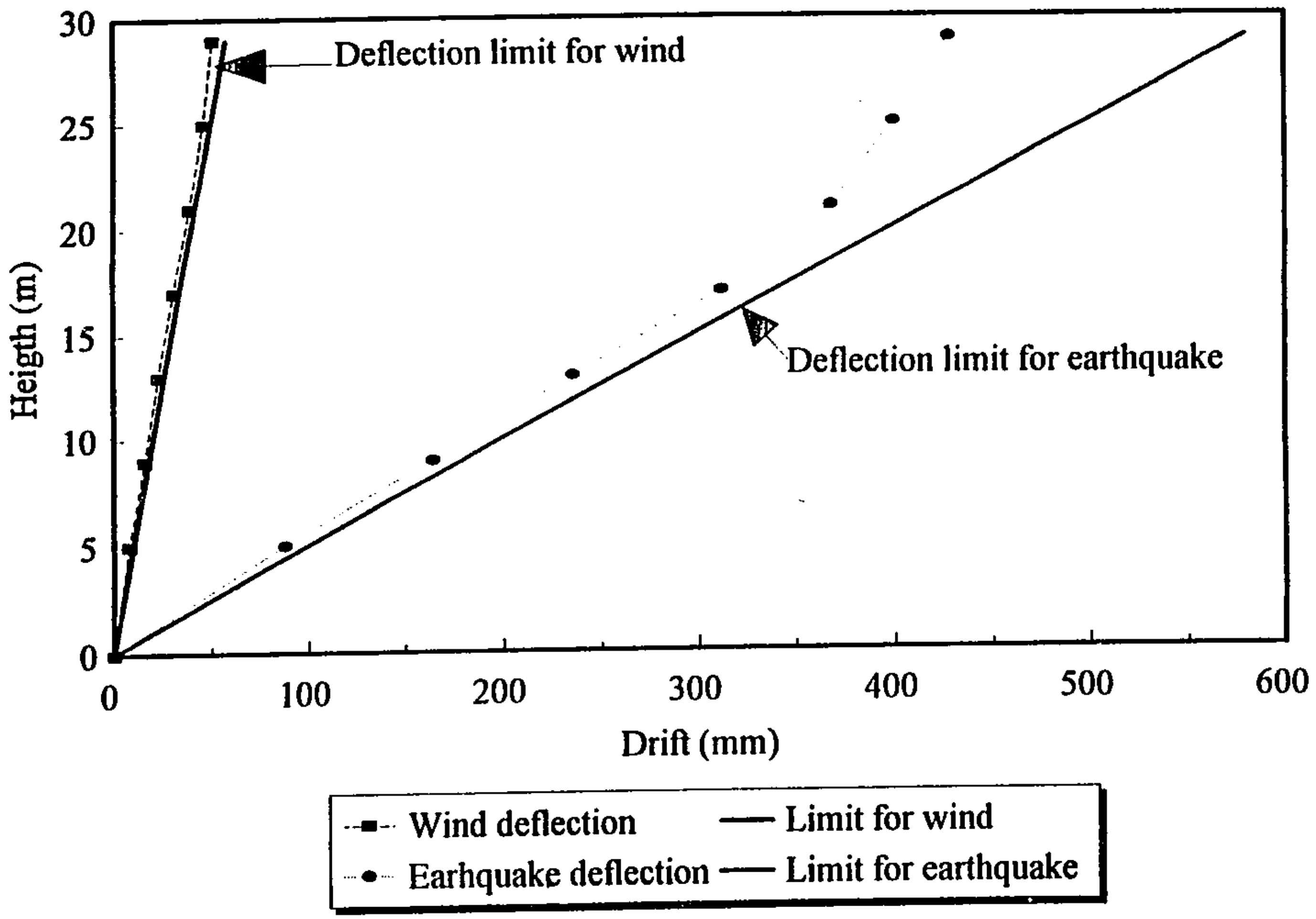

Fig. 6.6 Lateral deflections induced by wind and earthquake equivalent static loads

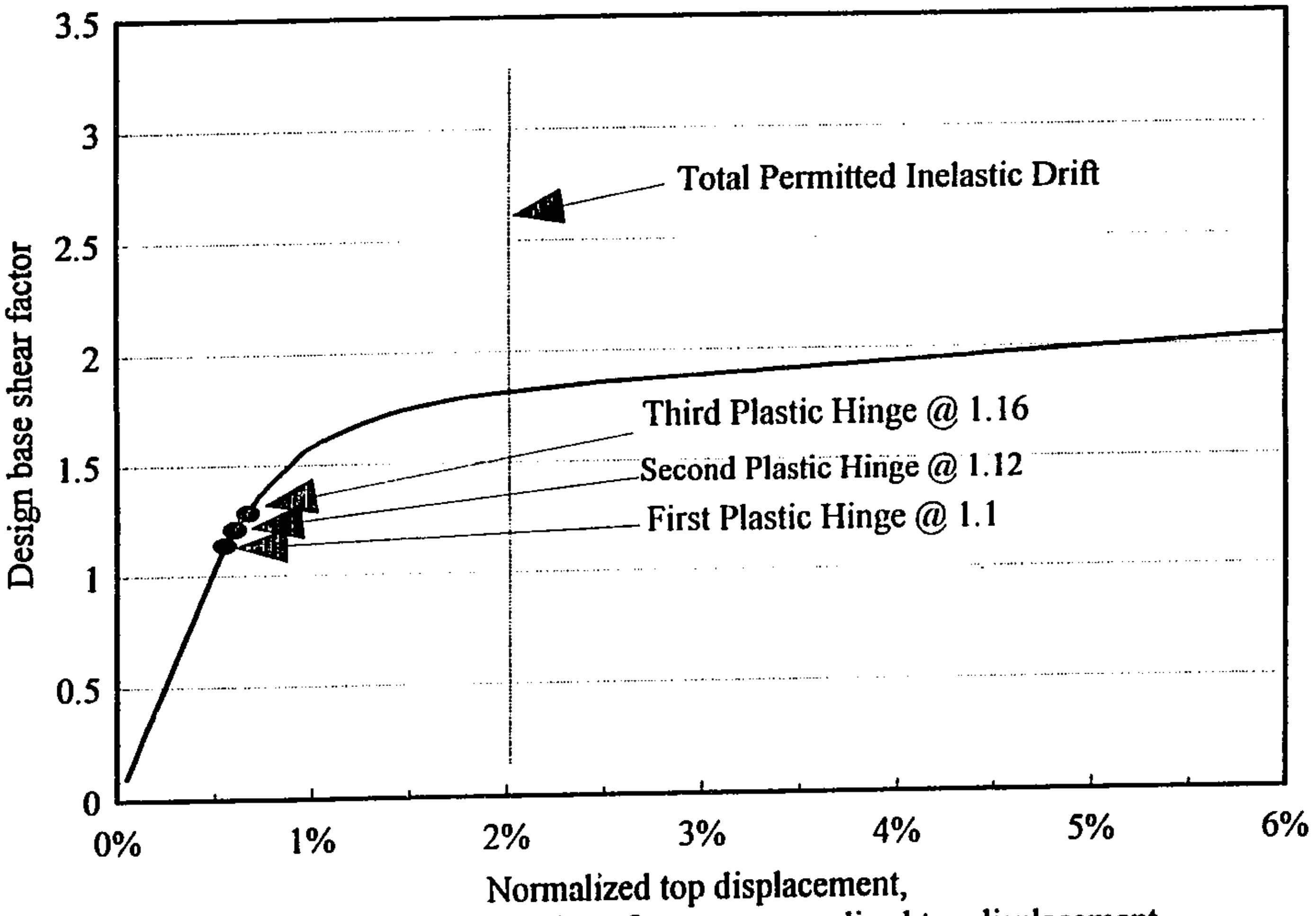

Fig. 6.8 Design base shear factor vs normalized top displacement

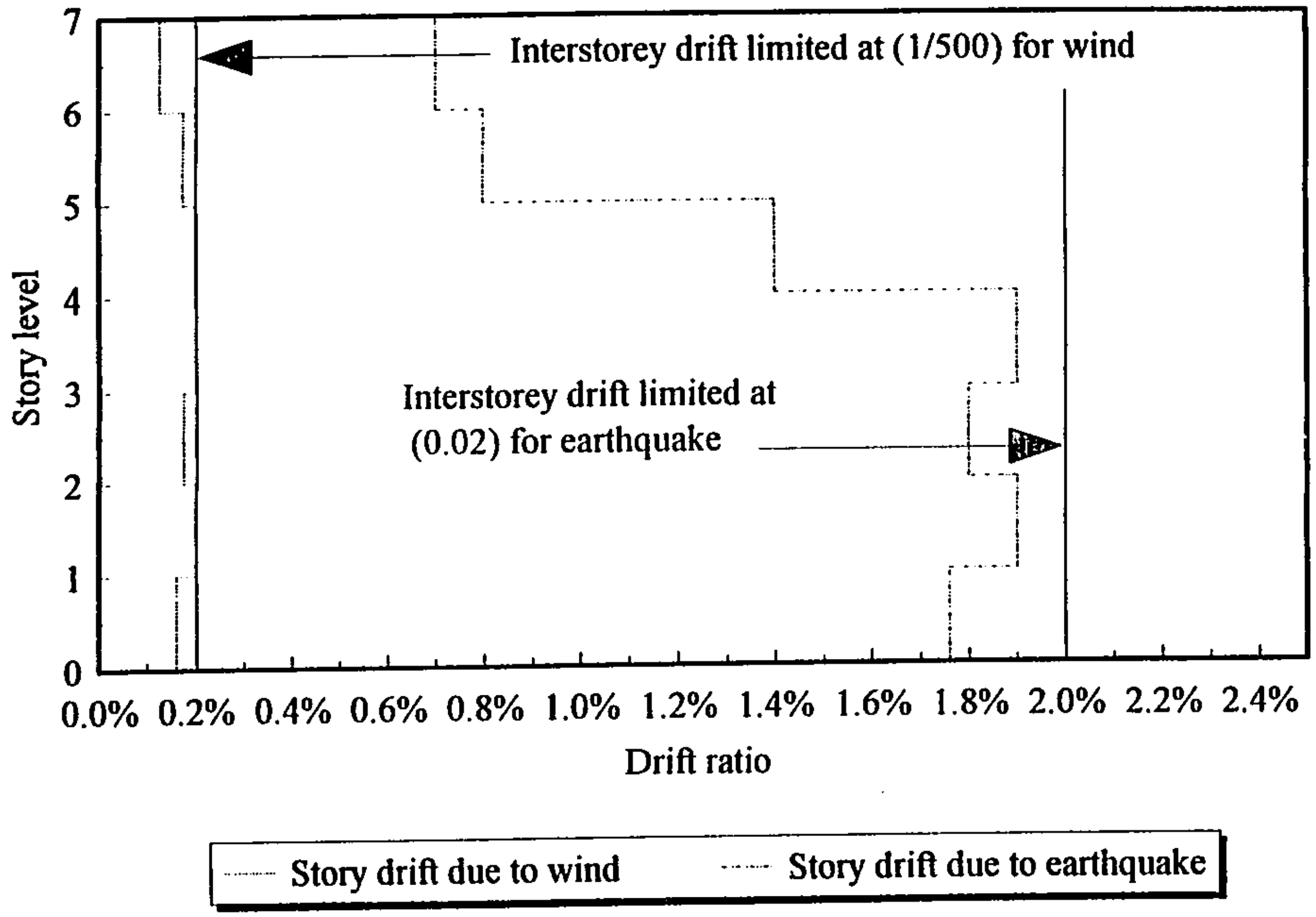

Fig. 6.7 Story drifts ratios induced by wind and earthquake equivalent static loads

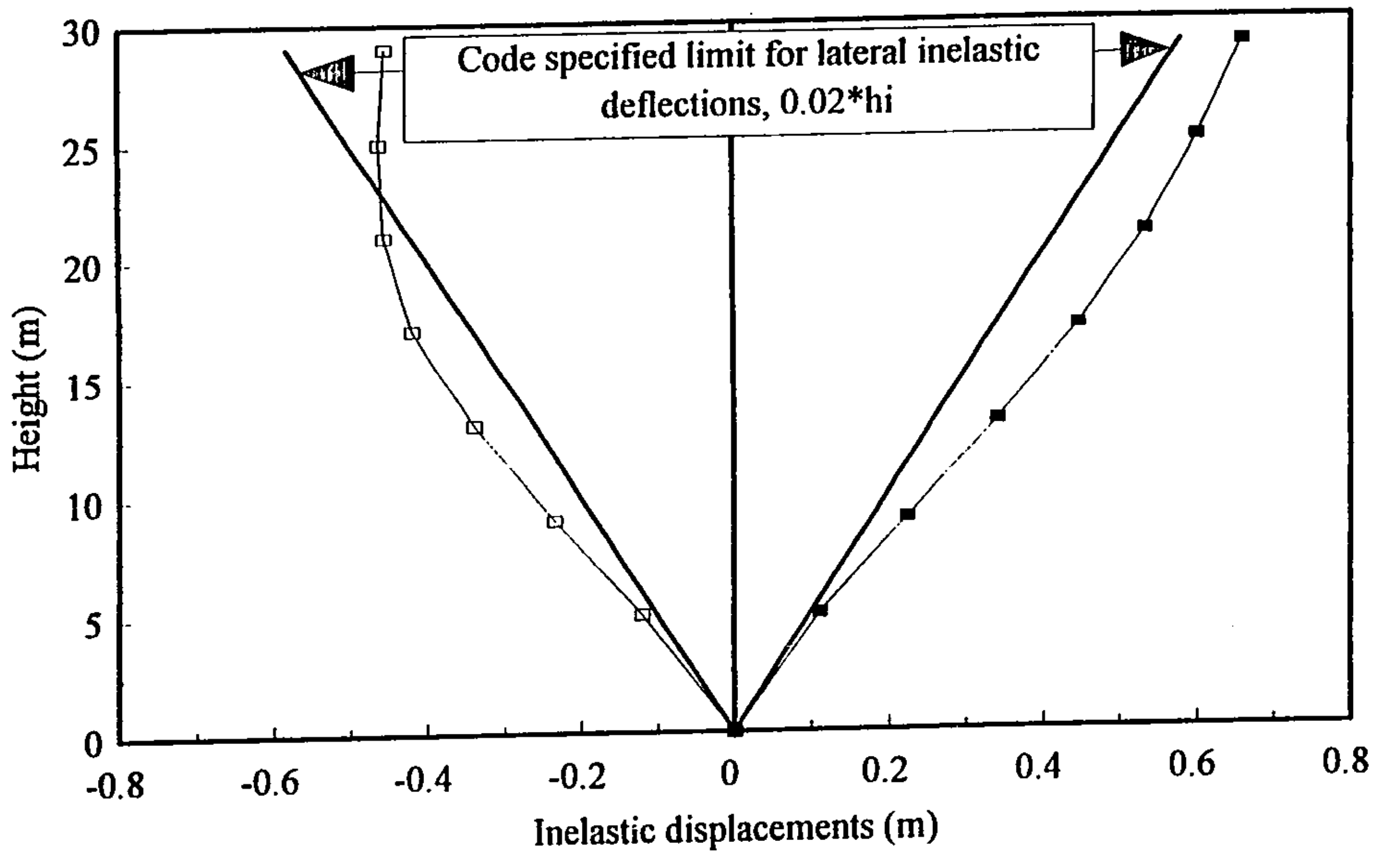

Fig. 6.9 Envelope of lateral displacements under the anticipated earthquake

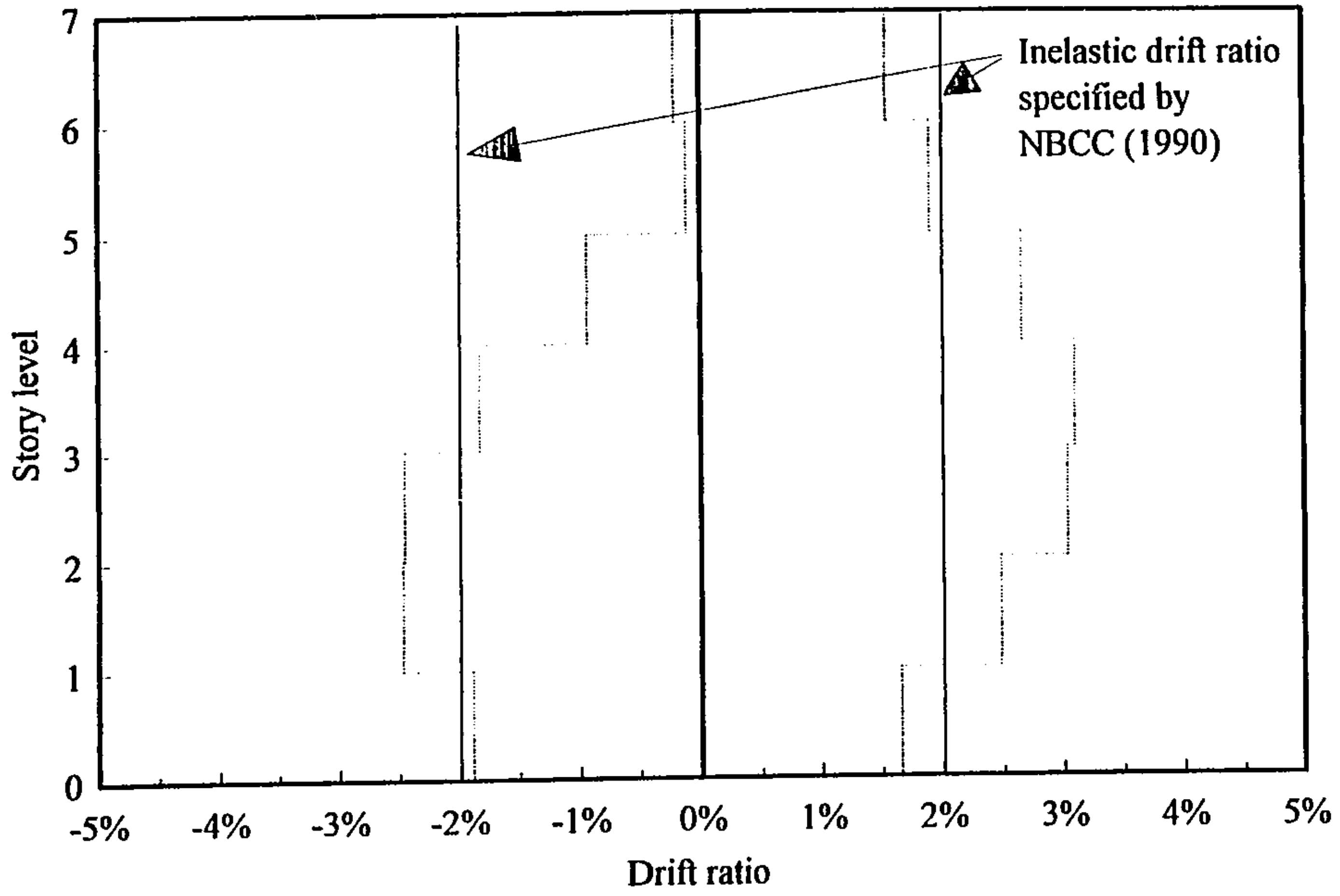

Fig. 6.10 Envelope for drift ratios and code specified inelastic drift ratio limit

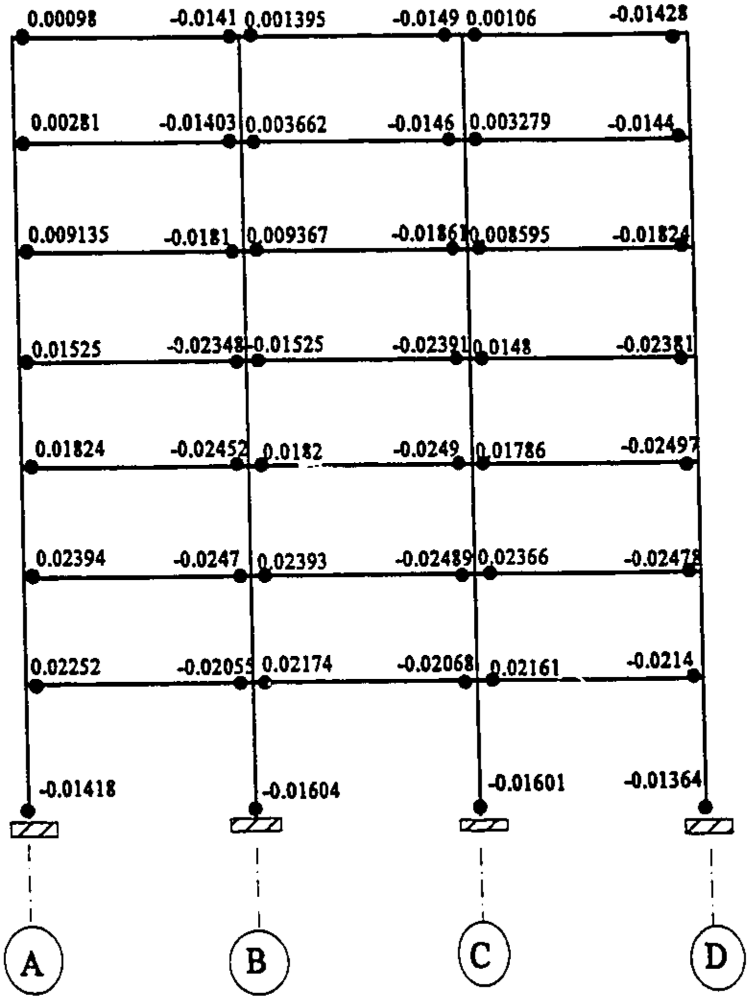

Fig. 6.11 Envelope of inelastic rotations

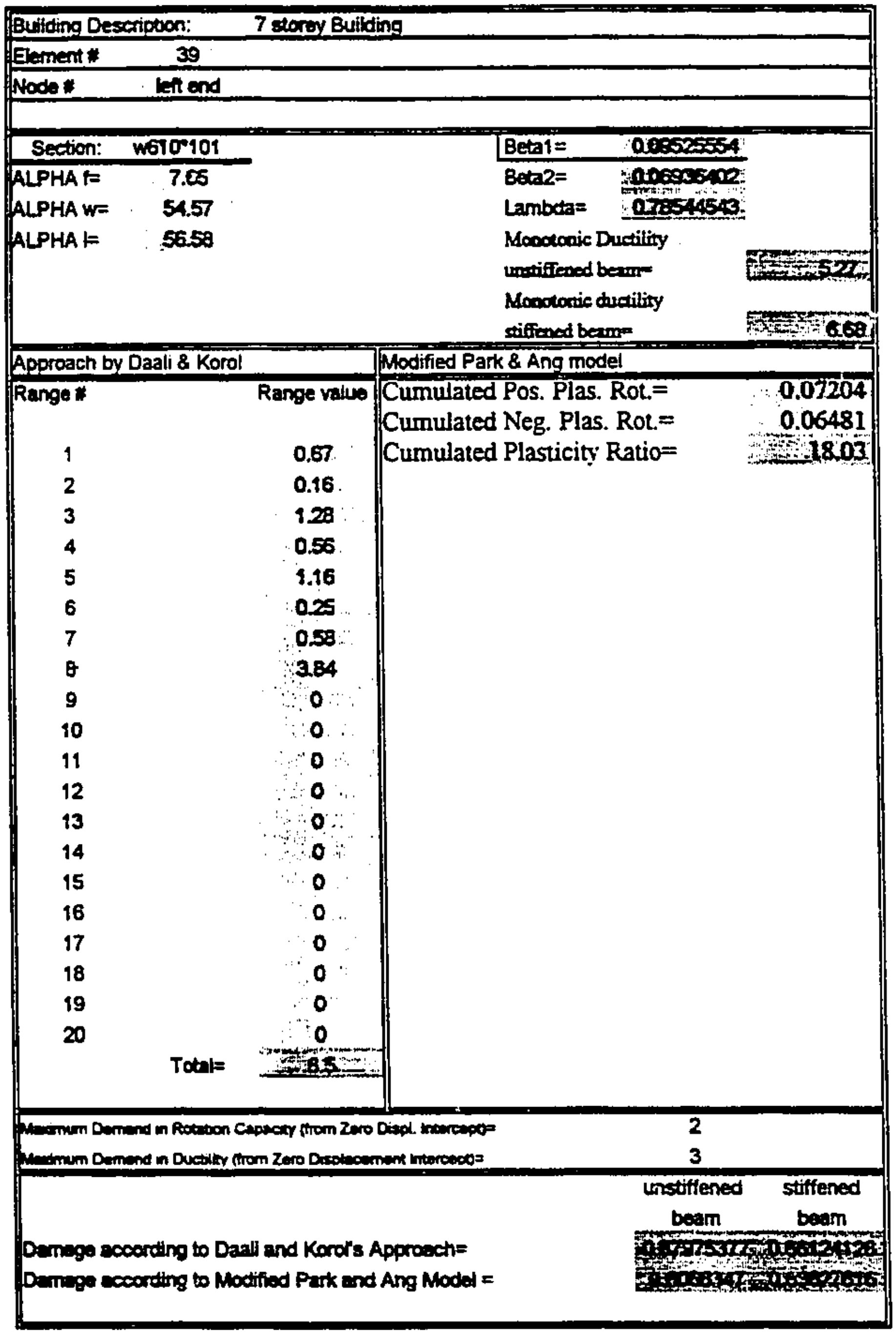

Building Description: 7 storey Building
Element # 39
Node # left end

Section: w610*101

ALPHA f=	7.65	Beta1=	0.08525554
ALPHA w=	54.57	Beta2=	0.06936402
ALPHA l=	56.58	Lambda=	0.78544543
		Monotonic Ductility unstiffened beam=	5.27
		Monotonic ductility stiffened beam=	6.68

Approach by Daali & Korol

Range #	Range value
1	0.67
2	0.16
3	1.28
4	0.56
5	1.16
6	0.25
7	0.58
8	3.84
9	0
10	0
11	0
12	0
13	0
14	0
15	0
16	0
17	0
18	0
19	0
20	0
Total=	8.5

Modified Park & Ang model

Cumulated Pos. Plas. Rot.=	0.07204
Cumulated Neg. Plas. Rot.=	0.06481
Cumulated Plasticity Ratio=	18.03

Maximum Demand in Rotation Capacity (from Zero Displ. Intercept)= 2
Maximum Demand in Ductility (from Zero Displacement Intercept)= 3

	unstiffened beam	stiffened beam
Damage according to Daali and Korol's Approach=	0.87975377	0.66124126
Damage according to Modified Park and Ang Model =	0.86068347	0.63627616

Fig. 6.12-a Application of the damage models to the beam of the central bay on the fourth floor: beam left end plastic hinge

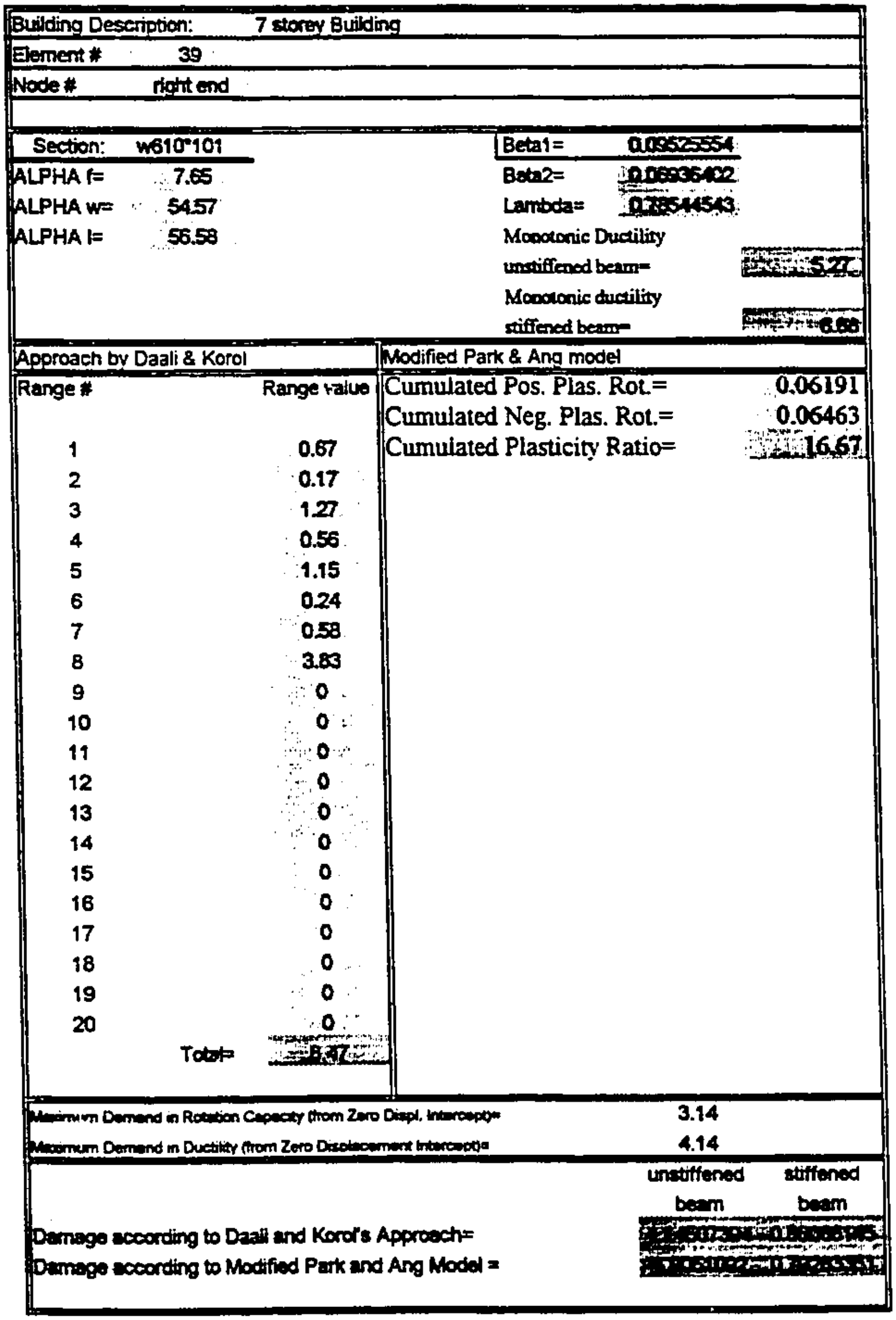

Building Description: 7 storey Building

Element # 39

Node # right end

Section: w610*101

ALPHA f= 7.65

ALPHA w= 54.57

ALPHA l= 56.58

Beta1= 0.09525554

Beta2= 0.06936402

Lambda= 0.78544543

Monotonic Ductility unstiffened beam= 5.27

Monotonic ductility stiffened beam= 6.66

Approach by Daali & Korol

Range #	Range value
1	0.67
2	0.17
3	1.27
4	0.56
5	1.15
6	0.24
7	0.58
8	3.83
9	0
10	0
11	0
12	0
13	0
14	0
15	0
16	0
17	0
18	0
19	0
20	0
Total=	8.47

Modified Park & Ang model

Cumulated Pos. Plas. Rot.= 0.06191

Cumulated Neg. Plas. Rot.= 0.06463

Cumulated Plasticity Ratio= 16.67

Maximum Demand in Rotation Capacity (from Zero Displ. Intercept)= 3.14

Maximum Demand in Ductility (from Zero Displacement Intercept)= 4.14

	unstiffened beam	stiffened beam
Damage according to Daali and Korol's Approach=	[illegible]	[illegible]
Damage according to Modified Park and Ang Model =	[illegible]	[illegible]

Fig. 6.12-b Application of the damage models to the beam of the central bay on the fourth floor: beam right end plastic hinge

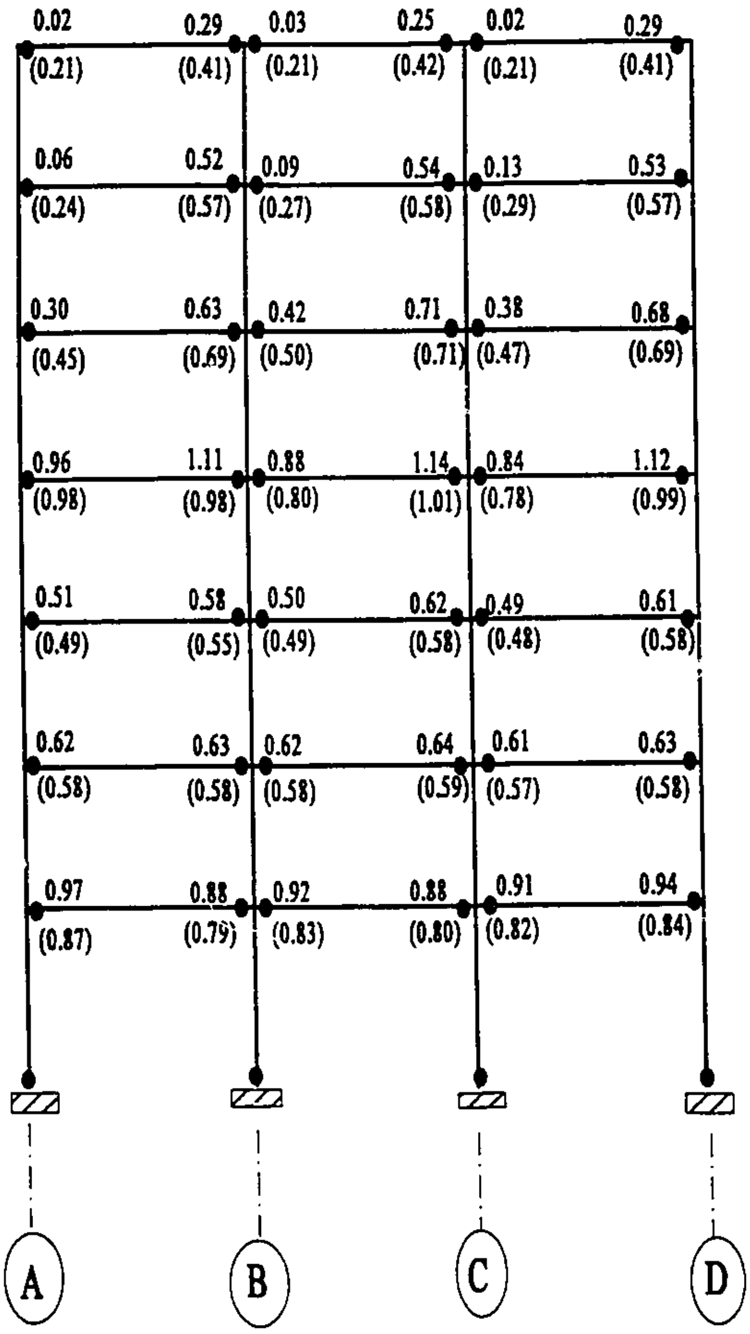

Fig. 6.13 Damage assessment using: a) Daali and Korol's Model (top numerals); b) Modified Park and Ang's Model (Numerals between parentheses).

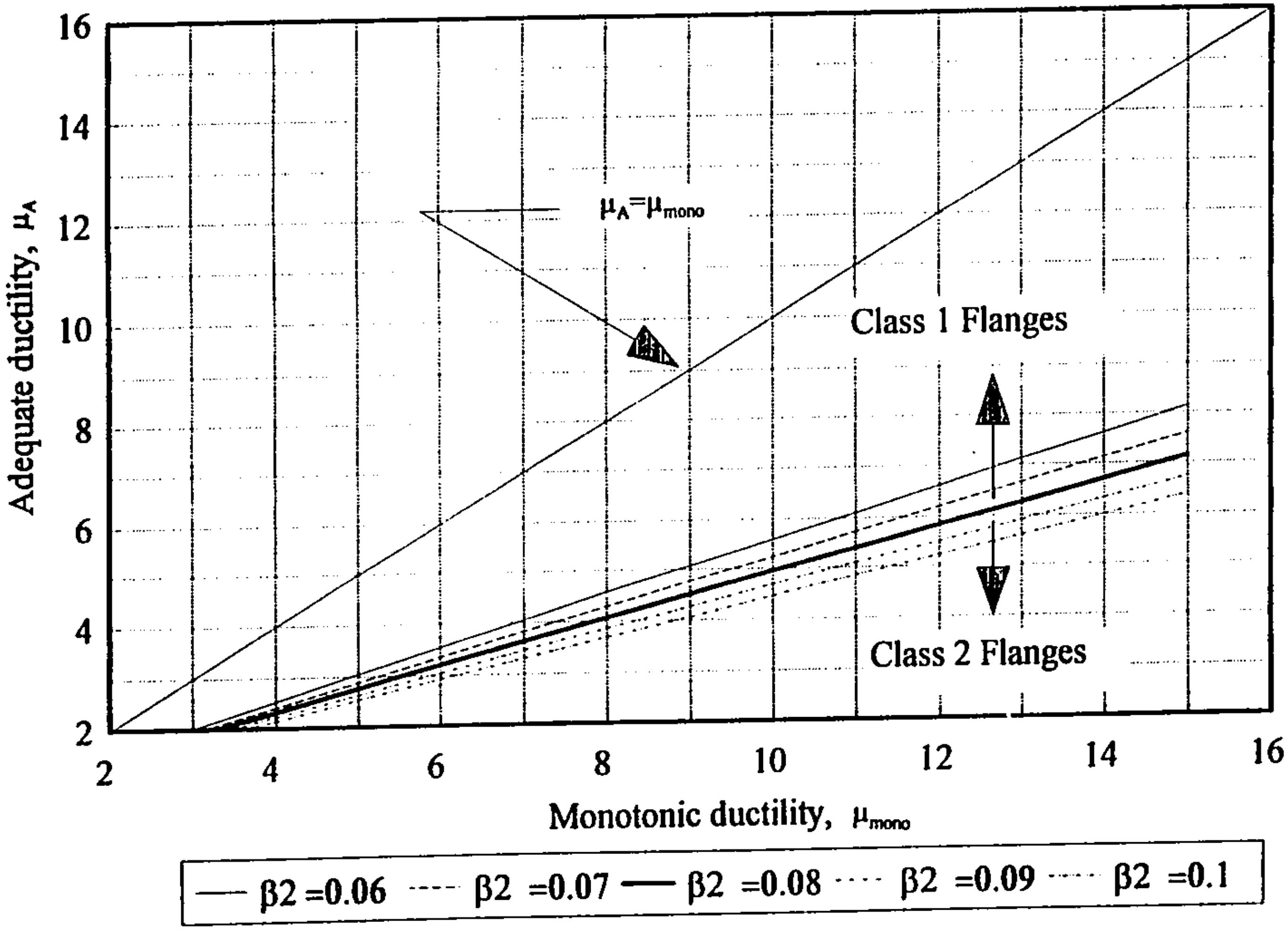

Fig. 6.14 Diagram for adequate ductility values

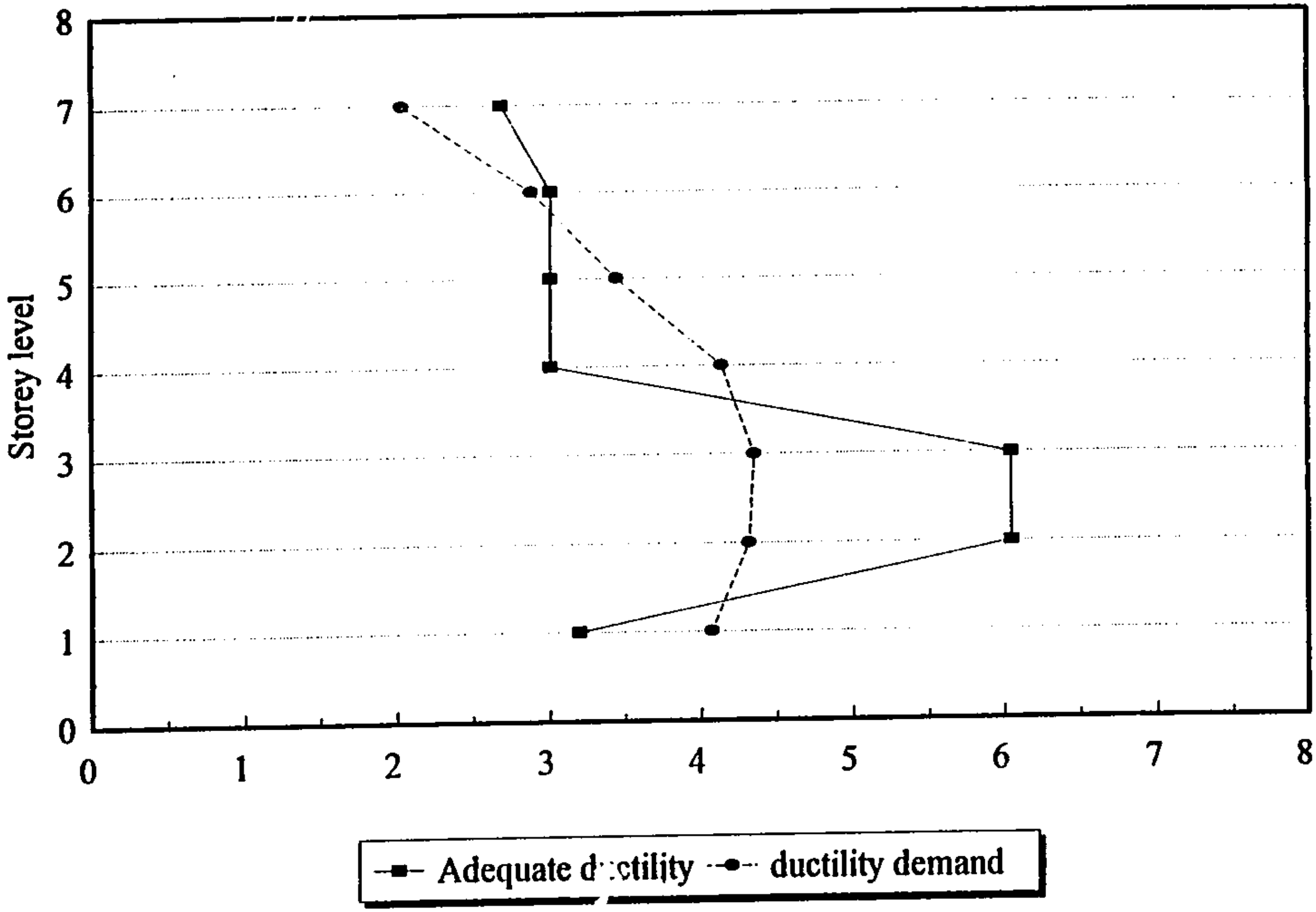

Fig. 6.15 Comparison of ductility demand and adequate ductility values

CHAPTER 7

SUMMARY AND CONCLUSIONS

7.1 Summary of research work

This study was concerned primarily with the assessment of the performance of steel beams and possible ways to enhance their response under a given loading; in particular, most of the emphasis has been devoted to an evaluation of current analysis and design methods dealing with ductility as they pertain to codes of practice. The objective of this part of the investigation was the assessment of a member's rotation capacity as it relates to plate slenderness. To reach this objective, an analytical study was undertaken to link ductility and the associated rotation capacity of a member's critical section. This was followed by a major experimental program in which twenty-two specimens were tested.

Findings from the experimental program resulted in a set of data obtained on locally stiffened and unstiffened beams tested under monotonic, progressively increasing cyclic and constant amplitude cyclic loading. Design guidelines and a simple design methodology for stiffened beams were then developed for establishing the ductility enhancement of locally web stiffened beams.

The research program also examined current techniques used in the prediction of seismic damage with a view towards building on existing knowledge in this area. A damage model was thence developed for the constant amplitude loading case. Two other realistic mathematical models were also formulated for the prediction of damage accumulation in beams of moment resisting frames. The models use the concept of a damage index to evaluate whether a member has suffered deterioration and the extent to which this damage might influence subsequent behaviour.

The above-mentioned models were then used with a non-linear dynamic analysis formulation to assess the performance of members selected on the basis of Canadian code design requirements. Following that, a design criterion for the selection of members anticipated to be used in earthquake prone zones is proposed. In the following we shall examine some of the conclusions reached from this study.

7.2 Conclusions

From the research pertaining to monotonic loading, one may conclude that designing a structure by employing the current local buckling rules (in other words, the flange, web and lateral slenderness ratios treated separately), as specified by most codes of practice, may lead to a selection of members unable to redistribute moments in accordance with plastic design requirements. As such, an approach that defines more accurately the slenderness limits of plate elements in relation to ductility demand at maximum moment was formulated. Furthermore, an effective slenderness quantity, α_e, that enables prediction of ductility at ultimate has been proposed based on empirical evidence, that recognizes the simultaneous coupling effects of the slenderness parameters, and which is defined as a normalized product of the flange, web and lateral slendernesses .

On the basis of the experimental work, a number of conclusions are forthcoming:

a) The use of Herring-bone stiffeners, welded to the flanges and the web, and positioned at about one and half times the buckling half wave-length of the flange is very beneficial to the enhancement of the rotation capacity; an increase from 37% to 63% and sometimes more are shown to be achieveable.

b) Simple design guidelines are proposed for Herring-bone stiffened specimens. If used, an appreciable gain in terms of ductility is likely to be obtained for those sections which are critical.

c) The use of vertically stiffened beams yielded rather indifferent behaviour in terms of improvement of the ductility or rotation capacity compared with unstiffened beams.

f) Stiffened specimens tested under constant amplitude exhibit smaller rates of deterioration than their unstiffened counterparts. The former behave in a superior manner from a strength and ductility point of view when compared to the unstiffened specimens.

A damage model that permits quantification of strength and energy deterioration under constant amplitude type loading has been proposed. The model was demonstrated on a beam element of a structure subjected to a strong motion earthquake. Based on experimental evidence, strength and energy deterioration appear to depend on the combined slenderness parameter, α_c, defined earlier.

Damage inflicted upon a structural member is a result of maximum deformation and repeated cyclic effects. Two damage indices that combine the maximum response and repeated cyclic effects through a calibration factor were developed. Owing to the development of the damage indices and their inclusion in the nonlinear dynamic analysis, the following conclusions may be cited:

a) Besides being based on deterioration from maximum response, damage indices may either include energy deterioration in the form of low cycle fatigue or demand in energy vs capacity in energy. Both approaches are shown to yield acceptable results.

b) Structural elements undergoing large inelastic excursions when subjected to an anticipated earthquake suffer strength and ductility deterioration in the form of low cycle fatigue. Their behaviour consequently differs from that expected in standards applicable to seismic design.

c) Duration as well as intensity of the strong motion plays a major role in the energy and strength degradation of a member and subsequently the structure as a whole as well. It is important therefore to include the effects of strong motion duration in designing a steel structure.

d) A criterion termed "**Adequate ductility**" is proposed for the selection of structural members. In addition to slenderness ratio limits, the selected section would be checked to satisfy a given adequate ductility. This criterion has the advantage of including a-priori the damage that may be inflicted on a member.

7.3 Recommendations for future work

This study has identified a number of areas where considerable future work is needed. One may cite general ideas only; no attempt is made to clearly define the specifics. However, the following general ideas are put forward as a suggestion for future research:

a) Damage quantification models are needed for beam-column members. Besides the displacement amplitude parameter or the ductility parameter, the models would include the effects of the level of axial force.

b) Methods for quantifying damage at the structural level as well as the member level should also be investigated. The developed models should preferably be included in a computer code thus cutting down enormously on the amount of post-processing work.

c) Damage assessment models for quantification of damage due to weld and material cracking should also be studied.

REFERENCES

AISC, (1992), "Seismic Provisions for Structural Steel Buildings," American Inst. of Steel Const., Chicago, USA.

AIJ LSD, (1990), "Standard for Structural Steel Structures," Architecture Inst. of Japan.

Bannantine, J.A. et al. (1990), Fundamentals of Metal Fatigue Analysis, Prentice Hall, Englewood Cliffs, NJ.

Banon H. et al., (1981), "Seismic Damage in Reinforced Concrete Frames", Journal of the Structural Division, ASCE, Vol. 107, No. ST9, pp. 1713-1729.

Banon H. and Veneziano. D., (1982), "Seismic Safety of Reinforced Concrete Members and Structures", Earthquake Eng. and Structural Dynamics, Vol. 10, 179-193.

Beamish, M.J., (1987), "Cyclic Loading Tests on Steel Portal Frame Knee Joints", Bulletin NZNSE, Vol. 20, #1.: 42-51.

Bild, S. & Kulak, G.L., (1991), "Local Buckling Rules for Structural Steel Members", J. Construct. Steel Research 20, 1991, pp. 1-52.

Bleich, F., (1952), "Buckling Strength of Metal Structures", McGraw-Hill Book Co., Inc., New York.

Canadian Standards Association, (1990), "Steel Structures for Buildings-Limit States Design", CAN/ CSA-S16.1-M89. Rexdale, Ontario, Canada.

Castiglioni, C.A. and Goss, G. (1989), "Sulla applicabilita della regola di Miner nella fatica a basso numero di cicli", Politecnico di Milano, 8/89.

Castiglioni, C.A. (1992), "Assessment of seismic damage in steel members using Miner's rule", Politecnico di Milano, 1/92.

Castiglioni, C.A. and Losa, P.L. (1992), "Local buckling and structural damage in steel members under cyclic loads", 10 WCEE, Rotterdam, pp. 2891-2895.

Castiglioni C.A. and Di Palma, (1989), "Experimental Behaviour of Steel Members under Cyclic Bending", Construzioni Metalliche, No. 2/3, pp. 97-114.

Calado, L. and Azevado, J. (1989), "A model for predicting the failure of structural steel elements", J. Construct. Steel Research 14, pp. 41-64.

Calado, L. (1992), "Influence of the cross-section of steel beam columns on the seismic design", Proc. 10 WCEE, Rotterdam, pp. 4469-4474.

Cheng F.Y., Oster K.B. and Kitipitayangkul P., (1979), "Establishment of Ductility Factor Based on Energy Absorption and Evaluation of Present Methods", Proceedings of 3rd Canadian Conference on Earthquake Engineering, Vol. I, pp. 719-744.

Chung Y.S. et al., (1987), "Seismic damage assessment of reinforced concrete members", Technical Report NCEER-87-0022, National Center for Earthquake Engineering Research, State University of New York @ Buffalo.

Cosenza E. et al., (1990), "An Evaluation of the Use of Damage Functionals in Earthquake-Resistant Design", 9th European Conference on Earthquake Engineering, Vol. 2, Moscow, pp. 303-312.

Cosenza et al., (1988), "A Rational Formulation for the q-Factor in Steel Structures," Proc. 9th WCEE, Tokyo, Japan, Vol. V.

Chopra, A.K. & Newmark, N.M., (1980), "Design of Earthquake Resistant Structures," E. Rosenblueth, Pentech Press.

Climenhaga, J.J. and Johnson, R.P., (1972), "Local Buckling In Continuous Composite Beams", The Structural Engineer, # 9, Vol. 50: 367-374.

Daali M.L. and Korol R.M., (1994), "Local buckling rules for rotation capacity", Engineering Journal, American Institute of Steel Construction, 2nd Quarter, Vol. 31, No 2.

Daali M.L. and Korol R.M., (1994), " Damage Assessment in Locally Stiffened Beams under Seismic Type of Loading", Eng. Mech. Symposium of C.S.C.E., Winnipeg.

Daali M.L. and Korol R.M., (1995), "Prediction of local buckling and rotation capacity at maximum moment", Accepted Feb. 1, 1994 in Journal of Constructional Steel Research.

Daali M.L. and Korol R.M., "Adequate ductility in steel beams subjected to earthquake type loading", Accepted in Engineering Structures, The Journal of earthquake, wind and ocean engineering.

Daali M.L. and Korol R.M., "Low cycle damage assessment in steel beams", Accepted in the Journal of Structural Engineering and Mechanics.

Dawe, J.L. and Kulak, G.L., (1984), "Local Buckling of W Shape Columns and Beams", ASCE, Vol. 110, No 6, 1984, pp.1292-1304.

Degenkolb, (1994), "No one expects a new building to fail", EVENTS, Earthquake Reconnaissance News.

Downing, S.D. and Socie, D.F. (1982), "Simple rain-flow counting algorithms", Int. J. Fatigue, pp 31-40.

El Dammatty, A. et al., (1994), "Large displacement formulation for consistent shell element", CANCAM, Kingston, pp. 315-686.

Fajfar P. and Fischinger M., (1990), "A Seismic Design Procedure Including Energy Concept", 9th European Conference on Earthquake Engineering, Vol. 2, Moscow, 312-321.

Fajfar. P., (1992), "Equivalent Ductility Factors, Taking into Account Low-Cycle Fatigue", Earthquake Eng. and Structural Dynamics, Vol. 21, 873-848.

Fukomoto & Itoh, (1992), "Width-to-Thickness Ratios for Plate Elements in Earthquake Engineering Design of Steel Structures," Stability & Ductility of Steel Structures Under Cyclic Loading, By Fukomoto & Lee, CRC Press, pp. 285-296.

Galambos, T.V., (1967), "Summary Report on Deformation and Energy Absorbtion Capacity of Steel Structures in the Inelastic Range", American Iron and Steel Institute, Civil and Environmental Engineering Dept., Sever Institute of Technology, Washington University, St. Louis, Missouri.

Ghobarah, A. et al., (1990), "Behaviour of Extended End-Plate Connections under Cyclic Loading", Engineering struct., Vol. 12: 15-27.

Gyoten, Y. et al. (1974), "Experimental study on low cycle fatigue of a structural member subjected to earthquake loads", Proc. 5 WCEE, Vol. 1, Rome, pp. 1153-1156.

Haaijer G. and Thurlimann B., (1958), "On Inelastic Buckling in Steel", Journal of the Engineering Mechanics Division, ASCE, Proc. paper 1581, pp. 1-48.

Hall, W.J., (1978), "Current Trends in the Seismic Analysis and Design of Structures and Facilities," Dept. of Civil Engng, University of Illinois, Urbana-Champain, Ill, pp. 147-163.

Hanson, R.D., (1966), "Comparison of static and dynamic hysteresis curves", Journal of the Engineering Mechanics Division, ASCE, Vol. 92, No. EM5, pp. 87-113.

Kasiraj, I and Yao, J.T.P. (1969), "Fatigue damage in seismic structures", The Journal of Structural Eng., ASCE, 95, ST8, pp. 655-670.

Kato, B., (1965), "Buckling Strength of plates in the Inelastic Range", IABSE, Vol. 25., pp. 127-141.

Kato, B., (1985), "Rotation Capacity of H-Section Members as Determined by Local Buckling", J. Construct. Steel Research 13, pp. 95-109.

Kato, B., (1990), "Deformation Capacity of Steel Structures," J. Constr. Steel Research 17, pp. 33-94.

Kemp, A.R., (1986), "Factors Affecting the Rotation Capacity of Plastically Designed Members," The Struct. Engineer, Vol 64B, # 2., pp. 28-35.

Kemp, A.R. and Dekker, N.W. (1991) "Available Rotation Capacity in Steel and Composite Beams," The Structural Engrg., Vol. 69, #5, pp. 88-97.

Kemp, A.R., (1986), "Interaction of Plastic Local and Lateral Buckling", The Journal of Structural Engineering, ASCE, Vol. 111, No. 10, pp. 2181-2195.

Krishnasamy, S. and Sherbourne, A.N., (1968), "Response of a plastic hinge to low cycle alternating deflections", Experimental Mechanics, Vol. 8, #6, pp. 241- 248.

Krawinkler, H. and Zohrei, M. (1983), "Cumulative damage in steel structures subjected to earthquake ground motions", Computers and Structures, Vol. 16, #1-4, pp. 531-541.

Krawinkler, H. (1982), "Selection of loading histories for seismic testing of structural components", Proc. Joint Conf. on Experimental Mechanics, Hawaii, pp. 335-341.

Krawinkler, H. (1987), "Performance assessment of steel components", Earthquake Spectra, Vol. 3, #1, pp. 27-41.

Krawinkler, H. et al., (1971), " Inelastic Behaviour of Steel Beam-to-Column Subassemblages", Earthquake Engineering Research Center, University of California, Berkeley, California.

Korol, R.M. and Daali, M.L., (1994), "Rotation Capacity and Energy Absorption Enhancement in Beams under Cyclic Loading", Eng. Mech. Symposium of C.S.C.E., Winnipeg.

Korol, R.M. and Daali, M.L., (1995), "Cyclic behaviour of locally web stiffened W-shape beams", Canadian Journal of Civil Engineering. Vol. 22. February.

Korol R.M. et al., (1990), "Extended End-Plate Connections Under Cyclic Loading: Behaviour and Design", J. of Construct. Steel Research 16, pp. 253-280.

Kuhlmann U., (1989), "Definition of Flange Slenderness Limits on the Basis of Rotation Capacity Values", J. Const. Steel Research 14, pp. 21-40.

Lay M.G., (1965), "Flange Local Buckling in Wide-Flange Shapes", Journal of the Structural Division, ASCE, Vol. 91, No. ST6, pp. 95-116.

Lay, M.G. and Galambos, T.V., (1965), "Inelastic Steel Beams Under Uniform Moment", ASCE, Vol. 91, No ST6, pp. 67-93.

Lay, M.G. and Galambos, T.V., (1967), "Inelastic Beams Under Moment Gradient", ASCE, Vol. 93, No ST1., pp. 381-399.

Lukey & Adams, (1969), "Rotation Capacity of Beams Under Moment Gradient.", ASCE, Vol. 95, #ST6, pp. 1173-1188.

Meskouris, K. and Kratzig, W.B., (1990), "Seismic damage assessment of buildings", Earthquake Resistant Construction and Design, Savidis (Ed.), pp. 427-441.

McCabe S.L. and Hall W.J., (1989), "Assessment of Seismic Structural Damage", Journal of Structural Engineering, Vol. 115, No 9, pp. 2166-2183.

Mitani I. et al., (1977), "Influence of Local Buckling on Cyclic Behaviour of Steel Beam-Columns", Proc. 6WCEE, Vol. III, New Delhi, pp. 3175-3180.

Mizuhata, K. et al. (1977), "Study on low cycle fatigue of structural frames due to randomly varying load", 6 Proc. WCEE, New Delhi, India, pp. 3031-3036.

Miner, M.A. (1945), "Cumulative damage in fatigue", Journal of the Mechanical Division, ASME, pp. 159-164.

Neale, K. and Schroeder, J. (1971), "Instability under cycles of plastic deformations", in H. Leipholz, Ed., Instability of continuous systems, Springer-Verlag, Berlin, pp. 329-333.

NBCC, (1990), "National Building Code of Canada. National Research Council of Canada", Associate committee on the National Building Research Code, National Research Council of Canada, Ottawa, Canada.

Naumoski et al., (1993), "Representative Ensembles of Strong Motion Earthquake Records", McMaster University, EERG Report 93-1.

Newmark, N.M. and Hall, W.J., (1982), "Earthquake Spectra and Design," Earthquake Eng. Research Inst., El Cerrito, Calif.

NEHRP, (1992), "Recommended Provisions for the Development of seismic Regulations for Buildings," Building Seismic Safety Council, Washington, D.C.

NZS 4203, (1984), "New Zealand Standards", Standards Association of New Zealand, New Zealand.

Park Y.J. and Ang, (1985), "A. Mechanistic Seismic Damage Model for Reinforced Concrete", Journal of Structural Engineering, Vol. 111, No 4, pp. 722-739.

Packer, J.A. and Morris, L.J., (1977), "A Limit State Design Method for the Tension Region of Bolted Beam-to-Column Connections", The Structural Engineer, SS(10), pp. 446-458.

Powell G. and Allahabadi R., (1988), "Seismic Damage Prediction by Deterministic Methods: Concepts and Procedures", Earthquake Eng. and Structural Dynamics, Vol. 16, pp. 719-734.

Popov E.P. and Stephen R.M., (1970), "Cyclic Loading of Full-Size Steel Connections", Report No. UCB/EERC-70/03, EERC, University of Berkeley, CA.

Popov E.P. and Bertero V.V., (1973), "Cyclic Loading of Steel Beams and Connections", Journal of the Structural Division, ASCE, Vol. 99, No. ST6, pp. 1189-1205.

Popov E.P. and Pinkney. B., (1969), "Cyclic yield Reversal in Steel Building Connections", Journal of the Structural Division, ASCE, Vol. 95, No. ST3, pp. 327-353.

Popov, E.P., (1980), "Seismic Behaviour of Structural Subassemblages," ASCE, Vol. 106, # ST7, pp. 75-93.

Popov, E.P. and Tsai, K.C., (1989), "Performance of Large Seismic Steel Moment Connections Under Cyclic Loads", Engineering Journal, AISC, 2nd Quarter, pp. 51-60.

Prakash. V. and Powell G.H., (1992), "DRAIN-2DX User Guide", Dept. of Civil Eng. University of California. Berkeley, California.

Redwood R.G. (1990), " Earthquake resistant design of steel moment resisting frames.", Canadian Journal of Civil Eng. 17, pp. 659-667.

Sherbourne, A.N. (1963), "Some preliminary experiments on the behaviour of ductile structures under repeated loads", Experimental mechanics, Vol. 3, #5, pp. 119-128.

Tavernelli, J.F. and Coffin, L.F. (1962), "Experimental support for generalized equation predicting low cycle fatigue", ASME, Paper 61, pp. 533-541.

Takanashi et al., (1973), "Failure of Steel Beams Due to Lateral Buckling Under Repeated Loads", IABSE, Lisbon, pp. 163-169.

Thurston, S.J., (1982), "Local Buckling of Universal Beam Flanges," Bulletin NZNSE, Vol. 15, # 2, pp 96-96.

Uniform Building Code, (1991), "International conference of Building Officials", Whittier, CA,.

Uang, C.M., (1991), "Establishing R (or R_w) and C_d Factors for Building Seismic Provisions", ASCE, Vol. 117, #1, pp. 19-29.

Yamada, M. (1969), "low cycle fatigue fracture limits of various kinds of structural members subjected to alternately repeated plastic bending under axial compression as an evaluation basis or design criteria for aseismic capacity", Proc. 4 WCEE, Santiago de Chile, pp. 137-151.

Walpole, W.R. and Butcher, G.W., (1985), "Beam Design", Bulletin NZNSEE, Vol. 18, #4.: pp. 337-343.

Wierzbicki, T. and Jones, N., (1989), "Structural Failure", Wiley Interscience.